UNIVERSITY OF LONDON THESIS

Degree phil Year 2007 Name of Author REBECCA SARA SAMSON

Optimisation of quantitative Magnetisation Transfer (qMT) MRI to study restricted protons in the living human brain

Rebecca Sara Samson

NMR Research Unit

Institute of Neurology

University College London

Queen Square

London

WC1N 3BG

United Kingdom

ProQuest LLC
789 East Eisenhower Parkway
P.O. Box 1346
Ann Arbor, MI 48106-1346

Declaration

I, Rebecca Sara Samson, confirm that the work presented in this thesis is my own. Where information has been derived from other sources, I confirm that this has been indicated in the thesis.

Acknowledgements

I would like to thank my supervisors Prof Paul Tofts and Dr Mark Symms, and also Dr Claudia Wheeler-Kingshott, who supervised me in my first year, for all their help, advice and encouragement and for all that I have learnt from them throughout the course of my PhD. I would also like to thank all the other physicists and clinicians of the NMR Research Unit who have answered my questions and helped me with my work.

I would also like to the Brain Research Trust for funding my research and also for supporting my attendance at various conferences to present my work.

Thanks also to all my friends and family for their continued support during this time.

Abstract

Magnetisation Transfer (MT) imaging exploits magnetisation exchange between 'free' protons and 'restricted' protons attached to macromolecules in biological tissue, to indirectly provide access to the restricted protons, which are invisible using conventional MR imaging techniques.

The Magnetisation Transfer Ratio (MTR) is calculated from a pair of images with different MT "weightings", however it reflects a complex combination of biological and acquisition dependent factors. Quantitative MT (qMT) imaging allows the examination of fundamental parameters underlying the MT exchange process independently of sequence details.

The effect of B_1 errors on MTR measurements was investigated, both theoretically and experimentally, and a method for correcting for B_1 errors was proposed, based on the collection of a B_1 map in addition to MTR data.

The temperature dependence of many quantitative MR properties may cause systematic errors in phantom Quality Assurance (QA) measurements, which could have an impact on the interpretation of quantitative changes observed in long-term clinical studies. Many traditional thermometry methods are unsuitable for use in an MRI scanner. Using localised ^{1}H-MRS acquisition sequences routinely available on clinical MRI scanners, and commonly available analysis packages, internal thermometry in phantoms using DSS (sodium 3-(trimethylsilyl)propane-1-sulphonate)) as a chemical shift reference was shown to be realistic, with a minimum detectable temperature difference of 100 (±20) mK.

The qMT acquisition parameters (combinations of MT pulse amplitude and offset frequency) were optimised, via the minimisation of the Cramer-Rao Minimum Variance

Bound (CRMVB). Compared to a conventional acquisition, the optimisation enables less data to be acquired, reducing acquisition time without compromising uncertainties in estimated parameters. Alternatively, for the same number of MT-weighted data points, the parameter map noise could be reduced. This analytical approach was verified numerically, using Monte Carlo simulations, and experimentally, and optimised acquisition schemes were shown to be applicable to a range of brain tissues.

Table of Contents

List of Figures

List of Tables

Glossary of medical/biological terms

- **Action potentials**

An action potential is a rapid change in the membrane potential due to a change in the membrane permeability. Such controlled changes in the permeabilities and therefore in the membrane potentials of nerves and muscles are central to their function. Action potentials are the electrical nerve impulses carried in the surface membrane of the axon.

- **Astrocytes**

An astrocyte is a cell comprising one of the major categories of neuroglia. Astrocytes are found in both the grey and white matter of the Central Nervous System. Astrocytes fill in the spaces that would otherwise exist between neurons and their processes, physically supporting neurons in the brain, and may also be involved in neuronal metabolism, potentially providing nutrients for neurons and possibly taking part in information storage processes.

- **Astrocytic hyperplasia**

Hyperplasia is the increased production and growth of normal cells in a tissue or organ. The affected part becomes larger but retains its normal form.

- **Atrophy**

Atrophy is the wasting away of a normally developed organ or tissue due to the degeneration of cells. Spinal cord atrophy is defined as a cord area of 2 standard deviations less than the mean for normal controls.

- **Autoimmune**

Autoimmune diseases arise from an overactive immune response of the body against substances and tissues normally present in the body. In other words, the body attacks its own cells.

- **Axon**

There are two definitions for an axon:

1. A neuronal protoplasmic process that conducts impulses away from the cell body. Usually a major process of the cell.
2. Any of the fibres in the nerve, spinal root or central tract

- **Axonal loss/damage**

Axonal loss and damage is strongly associated with the development of persistent, progressive functional impairment in Multiple Sclerosis (MS). Substantial axonal loss and injury occurs in MS in acute and chronic lesions. MR spectroscopy (MRS) has allowed the investigation of axonal loss and damage in vivo by allowing the quantification of N-acetylaspartate (NAA), an amino acid localised almost exclusively to neurons within the adult CNS.

- **Axoplasm**

The semi-fluid material of which the axon of a nerve cell is composed. It flows slowly outwards from the cell body.

- **Blood-brain barrier (BBB)**

This is a semi-permeable barrier that isolates the central nervous system from the bloodstream, allowing solutions necessary for it to function to pass through it, but preventing larger molecules/solids. This separates brain tissue from circulating blood. In MS, the breakdown of the blood-brain-barrier is a localised phenomenon that can occur either in fresh active plaques or on the periphery of chronic reactivated plaques.

- **Central Nervous System (CNS)**

The central nervous system includes the brain, optic nerves and spinal cord, as opposed to the cranial and spinal nerves and the autonomic nervous system, which together form the peripheral nervous system. The CNS is responsible for the integration of all nervous activities.

- **Central Pontine Myelinolysis (CPM)**

Central pontine myelinolysis (CPM) is a syndrome in which neurologic deficits occur after rapid correction of hyponatremia. CPM usually occurs in young to middle-aged adults and is often associated with alcohol abuse or malnutrition. Signs and symptoms usually begin 3 days after the start of sodium replacement and consist of changes in mental status, dysarthria and other signs of corticobulbar dysfunction, and spastic quadriplegia.

- **Choroid plexus**

The choroid plexus is a network of nerves and blood vessels between the retina and the sclera.

- **Contusions**

Contusions are 'bruising' of the brain resulting from head injury or trauma.

- **Cerebrospinal Fluid (CSF)**

The cerebrospinal fluid is a clear fluid that fills the ventricles and subarachnoid space in the brain and the ventricular system of the brain and spinal cord, and is produced by the choroid plexus, a tissue that partially lines the ventricles, and also by the ependymal lining of the brain's ventricles. It acts like a buffer for the cortex

- **Demyelination**

Demyelination is the damage to myelin sheaths, which surround nerve fibres in the central or peripheral nervous system. Demyelination, the characteristic pathological feature of MS, produces conduction block, which is the principal mechanism for functional loss, but does not necessarily or even usually lead to permanent loss of function. Neurologic function can fully recover after acute inflammation, despite persistent demyelination.

- **Dendrite**

Dendrites are typically short, branching processes and one or more arise from each nerve cell. The dendrites convey impulses towards the cell body.

- **Dura mater**

The dura mater is the outermost of the three meninges surrounding the brain and spinal cord.

- **Expanded Disability Status Scale (EDSS)**

The Extended Disability Status Scale (EDSS) was devised by Kurtzke in 1983. This non-linear scale quantifies a mixture of impairment and disability, and is heavily weighted towards locomotor disability, which is often due to spinal cord disease.

- **Epilepsy**

Epilepsy is a disorder of brain function characterised by recurrent seizures that have a sudden onset. The term idiopathic is used to describe epilepsy that is not associated with structural damage to the brain. Seizures may be generalised or partial.

- **Extracellular space**

The extracellular space is the space situated outside cells; for example, extracellular fluid is the fluid surrounding cells.

- **Glia (glial cells)**

Glia are between 5 and 10 times as numerous as neurons and comprise the supporting tissue of the CNS. Not all the functions of glia are known, but some of their functions include repair and maintenance, physical support, development and chemical regulation. There are three main types of glial cell; astrocytes, oligodendrocytes and microglia.

Glial cells, especially oligodendrocytes, are often destroyed at the sites of multiple sclerosis lesions, and this also postpones or even prevents repair of myelin.

- **Glioma**

A glioma is any tumour of non-nervous cells (glia) in the nervous system, but the term is sometimes used for all tumours in the CNS.

- **Gliosis**

Gliosis is the proliferation of astrocytes in response to disease/injury. It is one means of scar formation in the Central Nervous System. (glial means of/pertaining to neuroglia).

Gliosis occurs after demyelination, and gliosis at sites of demyelination, as indicated by increased signal on PD or T2-weighted images, is compatible with nerve conduction, which although slow, is often associated with virtually normal clinical function.

- **Grey/white matter (GM/WM)**

Grey matter is the cellular tissue in the nervous system. The brain and spinal cord are composed mainly of nerve cells (grey matter) and their conducting fibres (white matter) gathered into well-defined zones. The spinal cord is grey in the central column, surrounded by white matter. The brain consists of central grey matter clumped in nuclei, and an additional grey matter zone (cortex) over the surface of the cerebrum and cerebellum. Grey matter contains the cell bodies of neurons, each with a nucleus, embedded in a neuropil made up of delicate neuronal and glial processes. White matter consists primarily of long processes (axons) of neurons, the majority of which are surrounded by fatty myelin sheaths, which serve to increase the velocity of conduction of nerve impulses (ionic currents).

The cells of motor neurons and connector neurons lie within the CNS forming the *grey matter.*

The processes of the neurons which run through the CNS constitute the *white matter.*

- **Human Immuno-deficiency Virus (HIV) encephalitis**

Human Immuno-deficiency Virus is the retrovirus responsible for AIDS. Encephalitis is inflammation affecting the brain, which can be caused by a viral or bacterial infection or be part of an allergic response to a systemic viral illness or vaccination; here it is caused by the HIV virus.

- **Hydrocephalus**

Hydrocephalus is an abnormal increase in the amount of cerebrospinal fluid (CSF) within the ventricles of the brain. In children, the head size increases. In adults, the intracranial pressure rises, causing drowsiness and vomiting.

- **Infarction**

Infarction is the death of part or the whole of an organ that occurs when the artery carrying its blood supply is obstructed by a blood clot (thrombus) or an embolus. A small localised area of dead tissue produced as a result of an inadequate blood supply is known as an infarct.

- **Inflammation**

Inflammation is the response of any part of the body to injury/infection etc.

- **Leber's Hereditary Optic Neuropathy (LHON)**

Leber's Hereditary Optic Neuropathy is a rare disease which presents with rapid, progressive optic neuropathy, classically in young men between 20 and 30 years of age, but occasionally in women. Blurred vision and loss of central initially appear in one eye, with the other eye affected within days, weeks or months.

- **Lesion**

A lesion is a zone of tissue with impaired function as a result of damage by disease or wounding. Examples of primary lesions include abcesses, ulcers and tumours.

- **Lymphocyte**

A lymphocyte is a leukocyte of blood, bone marrow and lymphatic tissue. Lymphocytes play a major role in both cellular and humoral immunity.

- **Macrophage**

A macrophage is a cell found in many tissues in the body which is derived from the blood monocyte and has an important role in host defence mechanisms. It phagocytises and kills many bacteria and is the site of infection for a number of

intracellular parasites. Macrophages are a component of the inflammatory response, often as a result of bacterial invasion of the tissues.

- **Meninges**

The meninges separate the central nervous system from the peripheral nervous system.

- **Meningioma**

A tumour arising from the fibrous coverings of the brain and spinal cord (meninges).

- **Meningitis**

Meningitis is the inflammation of the meninges due to infection by viruses or bacteria or fungi.

- **Metastase**

Metastasis is the distant spread of malignant tumour from its site of origin. This occurs through three main routes: through the bloodstream, through the lymphatic system, across body cavities.

- **Microglia**

Microglia are derived from blood monocytes or macrophages. Resting microglial cells are equivalent to the resident macrophages of other tissues and can acquire phagocytic properties to protect the neurons of the CNS when the central nervous system is afflicted by injury or disease. They can also multiply in case of damage in the brain They may also be involved, although less conspicuously, in protecting the nervous tissue from viruses, microorganisms, and the formation of tumours.

- **Multiple Sclerosis (MS)**

Multiple Sclerosis is a chronic disease of the nervous system which affects young and middle age adults. The myelin sheaths surrounding nerves in the brain and spinal cord are damaged (demyelination), which affects the function of the nerves involved. The course of the illness is usually characterised by recurrent relapses followed by remissions, but a small proportion of patients run a chronic progressive course. The disease affects different parts of the brain and spinal cord, resulting in typically scattered symptoms.

- **Myelin**

Myelin is a complex material formed of protein and phospholipid that is laid down as a sheath around the axons of certain neurones, known as myelinated nerve fibres. The material is produced and laid down in concentric layers by Schwann cells at regular intervals along the nerve fibre. Myelinated nerves conduct impulses more rapidly than non-myelinated nerves.

- **N-acetyl aspartate (NAA)**

N-acetylaspartate is an amino acid localised almost exclusively to neurons within the adult central nervous system. Brain NAA concentration is used as a specific marker of axonal loss/damage and dysfunction.

- **Neoplasm**

Any new and abnormal growth; benign or malignant tumour is described as a neoplasm.

- **Nerve fibres**

Nerve fibres are like electrical cables. Signals are sent from the brain and spinal cord to muscles with "instructions", and sensory information returns to the brain.

- **Neurons**

A neuron is a nerve cell, one of the basic functional units of the nervous system: a cell specialised to transmit electrical nerve impulses and so carry information from one part of the body to another. Each neuron has an enlarged portion, the cell body (perikaryon, or soma), containing the nucleus; from the body extend several processes (dendrites) through which impulses enter from their branches. A longer process, the nerve fibre (axon) extends outwards and carries impulses away from the cell body. This is normally unbranched except at the nerve ending. The point of contact between one neuron and another is known as a synapse.

- **Neuroma**

A neuroma is any tumour derived from the cells of the nervous system.

- **Neurotransmitter**

Neurotransmitters are chemicals that are used to relay, amplify and modulate electrical signals between a neuron and another cell.

- **Node of Ranvier**

In myelinated fibres, the node of Ranvier is the interval between the plasma membrane systems of two Schwann cells. Voltage-gated ion channels are present in the neurolemma only at node positions. Consequently the action potential skips electrically from node to node and the transmission of a nerve impulse along a myelinated fibre is called salutatory conduction, and depends on adequate electrical insulation, i.e. the myelin sheath, between the internodal axoplasm and the extracellular fluid. Therefore the internodal spacing has a bearing on the conduction rate of the nerve impulse, and the thicker and longer the nerve fibre, the longer the internodes.

- **Oedema**

Oedema is the build-up of excess tissue fluid around a local disturbance.

- **Oligodendrocytes**

Oligodendrocytes are equivalent to the Schwann cells of the peripheral nerves – they are responsible for forming and maintaining the insulating myelin sheaths surrounding axons within the CNS, thus allowing nerve impulses to propagate more efficiently.

- **Parenchyma**

Parenchyma is the functional part of an organ, as opposed to the supporting tissue (stroma).

- **Pathology**

Pathology is the study of chemical changes in the body related to the cause of disease and of the way in which the normal structure and function of the body are altered by it.

- **Peripheral Nervous System (PNS)**

The peripheral nervous system consists of nerves and ganglia, and three layers of connective tissue that form the meninges (the outermost of which is the dura mater). The meninges separate the central nervous system from the peripheral nervous system.

- **Perivascular cellular infiltration**

Perivascular cellular infiltration is the abnormal entry of a substance into a cell.

- **Plasma**

Plasma is the fluid component of lymph.

- **Primary Progressive Multiple Sclerosis (PPMS)**

This subtype of MS is characterised by progressive deterioration from the outset, without any relapses or remissions.

- **Progressive Multifocal Leukoencephalopathy (PML)**

Progressive Multifocal Leukoencephalopathy is an opportunistic viral infection of the central nervous system associated with conditions that impair cell-mediated immunity (e.g. AIDS and other immunologic deficiency syndromes, haematologic neoplasms, immunosuppression, and collagen diseases). The disease is characterised by multiple areas of demyelination, resulting in such clinical manifestations as dementia, ataxia, visual disturbances; and other focal neurological deficits, generally progressing to a vegetative state within 6 months.

- **Remyelination**

Pathological studies reveal remyelination (production of new myelin) in a substantial number of lesions, but the new myelin is morphologically different and it is conceivable that such remyelinated lesions will still produce abnormal MR signal, even though there is no functional deficit.

Remyelination and repair of axonal dysfunction probably contribute to functional recovery. Most commonly, remyelination is scanty and confined to the edges of lesions.

- **Relapsing-remitting Multiple Sclerosis (RRMS)**

This subtype of MS is characterised by a history of relapses and remissions, without progressive deterioration; the illness is of less than 10 years duration.

- **Schwann cells**

Schwann cells in the peripheral nervous system compose the neurolemma and are equivalent to the oligodendrocytes of the CNS.

- **Secondary Progressive Multiple Sclerosis (SPMS)**

After an initially relapsing-remitting course, MS patients may enter a phase of progressive deterioration for at least six months, with or without superimposed relapses, known as secondary progressive MS.

- **Synapse**

Neurons communicate with one another at 'terminals' known as synapses. Neurotransmitters released by axonal terminals evoke changes in the membrane of the postsynaptic cell, either stimulating or inhibiting it.

- **Wallerian degeneration**

Wallerian degeneration is the degeneration of a ruptured nerve fibre that occurs within the nerve sheath distal to the point of severance.

List of Abbreviations

- **α**

Flip angle

- **α_E**

Ernst angle

- **ADC**

Apparent Diffusion Coefficient

- **B_0**

Static magnetic field

- **B_1**

Applied oscillatory (rotating) magnetic field

- **BBB**

Blood Brain Barrier

- **B_{eff}**

Effective field

- **BMS**

Benign Multiple Sclerosis

- **BSA**

Bovine Serum Albumin

- **CIS**

Clinically Isolated Syndrome

- **CNR**

Contrast-to-noise ratio

- **CNS**

Central Nervous System

- **CPM**

Central Pontine Myelitis

- **CPMG**

Carr-Purcell-Meiboom-Gill

- **CS**

Chemical Shift

- **CSA**

Chemical Shift Anisotropy

- **CSE**

Conventional spin echo

- **CSF**

Cerebrospinal fluid

- **CW**

Continuous Wave

- **CWPE**

Continuous Wave Power Equivalent

- **δ**

Chemical shift

- **δ_{H2O}**

Chemical shift of water

- **δ_{NAA}**

Chemical shift of NAA

- **δ_{DSS}**

Chemical shift of DSS sodium salt

- **Δf**

Offset frequency (of MT pulse)

- **D**

Diffusion coefficient

- **DAM**

Double Angle Method

- **DSS**

Sodium 3-(trimethylsilyl)propane-1-sulphonate)

- **E**

Energy

- **EAE**

Experimental Allergic Encephalomyelitis

- **EDSS**

Extended Disability Status Scale

- **EEG**

Electroencephalogram

- **ENR_{sat}**

Effective Nutation Rate

- **EPI**

Echo Planar Imaging

- **ETL**

Echo Train Length

- **φ**

Phase

- **f**

Restricted proton fraction

- **F**

Fraction of restricted protons relative to free protons

- **FA**

Fractional anisotropy

- **FA**

Flip angle

- **FFT**

Fast Fourier Transform

- **FID**

Free Induction Decay

- **FIS**

Free Induction Signal

- **FLAIR**

Fluid-Attenuated Inversion Recovery

- **FLASH**

Fast Low Angle Shot

- f_m

Myelin water fraction

- **FOV**

Field-of-View

- **FSE**

Fast Spin Echo.

- **FT**

Fourier Transform

- **FWHM**

Full Width at Half Maximum

- **γ**

Gyromagnetic ratio

- **G**

Magnetic field gradient

- **Gd-DTPA**

Gadolinium diethylene triamine pentaacetic acid

- **GM**

Grey matter

- $g_i(2\pi\Delta f)$

Lineshape for i spins

- **HIV**

Human Immuno-deficiency Virus

- **IR**

Inversion Recovery

- **ISIS**

Image Selected In vivo Spectroscopy

- **κ**

Thermal conductivity

- **k**

Boltzmann's constant k (1.3805×10^{-23} JK^{-1})

- $\mathbf{k_f}$

Pseudo-first order rate constant for Magnetisation Transfer (free to restricted pool)

- $\mathbf{k_r}$

Rate constant for Magnetisation Transfer from restricted to free pool

- **μ**

Magnetic moment

- **M**

Magnetisation

- $\mathbf{M_0}$

Equilibrium magnetisation

- $\mathbf{M_0^A}$

A pool magnetisation in the absence of MT saturation

- $\mathbf{M_0^B}$

B pool magnetisation in the absence of MT saturation

- **MCI**

Mild Cognitive Impairment

- **MR**

Magnetic Resonance

- **MRA**

Magnetic Resonance Angiography

- **MRI**

Magnetic Resonance Imaging

- **MRS**

Magnetic Resonance Spectroscopy

- **MS**

Multiple Sclerosis

- **MT**

Magnetisation Transfer

- **MTC**

Magnetisation Transfer Contrast

- **MTI**

Magnetisation Transfer Imaging

- **MTR**

Magnetisation Transfer Ratio

- M_{XY}

Transverse magnetisation

- M_Z

Longitudinal Magnetisation

- M_Z^A (or M_z^f)

Longitudinal Magnetisation of free proton pool in MT

- M_Z^B (or M_z^r)

Longitudinal Magnetisation of restricted proton pool in MT

- **NAA**

N-acetylaspartate

- **NABT**

Normal Appearing Brain Tissue

- **N_{av}**

Number of averages

- **NAWM**

Normal Appearing White Matter

- **NEX**

Number of excitations = number of signal acquisitions averaged to improve SNR.

- **NMR**

Nuclear Magnetic Resonance

- **NSR**

Noise-to-signal ratio

- **OIL**

Optimised Interleaved

- **PD**

Proton Density

- **PRESS**

Point RESolved Spectroscopy

- **PPMS**

Primary Progressive Multiple Sclerosis

- **qMT**

Quantitative Magnetisation Transfer

- **R**

Rate of exchange of magnetisation (cross relaxation) between 2 pools in MT

- **R_A**

Longitudinal relaxation rate of pool A (free pool) (i.e. $1/T_1^A$) (equivalent to R_1^f)

- **RARE**

Rapid Acquisition with Relaxation Enhancement

- **R_B**

Longitudinal relaxation rate of pool B (restricted pool) (i.e. $1/T_{1A}$)

- **RF**

Radio-Frequency

- **rms**

Root mean square

- **RM_0^A**

Rate of exchange of magnetisation from pool B to pool A (equivalent to k_r)

- **RM_0^B**

Rate of exchange of magnetisation from pool A to pool B (equivalent to k_f)

- **ROI**

Region of Interest.

- **R_{RFA}**

RF absorption rate for pool A (free pool) (rate at which longitudinal magnetisation is lost due to direct saturation of the free pool)

- **R_{RFB}**

RF absorption rate for pool B (restricted pool) (rate at which longitudinal magnetisation is lost due to direct saturation of the restricted pool)

- **RRMS**

Relapsing-Remitting Multiple Sclerosis

- **σ**

(Fractional) chemical shift relative to a reference compound (measured in ppm)

- **σ_{NAA}**

(Fractional) chemical shift relative to NAA (N-acetyl aspartate)

- **σ_{DSS}**

(Fractional) chemical shift relative to DSS sodium salt (sodium 3-(trimethylsilyl)propane-1-sulphonate))

- **σ_{SD}**

Uncertainty in the standard deviation (SD)

- **S**

Signal

- **SAR**

Specific Absorption Rate

- **SD**

Standard Deviation

- **SE**

Spin Echo

- **SEM**

Standard error in the mean

- **SLE**

Systemic lupus erythematous

- **SNR**

Signal-to-noise ratio

- **SPGR**

Spoiled Gradient Echo

- **SPM**

Statistical Parametric Mapping

- **SPMS**

Secondary Progressive Multiple Sclerosis

- **STIR**

Short TI Inversion Recovery

- **STEAM**

Stimulated Echo Acquisition Mode

- **SVS**

Single Voxel Spectroscopy

- τ_c

Correlation time for molecular tumbling (rotations/translations)

- **T**

Tesla

- **T**

Absolute temperature (measured in K)

- **T_c**

Temperature measured in °C

- **T_1**

Longitudinal relaxation time

- **T_1^A**

Longitudinal relaxation time of pool A (equivalent to T_{1f})

- **T_1^B**

Longitudinal relaxation time of pool B (equivalent to T_{1r})

- **$T_1^A{}_{sat}$**

The reduced longitudinal relaxation time in the presence of MT saturation

- **T_2**

Transverse relaxation time

- **T_2^***

Transverse relaxation time incorporating dephasing due to B_0

- **T_2^A**

Transverse relaxation time of pool A (equivalent to T_2^f)

- **T_2^B**

Transverse relaxation time of pool B (equivalent to T_2^r)

- **TE**

Echo Time

- **TE_{eff}**

Effective echo time

- **TI**

Inversion Time

- **TJ**

Delay or 'skip' time in an inversion recovery sequence

- **TM**

Mixing time

- **TOF**

Time-of-flight

- **TR**

Repetition Time

- **TR'**

Time between successive pulses, i.e. TR/no. of slices

- **TSE**

Turbo Spin Echo

- **VOI**

Volume of interest

- ω

Angular frequency

- ω_0

Angular frequency of $\mathbf{B_0}$

- ω_1

Angular frequency of $\mathbf{B_1}$

- **WM**

White Matter

- **1D**

One dimensional

- **2D**

Two dimensional

- **3D**

Three dimensional

List of Publications

Accepted papers

- Assessment and correction of B_1 induced errors in Magnetisation Transfer Ratio Measurements; S. Ropele, M. Filippi, P. Valsasina, T. Korteweg, F. Barkhof, P. S. Tofts, **R. S. Samson**, F. Fazekas: Magnetic Resonance in Medicine; 53(1): 134-140, 2005.

- A simple correction for B_1 inhomogeneities in Magnetisation Transfer Ratio (MTR) measurements; **R. S. Samson**, C. A. M. Wheeler-Kingshott, M. R. Symms, D. J. Tozer, P. S. Tofts: Magnetic Resonance Imaging; 24(3): 255-263, 2006.

- ^{1}H-MRS internal thermometry in test-objects (phantoms) to within 0.1K for quality assurance in long-term quantitative MR studies; **R. S. Samson**, J. S. Thornton, M. A. McLean, S. C. R. Williams, P. S. Tofts: NMR in Biomedicine; 19(5): 560-565, 2006.

Submitted papers

- Enhanced precision of quantitative Magnetisation Transfer (qMT) parameter estimation using improved acquisition schemes; **R. S. Samson**, M. R. Symms, M. Cercignani, D. J. Tozer, P. S. Tofts (submitted to MAGMA: Magnetic Resonance in Physics, Biology and Medicine)

Accepted abstracts

- A simple correction for B_1 inhomogeneities in Magnetisation Transfer Ratio measurements; **R. S. Samson**, C. A. M. Wheeler-Kingshott, P. S. Tofts; Book of Abstracts, 9th Annual Meeting of the British Chapter of the International Society for Magnetic Resonance in Medicine, 2003, London.

- A simple correction for B_1 inhomogeneities in MTR measurements; **R. S. Samson**, C. A. M. Wheeler-Kingshott, D. J. Tozer, P. S. Tofts; Book of abstracts: Twelfth Annual Meeting of the International Society for Magnetic Resonance in Medicine, 2004, Kyoto, Japan; 2703.

- Absolute Internal Thermometry in MRI Phantoms using ^{1}H-MRS to sub-degree level precision; **R. S. Samson**, J. S. Thornton, C. A. M. Wheeler-Kingshott, M. A. McLean, S. C. R. Williams, P. S. Tofts; Book of abstracts: 10th Annual Meeting of the British Chapter of the International Society for Magnetic Resonance in Medicine, 2004, Edinburgh.

- Absolute Internal Thermometry in MRI Phantoms using ^{1}H-MRS to sub-degree level precision; **R. S. Samson**, J. S. Thornton, C. A. M. Wheeler-Kingshott, M. A. McLean, S. C. R. Williams, P. S. Tofts; Book of abstracts: 21st Annual Meeting of the European Society for Magnetic Resonance in Medicine and Biology, 2004, Copenhagen, Denmark.

- Absolute Internal Thermometry in MRI Phantoms using ^{1}H-MRS to 50 milli-degree level precision; **R. S. Samson**, J. S. Thornton, C. A. M. Wheeler-Kingshott, M. A. McLean, S. C. R. Williams, P. S. Tofts; Book of abstracts: Thirteenth Annual Meeting of the International Society for Magnetic Resonance in Medicine, 2005, Miami, USA; 2511.

- Optimisation of quantitative MT (qMT) sequence acquisition parameters; **R. S. Samson**, M. R. Symms, P. S. Tofts; Book of abstracts: 11th Annual Meeting of the British Chapter of the International Society for Magnetic Resonance in Medicine, 2005, Oxford, UK

- Optimisation of quantitative MT (qMT) sequence acquisition parameters; **R. S. Samson**, M. R. Symms, P. S. Tofts; Book of abstracts: 22nd Annual Meeting of the European Society for Magnetic Resonance in Medicine and Biology, 2005, Basle, Switzerland; 417

- Optimisation of quantitative MT (qMT) sequence acquisition parameters; **R. S. Samson**, M. R. Symms, P. S. Tofts; Book of abstracts: Fourteenth Annual Meeting of the International Society for Magnetic Resonance in Medicine, 2006, Seattle, USA; 2493

1 Introduction

Magnetisation Transfer (MT) Magnetic Resonance Imaging (MRI) is based on the premise that protons in biological tissue exist in two compartments or 'pools', a free ('liquid') pool, in which protons are highly mobile, and a restricted proton ('semi-solid') pool consisting of protons which are associated with macromolecules and are thus relatively immobile. Exchange of magnetisation takes place between the two pools, primarily via dipole-dipole interactions, but also via chemical exchange and diffusion. The bulk of the observable signal in conventional MR images originates from the free proton pool, since the restricted proton pool has a very short T_2 (~10-20μs) and therefore its signal decays very rapidly, rendering this compartment 'invisible'. Magnetisation Transfer Imaging provides access to these protons, which are located in biologically interesting tissue regions. A novel form of contrast is achieved, and there exists the potential for more specific tissue characterisation than is provided by standard MRI techniques.

1.1 Motivation and Aims of Project

The most commonly used measure of MT is the Magnetisation Transfer Ratio (MTR) which is calculated by acquiring two sets of images, one highly MT-weighted and one with little or no MT weighting, and taking a ratio. However, the signal in an MT-weighted image, and hence also the MTR, reflects a complex combination of various biological factors. The MTR is also highly sequence and scanner dependent, and therefore difficult to compare across centres. More quantitative methods (quantitative MT (qMT) imaging) have therefore recently been developed, based on a two-compartment mathematical model in tissue, allowing the examination of the parameters underlying the MT exchange process, independently of particular sequence details. This type of method has the potential to give a better insight into the significance of alterations in the MT parameters in pathology. The fraction of macromolecular protons (relative to the sum of the free and restricted proton pool sizes) (f), and the T_2 relaxation time of the semi-solid pool (T_2^B) are thought to be of particular interest in the study of changes occurring in Multiple Sclerosis (MS), since the macromolecular component is likely to be related to myelin content. Quantitative MT imaging is thought to be a more biologically useful approach than MTR measurement, because it gives better insight into the significance of alterations in fundamental MT parameters in pathology.

The aims of this project were to further develop and optimise the quantitative MT (qMT) imaging technique used at this centre. This technique has applications to the study of

pathological changes that occur in neurological disorders such as MS, Epilepsy, Stroke, Tumours and Dementia.

1.2 Overview of Thesis

Firstly, in chapter 2, the NMR phenomenon is described, using both quantum mechanics and classical physics. Then the methods involved in the generation of an MR image are described, followed by a description of some basic MR imaging techniques. Relaxation theory is then explained, firstly for simple solutions, then the discussion is generalised to heterogeneous systems such as biological tissue. Chapter 3 describes the physical mechanisms taking place in Magnetisation Transfer (MT), a description of the effects of MT and the practical aspects of acquiring MT-weighted data. Finally, some examples of the clinical applications of MT imaging are discussed. Chapter 4 provides an introduction to basic neuroanatomy and neurological disease, with a particular emphasis placed on Multiple Sclerosis (MS), and the role of magnetic resonance imaging in the diagnosis and monitoring of MS disease pathology is also discussed. Chapter 5 outlines the development, mathematical modelling and implementation of quantitative MT imaging techniques, and finally describes some possible further work and potential methods of optimisation of these approaches.

In chapter 6, the effect of B_1 errors on MTR measurements is investigated, both theoretically and experimentally, and a method for correcting for B_1 errors was proposed, based on the collection of a B_1 map in addition to MTR data. It was shown that this simple correction scheme, based on the 'Continuous Wave Power Equivalent' model for qMT, could be applied to MTR maps with a known B_1 error, regardless of tissue type.

In the first section of chapter 7 two protein gels (Bovine Serum Albumin (BSA) and agarose) are assessed for their potential use as MT phantoms. The second section of the chapter describes the development of internal thermometry in MRI phantoms (test-objects). Due to the temperature dependence of many MR quantities, this could potentially be a large source of systematic error in phantom Quality Assurance (QA) measurements, which will, in turn, have an impact on the interpretation of quantitative changes observed in long-term clinical studies.

In chapter 8, firstly a brief introduction to Maximum Likelihood estimation theory is given, followed by a description of Cramer-Rao theory. This was used to optimise the quantitative MT sequence acquisition parameters (i.e. the selection of 'MT weightings', each a combination of MT pulse amplitude and offset frequency), in order to increase

the precision of the fundamental qMT model parameters estimated using this method. Compared to a conventional acquisition, the optimisation enables less data to be acquired, reducing acquisition time without compromising uncertainties in estimated parameters. Alternatively, for the same number of MT-weighted data points, the map noise could be reduced, thereby minimising uncertainties in estimated parameter maps.

Finally in Chapter 9, the findings of this thesis are briefly summarised and conclusions made about the studies undertaken. Future possible investigations in the field of quantitative MT are also suggested and discussed.

2 Principles of MRI

Introduction

Since its discovery in 1945, simultaneously by Bloch and Purcell, Nuclear Magnetic Resonance (NMR) has become an important medical imaging tool, and also has a wide range of applications in chemistry and solid state physics. The NMR experiment is based on the application of Radio-Frequency (RF) irradiation to a sample under the influence of an externally applied magnetic field. If the RF energy applied is at the 'natural frequency' of the nuclei being observed, a phenomenon known as resonance occurs. The subsequent signal emitted by the sample (also in the RF range) is then observed. This chapter gives an introduction to the classical and quantum mechanical basis of NMR, followed by a description of the basics of Magnetic Resonance (MR) imaging techniques. The quantum mechanical description will be given first, to demonstrate the behaviour of a single nucleus in an externally applied magnetic field. For the rest of this thesis, the discussion will be generalised to the macroscopic system, and for this the classical description of NMR will be used.

2.1 Quantum Mechanical description of NMR

Quantum mechanics gives a more complete description of NMR than classical physics, and here we first consider individual nuclei (commonly referred to in NMR as 'spins').

Atomic nuclei possess intrinsic angular momentum, which is dependent on a property of each nucleus known as 'spin', a quantum number commonly represented by the symbol I. The existence of the spin property was predicted by the quantum field theory of Dirac, and later shown experimentally in the Stern-Gerlach experiment.

The principles of NMR are based on the fact that certain nuclei have a magnetic moment associated with this angular momentum and also that each nucleus has a charge as well as the property of spin. Individual spins could be visualised as tiny bar magnets or magnetic 'dipoles', with their own associated magnetisation $\boldsymbol{\mu}$, known as the 'magnetic dipole moment'. The relationship between the magnetic dipole moment $\boldsymbol{\mu}$ (which has the same direction as the spin angular momentum) and the angular momentum $\mathbf{J}$ is given by [1]:

$$\boldsymbol{\mu} = \gamma \mathbf{J} \qquad 2.1$$

where γ is a constant (measured in rad s^{-1} T^{-1}) known as the gyromagnetic ratio (ratio of the magnetic moment to the angular momentum of a particle), which differs for each nucleus.

Almost every element in the periodic table has an isotope with a non-zero nuclear spin, but a high natural abundance of the particular isotope is also desirable to give a strong NMR signal. Nuclei routinely used in NMR experiments include ^{1}H, ^{2}H, ^{13}C, ^{14}N, ^{19}F, ^{23}Na, ^{31}P, although only ^{1}H, ^{13}C and ^{31}P NMR imaging are commonly performed *in vivo*. The gyromagnetic ratio $\gamma=2.675\times10^{8}$ rad s^{-1} T^{-1} (42.58 MHz T^{-1}) for the ^{1}H proton, which is the largest magnetic moment of any stable nucleus. For this reason, and also because the ^{1}H proton is also the most abundant nucleus in the body, the most common *in vivo* NMR performed is ^{1}H NMR.

The angular momentum of an individual nucleus is proportional to the spin's magnetic quantum number m, and can only take discrete values in the quantum mechanical regime:

$$|\mathbf{J}| = \{\hbar \mathrm{I}(\mathrm{I}+1)\}^{\frac{1}{2}} = \hbar \mathrm{m} \qquad 2.2$$

where $\hbar$ is Planck's constant h divided by 2π. The spin quantum number I can take half and whole integer values only and m is the magnetic quantum number, which can take any of the 2I+1 values I, I-1,...,-I i.e. the nucleus can have 2I+1 orientations with respect to the magnetic field, corresponding to 2I+1 energy levels, each of which has energy E, given by:

$$\mathrm{E} = -\boldsymbol{\mu} \cdot \mathbf{B} = -\mathrm{m}\mu_z \mathrm{B} \qquad 2.3$$

where μ_z is the z component of the magnetic dipole moment μ. From equations 2.1 and 2.2 μ_z is given by:

$$\mu_z = \gamma \hbar \mathrm{m} \qquad 2.4$$

This quantisation of energy levels, resulting from the interaction of the nucleus with the magnetic field, is known as the 'Zeeman effect' and each energy level is called a Zeeman energy level.

Figures 2.1 and 2.2 show the quantisation of energy levels for nuclei of spin 3/2 and 1/2 respectively in an externally applied magnetic field $\mathbf{B_0}$. This 'splitting' of energy levels due to the presence of an external magnetic field is also known as 'Zeeman splitting'.

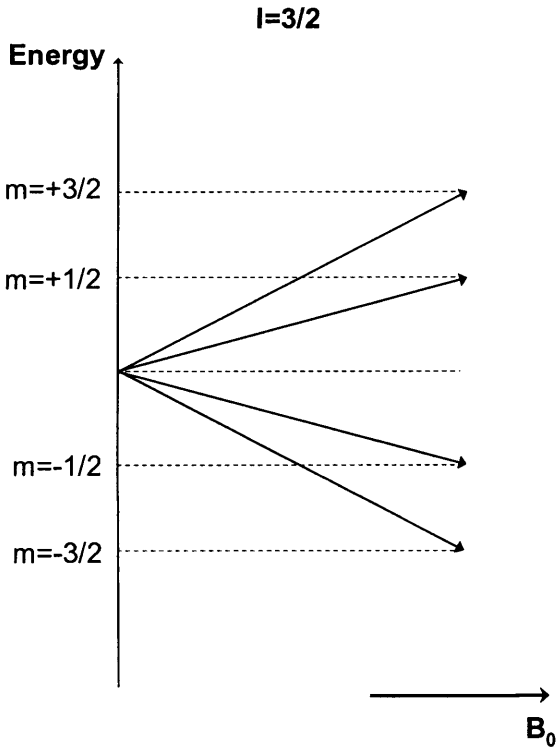

Figure 2.1: Energy levels for a nucleus of spin 3/2. Here the proton can take any of the magnetic quantum number values m=-3/2, -1/2, +1/2, +3/2.

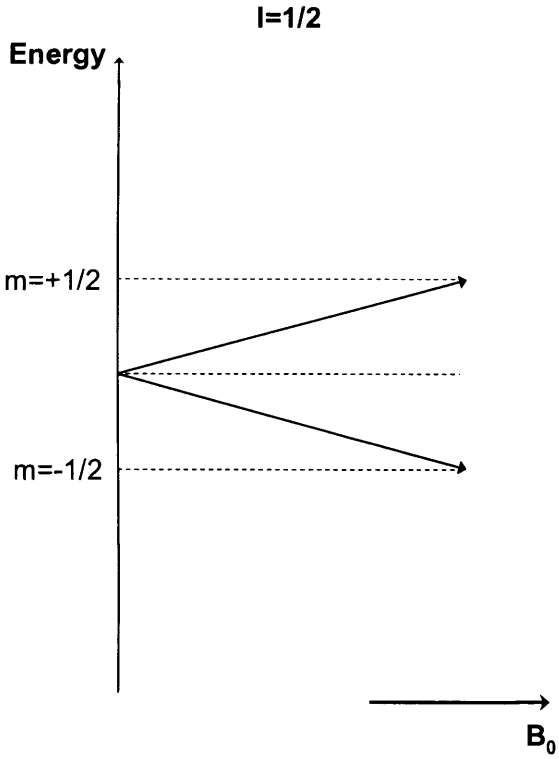

Figure 2.2: Energy levels for a nucleus of spin 1/2. Here the nucleus can only take the magnetic quantum number values m=±1/2.

2.1.1 Interaction of a nucleus with a magnetic field: Zeeman energy levels

If a static magnetic field of magnitude B_0 is applied (along a direction that we shall define as the z-axis), the nucleus acquires energy **E** (magnitude E) as a result of the interaction between the field $\mathbf{B_0}$ and the nuclear magnetic moment $\boldsymbol{\mu}$, given by:

$$E = -\boldsymbol{\mu} \cdot \mathbf{B_0} \qquad 2.5$$

which, from equations 2.3 and 2.4, is equivalent to:

$$E = -\gamma\hbar m B_0 \qquad 2.6$$

Since the magnetic quantum number m can possess any of the values I, I-1, I-2, ... -I, the adjacent energy states differ by 1 in their value of m. For a spin ½ nucleus, m can only take the values ±1/2, therefore the magnitude of the energy difference (ΔE) between adjacent energy levels is given by:

$$\Delta E = \gamma\hbar B_0\left(\frac{1}{2} - \left(-\frac{1}{2}\right)\right) = \gamma\hbar B_0 \qquad 2.7$$

It can be seen from equation 2.7 that the higher the externally applied field, the larger the Zeeman separation between energy levels. For a spin ½ nucleus, such as ^1H, the system is in its lowest energy state when the nucleus is aligned parallel to the field (also known as "spin-up"), and the energy of the system is at a maximum when the magnetic moment $\boldsymbol{\mu}$ lies anti-parallel to the field ("spin-down").

2.1.2 Energy Level Transitions

In the presence of a magnetic field of strength B_0 T, a nucleus possessing non-zero spin can absorb or emit quanta of energy, with frequency **ν** Hz, and angular velocity (or amplitude) **ω** rad s^{-1}, which, from Planck's law is given by:

$$\boldsymbol{\omega} = \frac{\Delta \mathbf{E}}{\hbar} \qquad 2.8$$

A transition from the lower to the higher energy state will take place when a quantum of energy equal to the energy difference between the two states (i.e. energy at the resonant ('natural') frequency) is absorbed. From equations 2.7 and 2.8 it can be seen that:

$$\boldsymbol{\omega} = \gamma \mathbf{B_0} \qquad 2.9$$

This equation (known as the Larmor equation) expresses the resonance condition for the NMR experiment, and the resonant (operating) frequency of the static magnetic field is usually denoted $\boldsymbol{\omega_0}$, and is known as the Larmor frequency. The Larmor frequency is in the radio-frequency (RF) range of the electromagnetic spectrum for the proton at typical NMR field strengths.

Clinical scanners have typical B_0 values of 1.5T, although current trends in research are leading to the development of higher field strength scanners, with scanners of field strength 3.0T in wide use in a clinical setting as well as for research.

For energy level transitions to take place, energy must be supplied to the system which matches the energy difference between the two states, i.e. the Larmor frequency of the proton for ^{1}H NMR, and this takes place via the application of a second, oscillating magnetic field.

2.1.3 Boltzmann statistics

If it is assumed that the spin system is at room temperature and in thermal equilibrium with its so-called surrounding "lattice" (local environment), the number of spins in the lower energy (spin-up) state, N^+, very slightly outnumbers those in the upper (spin-down) level, N^- (i.e. there is a slight preponderance for nuclei to align with the field, rather than against it). From the theory of Boltzmann statistics, the ratio of spins in the low energy to the high energy state is given by:

$$\frac{N^+}{N^-} = \exp\left(\frac{+\Delta E}{kT}\right) \qquad 2.10$$

where ΔE is the energy difference between the two spin states, k is Boltzmann's constant (1.38×10^{-23} J K^{-1}), and T is the temperature in Kelvin (K). Since $\hbar = 6.63\times10^{-34}$ Js, $\hbar\omega_0 \approx 6.74\times10^{-27}$J for a field strength B_0=1.5T. Therefore, $\hbar\omega_0 << kT$ (i.e. the thermal energy kT is very large compared to the quantum energy difference), the exponent in equation 2.10<<1,and equation 2.10 can be rewritten as follows:

$$\frac{N^+}{N^-} \approx 1 + \frac{\hbar\omega_0}{kT} \qquad 2.11$$

In other words, the population difference between states is very small:

$$\frac{N^+ - N^-}{N^-} \approx \frac{\hbar\omega_0}{kT} \qquad 2.12$$

The signal achieved in an NMR experiment is proportional to this very small population difference between adjacent energy levels, and in turn this is proportional to the externally applied magnetic field.

The application of an oscillating magnetic field (oscillating at the Larmor frequency of the protons) in addition to the static field $\mathbf{B_0}$ to a sample excites nuclei and induces transitions between energy states. After the oscillating magnetic field has been switched off the excited nuclei will return to the lower (equilibrium) energy state,

emitting energy ΔE. This emission of RF energy is the origin of the signal detected in an NMR experiment.

2.2 Classical description of NMR

2.2.1 Classical description of an isolated proton in an externally applied magnetic field

Although strictly the quantum mechanical description of NMR should be used, it is convenient to adopt the classical model, which, for spins with I=½, agrees with the predictions of the quantum mechanical model for a single nucleus. Therefore this convention will be used for the rest of this thesis.

In the classical regime, the proton can be considered a magnetic dipole moment with magnetic moment $\boldsymbol{\mu}$. In the presence of a static magnetic field $\mathbf{B_0}$, a spin experiences a torque Γ which acts in a direction which would align the proton with the field $\mathbf{B_0}$ (see figure 2.3). Classically spins can take any orientation within the field, in contrast to the quantum mechanical regime, where spins can only take discrete spin orientation values. For example, a spin ½ nucleus can only be aligned parallel or anti-parallel to the externally applied magnetic field in the quantum mechanical regime.

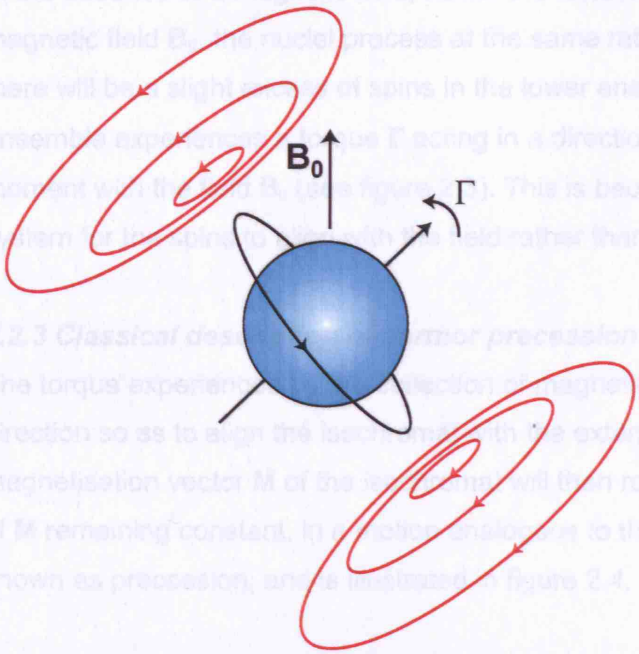

Figure 2.3: Magnetic dipole moment in an externally applied field B_0. The spin lies in the external (uniform) field B_0, applied in the vertical direction. The spin magnetic moment is spinning on its own axes (with its own magnetic field lines shown in red), whilst experiencing a torque Γ acting in a direction so as to align the spin magnetic moment with the direction of the static field B_0 (the torque is perpendicular both to the static magnetic field B_0 and to the magnetic moment μ).

The magnetic dipole moment torque Γ is given by [2]:

$$\boldsymbol{\Gamma} = \boldsymbol{\mu} \times \mathbf{B}_0 \qquad 2.13$$

The torque of the magnetic dipole moment is equivalent to the rate of change of angular momentum and therefore equation 2.13 can be rewritten:

$$\boldsymbol{\Gamma} = \frac{d\mathbf{J}}{dt} = \boldsymbol{\mu} \times \mathbf{B}_0 \qquad 2.14$$

2.2.2 Macroscopic magnetisation

In the classical regime, we consider a macroscopic 'ensemble' of 'spins', known as an isochromat, in which all the spins precess at the same frequency. If each individual spin can be thought of as a magnetic dipole moment, with magnetic moment $\boldsymbol{\mu}$, then the macroscopic or 'bulk' magnetisation vector $\mathbf{M}_{bulk}$ of i individual spins is given by:

$$\mathbf{M}_{bulk} = \sum_i \boldsymbol{\mu}_i \qquad 2.15$$

In the absence of a magnetic field, nuclei are randomly oriented. In an external magnetic field $\mathbf{B_0}$, the nuclei precess at the same rate (the Larmor frequency), and there will be a slight excess of spins in the lower energy state. Effectively the spin ensemble experiences a torque Γ acting in a direction so as to align its magnetic moment with the field B_0 (see figure 2.3). This is because less energy is required by the system for the spins to align with the field rather than against it.

2.2.3 Classical description of Larmor precession

The torque experienced by the collection of magnetic dipole moments acts in a direction so as to align the isochromat with the externally applied magnetic field $\mathbf{B_0}$. The magnetisation vector **M** of the isochromat will then rotate about $\mathbf{B_0}$, with the magnitude of **M** remaining constant, in a motion analogous to that of a spinning top. This motion is known as precession, and is illustrated in figure 2.4.

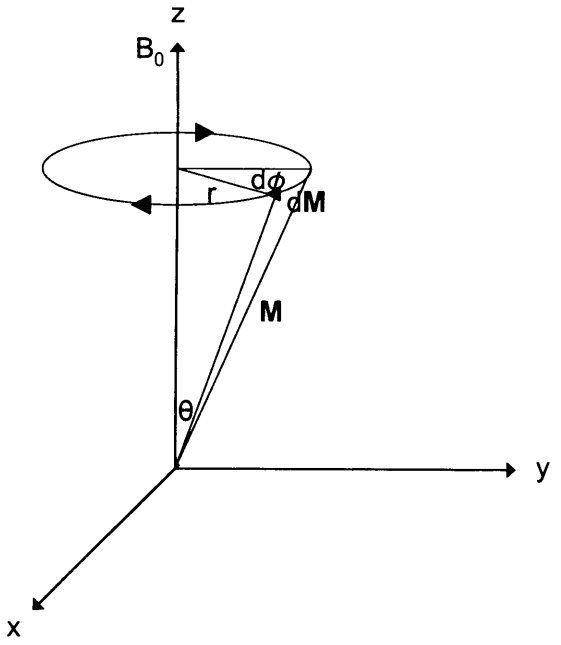

Figure 2.4: Larmor precession of an isochromat in an externally applied field B_0. The isochromat rotates about the B_0 field direction (z-direction) at an angle θ to B_0 (arrows indicate direction of motion). The magnitude of the magnetic moment M remains constant while its direction continuously changes.

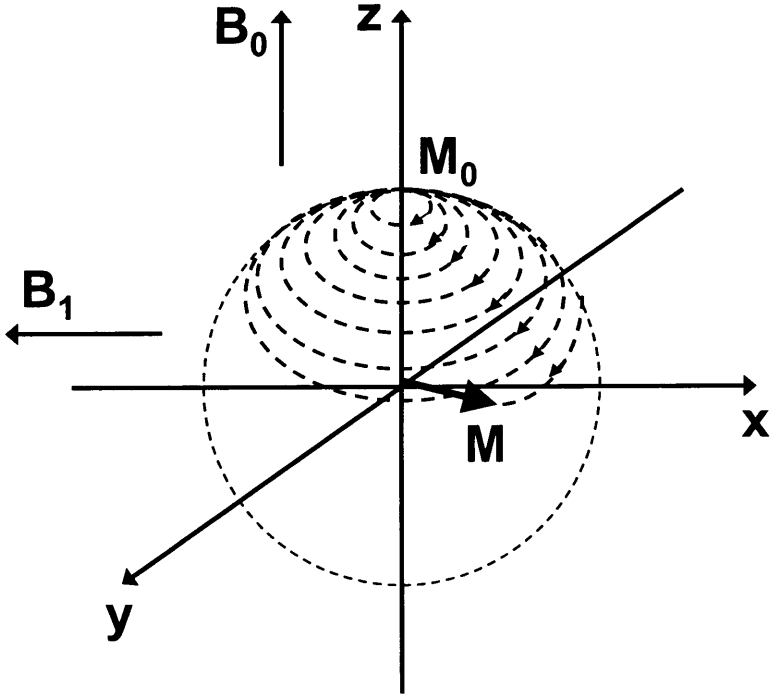

Figure 2.5: The trajectory of the magnetisation vector M during Larmor precession viewed in the laboratory frame

From figure 2.4 it can be seen that:

$$\frac{d\mathbf{M}}{dt}\delta t = \mathbf{M}\sin\theta\delta\phi \qquad 2.16$$

From equation. 2.1, $d\mathbf{M}=\gamma d\mathbf{J}$, and the torque $\boldsymbol{\Gamma}$ is equal to the rate of change of angular momentum, which in turn is equal to $\mathbf{M} \times \mathbf{B_0}$ (equation 2.14). Simplifying and dividing both sides of the equation by δt gives:

$$\frac{d\mathbf{M}}{dt} = \gamma\frac{d\mathbf{J}}{dt} = \gamma\boldsymbol{\Gamma} = \gamma\mathbf{M}\times\mathbf{B_0} = \gamma\mathbf{M}\mathbf{B_0}\sin\theta = M\sin\theta\frac{\delta\phi}{\delta t} \qquad 2.17$$

This then gives the equation for the frequency of precession, the Larmor frequency ω_0:

$$\boldsymbol{\omega_0} = \frac{d\phi}{dt} = \gamma\mathbf{B_0} \qquad 2.18$$

This is identical to the result obtained from quantum mechanics (equation 2.9).

There is no preferred orientation in the plane perpendicular to $\mathbf{B_0}$ (the transverse or xy plane), i.e. the net component of the magnetic moment in this plane is zero. The behaviour of the spin isochromat is analogous to that of a spinning top or gyroscope, precessing about the field $\mathbf{B_0}$ with a frequency equal to the Larmor frequency $\boldsymbol{\omega_0}$.

2.2.4 The resonance condition and the rotating frame of reference

The NMR experiment involves the application of a second, rotating (oscillatory) magnetic field which we shall call $\mathbf{B_1}$, perpendicular to the static field $\mathbf{B_0}$.

Consider a reference frame rotating with angular velocity ω rad s^{-1} about the z'-axis (z'=z). The equation of motion of the system (ensemble of isochromats with bulk magnetisation **M**, in an effective magnetic field $\mathbf{B_{eff}}$) then becomes (where primed symbols indicate the rotating frame of reference)

$$\left(\frac{d\mathbf{M}}{dt}\right)' = \gamma \mathbf{M} \times \mathbf{B_{eff}} \qquad 2.19$$

where $\mathbf{B_{eff}}=\mathbf{B}+\boldsymbol{\omega}/\gamma$, where the term ω/γ represents a fictitious magnetic field which arises because of the rotation (the rotation of the reference frame (at rate ω rad s^{-1}) in effect contributes to the effective field experienced by the ensemble of isochromats) **B** is the total applied field, given by $\mathbf{B}=\mathbf{B_0}+\mathbf{B_1}$ [1] (with $\boldsymbol{\omega_1}=\gamma\mathbf{B_1}$).

Let us assume that a constant field $\mathbf{B_0}$ is applied in the z-direction and a rotating (left circularly polarised) field is applied in the x-direction with angular velocity ω_1 rad s^{-1} and $\mathbf{B_1}=B_1(x \cos \omega_1 t - y \sin \omega_1 t)$. The vectors $\mathbf{B_0}$ and $\mathbf{B_1}$ can then be expressed in terms of the primed co-ordinates as $\mathbf{B_0}=B_0z'$, and $\mathbf{B_1}=B_1x'$. It then follows that:

$$\mathbf{B_{eff}} = \frac{[\mathbf{z}(\omega_0 - \omega) + \mathbf{x}\omega_1]}{\gamma} \qquad 2.20$$

It is obvious that if the time-varying field $\mathbf{B_1}$ is rotating at the Larmor frequency $\boldsymbol{\omega_0}$ in the stationary reference frame, the **z** term in equation 2.20 is zero, so that only an effective field along the x'-axis remains, i.e. $\mathbf{B_{eff}}=\mathbf{B_1}(=\omega_1/\gamma)$.

It is now simpler to describe the system using a reference frame rotating at the same angular frequency as that of the applied oscillatory field $\mathbf{B_1}$, with respect to the stationary (laboratory) frame of reference. This is illustrated in figure 2.6.

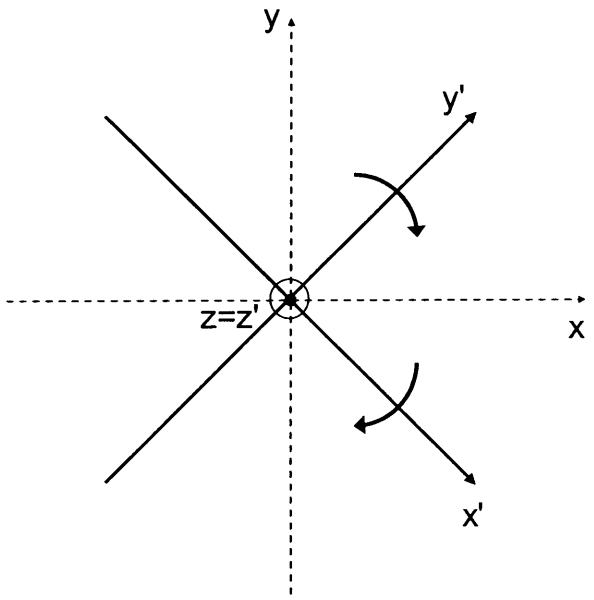

Figure 2.6: The rotating frame of reference. The rotating (primed) reference frame is rotating at a frequency equal to the Larmor precession frequency, clockwise around the z=z' axis (for a static magnetic field pointing in the +z direction according to an observer positioned above (z>0) the xy plane). From the rotating perspective, the spin axis is not moving at all.

Under this 'resonance condition', the $\mathbf{B}_1$ field can be selected to 'tip' the isochromat through a particular angle from the z'-axis. In order to detect the magnetisation of a sample in the presence of a static $\mathbf{B}_0$ field, it is necessary to perturb the sample magnetisation, and then allow it to return to equilibrium. Energy level transitions of spin isochromats as they return to equilibrium then result in the emission of RF energy. An RF receiver coil oriented perpendicularly to the static magnetic field will then detect this energy via Faraday induction. Perturbation of the equilibrium magnetisation of spin ensembles is achieved by applying a $\mathbf{B}_1$ field in the transverse plane. Since the resonance (Larmor) frequency is in the Radio-Frequency (RF) range, application of this $\mathbf{B}_1$ field effectively amounts to applying RF irradiation to the sample.

If the amplitude of RF irradiation ω_1 (in rad s^{-1}) of the oscillating field $\mathbf{B}_1$ is given by $\omega_1=\gamma\mathbf{B}_1$, and this RF energy is applied for a time τ s (i.e. the energy is applied in the form of 'RF pulses'), then the 'flip angle' θ (in radians) is given by equation 2.21:

$$\theta = \gamma B_1 \tau \qquad 2.21$$

Often these RF pulses have flip angles of $\pi/2$ radians (90°) or π radians (180°), which would tip the net magnetisation of the sample into the x'y' plane in the rotating frame of reference (along the positive y'-axis) or into the negative z' axis respectively.

2.3 Relaxation theory and the Bloch Equations

If the individual magnetic moments $\boldsymbol{\mu}_i$ of a collection of N isochromats in a volume element V, all precessing at the same frequency in a static magnetic field **B**, are summed, the macroscopic magnetic moment per unit volume **M** for the spin system is obtained:

$$\mathbf{M} = \frac{1}{V}\sum_{i=1}^{N}\boldsymbol{\mu}_i \qquad 2.22$$

And, for non-interacting spins, the equation of motion describing the precession of the ensemble of spins is:

$$\frac{d\mathbf{M}}{dt} = \gamma\mathbf{M}\times\mathbf{B} \qquad 2.23$$

and this can be rewritten as:

$$\begin{aligned}\frac{dM_x}{dt} &= \gamma(M_yB_z - M_zB_y)\\ \frac{dM_y}{dt} &= \gamma(M_zB_x - M_xB_z)\\ \frac{dM_z}{dt} &= \gamma(M_xB_y - M_yB_x)\end{aligned} \qquad 2.24$$

However, spins interact, thereby exchanging energy and also exchange energy with the surroundings (the so-called "lattice"), therefore relaxation terms describing these interactions during the return to thermal equilibrium must also be included. The inclusion of these terms, under the assumption that the relaxation is exponential, was performed by Felix Bloch in 1946 [3] and this is described in detail below.

Following perturbation of the spin system by RF irradiation, the whole system returns to equilibrium; it *relaxes.* The newly established transverse magnetisation disappears (transverse relaxation), and simultaneously the longitudinal magnetisation recovers to its original size (longitudinal relaxation).

2.3.1 Spin-lattice (longitudinal) relaxation

The spin system loses energy to its surrounding lattice, leading to the restoration of the longitudinal (z-direction) magnetisation M_0, via exponential recovery. The lattice is considered to be a large thermal reservoir consisting of energy states associated with atomic/molecular vibrations and rotations.

If, for example, a 90° RF pulse (which reduces the z-magnetisation to 0, since all the magnetisation is tipped into the xy plane) is applied to a sample at equilibrium, the timescale for recovery of longitudinal magnetisation is characterised by the 'longitudinal relaxation time' T_1 (the time for $(M_0 - M_z)$ to decay to e^{-1} of its value). This relaxation is described by equation 2.25 [4], [5]:

$$\frac{dM_z(t)}{dt} = \frac{M_0 - M_z(t)}{T_1} \qquad 2.25$$

where $M_z(t)$ is the longitudinal magnetisation at a time t after perturbation of the system by a RF pulse, and M_0 is the original longitudinal magnetisation (i.e. $M_0=M_z(0)$). This general equation is valid for an RF pulse of any nutation ('flip') angle.

Thus the relaxation of M_z following a 90° pulse applied to equilibrium magnetisation M_0 is described by an exponential curve, as shown in figure 2.7, and is expressed mathematically as:

$$M_Z(t) = M_0\left(1 - \exp\left(\frac{-t}{T_1}\right)\right) \qquad 2.26$$

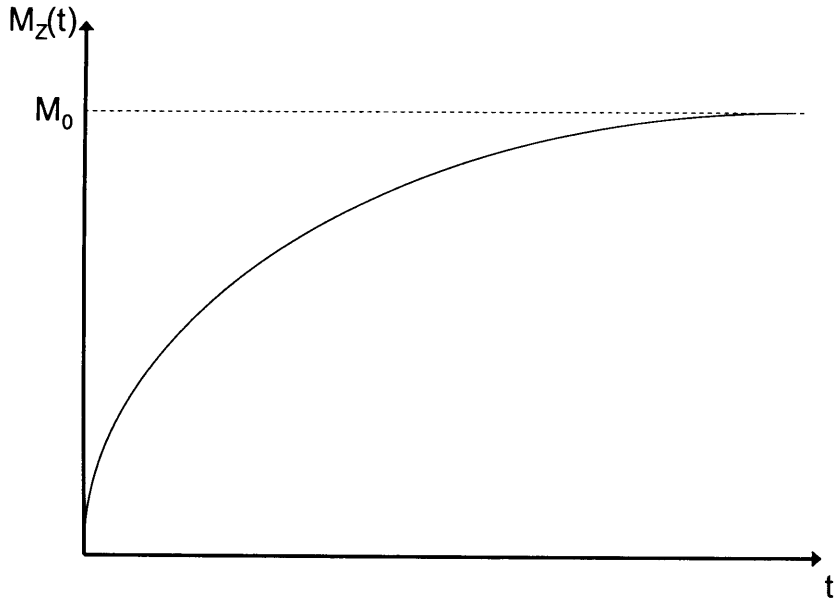

Figure 2.7: Exponential recovery of longitudinal ('spin-lattice') magnetisation. After perturbation of the spin system by a 90° RF pulse, the longitudinal magnetisation, which was destroyed by the pulse, begins to grow exponentially towards its original value (M_0) before perturbation, with time constant T_1.

The longitudinal (or spin-lattice) relaxation time (T_1) ranges from about 500-700ms in human white matter to about 4200ms in cerebrospinal fluid (CSF) at 1.5T (at body temperature) [6].

2.3.2 Spin-spin (transverse) relaxation

This process involves the exchange of energy between isochromats within the entire spin system, leading to the decay of the transverse (i.e. perpendicular to B_0) magnetisation to zero (its equilibrium value).

Transverse decay can be simply described as 'dephasing' of transverse magnetisation. At equilibrium the phases of the magnetic moments of the isochromats are randomly distributed (i.e. the transverse component of the isochromat magnetisation is $M_{xy}=0$ at equilibrium). If the magnetisation is tipped into the transverse plane by the application of a 90° RF pulse, the isochromats have a common phase. When the pulse is switched off, however, the isochromats experience slightly different local fields and therefore precess at different frequencies and dephase. Simply put, some isochromats precess faster than the Larmor frequency ω_0, and others slower, and the isochromats 'spread out' in the x'y' plane. The result is that positive and negative phases cancel each other out. This loss of phase coherence eventually results in the transverse magnetisation being completely destroyed. This process is illustrated in figure 2.8.

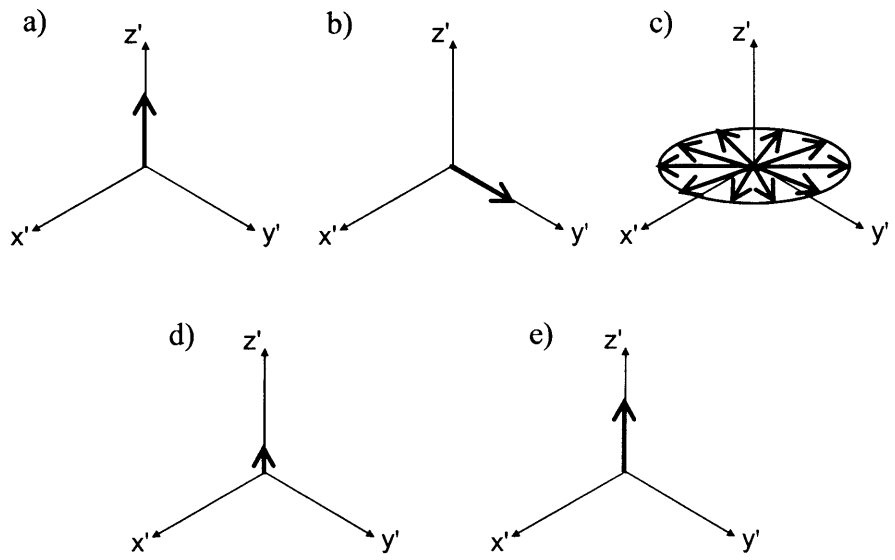

Figure 2.8 Dephasing of transverse magnetisation. The bulk magnetisation M of the spin system is initially aligned in the longitudinal direction (a). On application of a 90° RF pulse, the magnetisation is tipped into the transverse plane (b), and all the spins have a common phase at this instant. After the pulse is switched off, the spins begin to dephase (c) and simultaneous (but independently of the transverse relaxation process) longitudinal relaxation also begins. Eventually the transverse magnetisation is completely destroyed (d) and the magnetisation is aligned in the longitudinal direction (e).

Transverse relaxation is described by the equation:

$$\frac{dM_{xy}}{dt} = -\frac{M_{xy}(t)}{T_2} \qquad 2.27$$

where M_{xy} is the transverse magnetisation at a time t and T_2 is known as the 'transverse relaxation time', and is the time constant for the exponential decay of the transverse magnetisation.

The exponential decay of transverse magnetisation (illustrated in figure 2.9) is therefore expressed as:

$$M_{xy}(t) = M_0 \exp\left(\frac{-t}{T_2}\right) \qquad 2.28$$

T_2 is the time for the transverse magnetisation to decay to e^{-1} of its original value, and can range from less than 100ms in human grey and white matter [7] to 2200ms [1] in the cerebrospinal fluid (CSF) at 1.5T.

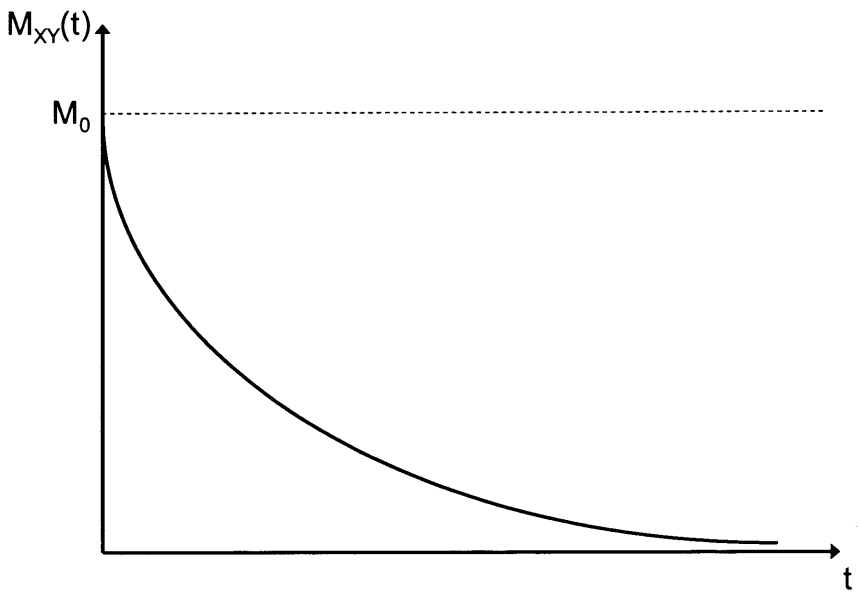

Figure 2.9 Exponential transverse magnetisation decay curve. The transverse magnetisation acquired as a result of the application of the 90° RF pulse (M_0, since all of the longitudinal magnetisation is tipped into the transverse plane) decays exponentially to zero.

T_2^* describes the total transverse relaxation, due to both spin-spin interactions and B_0 field inhomogeneities. If exponential decay is assumed in the time domain, so that the effect of B_0 field inhomogeneities is to give a Lorentzian lineshape in the frequency domain, T_2^* is described by the following relation:

$$\frac{1}{T_2^*} = \frac{1}{T_2} + \frac{1}{T_2'} \qquad 2.29$$

where T_2' is the time constant that describes the contribution due to B_0 field inhomogeneities. For this case the effect of B_0 inhomogeneities (magnitude ΔB_0) is described by the following relation:

$$\frac{1}{T_2'} = \gamma \Delta B_0 \qquad 2.30$$

Dephasing due to this type of B_0 field inhomogeneity can be recovered using spin echoes, as will be described in section 2.5. However, it should be noted that the B_0 distribution may not necessarily be Lorentzian in shape.

2.3.3 The Bloch Equations incorporating relaxation

Taking into account both precession and relaxation, the behaviour of the magnetisation vector **M** following perturbation by a radio-frequency pulse can be described fully by a single modified Bloch equation [8], [9], which can be separated into three simultaneous differential equations in the three orthogonal directions x, y and z to describe the time evolution of the magnetisation.

If a time varying field is applied in the x direction, the B_x, B_y and B_z components of the total field **B** in the rotating frame of reference (indicated by primed symbols) are as follows:

$$B_x' = \frac{\omega_1}{\gamma}$$
$$B_y' = 0 \qquad 2.31$$
$$B_z' = \frac{2\pi\Delta f}{\gamma}$$

where Δf is the frequency of the RF pulse in the rotating frame of reference. Substitution of the three field components into the Bloch equations (2.24) results in the following set of equations (without relaxation terms):

$$\frac{dM_x'}{dt} = -M_y(2\pi\Delta f)$$
$$\frac{dM_y'}{dt} = -\omega_1 M_z + M_x(2\pi\Delta f) \qquad 2.32$$
$$\frac{dM_z'}{dt} = \omega_1 M_y$$

After incorporating the relaxation terms (from equations 2.25 and 2.27) the result is:

$$\frac{dM_x'}{dt} = -M_y(2\pi\Delta f) - \frac{M_x}{T_2}$$
$$\frac{dM_y'}{dt} = -\omega_1 M_z + M_x(2\pi\Delta f) - \frac{M_y}{T_2} \qquad 2.33$$
$$\frac{dM_z'}{dt} = \omega_1 M_y + \frac{M_0 - M_z}{T_1}$$

2.3.4 Local field fluctuations and the dipolar interaction

The most important mechanism for relaxation in protons in biological tissue is the dipolar interaction between protons in different bonding environments. Relaxation can therefore be described in terms of the 'dipolar field', since each individual proton behaves as a magnetic dipole, producing its own field, and also experiences the dipolar field of neighbouring spins, due to molecular tumbling.

Let us first consider a single ^1H nucleus in a uniform static field B_0, as shown in figure 2.10. It can be observed that in the regions marked '+' the local field (B_{local}) that is produced by the proton itself adds to the B_0 field. But in the regions marked '-', the B_{local} is opposing the B_0 field. Therefore, in the region of the proton, the magnetic field is inhomogeneous, and these local field variations will be experienced by any other nuclei in the neighbourhood of this proton.

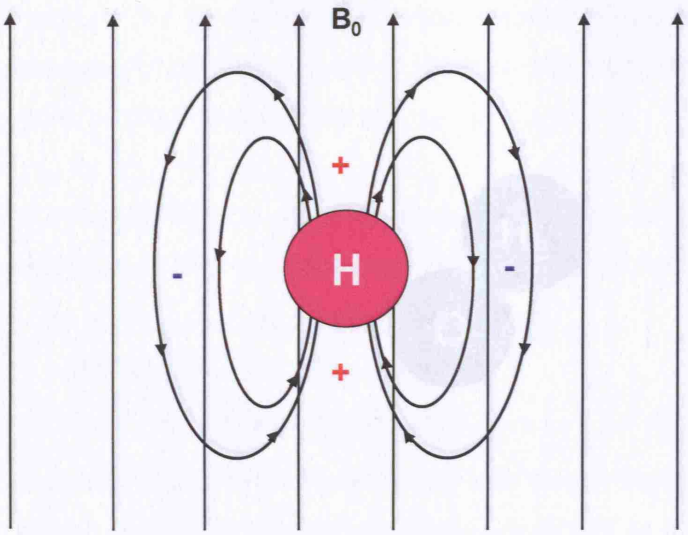

Figure 2.10: The effect of an external field B_0 on the magnetic moment of a single proton. The local field associated with the ^1H nucleus causes the net local field to be increased in the regions labeled '+' and decreased in the regions labeled '-'.

Let us now consider the two ^1H nuclei H_A and H_B in a water molecule, again in an external field B_0. For simplicity here, we only consider the effects on proton B arising from the local field due to proton A (i.e. the field lines due to the proton H_B are not shown here). Figures 2.11 and 2.12 show two different possible orientations of the water molecule. In figure 2.11, proton B lies in one of the regions labeled '-', so it experiences a decreased field compared with B_0, but in figure 2.12, proton B will experience a field slightly larger than the static field B_0. In reality, the water molecules are continuously 'tumbling' (rotating), and the proton B could experience a field anywhere between B_0-B_{local} and B_0+B_{local}, with B_0 being the mean field experienced.

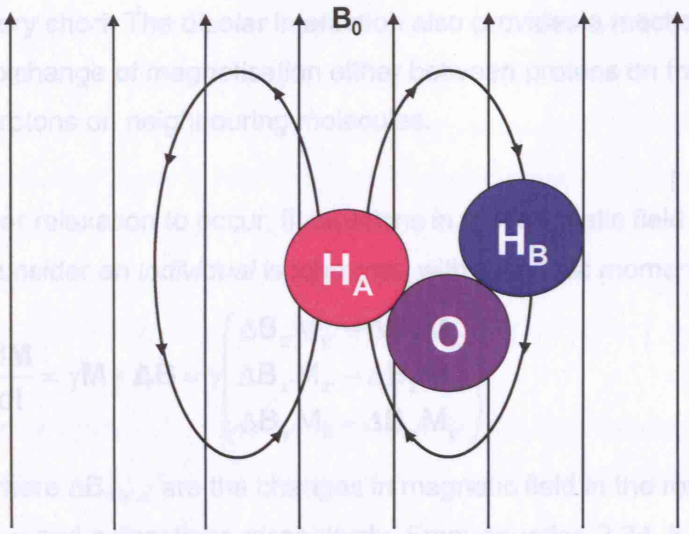

Figure 2.11: Dipolar interactions of ^{1}H nuclei (1). Here proton B experiences an increased local field since the local field associated with proton A adds to the static field B_0 in this region.

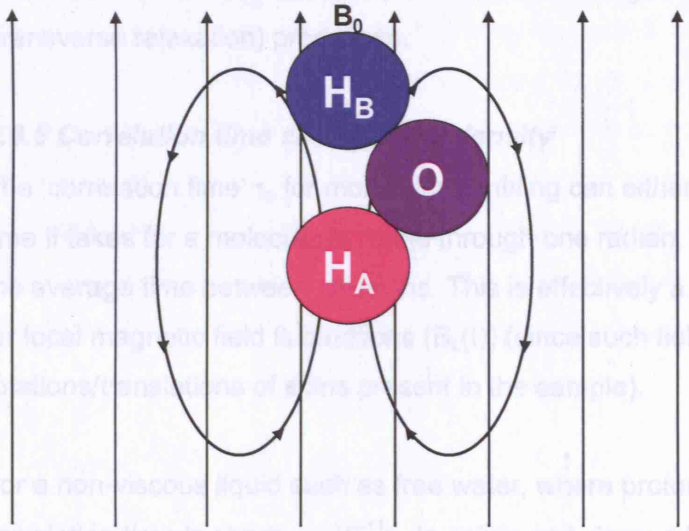

Figure 2.12: Dipolar interactions of ^{1}H nuclei (2). Here proton B experiences a decreased local field since the local field associated with proton A opposes the static field B_0 in this region.

Due to the translational and rotational motions of many different molecules, the dipolar field is continuously fluctuating. It is directional changes in the proton magnetic moment (the magnitude of the magnetic moment is fixed) that result in relaxation, by providing energy in order to induce transitions from one energy state to another. This approach to relaxation theory is known as "BPP theory", named after Bloembergen, Purcell and Pound, who developed the theory in 1948 [10], and is strictly only valid for spins in the liquid state, where the correlation time (τ_c) for molecular tumbling (see section 2.3.5) is

very short. The dipolar interaction also provides a mechanism for 'cross-relaxation', the exchange of magnetisation either between protons on the same molecule or between protons on neighbouring molecules.

For relaxation to occur, fluctuations in the magnetic field $\Delta\mathbf{B}(t)$ are required. Here we consider an *individual* isochromat, with magnetic moment **M**:

$$\frac{d\mathbf{M}}{dt} = \gamma\mathbf{M}\times\Delta\mathbf{B} = \gamma\begin{pmatrix}\Delta B_{z'}M_{y'} - \Delta B_{y'}M_{z'}\\ \Delta B_{x'}M_{z'} - \Delta B_{z'}M_{x'}\\ \Delta B_{y'}M_{x} - \Delta B_{x'}M_{y'}\end{pmatrix} \qquad 2.34$$

where $\Delta B_{x',y',z'}$ are the changes in magnetic field in the rotating frame of reference in the x, y and z directions respectively. From equation 2.34, it can be seen that magnetic field fluctuations in the x and y directions give rise to changes in $M_{z'}$ (the z component of the magnetic moment), i.e. T_1 (longitudinal relaxation) processes, whereas field fluctuations in all three directions contribute to changes in $M_{x'}$ and $M_{y'}$, i.e. T_2 (transverse relaxation) processes.

2.3.5 Correlation time and spectral density

The 'correlation time' τ_c for molecular tumbling can either be defined to be the average time it takes for a molecule to rotate through one radian, or, for molecular translations, the average time between collisions. This is effectively a measure of the time constant for local magnetic field fluctuations ($B_L(t)$) (since such field fluctuations are due to the rotations/translations of spins present in the sample).

For a non-viscous liquid such as free water, where protons are highly mobile, the correlation time is short; $\tau_c \sim 10^{-11}$s. In solids and viscous liquids, the molecules are less mobile, and therefore τ_c is longer.

The spectral density $J(\omega)$, defines the distribution of frequency components (i.e. the probability of molecular motions taking place at a particular angular frequency ω) present in local field fluctuations and is given by:

$$J(\omega) = \frac{\tau_c}{1+\omega^2\tau_c^2} \qquad 2.35$$

and the area under a spectral density curve (i.e. the integral of $J(\omega)$) is equal to unity ($\int J(\omega)d\omega = 1$).

The larger the value of $J(\omega)$ at $\omega=0$, the more efficient the T_2 process, and the larger the value of $J(\omega)$ at $\omega=\omega_0$ the more efficient the T_1 process. From equation 2.35, it can

be seen that for $\omega\tau_c<<1$, $J(\omega) \approx \tau_c$, i.e. the spectral density function is largest for large τ_c and there is very little/no ω dependence. For $\omega\tau_c>>1$, $J(\omega)\approx 1/(\omega^2\tau_c)$, i.e. $J(\omega)$ is largest at smaller τ_c values. At $\omega\tau_c\sim 1$, the dependence of T_1 on the correlation time is minimal (see also figure 2.14). This condition also corresponds to the sloping part of the spectral density curve (figure 2.13), therefore alterations in the static magnetic field will have the largest effect on $J(\omega)$ (and therefore also T_1) for a given τ_c when this is true, i.e $J(\omega)$ is most strongly field dependent for $\omega\tau_c\sim 1$.

From figure 2.13 it can be observed that $J(\omega_0)$ is largest for a viscous liquid (dashed line), and here $\omega_0\tau_c\sim 1$, therefore T_1 is most strongly field dependent for this type of system. It can also be seen that $J(0)$ simply increases with decreasing correlation time, therefore there is no field dependence of relaxation times associated with field fluctuations at frequencies close to $\omega=0$.

The field dependence of T_2 processes is much smaller than for T_1 processes due to the static field contribution to T_2 relaxation (which is not ω dependent). T_2 relaxation occurs as a result of the loss of phase coherence between spins, i.e. when spins within a sample begin to precess at different frequencies, as a result of static magnetic field inhomogeneities. T_2 relaxation does not result in a loss of energy from the spin system unlike T_1 relaxation, which does involve a change in the net energy of the system, since it involves the interaction of spins with the surrounding lattice.

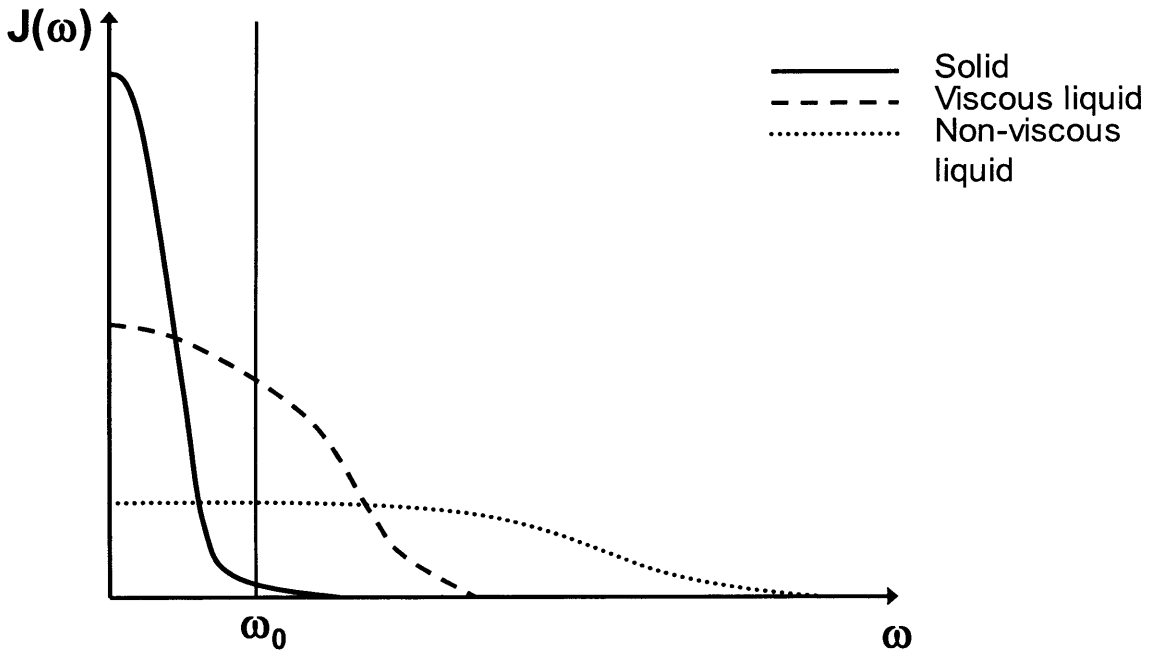

Figure 2.13: Spectral density plot as a function of frequency (logarithmic scale) for solids, viscous and non-viscous liquids. The area under each curve is the same (unity). J(ω) describes the ability to induce relaxation as a function of the frequency distribution of the motion (rotational/translational) of a molecule. For very non-viscous liquids the correlation time is very short, so that the system operating frequency $\omega_0<1/\tau_c$, and neither T_1 nor T_2 processes are efficient (both T_1 and T_2 are long). For more viscous liquids, with intermediate τ_c, such that $\omega_0=1/\tau_c$, T_1 processes are at their most efficient (see also equation 2.39 and figure 2.14). For solids (with very long τ_c), local field fluctuations are slow, therefore low frequency components dominate ($\omega_0>1/\tau_c$), and T_2 processes are most efficient since T_2 is more responsive to very low frequency field fluctuations. The frequencies are low enough for "static dephasing" of the transverse magnetisation. This effect is not important for T_1 relaxation (see equation 2.39), and contributes to the fact that the T_2 of biological samples is always shorter than T_1. As stated above, for $\omega\tau_c<<1$, $J(\omega)\approx\tau_c$, i.e. the spectral density function is largely independent of ω and is largest for large τ_c (i.e. solids). For $\omega\tau_c>>1$, $J(\omega)\approx1/(\omega^2\tau_c)$, i.e. J(ω) is largest at smallest τ_c values (non-viscous liquids). At $\omega\tau_c\sim1$ (intermediate τ_c values such as for viscous liquids), J(ω) is most strongly field dependent and much less dependent on correlation time.

The spectral density is the Fourier Transform of the "correlation function" G(τ), which is assumed to be an exponential function of time for simple systems. The correlation

function is defined to be the time averaged value of all local field fluctuations $B_L(t)$ in the time from t to $t+\tau$, i.e.:

$$G(\tau) = \overline{B_L(t)B_L(t+\tau)} \qquad 2.36$$

$$J(\omega) = \int_{-\infty}^{+\infty} G(\tau)\exp(i\omega\tau)d\tau \qquad 2.37$$

where $G(\tau)$ is given by:

$$G(\tau) = \exp\left(-\frac{\tau}{\tau_c}\right) \qquad 2.38$$

It should be noted that BPP theory [11] is only strictly valid for spin systems which have $\tau_c<T_2$, i.e. spins in the liquid state. *In vivo* the situation is actually much more complicated, since multiple compartments are present in tissue, each with a different T_2 relaxation time.

The relaxation times T_1 and T_2 are given by [12]:

$$\frac{1}{T_1} = k[J(\omega) + 4J(2\omega)] \qquad 2.39$$

$$\frac{1}{T_2} = \frac{k}{2}[3J(0) + 5J(\omega) + 2J(2\omega)] = \frac{k}{2}[3\tau_c + 5J(\omega) + 2J(2\omega)] \qquad 2.40$$

where k is a constant (a function of Planck's constant, the proton gyromagnetic ratio and the distance between dipoles) and the term independent of ω in equation 2.40 is known as the "static contribution" (since it is a function of the field fluctuation frequency, which is very close to zero) to T_2 processes. It should be noted that since equations 2.39 and 2.40 are derived from BPP theory, they are strictly only valid for spin systems which have $\tau_c<T_2$, i.e. spins in the liquid state. For $\omega\tau_c<<1$ (e.g. in a liquid), $J(0)=J(\omega)=J(2\omega)$, hence $T_1=T_2$ in a very non-viscous liquid. The terms in 2ω cannot be explained using the classical model, but require a quantum mechanical description; they are present to take into account relaxation occurring in the presence of field fluctuations at twice the Larmor frequency, due to the exchange of two energy quanta simultaneously by two coupled spins.

It can be seen from figure 2.13 that for a solid, where molecular motions are slow, and τ_c is large, local magnetic field fluctuations are slow (i.e. the frequency of field fluctuations ω is low, and $\omega>1/\tau_c$), therefore low frequency ($\omega\approx0$) components dominate. Since T_2 processes are sensitive to very low frequency field fluctuations, T_2 processes are most efficient in this region. In other words, solids have very short T_2 times and long T_1 relaxation times (see also figure 2.14). In contrast, if molecules are not tightly bound and therefore able to move rapidly, e.g. in a non-viscous liquid, the

correlation time is much shorter and field fluctuation frequencies are high ($\omega<1/\tau_c$). In this region neither T_1 or T_2 processes are very efficient, i.e. both T_1 and T_2 are long. A non-viscous liquid has a small contribution from field fluctuations at angular frequencies of both $\omega \approx 0$ and $\omega \approx \omega_0$ rads^{-1}, and from equations 2.39 and 2.40 it can be observed that for very non-viscous liquids, $T_1 \sim T_2$. In the intermediate region between these two extremes, there is a region where $\omega\tau_c \approx 1$, and at this frequency T_1 processes are at their most efficient (i.e. the minimum T_1 value is reached), and this is where dipole-dipole interactions are the most important. Temperature can also cause variations in the correlation time τ_c, since changes in temperature would cause changes in the frequency of local magnetic field fluctuations caused by molecular motions; as the temperature increases, τ_c decreases. T_1 processes are also most strongly field dependent when $\omega\tau_c \approx 1$ (see also equation 2.35).

The relaxation times T_1 and T_2 as a function of τ_c are shown in figure 2.14.

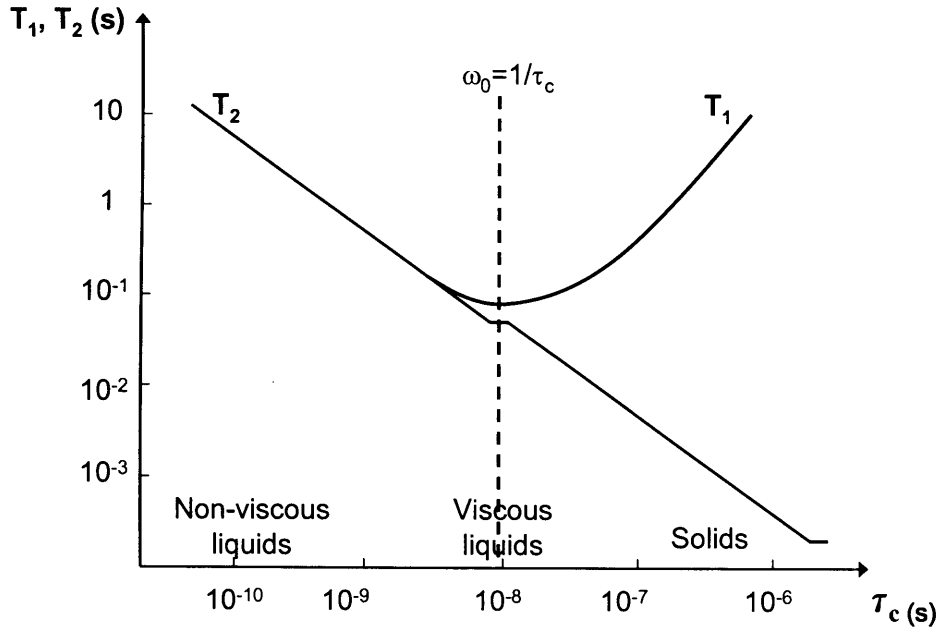

Figure 2.14: Relaxation times T_1 and T_2 as a function of correlation time (see equations 2.39-2.40). At low τ_c, molecules are "free" i.e. they are able to move rapidly, and field fluctuation frequencies are high, so that $\omega_0\tau_c$ is much less than 1, and neither T_1 nor T_2 processes are efficient, i.e. both are long. A minimum in T_1 occurs at the point $\omega_0 \approx 1/\tau_c$ i.e. this is the point at which the longitudinal relaxation process is most efficient [13]. Also at this point T_1 values deviate from T_2 values, and for solids (where protons are restricted and correlation times are longer), $T_1 >> T_2$, since T_2 has an additional contribution from very low frequency field fluctuations close to $\omega_0=0$ known as the "static contribution" (see equations 2.39-2.40).

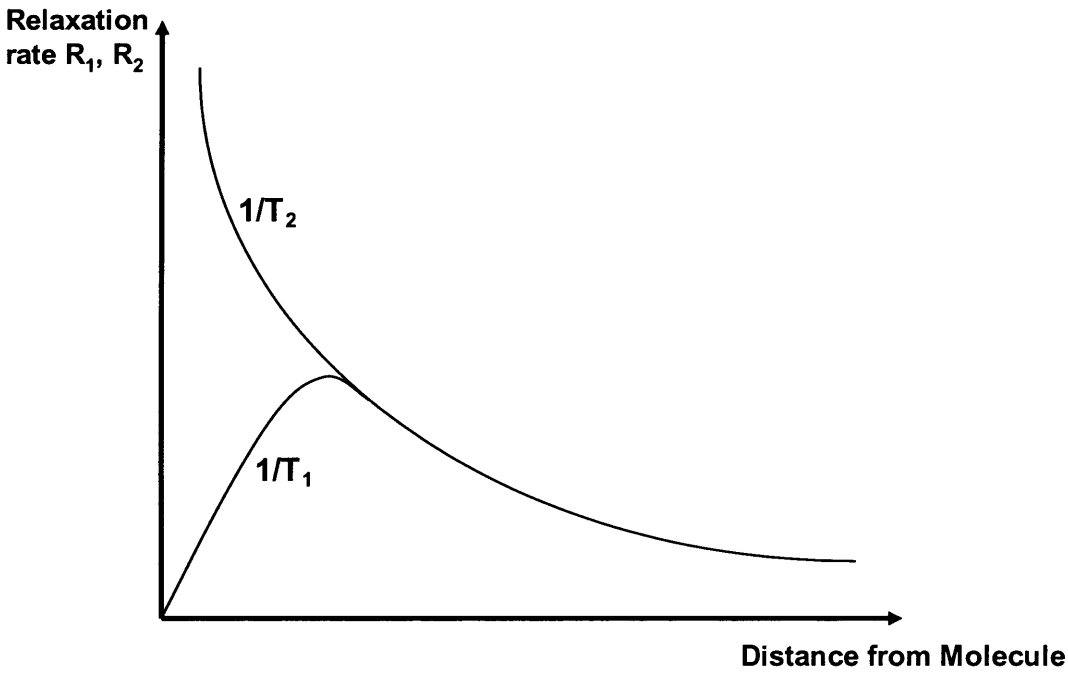

Figure 2.15: Relaxation rates R_1 ($1/T_1$) and R_2 ($1/T_2$) as a function of proton distance from molecule surface. Again, it can be seen that for very non-viscous liquids (where the protons are less 'tightly bound' to molecules and the distance from the molecule is longer), $T_1 \sim T_2$.

The relaxation times T_1 and T_2 are plotted as a function of the distance of the spin from the binding surface of a molecule in figure 2.15. The closer the proton is to the molecular surface (i.e. the more "tightly bound" the protons are), the shorter the correlation time τ_c, the more solid-like the behaviour of the spin system and the more distinct the T_1 and T_2 relaxation times of the proton are, with $T_1 >> T_2$.

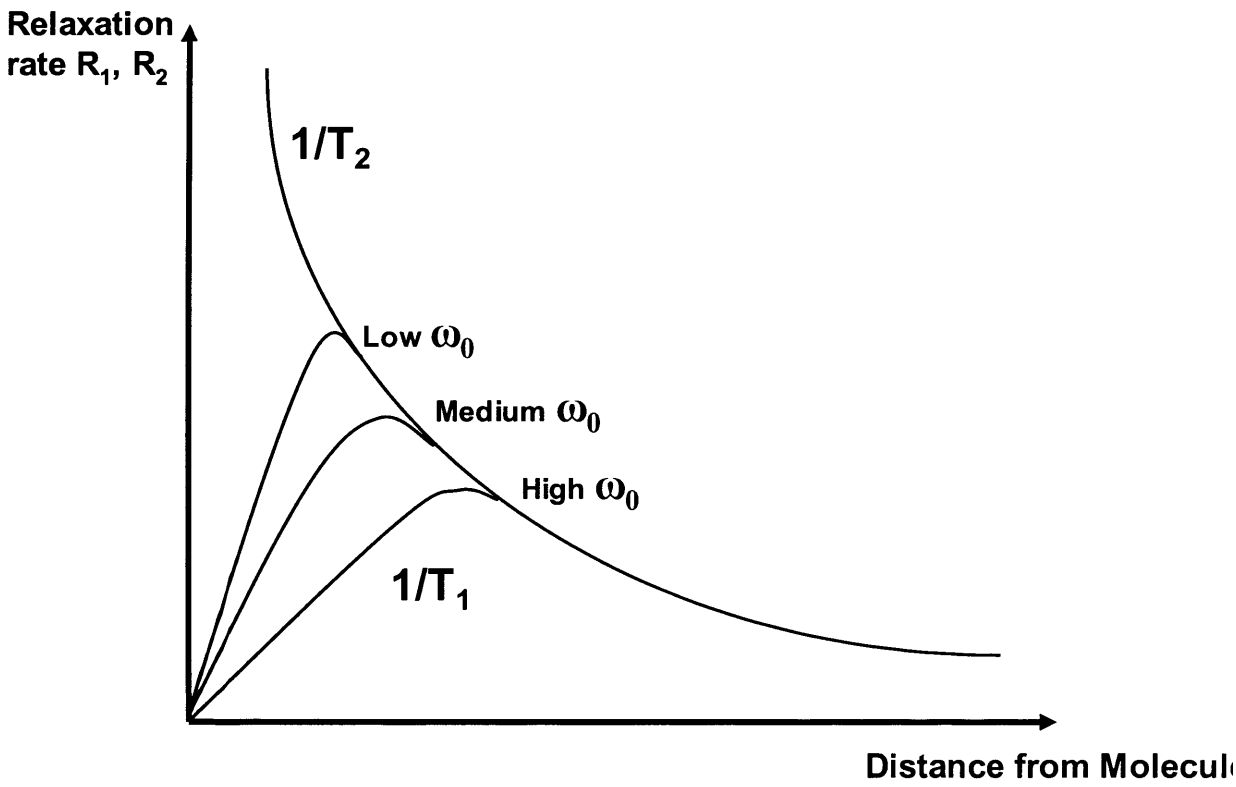

Figure 2.16: Effect of measurement frequency ω_0 on relaxation rates R_1, R_2. As the measurement frequency (i.e. B_0) is increased, the rate of longitudinal relaxation R_1 decreases (i.e. T_1 increases), but the transverse relaxation rate R_2 is unaffected, due to the static field contribution to T_2 relaxation.

2.3.6 Relaxation Mechanisms

All relaxation mechanisms require fluctuating local magnetic fields and various physical mechanisms (described below) can provide the appropriate conditions [14], [15].

2.3.6.1 Magnetic dipole-dipole interactions

For spin ½ nuclei, dipolar interactions between spins are very important in inducing relaxation in tissue. Nuclei are affected by the local environment: neighbouring nuclei cause time dependent fluctuating fields, proportional to $1/r^6$ i.e. these are very short range interactions. There is also a strong dependence on the gyromagnetic ratio γ, which is why this interaction is very important in protons, since ^1H atoms have the highest γ of any naturally occurring stable isotope. These interactions can be intra- or inter-molecular, but are more likely to be intra-molecular, due to their very short range. Therefore the effect is mostly rotational; vibrational effects are not seen because the frequency of vibrational interactions is too high (in the infra-red region). It should be noted, however, that, due to the rapid reorientation of liquid molecules (due to their short correlation times), the directionality of dipolar interactions in non-viscous liquids is

averaged out. Hence liquids have long T_1 and T_2 relaxation times, i.e. relaxation is less efficient in liquids (see also figure 2.14).

2.3.6.2 Dipolar interactions with unpaired electrons (electron paramagnetism)

This is a much stronger type of dipolar interaction; unpaired electrons in paramagnetic ions exhibit a very large magnetic moment (about six hundred times the size of the proton magnetic moment), whereas if an ion has two electrons in its outer orbital, the two spins oppose each other and the magnetic moments cancel out. Dipole-dipole interactions are proportional to the gyromagnetic ratio of the nucleus, hence the interaction is very strong for the unpaired electron. As a paramagnetic ion tumbles through a tissue environment, relaxation is induced via dipolar interactions as described above and hence relaxation times are reduced. Both T_1 and T_2 are decreased (i.e. relaxation rates are increased) via this mechanism, but the effect on the longitudinal relaxation time T_1 is more dramatic, therefore this approach is most commonly applied in T_1-weighted imaging sequences.

The main application of this phenomenon is in the use of paramagnetic contrast agents in T_1-weighted imaging to increase tissue contrast. Transition metal ions are paramagnetic, however, many paramagnetic substances are toxic and must therefore be bound in chelates to prevent them from complexing with molecules in the body. For example, Gadolinium chelates such as Gadolinium diethylene triamine penta-acetic acid, or Gd-DTPA are often used as contrast agents to observe Blood-Brain Barrier (BBB) leakage [16]. The large Gd-DTPA molecules are not able to penetrate a healthy BBB, but damage to the BBB, commonly hypothesised to be an early event in the development of a Multiple Sclerosis lesion, results in the semi-permeable BBB being infiltrated by these molecules. Then "enhancement" on T_1-weighted images occurs in these regions, i.e. the relaxation time T_1 is reduced (and the signal in a T_1-weighted image is therefore increased) where damage to the BBB has occurred. Iron is also highly paramagnetic, and has also been used clinically [17], [18].

2.3.6.3 Electric quadrupolar interactions

This type of interaction is not observed in ^{1}H NMR imaging, since this mechanism only affects nuclei with spin≥1. A nucleus with this property is characterised by a non-spherical distribution of electrical charges and has an electric magnetic moment, which can interact with the electric fields of other nuclei. The quadrupole coupling constant is in the MHz range (very efficient). When this relaxation process is present, it dominates over other mechanisms and results in very large field gradients.

2.3.6.4 Chemical Shift Anisotropy (CSA)

Electron clouds shield the nucleus slightly from the externally applied magnetic field so that the nucleus 'sees' an effective field $B_{effective}$ given by

$$B_{effective}=B_0(1-\sigma) \qquad 2.41$$

where σ is the shielding constant [19]. Thus the effective frequency $\omega_{effective}=\gamma B_{effective}$ is shifted relative to the Larmor frequency ω_0. It can be seen from equation 2.41 that this mechanism is also field dependent and therefore increasingly important at higher field strengths. The chemical shift=$\omega_0-\omega_{effective}$ depends on the distribution of electrons in the molecule, i.e. at different chemical locations (orientations of molecule), a different field is experienced, therefore this is an intramolecular effect. Since this interaction depends on the orientation of a molecule with respect to the external magnetic field, it is known as chemical shift anisotropy. Chemical shifts are rather small for protons, therefore this is not a dominant relaxation mechanism. In solution, the CSA is averaged out by rapid molecular tumbling and a sharp isotropic shift is observed; but the modulation of the shielding can provide a relaxation mechanism in the absence of any other mechanism. At higher fields T_2 is reduced by this effect, and CSA also causes problems in MR spectroscopy, especially at higher fields.

2.3.6.5 Spin-rotation interactions

This interaction is due to coherent rotation of the molecule, causing a magnetic field change due to the rotation. As the molecules move, an electric current is induced by the motion of the electrons, which induces a magnetic field. Collisions with other molecules interrupt the field, causing time-dependent field fluctuations. This is an intramolecular dynamic process (like the rotation of a methyl group).

2.3.6.6 Scalar-coupling interactions (chemical exchange)

In scalar coupling (J-coupling), two nuclei on the same molecule are coupled to each other via their electrons. Chemical exchange (the physical exchange of two nuclei between molecules) induces a time dependent magnetic field. This only occurs if the two interacting nuclei have very close frequencies, which is rare. This mechanism usually contributes more to T_2 relaxation than T_1 relaxation, since the field is modulated slowly (i.e. the frequency of local field fluctuations ω is closer to 0 than to ω_0).

2.3.6.7 Magnetisation Transfer (MT) (see also chapter 3)

Protons may exist in different bonding environments in biological tissue, giving rise to different levels of mobility, different intra- or intermolecular interactions and therefore relaxation properties, in particular T_2 relaxation times (see also figures 2.14-2.16). It is often assumed that there exists a restricted proton pool (comprising protons associated

with macromolecules), and a free proton pool (consisting of highly mobile protons, likely to be associated with water/liquid). The coupling of these two pools results in the exchange of magnetisation (Magnetisation Transfer, or MT) between the pools via dipolar interactions and diffusion. The net effect of this exchange is the saturation (attenuation of longitudinal magnetisation) of the restricted pool, which is then transferred to the free pool via MT exchange and results in an associated reduction in the free pool longitudinal relaxation time T_1.

Relaxation times of ^1H nuclei are considerably shorter in biological tissues than in pure water, since protons attached to macromolecules in tissue (presumably due to hydrogen bonding with nuclei at certain sites on the macromolecular surface) are less mobile and therefore have longer correlation times than free protons in water. This effect can also be observed in protein solutions (for example), where the relaxation rates of water increase in proportion to the amount of protein present [20], and larger proteins also tend to shorten relaxation times to a greater degree. There will also therefore be differences in relaxation properties between healthy and diseased tissue and hence these properties can be used to generate contrast in MR images. Damadian [21] reported an increase in the relaxation rates (i.e. a decrease in relaxation times) of malignant tissues when compared with healthy tissue, and this was later confirmed by Bottomley [22], who measured relaxation times in rat tumour tissue. These differences could result from a number of factors including water and protein content, which would affect the ratio of restricted to free protons and the presence of paramagnetic ions. Tissue breakdown may lead to an increase in "relaxation centres", due to e.g. cellular debris, resulting in increases in relaxation rates, but it is recognised that many kinds of changes in molecular structure may cause changes in relaxation. Since the relaxation rate of a heterogeneous tissue is a weighted average of all of the relaxation components within the tissue, these changes can result in alterations in the tissue relaxation times.

2.4 Signal detection

In the simplest NMR experiment, the sample is placed in a uniform magnetic field $\mathbf{B_0}$, applied along the z-direction, and a 90° RF pulse is applied in the x-direction, so that the magnetisation, initially aligned along the z-direction, is tipped through an angle of 90° into the transverse (xy) plane, where it can be detected (see also section 2.3). Following the application of the RF pulse, the transverse components of the magnetisation vector (M_x and M_y) begin to decay exponentially with a time constant T_2, due to spin-spin relaxation. Changes in the transverse magnetisation induce an alternating voltage (at the Larmor frequency) in a suitably placed receiver coil (which

may also be the transmit coil used to transmit the $\mathbf{B}_1$ field). The amplitude of the received signal decays with the time constant T_2, and has the characteristics of a damped sine wave. This is called the Free Induction Decay or FID, and is illustrated in figure 2.17.

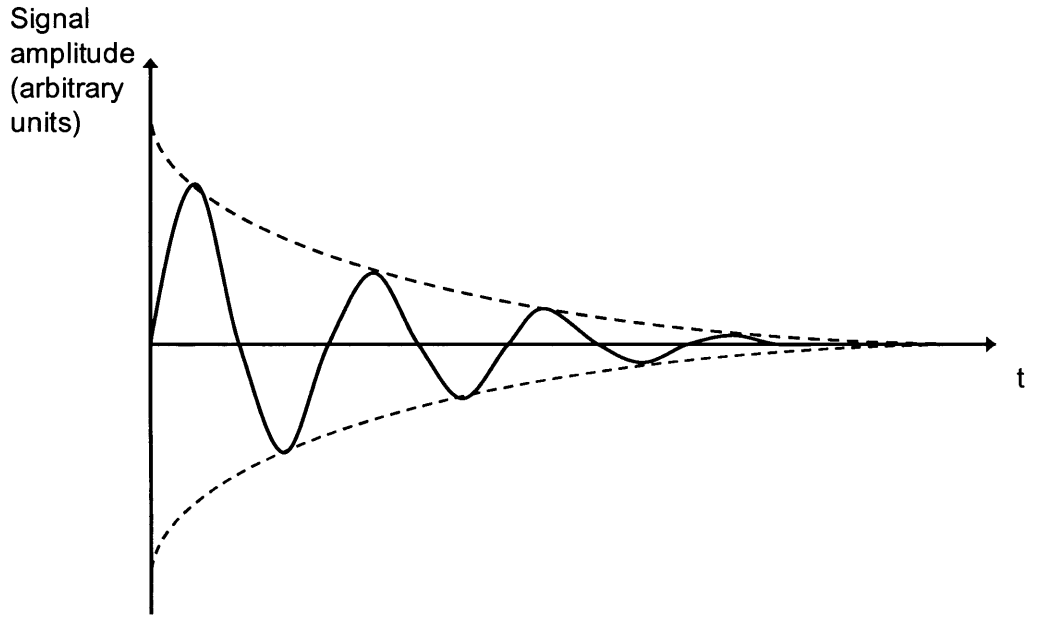

Figure 2.17: The Free Induction Decay (FID). The oscillating sine wave decay of the signal amplitude (proportional to the transverse magnetisation M_{XY}) due to T_2 relaxation.

It should be noted that the original signal (i.e. the magnitude or height of the FID) at t=0 (proportional to M_{XY}) is also a measure of the number of excited isochromats within a given volume, known as the (apparent) proton (spin) density and the oscillation frequency is equal to the Larmor frequency.

To measure the T_1 relaxation time of a sample (subject), the simplest method is to use an inversion recovery sequence, which is described in section 2.10.2. The spin echo sequence (described below) can be used to measure the T_2 relaxation time.

2.5 Spin echo imaging

The spin echo sequence, originally developed by Hahn *et al* in 1950 [23], forms the basis of many modern imaging sequences. RF pulses are used to refocus the dephasing caused by B_0 field inhomogeneities (see figure 2.8). The basic design of the spin echo sequence is to apply an RF pulse (here we consider the example of a pulse of flip angle 90˚) to tip the magnetisation away from the longitudinal plane, followed by

a 180° pulse, which refocuses (or "rephases") the isochromats, before signal acquisition. This example is illustrated in figure 2.18 and described below.

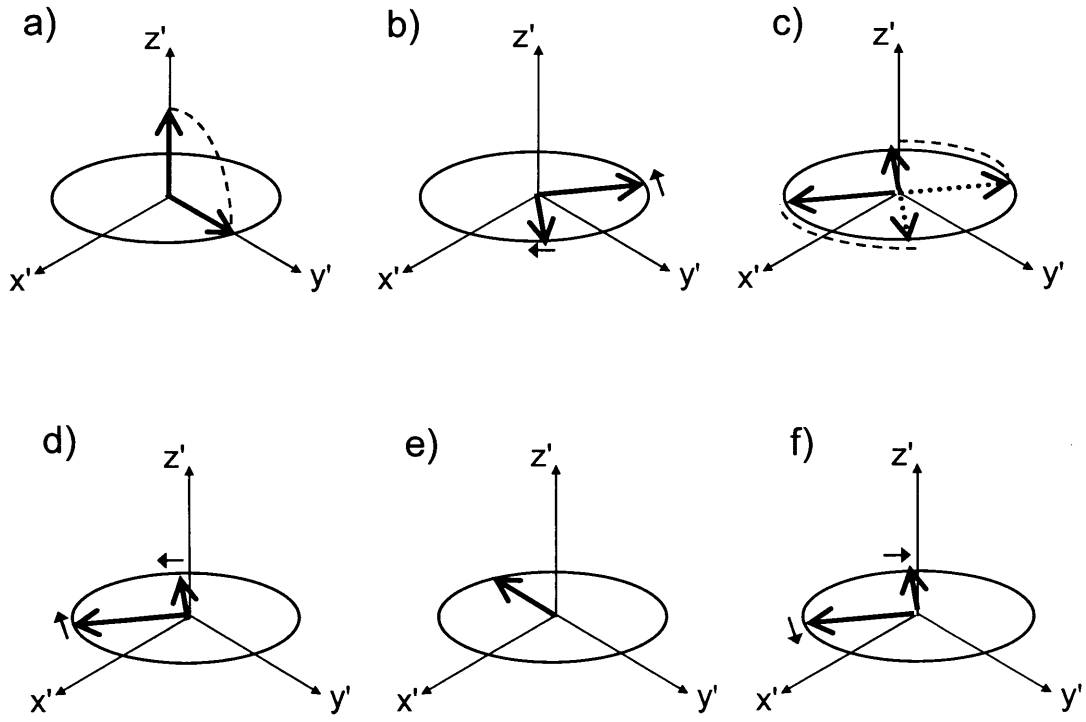

Figure 2.18: Rephasing of isochromats using spin echoes [24].

In figure 2.18(a), a 90° pulse is applied along +x' (although this first pulse can differ from 90°), which has the effect of rotating the longitudinal magnetisation M_Z into the transverse plane, along the positive y' axis. Immediately following the application of the pulse, the individual magnetic moments of the spins begin to dephase (b). Then a 180° RF pulse is applied again along the positive x' axis (c), which reverses the direction of the magnetisation, so that it is now along the -y' axis. The spins continue to move in the same direction as they were travelling before the 180° pulse (d), i.e. they are now moving towards each other. There is a time point (known as the 'spin echo') where the isochromats rephase and the magnetisation of the entire spin ensemble reaches a maximum again (e). The centre of the spin echo (where the signal will reach a maximum) occurs at a time referred to as the "echo time" or TE of the sequence and the sampling or acquisition window will be centred around this time point. Finally the isochromats begin to dephase again (f).

As a result of the phase reversal by the 180° pulse, the acquired spin echo data is T_2-weighted rather than T_2^*weighted, in other words it is not affected by susceptibility-induced changes or B_0 field inhomogeneities.

Carr and Purcell [25] modified Hahn's original spin echo sequence ($90_x - 180_x$) by including additional 180° refocusing pulses, resulting in a sequence of the form $90°_x$-TE/2-$180°_{+x}$-TE-$180°_{+x}$-TE-$180°_{+x}$-... etc. This sequence produces a series of spin echoes alternately aligned along the -y' and +y' directions (figure 2.18(e)), thus allowing T_2 to be determined in a single experiment. However, a problem associated with this type of technique is that any potential errors in the 180° pulse (caused by inaccurate setting up of the pulse during prescan procedures) are amplified with each additional imperfect 180° pulse, therefore giving a T_2 value lower than the true T_2 value.

To overcome this problem, the sequence was further modified by Meiboom and Gill [26] (known as the Carr-Purcell-Meiboom-Gill (CPMG) sequence). Here a 90° pulse is applied first along +x', producing transverse magnetisation along the y'-axis, then the subsequent 180° pulses are applied consecutively along the +y' axis (i.e. the CPMG sequence can be written $90°_x$-TE/2-$180°_{+y}$-TE-$180°_{+y}$-TE-$180°_{+y}$-... etc). Any errors in the 180° pulse are cancelled out on every even echo using this method.

T_2 values can be measured using the Hahn spin echo sequence. Data are acquired at a number of different echo times in order to determine the signal as a function of time. The T_2 relaxation time can then be obtained by fitting the exponential decay curve given by equation 2.42 [27] to the data.

$$S = C\exp\left(\frac{-TE}{T_2}\right) \qquad 2.42$$

where S represents the signal amplitude in the frequency domain and C is a constant determined by the intrinsic proton density and a factor related to the scanner receiver gain (determined by the prescan procedure).

2.6 Gradient echo imaging

In a spin echo experiment, a 180° pulse is used to form an echo. It is, however, also possible to use field gradients, superimposed on the main static magnetic field (so that the field varies linearly with position in a particular dimension), to form an echo. In a gradient echo experiment, usually RF pulses of flip angles less than 90° are usually applied, so that only some of the magnetisation is tipped into the transverse plane. If a pulse of flip angle θ° is applied to an initial magnetisation vector of magnitude $|\mathbf{M}|$, following the pulse the amount of magnetisation tipped into the transverse plane is $|\mathbf{M}|\sin\theta$, and $|\mathbf{M}|\cos\theta$ remains aligned longitudinally. Therefore, the spin system is able to relax more quickly, since a large proportion of the magnetisation is undisturbed, and shorter repetition times (TRs) and hence acquisition times may be used, without necessarily resulting in heavily T_1-weighted images.

Again, in order to observe the NMR signal, an echo must be generated (i.e. the spins must be 'rephased' to remove the effects of phase dispersion). In contrast to a spin echo, however, the echo is produced using gradients rather than a 180° refocusing pulse, and is therefore known as a gradient echo. A gradient echo is formed by first dephasing and subsequently rephasing the FID so that all the isochromat magnetisation vectors are back in phase with one another at the centre of the gradient echo. The gradient echo occurs at the point in time where the net phase is zero, i.e. the amount of dephasing is equal to the amount of rephasing, and the signal reaches a maximum at the gradient echo (see figures 2.19-20). However, there is some T_2^* dependence in the signal derived from a gradient echo experiment, unlike a spin echo experiment, because there is no 180° pulse to refocus dephasing of isochromats due to $\mathbf{B_0}$ field inhomogeneities.

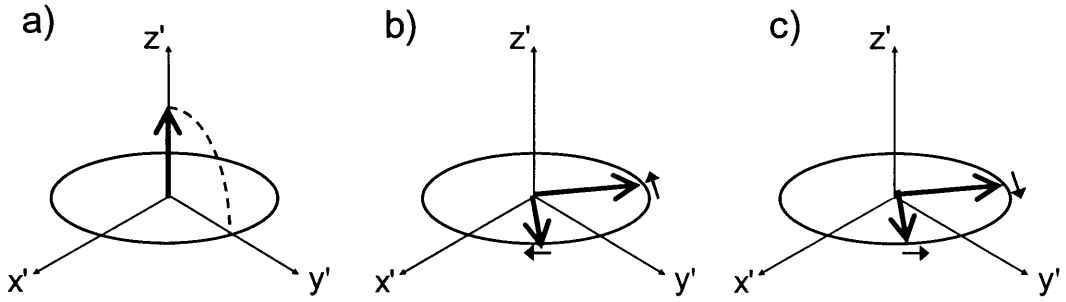

Figure 2.19: Formation of a gradient echo (1).

In figure 2.19(a) a 90° pulse is applied (although typically lower flip angle pulses are used in gradient echo sequences) and isochromats are tipped into the transverse plane (where they also begin to dephase due to B_0 field inhomogeneities). In (b) a dephasing gradient is applied, and the isochromats dephase as a result of this gradient. In (c) an equal and opposite gradient is applied (a rephasing gradient), isochromat phases are reversed and a gradient echo is formed at the point in time where the amounts of rephasing and dephasing by gradients are exactly equal. However, T_2^* decay cannot be compensated for using this method, as it is with a spin echo.

As noted above, dephasing caused by T_2^* processes (i.e. $\mathbf{B_0}$ field inhomogeneities) cannot be reversed using gradient reversal. This is illustrated in figure 2.20.

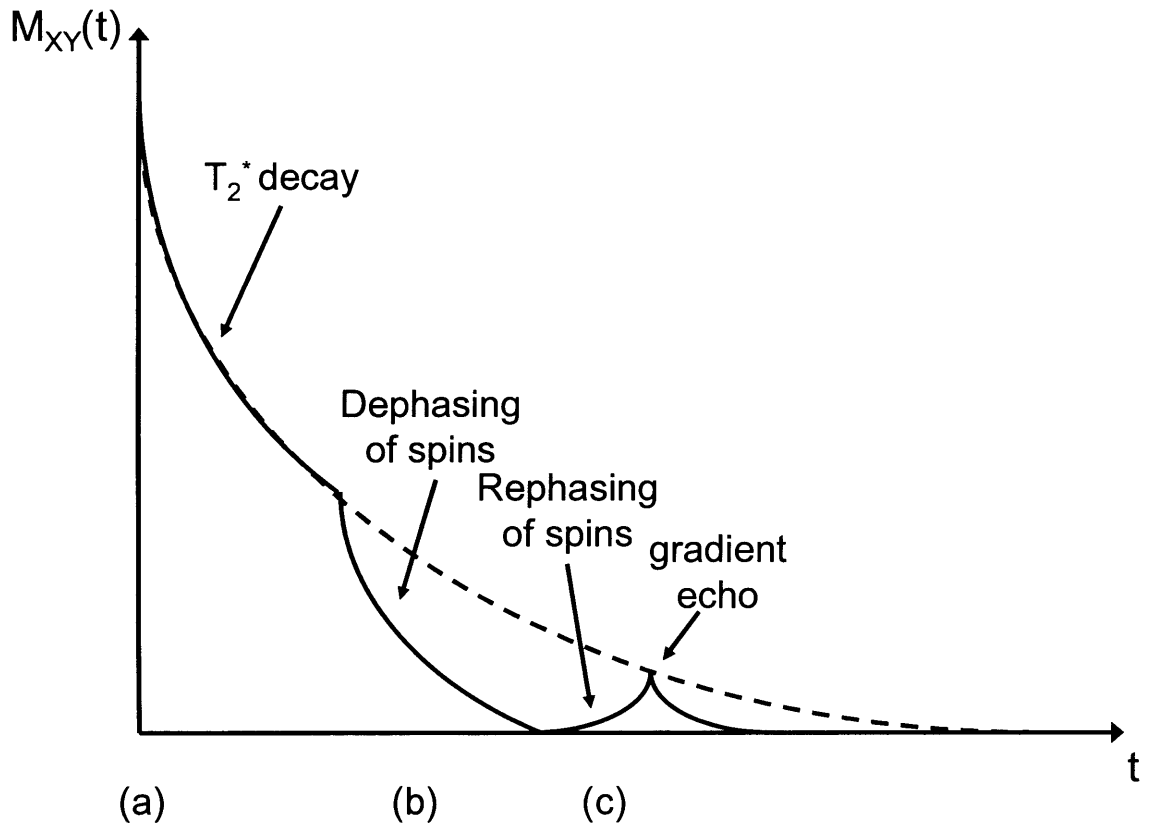

Figure 2.20: Formation of a gradient echo (2).

In figure 2.20(a) a 90° pulse is applied and isochromats are tipped into the transverse plane (where they also begin to dephase due to B_0 field inhomogeneities (T_2^* processes)). In (b) a dephasing gradient is applied, and the isochromats dephase as a result of this gradient. In (c) an equal and opposite gradient is applied (a rephasing gradient) causing a reversal of all phases (T_2^* processes) and a gradient echo is formed at the point in time indicated, where the amounts of rephasing and dephasing by gradients are exactly equal. It can be seen, however, that B_0 inhomogeneities cannot be compensated for using gradient reversal to form an echo, as with a spin echo, therefore gradient echo images exhibit T_2^* weighting rather than T_2 weighting.

2.7 The stimulated echo

Let us consider a sequence consisting of 3 90° pulses with pulse sequence timings 90° - τ - 90° - TM - 90° - τ – acquire, where TM is a delay time known as the mixing time, and the total echo time TE=2τ, since the stimulated echo occurs at a time τ following the third 90° pulse (in the absence of B_0 field gradients). Since T_2^* is short, spin isochromats dephase during a time τ following the first 90° pulse. The application of the second 90° pulse results in half the signal remaining in the transverse plane, which dephases quickly (during the mixing time TM) due to T_2^* processes, and a spin echo containing half the signal is then generated at a time τ following the second 90° pulse.

The other half of the magnetisation is stored along z' and following the third 90° pulse the magnetisation has equal and opposite components in the x'y' plane. After a further time τ a stimulated echo containing the remainder of the signal occurs.

It is usually assumed that T_2^* is short enough to allow dephasing of spins during the times τ and TM; but this may be enforced by dephasing of spins using B_0 gradients.

The generation of a stimulated echo is illustrated in figure 2.21.

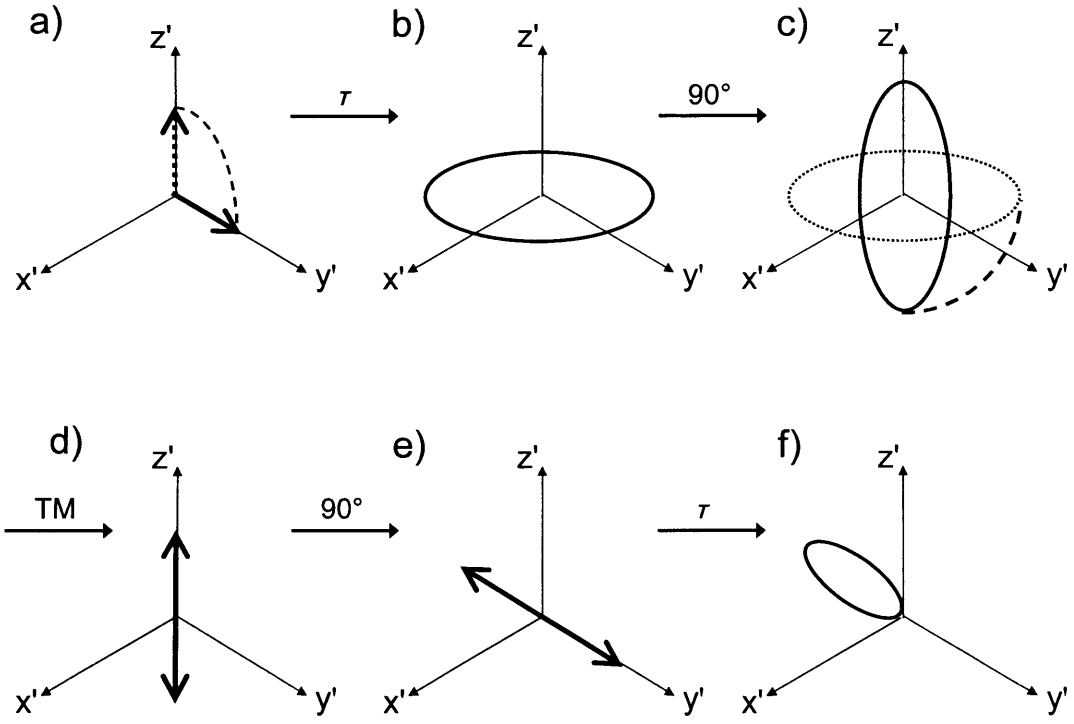

Figure 2.21: Formation of a stimulated echo.

Firstly in figure 2.21, a 90° pulse is applied and the isochromat magnetisation vector is tipped from the longitudinal direction into the x'y' plane (a). The magnetisation dephases within the x'y' plane during a time τ (b). A second 90° pulse is then applied which rotates the dephased spins (displayed as a disc of "fanned out" spin vectors) into the yz plane (c). During a time TM (the mixing time) the transverse magnetisation decays quickly (it dephases since T_2^* is very short) but the other half of the magnetisation, which remains in the longitudinal plane, decays relatively slowly via T_1 relaxation (d). A third 90° pulse is applied (e), and following this pulse, the magnetisation has equal and opposite components along + and –y' (rotated by 90° from the z' direction). There is no observed signal at this time because the signal is proportional to the transverse magnetisation, and the two components cancel each other out. After a further time τ the transverse magnetisation has dephased such that the magnetisation components are all in the same half of the xy plane, and half the

original signal remains. A stimulated echo is generated at this time point and the echo time TE=2τ. However, the main disadvantage of a stimulated echo experiment is that the maximum signal intensity is just 50%. It should also be noted that the 90° pulses may be applied in the presence of orthogonal B_0 gradients for localisation (e.g. in the STEAM sequence, see section 2.10.4.1), which also cause dephasing in the first τ interval, and that an additional spoiler gradient may be applied to ensure that the transverse component is dephased during TM.

2.8 Image formation

2.8.1 Gradients

In order to produce an image from NMR data, magnetic field gradients are applied in addition to the main magnetic field. These field gradients generate a field whose strength varies linearly with position [28], thereby allowing the encoding of spatial information. Since the Larmor frequency depends on the field strength, the spins at different positions will precess at different frequencies, and the FID will contain a range of precessional frequencies, each corresponding to a different intrinsic proton density (and may depend on other factors such as T_1 and T_2 etc) at a particular position (along one dimension). This can be seen in figure 2.22, an example of 'frequency encoding' using a field gradient.

If a time dependent gradient is applied in the same direction as the static external field $\mathbf{B_0}$ (i.e. the z-direction), the z-component of the field ($B_z(z,t)$) will be given by:

$$B_z(z,t) = B_0 + zG_z(t) \qquad 2.43$$

where $G_z(t)$ is the (spatially) uniform gradient in the z-direction which can also be written as:

$$G_z(t) = \frac{\partial B_z}{\partial z} \qquad 2.44$$

The variation in the angular frequency of the isochromats is then given by:

$$\omega(z,t) = \gamma B_0 + \gamma z G_z(t) = \omega_0 + \Delta\omega(z,t) \qquad 2.45$$

i.e. the precessional frequency varies with position along the z- direction due to the (time dependent) field gradient $G_z(t)$ in the z-direction, which results in a small change in the precessional frequency $\Delta\omega(z,t)$ superimposed on ω_0, thereby enabling positional encoding of data in one dimension.

2.8.2 Spatial encoding and 2D FT Imaging

In order to determine the origin of the signal collected in an MR image, it is necessary to 'encode' the information spatially in three dimensions, and this is achieved using additional gradients, in a method analogous to that described in the section above. For the rest of this thesis, it will be assumed that the three procedures involved in spatial encoding are always applied in the following directions; slice selection in the z direction, frequency encoding in the x direction, and phase encoding in the y direction.

2.8.2.1 Slice selection

For 2 dimensional MR imaging It is necessary to collect data from one slice only of an object at a time (to produce a 2D image from 3D data), without exciting other slices simultaneously. In other words only the isochromats within that slice should experience the RF pulse. This is achieved firstly by using a narrow bandwidth RF pulse, and secondly by using another gradient in the slice select (z) direction during the application of the RF pulse in a method proposed by Lauterbur *et al* [29], [30]. Then, when the longitudinal magnetisation within the particular slice being imaged is tipped into the transverse plane for detection, there is no detectable magnetisation in any other region of the object being imaged.

For example, to excite a slice in the xy plane, a slice select gradient is applied in the z-direction. The slice Larmor frequency of spin isochromats varies as a function of the slice position z. The RF pulse is applied with only a limited bandwidth ($\Delta\omega$) of frequencies, and will therefore only excite isochromats with resonant frequencies within that particular range, and since each possible frequency corresponds to a particular slice position, only a specific slice in the object (of thickness Δz) will be excited. The slice thickness depends on the bandwidth of the RF pulse and the amplitude of the slice select gradient (see figure 2.22).

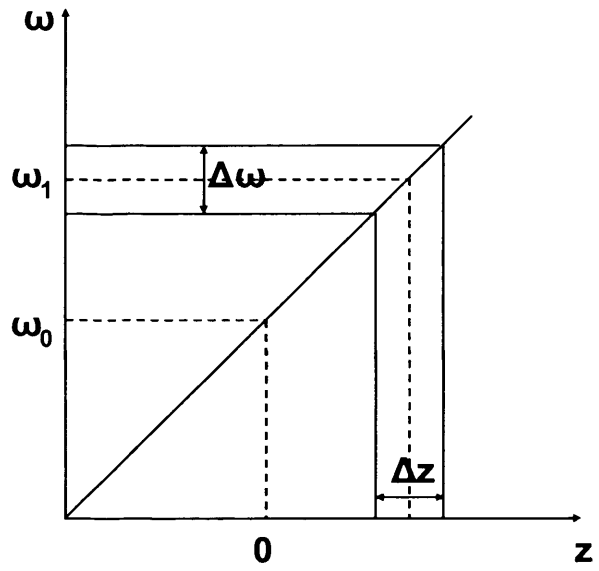

Figure 2.22: Slice selection in the z-direction. The RF pulse is applied with a frequency bandwidth of Δω centred on the frequency ω_1, such that only spins with frequencies within this bandwidth are excited. Δω corresponds to a slice thickness Δz.

The slice profile should ideally be a perfect 'top hat' (rectangular) function in order to excite only spins within the selected slice, but will depend on the pulse shape. In the limit of low flip angle pulses, the slice profile is fairly well approximated by the Fourier Transform (FT) of the pulse shape in the time domain). However, the effect of most pulses must be explicitly modelled using numerical integration of the Bloch equations and various approximations to design and optimise RF pulses.

Non-uniformities of both the main and gradient fields can cause changes in the slice profile. These effects are usually minimised in the centre of the image plane, but can be considerable at the outer edges of a slice. Examples of commonly used RF pulse shapes include the Gaussian, which when Fourier transformed gives a Gaussian slice profile, and the (truncated) Sinc shape, which yields a much closer approximation to a rectangular slice profile when transformed. Side lobes in the slice profile can also be reduced using apodisation, or windowing, where the slice profile is multiplied by a particular function in order to produce a more rectangular shaped profile, with edges tapering smoothly down to zero. However, this is at the expense of widening the lines and therefore decreasing the resolution. Examples of commonly used apodisation or windowing functions are the Hamming (used to minimise the height of the highest sidelobe) and Hanning (used to reduce aliasing) functions [31]. A non-ideal slice profile can lead to contamination by signal from outside the selected slice, causing less well defined slice edges. A "rephasing" gradient lobe (of approximately half the area of the

slice selection gradient lobe) is also required in order to compensate for the distribution of phases that result from the application of the RF pulse and slice selection gradient.

2.8.2.2 The Fourier Transform (FT)

The Fourier Transform (FT) of the FID in one dimension as a function of time, in the presence of a field gradient (as described in section 2.8.1) has been shown to be equivalent to the proton density of the imaged object in one dimension, assuming that the TR of the sequence is >> T_1 (to allow complete longitudinal recovery), and that T_2 is long and isotropic [32].

2.8.2.3 Frequency encoding: spatial encoding in a 2nd dimension

Following selective slice excitation, the signal intensity in an MR image must be encoded along the 2 other directions. In the rotating frame, a gradient is applied along the x'-direction, so that the resonant frequency varies linearly along the x' ("read") direction (see figure 2.23).

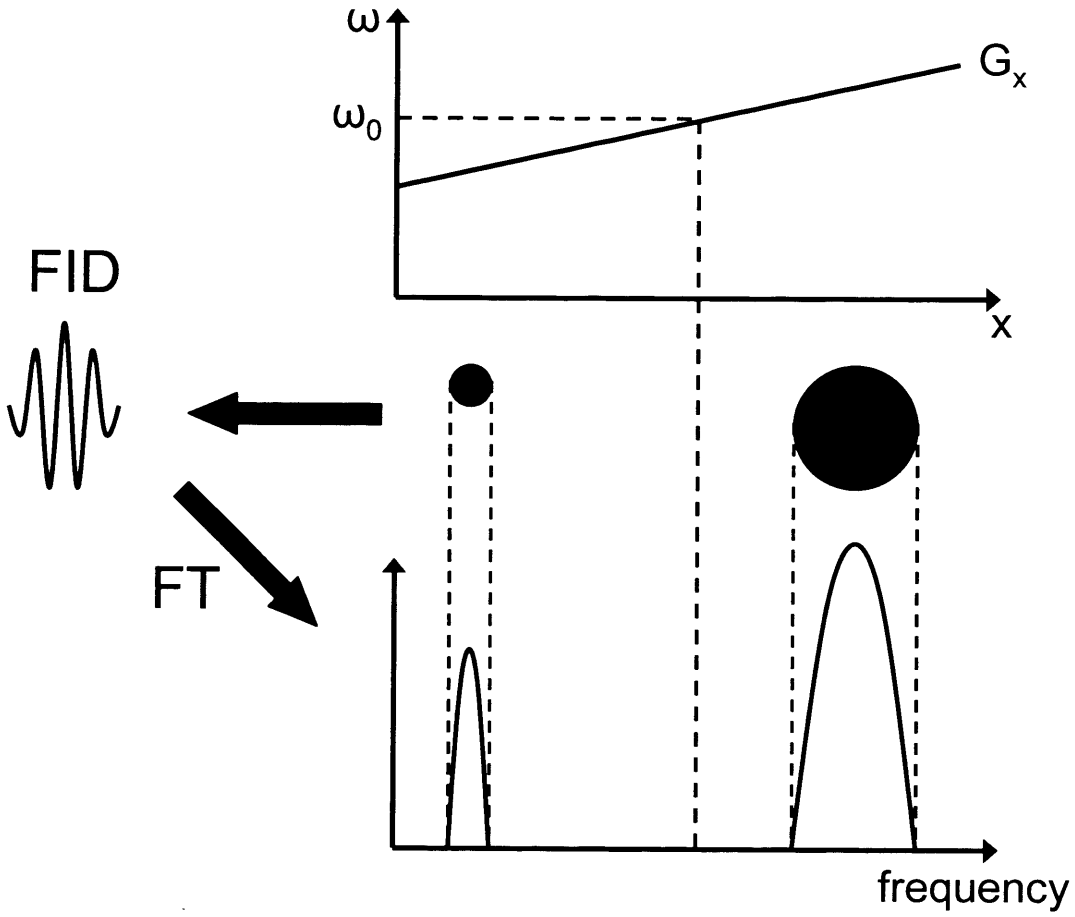

Figure 2.23: Frequency encoding: a one-dimensional projection of an object is obtained from the Fourier Transform (FT) of NMR signal (FID) obtained in the presence of a "readout" or frequency encoding gradient.

If, for example, a 90° 'readout' pulse were applied to a sample prior to a frequency encoding gradient, the signals output would contain a range of angular frequencies corresponding to different positions within the sample, each with its signal amplitude proportional to the number of excited nuclei at that particular position. This collection of signals is known as the Free Induction Signal (FIS).

If a linear field gradient $G_x(x,t)$ were applied along the x direction, the resonant frequency ω as a function of position x would be given by:

$$\omega(x) = \gamma(B_0 + G_x x) \qquad 2.46$$

The quantity to be measured at each point is the magnetisation in the x direction, $M_{xy}(x)$, but the detected signal S(t) is given by

$$S(t) = \int C M_{xy}(x) \exp(-i\gamma G_x x t) dx \qquad 2.47$$

where C is a constant including factors such as the receiver gain, and the intrinsic proton density of the sample (although in practice the magnetisation would also have a y dependence). S(t) is therefore the Fourier transform of $M_{xy}(x)$, and $M_{xy}(x)$ can therefore be determined from (with C' another constant):

$$M_{xy}(x) = \frac{1}{C'} \int S(t) \exp(+i\gamma G_x x t) dt \qquad 2.48$$

2.8.2.4 Phase encoding and 2D FT ('spin-warp') imaging

In order to encode the spins along the y direction, an additional time dimension, commonly referred to as 'pseudo time' t', is introduced, such that the FIS effectively also evolves in the presence of a second field gradient, perpendicular to the first. The 2D FT of this data (as a function of time and pseudo time) will produce a 2D image. The acquisition of the FIS is repeated many times, with the pseudo time (or 'sequence number' as it is sometimes called) incremented in each case. The amplitude of the field gradient G_y is varied linearly with each repetition by a factor known as the phase-encode step size n (equivalent to pseudo time). This second gradient is often known as the 'phase encoding' gradient, since spatial information is encoded into the phase of the magnetisation. Together with the other spatial encoding mechanisms (slice selection and frequency-encoding), this provides the basis for 'spin-warp imaging', first proposed by Edelstein *et al* in 1980 [33]. An example sequence diagram for a very simple spin-warp spin echo imaging experiment is shown in figure 2.24.

The application of the field gradient $G_y(t)$ in the y (phase encoding) direction will alter the phase of the magnetisation by an amount given by (where the gradient is switched on at a time t=0, and switched off at time T):

$$\Delta\phi = \int_0^T \gamma y G_y(t)dt \qquad 2.49$$

If the gradient amplitude is stepped up from a negative to a positive value in N equal steps, this can be written as:

$$\Delta\phi = \int_0^T \gamma G_y(t)ydt = \gamma \Delta G_Y yT\left(n - \frac{N+1}{2}\right) \quad n=1,N \qquad 2.50$$

where ΔG_y is a constant known as the phase encode step size. The detected signal therefore becomes:

$$S(t,n) = \int\int CM_{xy}(x,y)\exp(-i\gamma G_x xt)\exp(-i\gamma G_y yT)dxdy \qquad 2.51$$

where the signal S(t,n) is complex, and is a function of both the time t and the phase encode step number n (real and pseudo times).

The 2D FT of the complex signal intensity function S(t,n), gives the net magnetisation $M_{xy}(x,y)$ at each position (x,y), or the proton density image [34]:

$$M_{xy}(x,y) = \frac{1}{C'}\int\int S(t,n)\exp(+i\gamma G_x xt)\exp(+i\gamma G_y yTn)dtdn \qquad 2.52$$

It should also be noted that although a complex value is obtained for the magnetisation (due to extra phase shifts induced by B_0 inhomogeneities), the resulting image is usually displayed as a magnitude image (rather than the two separate real and imaginary components of the image). This is known as magnitude reconstruction. It is also important to note that the signal S(t,n) cannot be sampled continuously at all time points, and therefore $M_{xy}(x,y)$ is not a continuous function of t and n. A Discrete Fourier Transform (DFT) is used to transform the acquired signal at discrete points in (t,n) space to a digitised magnetisation value P(k,l), with the double integral in equation 2.52 replaced by a double summation in equation 2.53 (k and l are the summation indices in the time and pseudo-time axes respectively).

$$P(k,l) = \frac{1}{C'}\sum_{m=1}^{M}\sum_{n=1}^{N} S(m,n)\exp\left(-2\pi ik\frac{m}{M}\right)\exp\left(-2\pi il\frac{n}{N}\right) \qquad 2.53$$

The signal has been sampled N times along the time (readout) axis (or frequency encoding direction x in this example) and M times along the pseudo-time (phase encoding direction y). Equation 2.53 therefore describes the transformation of the signal matrix S of M x N data points or 'voxels' to an image matrix P also containing M x N data points or 'pixels' (since a volume element (voxel) in the original object becomes a 2D element in the resulting image). The resulting Fields-of-View of the image in the readout direction x (FOV_x) and phase encoding direction y (FOV_y) are then given by:

$$FOV_x = \frac{2\pi}{\gamma G_x t_{sample}} \quad FOV_y = \frac{2\pi}{\gamma G_y T} \qquad 2.54$$

where t_{sample} is the time interval between sampling data points in the readout (x) direction.

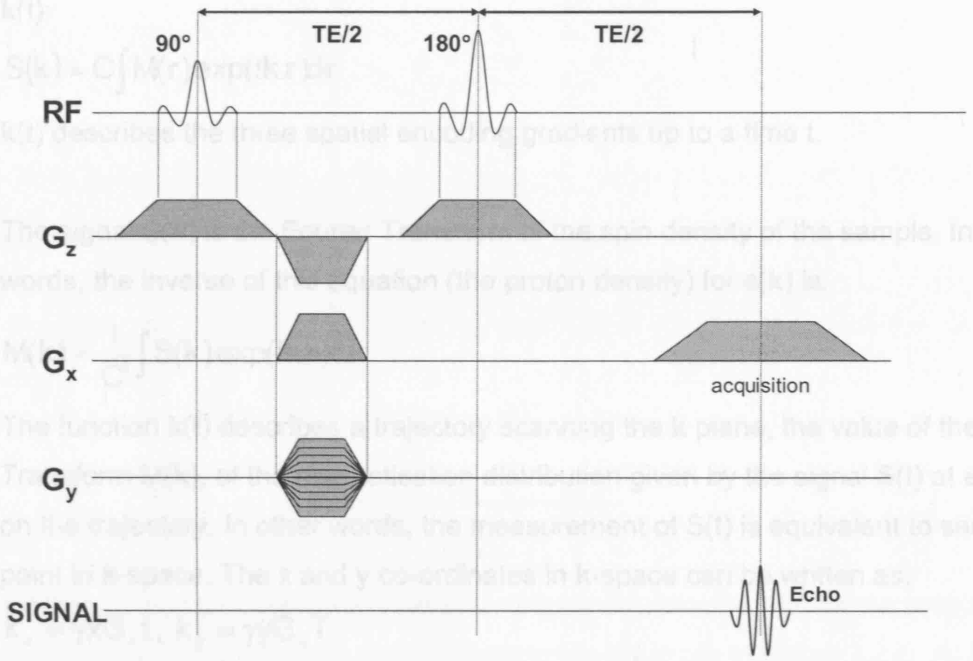

Figure 2.24: Sequence diagram for spin-warp (2D FT) imaging using a spin echo sequence.

2.8.3 k-space

It is useful to discuss NMR experiments in terms of 'k-space', a concept devised by Tweig *et al* [35]. k-space is essentially the Fourier Transform of image (**r**) space (i.e. k-space data is the array of raw data, which is Fourier transformed to give proton (spin) density data).

Let us first consider the phase acquired as a result of the application of the three gradients required for spatial encoding of the data (in the rotating frame):

$$\boldsymbol{\phi} = \gamma\int_0^t \left(xG_x(t') + yG_y(t') + zG_z(t')\right)dt' = \gamma\mathbf{r}.\int_0^t \mathbf{G}(t')dt' \qquad 2.55$$

where **G**(t) is the gradient of the magnetic flux density in all three directions, and t is the time since the application of an RF pulse.

The **r**-dependence (equation 2.55) of the phase leads to the following expression for the complex FID signal S(t):

$$S(t) = C\int \mathbf{M}(\mathbf{r})\exp\left(i\gamma\mathbf{r}.\int_0^t \mathbf{G}(t')dt'\right)d\mathbf{r} \qquad 2.56$$

where M(**r**) is the proton density of the sample and C is a constant. This can be further simplified by introducing the time dependent 'spatial frequency' **k**(t), defined by:

$$k(t) = \gamma \int_0^t G(t')dt' \qquad 2.57$$

The signal and therefore also the magnetisation can then be written as a function of **k**(t):

$$S(k) = C \int M(\mathbf{r}) \exp(i\mathbf{k}.\mathbf{r}) d\mathbf{r} \qquad 2.58$$

k(t) describes the three spatial encoding gradients up to a time t.

The signal S(**k**) is the Fourier Transform of the spin density of the sample. In other words, the inverse of this equation (the proton density) for s(**k**) is:

$$M(\mathbf{k}) = \frac{1}{C'} \int S(\mathbf{k}) \exp(i\mathbf{k}.\mathbf{r}) d\mathbf{k} \qquad 2.59$$

The function **k**(t) describes a trajectory scanning the **k** plane, the value of the Fourier Transform M(**k**), of the magnetisation distribution given by the signal S(t) at each point on the trajectory. In other words, the measurement of S(t) is equivalent to sampling a point in **k**-space. The x and y co-ordinates in **k**-space can be written as:

$$k_x = \gamma x G_x t, \; k_y = \gamma y G_y T \qquad 2.60$$

and it is easy to see the relationship between these quantities and the resolution and FOV in image (**r**) space (here the resolution and FOV in the x (frequency encoding) direction are given as an example):

$$\text{resolution} = \Delta x = \frac{1}{2k_{x\max}} \qquad 2.61$$

$$FOV_x = \frac{1}{\Delta k_x} \qquad 2.62$$

By considering these expressions, field gradients can be manipulated to achieve a particular desired coverage of k-space, and thus the resolution and FOV are established. However, k-space can be sampled in many different orders (k-space 'trajectories'), depending on the particular requirements of the experiment. For example, the centre of k-space (k=0) corresponds to the centre of a spin echo in a spin echo imaging experiment and low spatial frequencies correspond to large scale components of the image, whereas higher spatial frequencies (as k becomes further away from 0) correspond to the detail in the image, and k-space sampling strategies are designed with this in mind. Figure 2.25 is an example illustrating one method of sampling k-space (for the spin-warp spin echo imaging sequence), although many other sampling strategies are now in use which make it possible to sample all of k-space using fewer excitations. For example, echo-planar imaging (EPI) is an imaging technique in which multiple lines of k-space are acquired per excitation, significantly speeding up acquisition time.

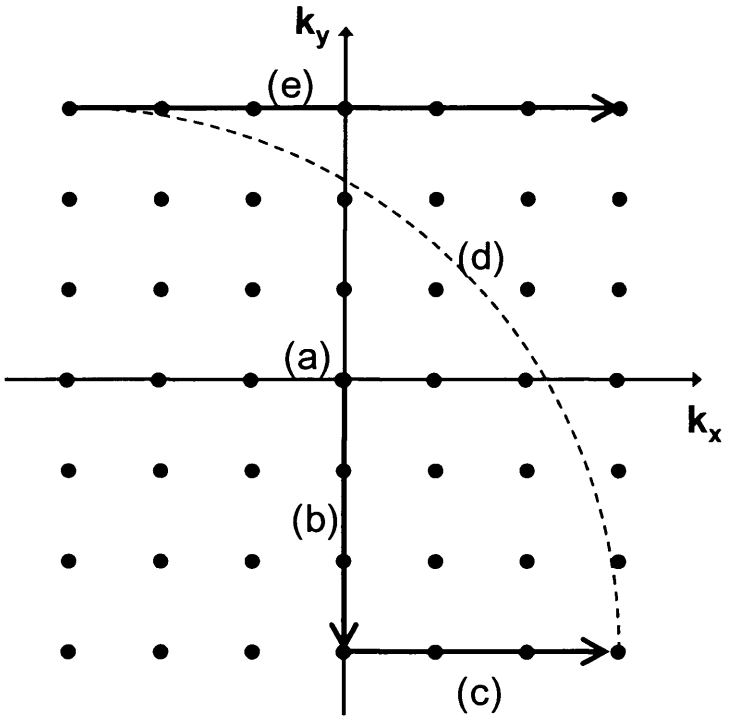

Figure 2.25: A possible k-space sampling trajectory for spin-warp imaging (for the spin echo sequence – see the sequence diagram in figure 2.24). At (a) the initial 90° pulse is applied, and the FID is produced. A phase encoding gradient is then applied in the –y direction (b), causing so that the magnetisation vector in k-space moves in the $-k_y$ direction. A positive dephasing gradient is then applied in the x direction (c). At a time TE/2 after the 90° pulse the 180° pulse is applied, which reverses the direction of the magnetisation in the xy plane (d). Finally a readout gradient is applied in the x-direction, and the signal is actually collected, with sampling performed along the positive k_x direction. This acquisition procedure is then repeated for each sequence number n, with a repetition time TR. The phase encoding gradient is incremented at each n value until all of k-space has been sampled.

2.9 Multi-slice imaging and 3D acquisition methods

2.9.1 Multi-slice imaging

Following the excitation of a particular slice using a slice selective RF pulse, the frequency of the RF pulse is shifted and the excitation and subsequent acquisition of a different slice is performed. Any unused time within a single repetition time of a sequence can be used to acquire multiple slices, to make this technique as efficient as possible. For example, if the total time from the beginning of the slice select gradient to the end of the readout gradient is t_s, then in one TR time, it is possible to excite a maximum of TR/t_s slices.

2.9.1.1 MT effects in multi-slice imaging

However, it should be noted that multiple slice imaging is complicated by the effects of slice overlap and, for some substances, the Magnetisation Transfer (MT) effect discovered by Wolff and Balaban [36] (see also Chapter 3). Careful design of slice selective pulses brings slice profiles closer to the ideal rectangular shape, or at least to the ideal of non-overlapping profiles. However, neither of these is truly possible, and overlap of slice profiles can be significant, resulting in the side-lobes of one slice reducing magnetisation in nearby, nominally non-overlapping slices.

Dixon *et al* [37] set out to determine whether Magnetisation Transfer Contrast (MTC) is significant in conventional multi-slice imaging. In the first MT experiments performed by Wolff and Balaban [36] the MT pulses were applied at an offset frequency of 5kHz (frequency shift relative to the resonant frequency), but the MT effect is much stronger at smaller offset frequency, and since in multi-slice imaging, slices are often are separated by 1-2kHz, clinical images are likely to be more sensitive to MT than these original experiments. In the original experiments performed by Wolff and Balaban [36] off resonant RF irradiation of duration 4s was used, which is longer than that used in conventional clinical MR imaging techniques, but this does not rule out significant MTC in clinical work.

They determined the effect of multiple slices on image intensity by comparison with single slice images, then separated the possible MTC effect from slice overlap effects. They consistently observed a signal loss of ~10-20% in brain tissue and muscle and attributed this to MTC, and found the effect not to be strongly TR or slice number dependent. This MTC effect may have a significant effect on the choice of 2D vs 3D multi-slice techniques because off-resonant pulses are used in 2D but not in 3D imaging (see section 2.9.2). Assuming perfectly rectangular slice profiles and identical voxel matrices with a small enough number of slices for multi-slice imaging in 1 pass (and ignoring MTC) imaging time and SNR should be identical for 2D and 3D imaging. MTC lowers the signal, which may increase or decrease contrast, in 2D images, depending on factors such as the T_1 relaxation time of the tissues being imaged, and acquisition parameters. This effect means that quantitative measurement of T_1 from multi-slice images is inadvisable.

2.9.1.2 Perfusion (flow) effects in multi-slice imaging

An effect known as high-velocity signal loss occurs in spin echo images, due to the presence of the 180° pulse. The tissues in a particular imaging slice will receive both the 90° pulse and the 180° pulse, which are both slice selective. However, the blood

that was in the slice when the 90° pulse was applied could have left the slice by the time the 180° pulse is applied (time TE/2), with the result that there is no prepared magnetisation to refocus and form an echo. Therefore when blood flows out of the slice, so-called "black blood" is observed in the image (there is an absence of signal). This effect can be partial if only some of the excited blood has left the imaging slice between the two RF pulses. However, this effect does not occur in gradient echo images since a gradient is used to form the echo, and this is not slice selective. There is a second flow-related effect which occurs in multi-slice imaging known as 'flow-related enhancement'. As data is acquired from a slab or slice during a gradient echo imaging pulse sequence, the magnetisation of the tissues in the slice become partially saturated. This means that the longitudinal magnetisation cannot fully recover between each repetition of the pulse sequence. However, blood which is not in the imaging slice has not had any prior RF pulses applied to it. If this blood flows into the slice, then its full longitudinal magnetisation will produce a brighter signal when a portion of it is flipped into the transverse plane (by the excitation pulse) for signal measurement. When multiple slices are scanned, this occurs most prominently in the first slice into which the fresh blood flows, therefore it is sometimes referred to as the "entry slice" phenomenon. In a spin echo imaging experiment, fresh blood which flows into a slice can also cause a higher signal if the fresh blood has not left the slice by the time of application of the 180° pulse, which may be the case in slow venous flow, or when the direction of flow is not perpendicular to the slice.

2.9.2 3D MRI

For 3D MRI acquisition, signal is collected from a 'slab' or large volume of the object being imaged, and this is later subdivided into thinner slices when processing the data. A variable phase encoding gradient is applied in the z-direction, so that variable frequencies along the z direction can be distinguished. Short repetition times must be used otherwise sequences may be very time consuming because the sequence must be repeated for the desired number of slices and for each phase encoding step. The advantages of 3D data acquisition are the associated increases in the signal-to-noise ratio (SNR) of image data and resolution, since slice thicknesses can be reduced.

2.10 MR imaging sequences

In this section, a short description of the theory involved in some of the sequences relevant to this thesis will be given. Here only 2D methods are described.

2.10.1 Fast Spin Echo (FSE) sequence

Also known as Turbo Spin Echo (TSE), the speed of acquisition of the spin echo sequence (described in section 2.5) is increased in this technique by using several consecutive 180° pulses to repeatedly refocus the spin echo within a single repetition time (TR) (see figure 2.26). Each of the echoes is phase encoded, resulting in additional lines of k-space. The number of echoes formed within a single repetition time is known as the Echo Train Length (ETL). The acquisition time is reduced by a factor up to the value of the ETL when compared with a conventional spin echo technique. However, eventually, spin-spin relaxation will result in the decay of the signal and there is therefore a limit on the number of echoes that can be acquired in a single repetition. The limiting case of the FSE technique is known as Rapid Acquisition with Relaxation Enhancement (RARE) [38], in which all data are collected in a 'single shot' (the conventional spin echo experiment is referred to as 'multi-shot' since several excitations are required in order to collect all the data). The extent of T_2 weighting of the images acquired using this technique is determined by the effective echo time TE_{eff}, the echo time of the k=0 echo, which is acquired without a net phase encoding gradient. The TE_{eff} is altered by changing the amplitude of the phase encoding gradients, so that a particular echo in the echo train corresponds to k=0.

The slice thickness and position are determined by applying a slice selective gradient G_z simultaneously with an RF pulse of pre-defined bandwidth and frequency. The negative 'rephase lobe' of the slice select gradient ensures that any dephasing caused by the 90° pulse is reversed such that all spins are in phase again at the time of application of the 180° RF pulse. The starting point for sampling of k-space is then selected using the "dephase lobe" of the frequency encoding gradient and the phase encoding gradient. The magnetisation then recovers towards its equilibrium value, before the above steps are repeated with an incremented phase encoding gradient amplitude.

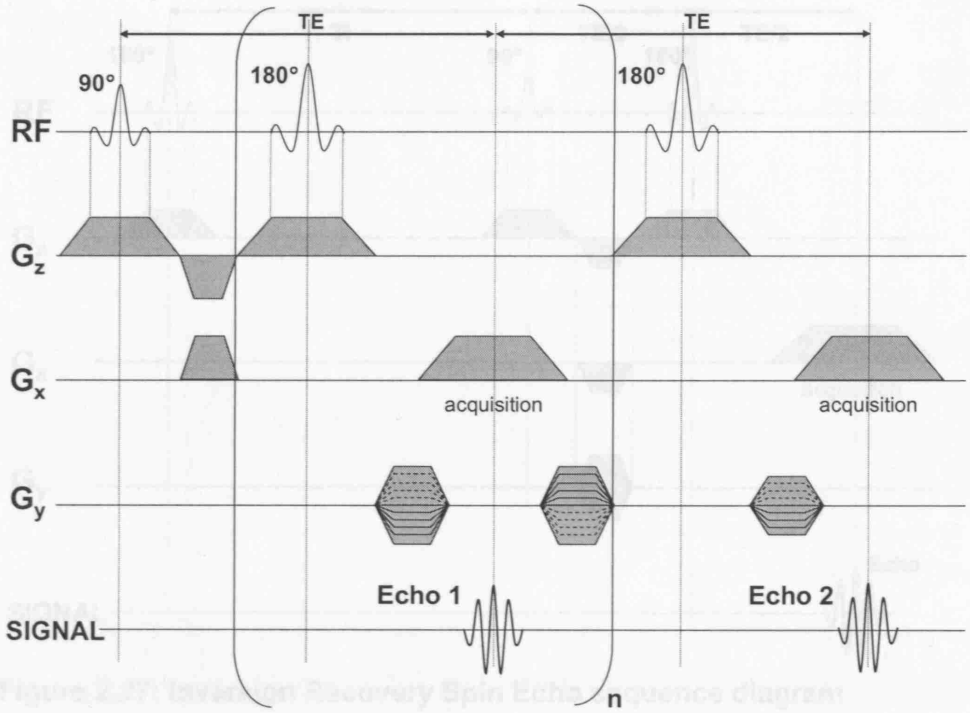

Figure 2.26: Fast Spin Echo sequence diagram. Several 180° pulses are applied consecutively to repeatedly rephase the spins, producing several spin echoes (the section of the sequence in brackets can be repeated n times, resulting in n spin echoes). Each echo is phase encoded, resulting in a reduction in acquisition time, by a factor equal to the Echo Train Length (ETL) (or the number of echoes formed within a single TR).

2.10.2 Inversion Recovery (IR) sequence

The title "inversion recovery" often refers to an inversion recovery (IR) spin echo (or IR-FSE, or inversion recovery echo planar imaging (IR-EPI)) sequence, but the basic sequence simply consists of a 180° pulse which inverts the equilibrium magnetisation $+M_0$ to $-M_0$, i.e. it is rotated through 180° to lie in a direction along the –z axis (i.e. anti-parallel to B_0). There is then a delay period, known as the inversion time TI, in which the magnetisation relaxes exponentially towards $+M_0$ with a time constant T_1. At time TI, a 90° pulse is applied which rotates the magnetisation aligned in the z-direction into the xy plane, where it can then be detected. For a spin echo inversion recovery sequence, a 180° pulse is applied at a time TE/2 following the 90° pulse, and an echo can then be detected at time TE after the 90° pulse. An example of a conventional spin echo inversion recovery sequence diagram is shown in figure 2.27.

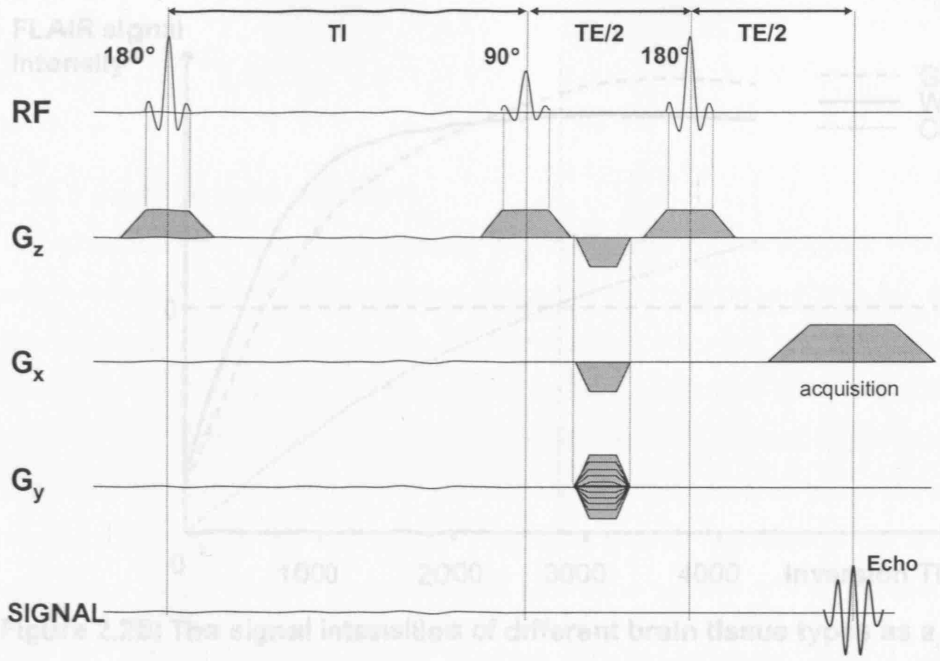

Figure 2.27: Inversion Recovery Spin Echo sequence diagram

In the past the inversion recovery sequence was often used to measure the T_1 relaxation time by acquiring data at several different TI times and calculating the T_1 time constant using measurements of the signal in the longitudinal direction at each time point. However, this type of sequence is no longer used for T_1 measurement, since it is rather time consuming to wait for complete longitudinal recovery between successive inversion pulses.

The inversion time TI (time from the first 180° pulse to the 90° pulse) can be selected in order that the signal from a particular tissue type is zero at the time of acquisition, using knowledge of the T_1 of the particular tissue. For example fat could be suppressed in a technique known as Short TI Inversion Recovery (STIR), or the signal from CSF could be nulled, using Fluid Attenuation by Inversion Recovery (FLAIR).

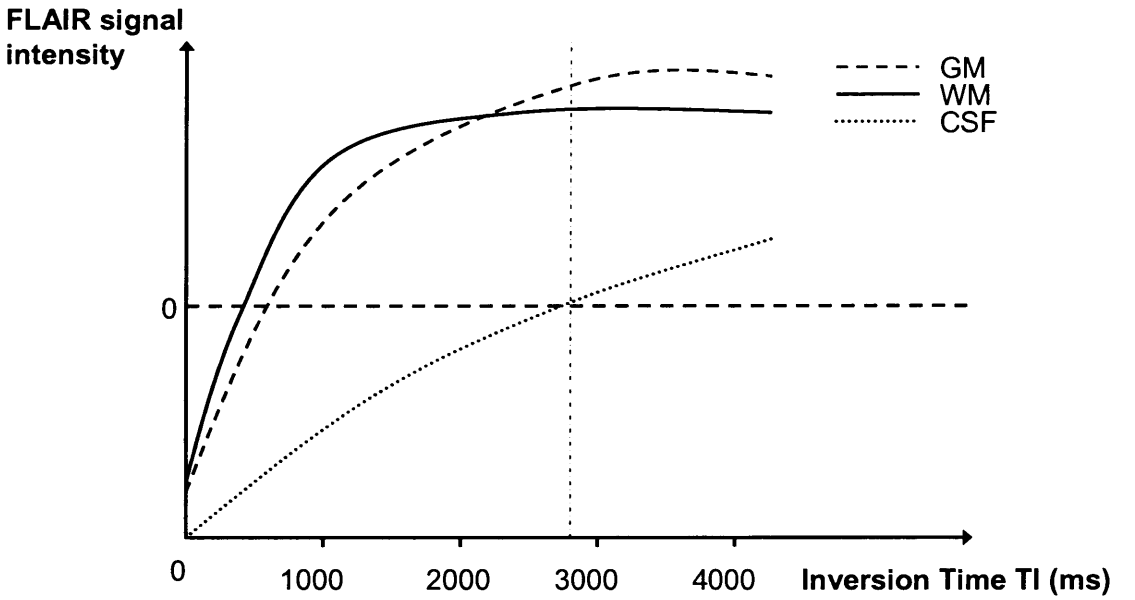

Figure 2.28: The signal intensities of different brain tissue types as a function of the inversion time TI in a FLAIR sequence. In FLAIR, the TI is selected such that the CSF signal is zero (i.e. suppressed).

The variation of the WM, GM and CSF signal intensities with inversion time TI in a FLAIR sequence is shown in figure 2.28. In FLAIR, the inversion time TI is selected such that the signal from the CSF is nulled. At TE=0 the GM and WM are almost iso-intense, since the PD and T_1 weighting effects oppose each other. As the TE is increased, the GM signal falls off more slowly than the WM, due to its longer T_2. Long echo times are required to achieve significant T_2 contrast.

If the TR of the sequence is long enough to allow complete longitudinal relaxation (i.e. $TR>>T_1$), the signal intensity for a simple inversion recovery sequence (180°-90°) can be written as [27]:

$$S = C\left(1 - 2\exp\left(\frac{-TI}{T_1}\right)\right) \qquad 2.63$$

It can be seen from this equation that in order to null the signal from a particular tissue, the requirement is that the inversion time TI of the sequence is equal to $TI=T_1(\ln 2)$ ($\approx 0.69T_1$). Therefore to completely null the signal from CSF, which has a T_1 of approximately 4s [39], an inversion time TI of approximately 2.9s is required.

The signal intensity for a spin echo inversion recovery sequence (180° - TI - 90° - TE/2 - 180° - TE/2 - acquire), incorporating T_2 relaxation during the time TE can be written as:

$$S = C\left[\left(1-2\exp\left(\frac{-TI}{T_1}\right)\right)\exp\left(\frac{-TE}{T_2}\right)\right] \qquad 2.64$$

2.10.3 Gradient echo sequence

In a gradient echo sequence, typically an initial pulse of θ° is applied, where θ<90°, which results in some magnetisation aligned in the transverse plane, but some remains aligned longitudinally. After a time TE, the signal is acquired, and subsequently additional small flip angle (θ°) pulses are applied, separated by the repetition time TR. After each θ° pulse, some of the magnetisation remains aligned in the longitudinal direction, and can be used by the next RF pulse, whereas a 90°pulse leaves no magnetisation along the z-direction. Therefore, shorter repetition times and hence acquisition times than for a conventional spin echo sequence may be used (see also section 2.6).

It can be shown that following an RF pulse, the maximum signal will result if the pulse flips the magnetisation through an angle known as the Ernst angle (α_E) [40] given by:

$$\cos\alpha_E = \exp\left(\frac{-TR}{T_1}\right) \qquad 2.65$$

This demonstrates the increased speed of this type of sequence, since the maximum signal will be given by a flip angle of 90° only if $TR >> T_1$.

The sequence diagram for a gradient echo sequence is shown in figure 2.29.

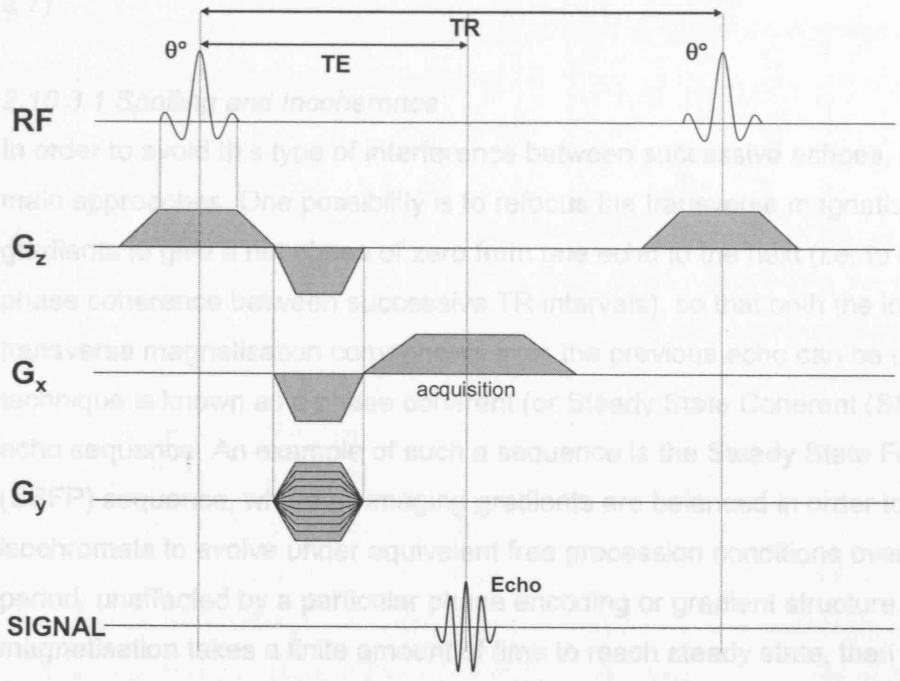

Figure 2.29: Pulse sequence diagram for a gradient echo sequence

Following the application of the RF pulse and slice select gradient, a negative readout gradient lobe is applied (in the x direction) in order to dephase the spin isochromats, then the readout gradient polarity is reversed and a gradient echo is formed at the point where the areas under the dephase and rephase gradient lobes cancel (i.e. where the net phase is zero). This gradient reversal only rephases spins that were dephased by the gradient dephase lobe. PD, T_1 andT_2* weighted images can be achieved using a gradient echo sequence, depending on the flip angle, TE and TR used for the sequence. The amount of T_2^* weighting is controlled by varying the TE and the amount of T_1 contrast generated is dependent on the flip angle and TR of the sequence. The disadvantage of rephasing using gradients (rather than using a 180° refocusing pulse as in a spin echo experiment) is that magnetic field inhomogeneities are not compensated for, i.e. there will be some inherent T_2^* weighting in a gradient echo experiment (see also equation 2.66).

The signal intensity resulting from a gradient echo sequence can be written as [27]:

$$S = C\frac{\left(1-\exp\left(\frac{-TR}{T_1}\right)\right)}{1-\cos\theta\exp\left(\frac{-TR}{T_1}\right)}\sin\theta\exp\left(\frac{-TE}{T_2^*}\right) \qquad 2.66$$

It should also be noted that in a gradient echo sequence, since short TRs are typically used to limit acquisition time, some magnetisation may remain aligned in the longitudinal direction and this will contribute to the next echo. Interference between these echoes can occur, and may cause unwanted stimulated echoes (see also section 2.7).

2.10.3.1 Spoiling and Incoherence

In order to avoid this type of interference between successive echoes, there are two main approaches. One possibility is to refocus the transverse magnetisation using gradients to give a net phase of zero from one echo to the next (i.e. to improve the phase coherence between successive TR intervals), so that both the longitudinal and transverse magnetisation components from the previous echo can be used. This technique is known as a phase coherent (or Steady State Coherent (SSC)) gradient echo sequence. An example of such a sequence is the Steady State Free Precession (SSFP) sequence, where all imaging gradients are balanced in order to allow all isochromats to evolve under equivalent free precession conditions over each repetition period, unaffected by a particular phase encoding or gradient structure. The magnetisation takes a finite amount of time to reach steady state, then the SSFP signal

is a complicated function of the imaging flip angle, TR, TE, T_1, T_2 and gradient and static field-induced offset frequencies.

The second method produces phase incoherent (Steady State Incoherent (SSI)) gradient echo sequences, where the phase coherence of the transverse magnetisation between successive TRs is destroyed via spoiling. This can be achieved either through the use of RF or gradients, and these two approaches are described below.

2.10.3.1.1 RF spoiling [41]

In RF spoiling, the coherence of the transverse magnetisation M_{xy} between successive repetition times is destroyed by semi-randomly altering the phase of each RF excitation pulse, using a different phase change each time. Thus the residual M_{xy} direction is different each time, preventing the build-up of transverse magnetisation towards a steady state (where there is not enough time for the transverse magnetisation to decay before the next repetition, thereby allowing interference of echoes between successive TR periods). However, since the altered phase of the excitation pulse will alter the phase of the received signal, appropriate measures to deal with this must be taken during either signal reception or image reconstruction (usually the receiver phase is altered in exactly the same way as the phase of the RF pulse).

2.10.3.1.2 Gradient spoiling

The alternative to RF spoiling is gradient spoiling, which entails employing strong additional gradients ("crushers") of variable strength in the slice select direction after frequency encoding but prior to the application of the next pulse. However, RF spoiling is often preferred because the spoiling produced is more homogeneous and does not require higher gradient power or longer TR.

2.10.4 Spectroscopy

Nuclei in a magnetic field actually experience an effective field $\mathbf{B}_{effective}$ (see equation 2.41), which has been modified by the electron cloud surrounding the nucleus, and is proportional to the main static magnetic field $\mathbf{B}_0$ (the field is reduced by the 'shielding constant σ' multiplied by $\mathbf{B}_0$). The nucleus precesses about this effective field with a frequency $\omega_{effective}=\gamma\mathbf{B}_{effective}$, and the chemical shift is usually defined to be the fractional difference between this new precession frequency $\omega_{effective}$ and the Larmor frequency ω_0 for the particular nucleus under investigation, measured in parts per million (ppm). The electron structure and chemical shift of the field depend on the chemical environment of the nucleus, hence the name chemical shift, and the chemical shift is also field dependent. Parts per million are used as the units of chemical shift, in

order to remove this field dependence. A spectrum displays the signal distribution as a function of frequency.

Tetramethylsilane (TMS) is commonly used as a ^{1}H NMR spectroscopy reference standard [42]; 0ppm is defined to be at the position of the methyl resonance of TMS, and all other chemical shifts are measured relative to that position. TMS was chosen because the protons in its methyl group are very highly shielded, i.e. it has a very dense electron cloud, and is therefore located near the right hand side of the spectrum, far from other proton resonances. It should be noted that, for historical reasons, spectra are plotted with chemical shift increasing from right to left (i.e. in the direction of decreasing electron shielding). A schematic of a very simple spectrum is given in figure 2.30.

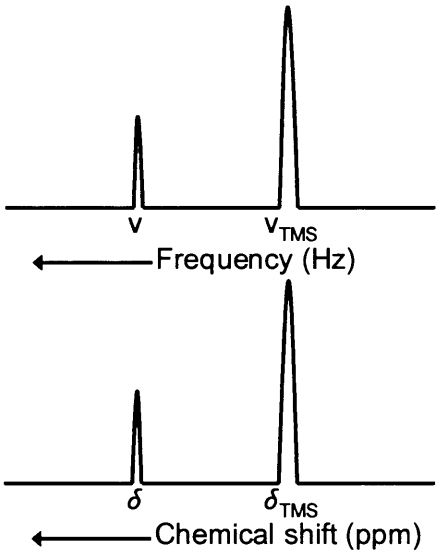

Figure 2.30: A simple example of a spectrum, viewed both in frequency units (Hz) and chemical shift units (ppm), where the chemical shift is measured relative to that of the reference compound TMS.

The area under a spectral peak for the particular bonding environment of a nucleus is proportional to the concentration of the metabolite of interest, and the linewidth (or Full Width at Half Maximum (FWHM=$\Delta\nu_{1/2}$)) of the peak is related to the T_2^* of the substance by the following expression (assuming that signal follows an exponential decay function, since the Fourier Transform of an exponential function is a Lorentzian lineshape):

$$\Delta\nu_{\frac{1}{2}} = \frac{1}{\pi T_2^*} \qquad 2.67$$

It can therefore be seen that if the field is more inhomogeneous, resulting in signal losses due to T_2^* decay, spectral peaks will be broader (with an associated decrease in

signal magnitude). The "natural linewidth" of a peak is $1/\pi T_2$ (i.e. if no field inhomogeneities are present) and these inherent linewidths are constant [14]. The advantage of using higher field strengths in NMR spectroscopy can be seen from equation 2.41, since this will result in increased SNR and peak separation in Hz (although conventionally ppm are used to remove field dependence), allowing better distinction between overlapping peaks at lower fields. It should also be noted that intermolecular dipolar interactions are "averaged out" in aqueous solutions since protons are highly mobile but in solids the directionally dependent and restricted mobility of protons causes spectral line broadening.

There are two principal spectroscopic methods; Single Voxel Spectroscopy (SVS), in which a single volume of interest is defined and spectra are acquired from that particular region, and Chemical Shift Imaging (CSI), where images of the brain are acquired using spectroscopic methods. Here, SVS will be discussed in more detail.

2.10.4.1 Spectroscopic Localisation

For single voxel spectroscopy (SVS), there are currently two main approaches, one in which no spectroscopic localisation is performed (simple pulse-acquire type technique), and another in which a localisation method is required in order to select the voxel to be imaged (echo (spin or stimulated echo) - based approaches).

1. Simple pulse-acquire technique (i.e. 90° pulse, then the FID is collected (no echo is formed))

2. Echo-based approaches:
   (a) Spin Echo acquisition, for example PRESS (Point RESolved Spectroscopy) [7]
   (b) Stimulated Echo acquisition, for example STEAM (STimulated Echo Acquisition Mode) [43], [44].

1 Simple pulse-acquire type approach: ISIS (Image Selective *In vivo* Spectroscopy)

The advantage of this type of approach is simply that the FID is measured (i.e. no echoes are collected), therefore short T_2 metabolites can be observed. A slice selective 180° hyperbolic secant pulse is used to prepare the magnetisation because it is relatively insensitive to B_1 field inhomogeneities. The signal results from the subtraction of the signal acquired from that acquired without inversion. On – off periods of the 180° pulse are cycled through the three directions in order to define a cube. However, this

method is rarely used in practice, since it is sensitive to motion or instability, especially if small voxels are used, and shimming is difficult since it is a multi-shot sequence.

2(a) PRESS (Point RESolved Spectroscopy) [7]

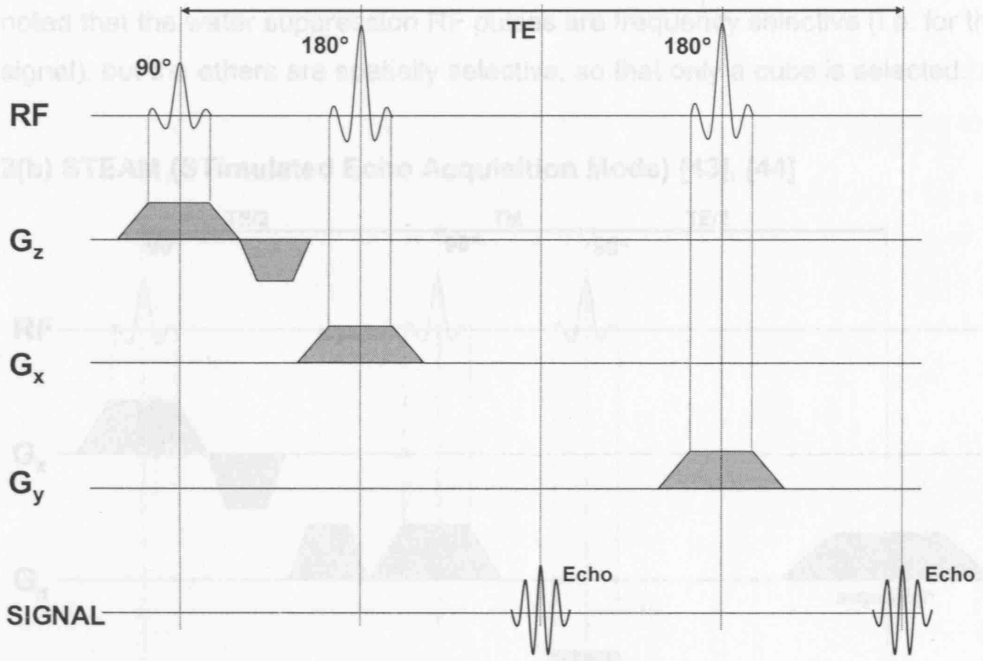

Figure 2.31: Sequence diagram for a PRESS localisation sequence

In PRESS, firstly slice selective excitation is performed, using a 90° pulse, so that a slice is specified in the slice select (z) direction, then in the readout (x) direction, a column is specified (which intersects with the slice) using a selective 180° pulse. The first spin echo is generated by these two pulses but not collected. Finally, in the third (phase encoding) direction a cube is specified, whilst the second 180° RF pulse is acting, and following this pulse, at a time TE after the 90° pulse, a second spin echo is generated and collected.

It is important that no gradients are present when collecting the echo (i.e. during readout) because frequency information is required to determine chemical shifts.

The main problem associated with this technique is the very long TE required, which means that little or no signal from the short T_2 metabolites can be observed.

However, the technique is single shot and thus tolerates movement well and shimming is straightforward. The sequence is also very easy to implement (although good selective 180° pulses are required) and the size and position of the cube can be easily manipulated by altering the gradients. It has become the method of choice now that fast gradient switching is possible, and shorter echo times can be used.

It is often desirable to suppress the water signal; in this case the sequence is preceded by a water suppression module (usually a Gaussian pulse without gradients is applied to excite the water and then the signal is spoiled before the sequence). It should be noted that the water suppression RF pulses are frequency selective (i.e. for the water signal), but the others are spatially selective, so that only a cube is selected.

2(b) STEAM (STimulated Echo Acquisition Mode) [43], [44]

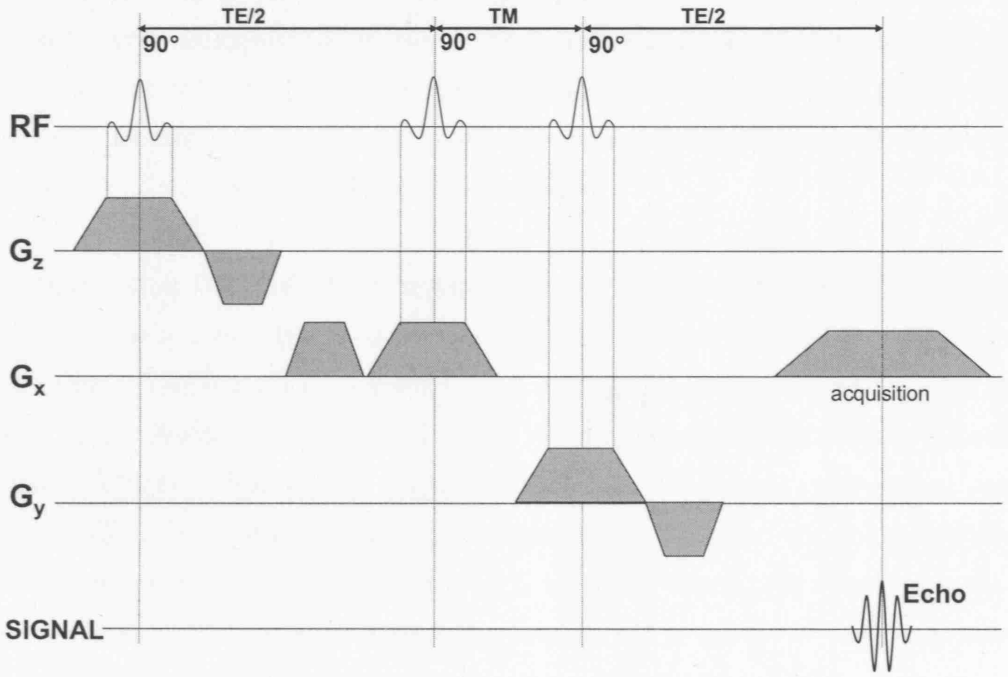

Figure 2.32: Pulse sequence diagram for the STEAM localisation technique

In this approach 3 90° pulses are applied, with gradients in the x, y, and z directions accompanying them respectively (each with a refocusing pulse for the 90° pulses). The time between the second and third pulses is the mixing time TM, and during this time half the magnetisation is aligned longitudinally, and the other half lies in the xy (transverse) plane (see also section 2.7). The magnetisation in the xy plane is crushed (using crusher gradients not illustrated in the sequence diagram), so that only T_1 relaxation needs to be considered during this time, but this can be ignored since T_1>>TM. A stimulated echo is produced, as are other spin echoes (not illustrated in the sequence diagram), in particular the third 90° pulse results in the generation of an FID. It is therefore important that the signal from these other echoes is crushed without crushing the stimulated echo.

The main advantages of this technique over PRESS are the use of 90° pulses (rather than 180° pulses), which give more rectangular slice profiles and obviously require less

RF power (and the sequence is also tolerant to flip angle errors), and that the short T_2 metabolites can be observed more easily since a shorter TE can be achieved (since the spins of interest are aligned along the z-axis during TM, resulting in less signal loss due to T_2 decay.

However the disadvantages of the STEAM approach are the inherently low SNR (as with all stimulated echoes, half the signal is lost) and the greater sensitivity to motion effects (since the gradient lobes are separated).

3 Magnetisation Transfer Imaging

Introduction

As described in section 2.3.4, interactions between restricted and free protons such as the physical exchange of water protons between molecules and the diffusion of water protons at the surface of macromolecules in biological tissue can have important effects on the relaxation properties of tissue. Such properties are a weighted average of the properties of the different proton compartments and the characterisation of such effects within biological tissue may prove to enhance understanding of the structure and function of heterogeneous tissue. In particular the MT technique provides access to the "invisible" protons (not observable on conventional MR images), which are located in biologically interesting tissue regions.

Magnetisation Transfer (MT) Imaging has found a wide range of clinical applications since its introduction to *in vivo* MRI in 1989 [36]. The two main areas in which the method is used are contrast manipulation or Magnetisation Transfer Contrast (MTC), and tissue characterisation. In the first of these approaches, the MT phenomenon is used in Magnetic Resonance Angiography (MRA) to suppress tissue signal, resulting in increased blood-tissue contrast and has also been combined with the administration of a Gadolinium chelate contrast agent on T_1 weighted scans to increase contrast between enhancing and non-enhancing tissues. MT imaging has also been shown to be valuable in the characterisation of normal and pathological tissue in neurological disorders such as Multiple Sclerosis (MS), Epilepsy and Alzheimer's Disease. In particular, measurement of the Magnetisation Transfer Ratio (MTR) is very widely performed, and volumetric methods such as histogram-based analyses are also useful. This chapter gives an overview of the physical mechanisms taking place in MT, a description of the effects of Magnetisation Transfer and the practical aspects of acquiring MTR data. Finally, some examples of the clinical applications of MT are discussed. The use of MT imaging in Multiple Sclerosis is also discussed briefly in chapter 4.

3.1 Mechanism and Physical Basis

Magnetisation Transfer (MT) MRI, first performed *in vivo* by Wolff and Balaban in 1989 [36], is based on the premise that protons in biological tissue exist in two compartments or 'pools', which display different behaviour under RF excitation. There is a free proton ('liquid') pool (conventionally labelled pool A) in which the protons are mobile and have rapid motions, and a restricted ('semi-solid') pool (pool B) in which the protons are attached to macromolecules, and are less mobile.

A possible relaxation pathway between mobile water protons and protons bound to macromolecules in structures such as proteins and lipids is illustrated in figure 3.1 (adapted from Eng *et al* [45]).

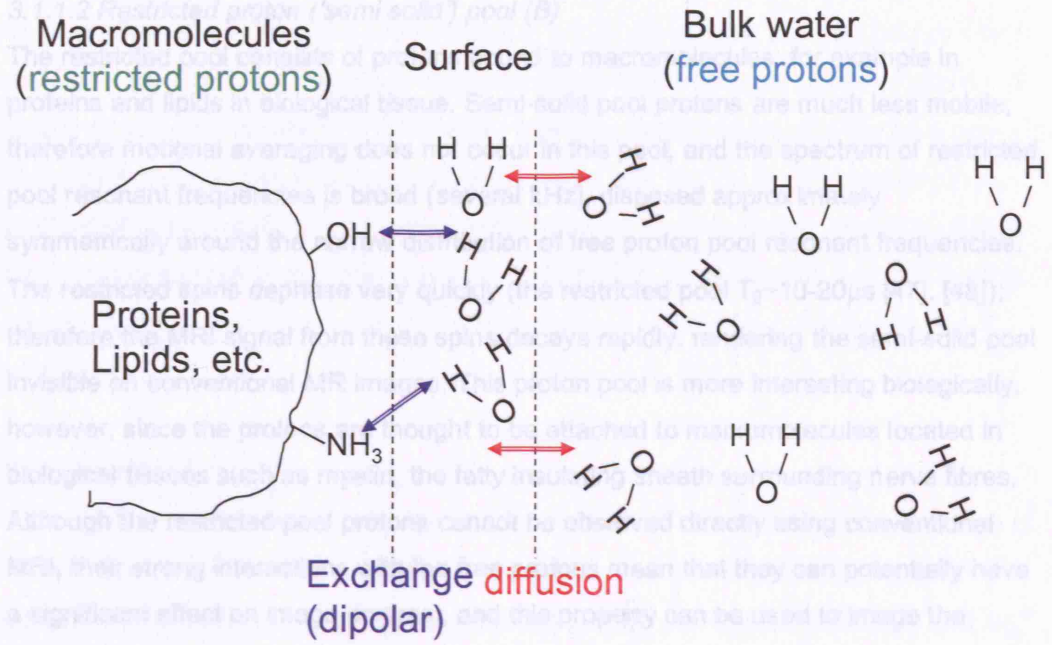

Figure 3.1: Relaxation pathway of restricted and free protons in biological tissue (adapted from Eng *et al* [45])

In the model proposed by Eng *et al* [45], rapid transfer (diffusion) occurs among bulk water protons (pool A) and protons attached to macromolecules (pool B) at the surface or "hydration layer". In other words, the surface layer protons 'communicate' with bulk water protons via diffusion processes. Magnetisation is exchanged between the macromolecular (restricted) protons and protons at the periphery of the macromolecular interface via dipolar interactions and chemical exchange, and the magnetisation is then distributed to other macromolecular protons via diffusion. Both of these mechanisms are thought to contribute to Magnetisation Transfer.

3.1.1 Two tissue compartments

3.1.1.1 Free proton ('liquid') pool (A)

The free proton pool consists of highly mobile protons, such as those in water, which experience rapid rotational and translational motions. This results in so-called "motional narrowing", where dipolar interactions are "averaged" to give a net zero dipolar Hamiltonian contribution (see also section 5.1.4.3). Therefore the free proton pool exhibits a very narrow spectrum of Larmor (resonant) frequencies (several Hz), and, in comparison to the semi-solid pool, a relatively long T_2 (≈80-200ms [46], [47]) relaxation

time. The free pool provides the bulk of the signal observed using conventional MRI scanning techniques, since the signal from the short T_2 component decays very rapidly, rendering that compartment "invisible" using conventional MRI techniques.

3.1.1.2 Restricted proton ('semi solid') pool (B)

The restricted pool consists of protons bound to macromolecules, for example in proteins and lipids in biological tissue. Semi-solid pool protons are much less mobile, therefore motional averaging does not occur in this pool, and the spectrum of restricted pool resonant frequencies is broad (several kHz), disposed approximately symmetrically around the narrow distribution of free proton pool resonant frequencies. The restricted spins dephase very quickly (the restricted pool T_2~10-20μs [47], [48]); therefore the MRI signal from these spins decays rapidly, rendering the semi-solid pool invisible on conventional MR images. This proton pool is more interesting biologically, however, since the protons are thought to be attached to macromolecules located in biological tissues such as myelin, the fatty insulating sheath surrounding nerve fibres. Although the restricted pool protons cannot be observed directly using conventional MRI, their strong interactions with the free protons mean that they can potentially have a significant effect on image contrast, and this property can be used to image the restricted proton pool via indirect means.

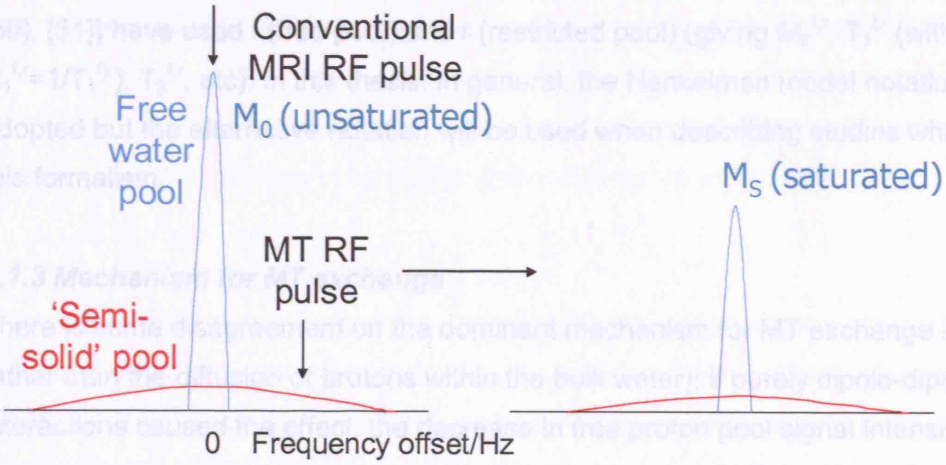

Figure 3.2: Spectra of RF absorption frequencies of the free and restricted proton pools in the MT experiment. Both pools have the same central resonant frequency, but the restricted pool has a much wider range of resonant frequencies and can therefore be selectively excited using RF irradiation within the restricted pool's range of resonant frequencies but slightly off resonance for the free proton pool.

MT pulses, typically applied prior to a conventional imaging sequence, result in attenuation of the restricted pool longitudinal magnetisation (i.e. there is insufficient time for the longitudinal magnetisation to recover to its equilibrium value M_0 within each repetition time TR), so that there is little or no transfer of magnetisation from it to the free pool. Transfer of magnetisation actually takes place from the free pool to the restricted pool since the free pool 'size' (magnetisation) is larger, but this can be thought of as a transfer of MT 'saturation' from the restricted pool to the free pool. The resultant decrease in the free pool magnetisation and hence signal intensity is a measure of the MT exchange taking place between the two pools. There is also an associated decrease in the free pool longitudinal relaxation time T_1 and it is for this reason that MT experiments are often performed in such a way as to minimise T_1 weighting.

3.1.2 Notation

There are two main formats for the notation used in MT modelling. Henkelman *et al* [49] introduced the formalism of labelling the free and restricted pools A and B respectively (i.e. the longitudinal magnetisation of the pools is labelled M_Z^A and M_Z^B (equilibrium longitudinal magnetisations ('pool sizes') M_0^A and M_0^B), with longitudinal and transverse relaxation times $T_1^{A,B}$ and $T_2^{A,B}$ etc), whilst others (e.g. Sled and Pike [50], [51]) have used f (free pool) and r (restricted pool) (giving $M_Z^{f,r}$, $T_1^{f,r}$ (with $R_1^{f,r}=1/T_1^{f,r}$), $T_2^{f,r}$, etc). In this thesis, in general, the Henkelman model notation will be adopted but the alternative notation will be used when describing studies which used this formalism.

3.1.3 Mechanism for MT exchange

There is some disagreement on the dominant mechanism for MT exchange itself (i.e. rather than the diffusion of protons within the bulk water); if purely dipole-dipole interactions caused the effect, the decrease in free proton pool signal intensity would correspond to a rotational correlation time τ_c (see also sections 2.3.5 – 2.3.6) of the water-molecular complex on the order of 10^{-8}s, which is reasonable. However, if chemical exchange were the dominant mechanism, the effect of restricted proton pool relaxation (with time constants T_1^B and T_2^B) on the observed free proton pool relaxation times in the presence of MT is (ignoring T_2^B mechanisms since T_2^B is so short) would be described by [45]:

$$\frac{1}{T_{1obs}^A} = \frac{1}{T_1^A} + \frac{X_B}{T_1^B + (1/k_r)} \qquad 3.1$$

where X_B is the molar fraction of the restricted protons, k_r is the rate of transfer of magnetisation from the restricted to the free pool, $T_1^{A,B}$ are the T_1 relaxation times of

the free (A) and restricted (B) pools in the absence of MT exchange, and $T_1{}^A{}_{obs}$ is the observed longitudinal relaxation time of the free proton pool.

Preliminary data suggests that dipole-dipole interactions between spins are the dominant cause of MT exchange processes [45]. Also, if chemical exchange were the principal mechanism taking place, one would expect to see similar effects for other isotopes such as deuterium (which has a very low dipolar moment due to its low gyromagnetic ratio). No such transfer has been observed between restricted ^2H and free ^2H [36]. However, it should be pointed out that diffusional exchange of spins to and from the macromolecular interaction sites is still a potential rate-limiting step in the transfer of magnetisation from the macromolecules to the bulk water protons (see figure 3.1).

3.2 Early models for MT in tissue

3.2.1 The two-pool model

Most models of Magnetisation Transfer involve modelling the interaction of two reservoirs or 'spin baths' (whether by diffusion or dipolar coupling) using the Bloch equations, modified to incorporate the coupling of the two pools.

The first two-pool model for magnetisation exchange was developed by McConnell *et al* in 1958 [52] and used to study various biological tissue and MRI test object (phantom) materials including agar, lipid bilayers, rat muscle, calf lens homogenate, heat denatured egg albumin and cross-linked bovine serum albumin (BSA).

3.2.2 The 'Saturation Transfer' experiment

Forsen and Hoffman performed the first 'saturation transfer' experiment in 1963, and proposed a mathematical description for this transfer of magnetisation between two distinct spin environments that were relatively weakly coupled to one another [53]. RF irradiation was used to saturate protons of one species, and the effect on the other species in the two-pool system was observed. 'Saturation transfer' occurred between the two pools, and a decrease in the net magnetisation of the non-irradiated pool of spins was observed, as the two spin populations equilibrated via the process of chemical exchange. This resultant decrease in magnetisation could then be used to quantify the rate of exchange of magnetisation between the two interacting species. In this experiment, unlike the *in vivo* situation, the two species studied were in different chemical environments, and therefore had different resonant frequencies. Edzes and Samulski later extended this approach to study systems where each component absorbed RF energy at the same resonant frequency [54]. A significant decrease in the

free pool longitudinal relaxation time from T_1^A to a value $T_1^A{}_{sat}$ was observed in addition to the decrease in the longitudinal magnetisation of this pool. A mathematical model to describe the exchange of magnetisation between the two pools of spins was developed and this is discussed further in chapter 5.

3.2.3 Tissue Magnetisation Exchange

In 1989 Wolff and Balaban performed the first magnetisation transfer experiment *in vivo*, in rabbit kidney and muscle [36]. The MT effect was observed to be stronger at lower frequency offset from the free proton pool resonance. However, as it is important that the frequency of RF irradiation is not too close to the liquid pool water resonant frequency, in order that direct saturation of the free proton pool magnetisation is minimised, experiments were performed with a frequency offset of at least 5kHz.

3.2.4 Pseudo first order rate constant k_f and $T_1^A{}_{sat}$

If pool B could be fully saturated (it is not possible to completely saturate the spins, but the experiment can be performed in such a way that very little magnetisation remains following MT saturation), there is no transfer of magnetisation from pool B to pool A, but MT from pool A to pool B still occurs. The recovery of longitudinal magnetisation in pool A following the complete saturation of pool B would be characterised by a time constant $T_1^A{}_{sat}$ (where $T_1^A{}_{sat}<T_1^A$ (see section 3.2.2)), given by [52]:

$$\frac{1}{T_{1sat}^A} = \frac{1}{T_1^A} + \frac{1}{\tau_A} \qquad 3.2$$

where τ_A is the "lifetime" of the spins in pool A (i.e. the average time of transfer for a spin from pool A to pool B). The Bloch equation describing the effect of MT saturation on the free proton pool longitudinal (z-direction) magnetisation is (i.e. modified to account for the magnetic coupling of the two pools) [54]:

$$\frac{dM_Z^A}{dt} = \frac{M_0^A - M_Z^A}{T_1^A} - k_f M_Z^A + k_r M_Z^B \qquad 3.3$$

where k_f is the exchange rate constant from pool A to B (i.e. $1/\tau_A$) and k_r is the rate constant for MT exchange from pool B to pool A. M_0^A is the free pool equilibrium magnetisation (i.e. in the absence of MT saturation), and M_Z^A is the (time-dependent) longitudinal magnetisation of the free pool following MT saturation.

So, by integration of dM_Z^A/dt combined with the above equation for $T_1^A{}_{sat}$, it is found that the A pool longitudinal magnetisation as a function of time after the end of the MT pulse (where the equilibrium magnetsation $M_Z^A(0)=M_0^A$) is given by (since M_Z^B is assumed to have been completely and indefinitely saturated (such that $M_Z^B=0$ at all t values), therefore terms in k_r and M_Z^B are eliminated, and $k_f=1/\tau_A$ (see above)) [53]:

$$M_Z^A = (M_0^A - M_{sat}^A)\exp(-\frac{t_{sat}}{T_{1sat}^A}) + M_{sat}^A \quad 3.4$$

where t_{sat} is the time for which the B pool has been held at saturation and M_{sat}^A is the final equilibrium longitudinal magnetisation that the A pool would attain if the B pool were held in a state of saturation indefinitely, and is given by:

$$M_{sat}^A = \left(\frac{T_{1sat}^A}{T_1^A}\right) M_0^A \quad 3.5$$

Following application of the saturating pulse, the equilibrium longitudinal magnetisation M_0^A is reduced exponentially with a time constant $T_1{}^A{}_{sat}$. If the saturating pulse were applied indefinitely, the magnetisation would be reduced to a final equilibrium magnetisation value of M_{sat}^A, as illustrated in figure 3.3. However, this is not realistically achievable *in vivo*.

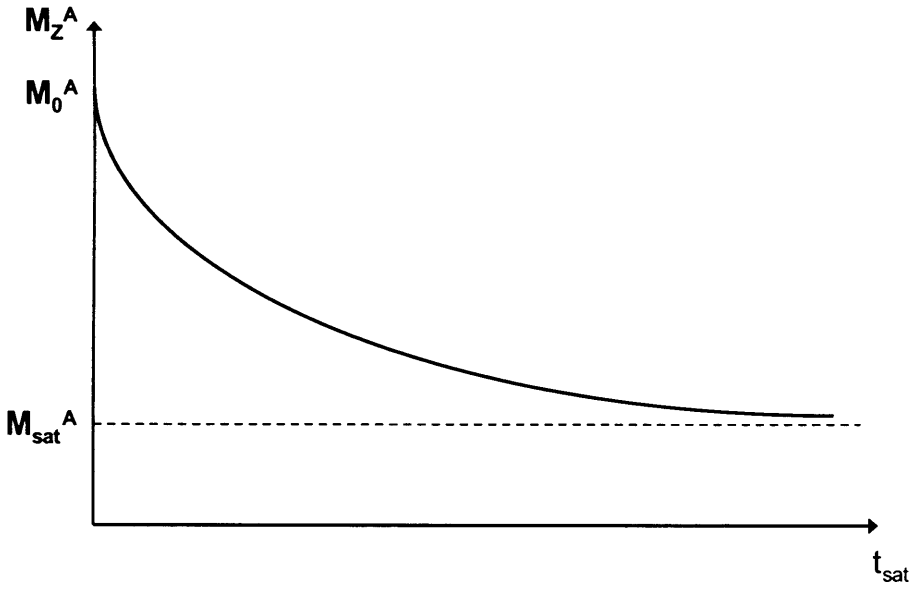

Figure 3.3: The exponential decay of the free pool longitudinal magnetisation, with time constant $T_1{}^A{}_{sat}$. If the saturating pulse were applied indefinitely, the longitudinal magnetisation of the free proton pool would be decreased to M_{sat}^A.

3.2.5 Magnetisation Transfer Ratio (MTR)

The most widely used measure of the amount of MT exchange taking place is the Magnetisation Transfer Ratio or MTR, given by equation 3.6. The MTR is often measured in percent units (pu) [55], used to avoid ambiguity with actual percentages. For example, a 5% reduction in an MTR value of 40pu could mean a 2pu reduction (to 38pu) or a 5pu reduction (to 35pu), whereas a reduction of 5pu is unambiguous.

$$MTR = 100\left[\frac{M_0^A - M_Z^A}{M_0^A}\right] \text{ pu} \quad 3.6$$

One set of images is acquired in the presence of MT saturation (i.e. these images are highly MT-weighted), resulting in a decrease of the free pool longitudinal magnetisation from the equilibrium value M_0^A to a value M_Z^A, and another set of images are acquired without an MT pulse and the fractional reduction in the equilibrium magnetisation is calculated (equation 3.6). The MTR increases where exchange is taking place between the two proton pools, and depends on (amongst many other biological, sequence and scanner related factors) the fraction of restricted protons in the tissue being observed. The MTR has been shown to be reduced in many pathological processes, including demyelination (destruction/loss of the fatty sheath (myelin) surrounding nerve fibres (axons), and one of the dominant mechanisms taking place in Multiple Sclerosis (MS)). This is because the relative magnetisations of the pools are altered in neurological diseases (in particular, the restricted proton fraction f (fraction of protons that are restricted relative to both free and restricted protons; see also chapter 5) is often decreased as a result of increased water content or decreased macromolecular content).

Equation 3.3 gives the Bloch equation for the free pool in the longitudinal (z) direction, modified for the coupling of the two pools. If complete and continuous saturation occurs, then the restricted pool longitudinal magnetisation $M_Z^B=0$ for all times t.

The demonstrated shortening of the free proton pool T_1 (T_1^A) to a value $T_1^A{}_{sat}$ for complete saturation of the restricted proton pool is described by equation 3.2, with $k_f=1/\tau_A$, as defined previously [54].

Combining equations 3.5 and 3.2 results in the expression:

$$k_f = \left[\frac{1}{T_{1sat}^A}\right]\left(1-\frac{M_Z^A}{M_0^A}\right) = \frac{MTR}{T_{1sat}^A} \qquad 3.7$$

Thus, the apparent rate constant k_f of MT exchange from pool A to pool B could be determined from a knowledge of M_Z^A/M_0^A (or the MTR, measured with complete saturation of the restricted pool) and $T_1^A{}_{sat}$. k_f is a more physically meaningful parameter than the MTR, and is related to tissue structure.

Measurements of the MTR and $T_1^A{}_{sat}$ have previously been used to estimate the pseudo first order rate constant k_f [56], [57], but the above equations only hold true for complete saturation of the restricted pool, and in practice it is impossible to achieve complete saturation, not least because this would breach limits on power deposition in humans (the Specific Absorption Rate, or SAR is a limit on the heat deposition allowed in humans).

3.3 Methods for Magnetisation Transfer Imaging

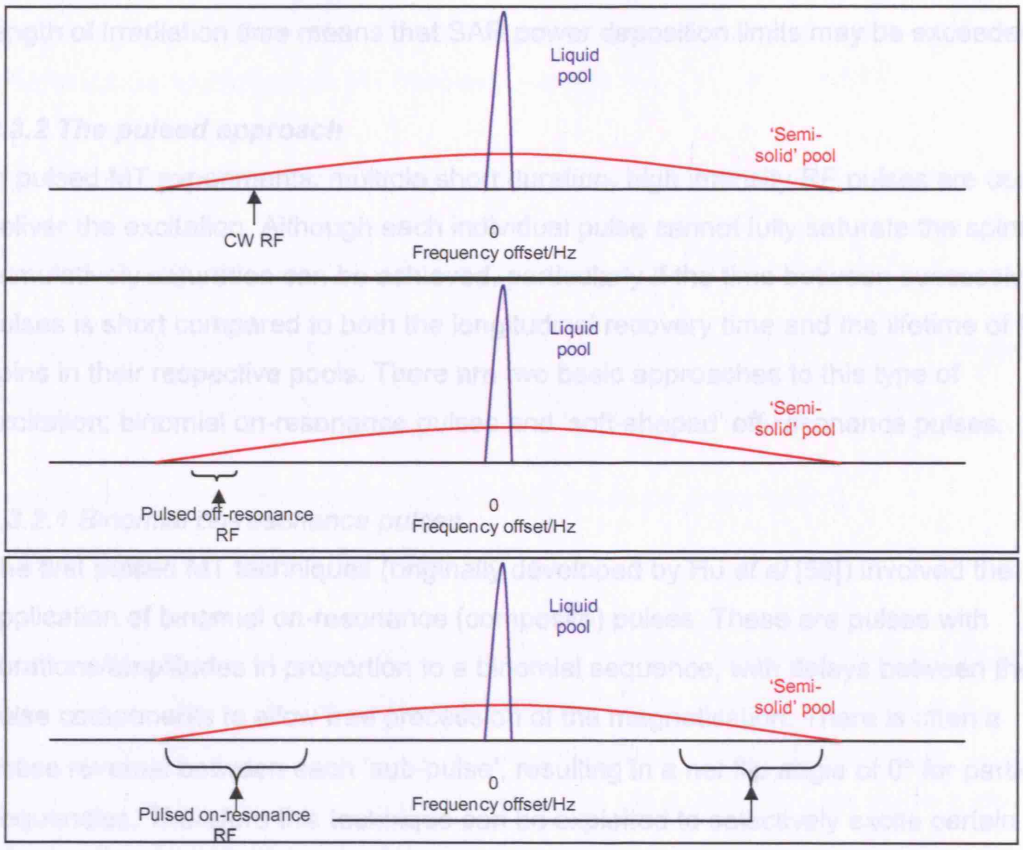

Figure 3.4: Methods for Magnetisation Transfer MRI. The three basic approaches to selectively exciting the semi-solid pool in MT imaging are illustrated in this figure; continuous wave (CW) RF irradiation, off-resonance 'shaped' RF pulses and on-resonance binomial pulsed irradiation

3.3.1 The Continuous Wave (CW) approach

The earlier models of MT, such as the Henkelman model [49], assume the use of Continuous Wave (CW) RF irradiation to excite the spins, where an RF waveform, $B_1(t)$ of long duration is applied off-resonance, given by:

$$B_1(t) = \frac{\omega_1}{\gamma} e^{i2\pi\Delta ft} \qquad -\tau_{sat}/2 < t \leq \tau_{sat}/2 \qquad 3.8$$

ω_1 is the nutation frequency on resonance (in the rotating frame), γ is the proton gyromagnetic ratio, Δf is the frequency difference between the irradiation frequency and the proton resonant frequency (the offset frequency) and τ_{sat} is the pulse duration.

However, this type of experiment is impractical for use *in vivo* for a number of reasons, namely that such an experiment may require hardware modification, since most commercial imagers do not operate in the CW mode (although some spectrometers

can produce long pulses), the MT pulse needs to be turned off for imaging and the length of irradiation time means that SAR power deposition limits may be exceeded.

3.3.2 The pulsed approach

In pulsed MT experiments, multiple short duration, high intensity RF pulses are used to deliver the excitation. Although each individual pulse cannot fully saturate the spins, cumulatively saturation can be achieved, particularly if the time between successive pulses is short compared to both the longitudinal recovery time and the lifetime of the spins in their respective pools. There are two basic approaches to this type of excitation; binomial on-resonance pulses and 'soft-shaped' off-resonance pulses.

3.3.2.1 Binomial on-resonance pulses

The first pulsed MT techniques (originally developed by Hu *et al* [58]) involved the application of binomial on-resonance (composite) pulses. These are pulses with durations/amplitudes in proportion to a binomial sequence, with delays between the pulse components to allow free precession of the magnetisation. There is often a phase reversal between each 'sub-pulse', resulting in a net flip angle of 0° for particular frequencies. Therefore this technique can be exploited to selectively excite certain spins on the basis of their frequency or T_2 value. 1-$\bar{1}$, 1-$\bar{2}$-1, or 1-$\bar{3}$-3-$\bar{1}$ type pulses are most often used (where the number indicates the (relative) nutation angle of the sub-pulses and the bar indicates a negative sense nutation i.e. a phase reversal). This type of approach was used in early MT experiments due to hardware limitations; by sweeping the phase slowly with time it was possible to saturate restricted protons whilst remaining on resonance.

In the simplest (1-$\bar{1}$) case the free protons are flipped into the transverse plane, and then returned to the z-axis, so that all the magnetisation ends up along the z-axis (i.e. the net result of the pulse is effectively a 0° flip angle, as the free protons do not relax during the binomial pulse). The macromolecular protons are also flipped, but due to their short T_2, they lose some of their magnetisation due to T_2 decay while they are still in the transverse plane, and the longitudinal magnetisation of the restricted pool is therefore saturated [59]. This technique is very time-efficient (binomial pulse durations are typically < 3 ms), and causes a large signal reduction, but there is intrinsic direct saturation associated with the technique caused by the poor Fourier Transform profile of the pulses. Binomial pulsed on-resonance saturation has been used in several MT studies [60], [61], [62]. However, an identical duration off resonance pulse allows much better control of the pulse in frequency space than a binomial pulse.

3.3.2.2 'Soft-shaped' off-resonance pulses

These are typically Gaussian or Sinc-shaped pulses, of duration 5-50ms, applied off-resonance through the main RF transmit channel.

The Gaussian pulse shape is widely used and is given by the equation [27]:

$$B_1(t) = \frac{\omega_1}{\gamma}\frac{1}{\sqrt{2\pi\sigma}}\exp\left(\frac{(t-\tau_{sat})^2}{2\sigma^2} + i2\pi\Delta f t\right) \qquad -\tau_{sat}/2 < t \leq \tau_{sat}/2 \qquad 3.9$$

where σ is the standard deviation of the Gaussian envelope, Δf is the offset frequency and ω_1 is the maximum nutation frequency during the application of the pulse.

Sinc-shaped pulses are also often used, with envelope given by [27]:

$$B_1(t) = \frac{\omega_1}{\gamma}\sin c(\pi\Delta f t) = \frac{\omega_1}{\gamma}\frac{\sin(\pi\Delta f t)}{\pi\Delta f t} \qquad -\tau_{sat}/2 < t \leq \tau_{sat}/2 \qquad 3.10$$

Sinc-shaped pulses give slice profiles much more closely approaching a rectangular shape, particularly if they are apodised ("windowed") by another function e.g. a Hanning or Hamming (i.e. multiplied by that particular function, which usually closely approximates a rectangular shape). However, the main disadvantage of this pulse shape is its high power deposition.

This type of off-resonance pulsed saturation method has been incorporated into many different spin echo [55], [61] and gradient echo [63], [64] sequences for MT imaging.

3.3.3 Practical details of MTR sequences

An off-resonance shaped MT pulse (or binomial on-resonance pulse) is typically applied prior to the acquisition of a standard spin echo or gradient echo sequence. If a gradient echo sequence is used, the liquid pool transverse magnetisation is usually spoiled to avoid complication of the interpretation of the MT effect; if the direct saturation of the free proton pool were significant, it would be necessary to analyse stimulated echo contributions to the free pool signal. The repetition time (TR) and excitation flip angle are also usually carefully selected in order to minimise T_1 weighting (i.e. low flip angle, reasonably long TR, therefore this sequence is rather slow). MT experiments are typically performed with lower offset frequencies than the initial experiments performed by Wolff & Balaban [36], in order to give a stronger MT effect. However, the offset frequency of the MT pulse is typically kept to a minimum of around 1500-2000Hz in order to prevent direct saturation of the free proton pool.

MT pulses are not slice selective, therefore the extent of saturation is actually determined by the time between successive pulses, TR'. This is equal to the repetition time in 3D sequences, but in multi-slice 2D sequences TR' = TR/number of slices.

3D imaging is attractive for use in MT experiments because of its increased SNR per unit time and resolution compared to 2D sequences, and less errors caused by poor slice profiles, incidental MT from neighbouring slices, or crosstalk (partial excitation of adjacent slices during RF excitation/refocusing) between adjacent slices. However, short TR's must be used in 3D imaging to limit acquisition times, resulting in some T_1 weighting. Therefore, low excitation pulse flip angles must be applied in 3D gradient echo imaging sequences used for MT, to limit this effect. However, since 3D imaging provides an inherently higher SNR than 2D imaging, good quality images result despite the use of low imaging flip angles.

3.3.3.1 Protocols for MTR measurement

An interleaved dual spin echo (with TE times of 30 and 80ms) MTR sequence was developed by Barker *et al* [55]. The sequence consists of four parts in each phase encoding step; firstly there is a time lasting a few TR periods nTR in which the restricted proton pool is allowed to relax, then data are acquired to form the unsaturated image, the MT pulses are then switched on for a period nTR, without data collection, in order to allow the free pool magnetisation to decay, then with the pulses still on, data are acquired to form the saturated images. The advantages of this approach are the acquisition of the dual echo (PD and T_2-weighted) data, which can then be used for other purposes, and the fact that the sequence is interleaved, so that errors introduced by subject motion are minimised. The approach is not very susceptible to B_0 inhomogeneities since it is a spin echo sequence rather than a gradient echo. However, the acquisition time is long for this sequence (19 minutes), and there may be some intrinsic T_1 weighting due to the relatively short TR (1500ms).

A 2D gradient echo Euro-MT sequence [63], [65] (the pulse sequence diagram is shown in figure 3.5) was developed at our centre in collaboration with a European multi-centre MT study. This is a faster method than the interleaved spin echo MTR sequence described above, and the T_1 weighting of the sequence can be controlled by adjusting the gradient echo sequence excitation flip angle and/or TR. However, the main disadvantage of the approach is the potential for movement artefacts, since the images collected are not interleaved. 3D gradient echo sequences have also been employed [66], [67], [68].

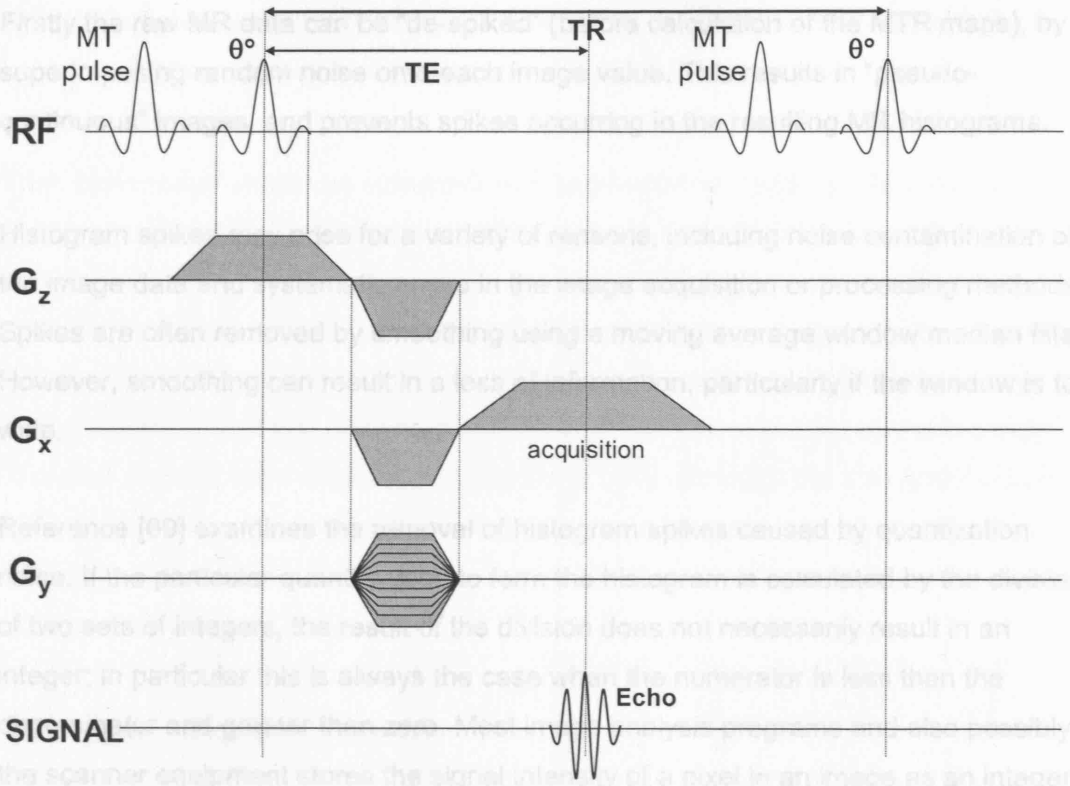

Figure 3.5: An MT-prepared RF spoiled gradient echo sequence diagram, such as the Euro-MT sequence. A 'shaped' MT RF pulse is applied prior to the acquisition of each spoiled gradient echo sequence, with excitation flip angle θ° (<<90°).

However, the MTR is only 'semi-quantitative'; it is highly sequence dependent, and difficult to reproduce across centres. Therefore a more quantitative approach is necessary, from which fundamental parameters relating to the pathological changes occurring in tissues can be obtained.

It is also sensitive to all pathological processes occurring in a particular tissue, and is not specific to a particular pathology/disease.

A newer technique, known as quantitative MT (qMT), to be discussed in chapter 5, allows the examination of the parameters underlying the MT exchange process, independently of particular sequence details.

3.3.4 MTR Histograms

Whole brain histograms are used to characterise diffuse pathological changes occurring in disease in quantitative MR parameters, such as the MTR. To generate reproducible MTR histograms that can be compared within and across centres, the standard procedure employed at our centre is as follows [6]:

Firstly the raw MR data can be "de-spiked" (before calculation of the MTR maps), by superimposing random noise onto each image value. This results in "pseudo-continuous" images, and prevents spikes occurring in the resulting MR histograms.

Histogram spikes may arise for a variety of reasons, including noise contamination of the image data and systematic errors in the image acquisition or processing methods. Spikes are often removed by smoothing using a moving average window median filter. However, smoothing can result in a loss of information, particularly if the window is too wide.

Reference [69] examines the removal of histogram spikes caused by quantization noise. If the particular quantity used to form the histogram is calculated by the division of two sets of integers, the result of the division does not necessarily result in an integer; in particular this is always the case when the numerator is less than the denominator and greater than zero. Most image analysis programs and also possibly the scanner equipment stores the signal intensity of a pixel in an image as an integer (by scaling), therefore this is a problem frequently observed in the calculation of histograms of MR quantities such as T_1 and MTR. The cause of histogram spikes is the natural abundance of fractions such as 1/2, 2/3 and 3/4 when two integers are divided. The distribution of the fractional results of the division a/b, where b can take each integer value between 1 and the maximum intensity value in an image, and a loops between 1 and b-1, is not even. The highest spike occurs at a ratio of 1/2, 2 lower spikes occur at 1/3 and 2/3, and then two more at values of 1/4 and 3/4, and so on. It should be noted that for every high point in the distribution there is also a corresponding low point where the histogram value is decreased.

The occurrence of spikes in histograms could be reduced by increasing the histogram bin width. Storing the data in floating point format could solve the problem, as the precision of the data could be made smaller than the bin width.

Tozer and Tofts [69] showed that the addition of noise to the signal intensity integer values prior to division removes artifactual histogram spikes caused by the uneven distribution of the quotients of two integers. They also demonstrated that their correction method had no significant effect on the histogram in regions unaffected by spikes, and that there were no differences observed between different noise addition schemes (normally distributed, uniformly distributed and estimating the gradient of the histograms of the two input images as a linear function for each signal intensity and

using this as the probability distribution function for the addition of noise, with the same range as above each point with this signal intensity).

Then brain tissue should be extracted, and segmentation performed to select the tissue of interest, if necessary. The data are then split into pre-defined intervals (bin widths), and plotting the histogram values gives an absolute histogram, which will have an area equal to the total number of voxels included. However, in order to account for variations in brain size between individuals, it is desirable to normalise histograms by summing all the histogram values and dividing each value by the total multiplied by the bin width. The area under a fully normalised histogram is unity, although the histogram values are often multiplied by 100 to give percentage values. If a small bin width is chosen in order to preserve structure in the histogram, it may also be advantageous to perform some histogram smoothing.

3.4 Clinical Applications of MTI

The clinical applications of MT imaging can be divided into two main categories. The first is contrast manipulation or Magnetisation Transfer Contrast (MTC), where the signal from certain tissue is suppressed, such as in MR Angiography or in combination with Gadolinium enhancement, thereby increasing contrast. The second application is tissue characterisation, which encompasses both regional MT and volumetric (MT histogram) analysis. This branch of MT includes application to Multiple Sclerosis, Epilepsy, Dementia, Traumatic Brain Injury, Tumours and Abcesses, and many other disorders.

3.4.1 Contrast augmentation

3.4.1.1 Magnetic Resonance Angiography (MRA)

Time-of-flight (TOF) MR angiography, based on flow-related enhancement, is widely used for imaging of intracranial vessels. A 90° pulse is applied, and partially saturates the slice/slab (2D/3D), then fresh, unsaturated blood flows in during the TR. Flowing blood, therefore, has a high signal compared to stationary blood. The contrast between the vessels and brain tissue depends on the flow velocity, but also the flip angle and TR.

MT pulses applied prior to the MRA sequence suppress background (healthy) tissue such that an increase in the inflowing blood – background contrast is observed. The semi-solid pool spins are preferentially saturated due to their short T_2, whilst the liquid spins remain relatively unaffected. Thus fresh inflowing blood is less saturated than neighbouring tissues containing stationary spins. Edelmann *et al* [70] applied an MT

pulse prior to an RF-spoiled gradient echo MRA sequence with flow compensation, and found a significant improvement of the conspicuity of small vessels. However, an increase in TR was required to allow the inclusion of the MT pulse in the sequence.

Pike *et al* [60] implemented a 1ms on-resonance MT pulse with a velocity-compensated 3D TOF MRA sequence, which increased the TR by a smaller amount, and gave significantly improved blood-tissue contrast.

3.4.1.2 Gadolinium enhancement

Gadolinium chelates (e.g. Gd-DTPA) are often used as paramagnetic contrast agents in combination with T_1-weighted imaging (see also section 2.3.6.2), by inducing relaxation via dipolar interactions and hence reducing relaxation times. The large Gd-DTPA molecules are not able to penetrate a healthy BBB, but damage to the BBB results in leakage of these molecules through the barrier. Then "enhancement" on T_1-weighted images occurs in these regions, (i.e. the relaxation time T_1 is reduced) where Gd-DTPA molecules have penetrated the BBB. The breakdown of the blood-brain-barrier is thought to be one of the earliest events in the development of an MS lesion [71].

MT imaging suppresses the signal from normal tissue so that areas of enhancement are more easily observed (i.e. tissue contrast is increased). MT contrast complements the T_1 shortening effects of the Gadolinium contrast agent.

Tanttu *et al* [72] were the first to use this technique in conjunction with MT, and investigated its effects in MS, neuromas and meningiomas, and compared results with the effects of both MT and Gadolinium enhancement alone. The best contrast was achieved with a combination of MT and Gadolinium enhancement.

Van Waesberghe *et al* [73] showed that the use of a single dose of Gadolinium combined with MT imaging gave equivalent contrast to a standard T_1 weighted sequence with a triple dose of Gadolinium, which could have significant economic implications.

Mehta *et al* [74] used this technique to study tumours and MS lesions and found both the extent of the enhancement and the edge distinction to be improved due to the combined use of Gadolinium and MT.

Finelli *et al* [75] demonstrated an increased contrast-to-noise ratio (CNR) in post-Gadolinium T_1-weighted MT images in a wide variety of enhancing brain lesions, including primary neoplasms, metastases, extra-axial lesions, cerebral infarctions, MS plaques, meningitis, vascular malformations and contusions.

3.4.2 Tissue characterisation

3.4.2.1 Normal Variation

Despite the semi-quantitative nature of the parameter, the MTR has been shown to be highly reproducible for a particular sequence in an individual centre [55], [76], [77]. For example, Barker *et al* [55] measured a standard deviation of less than 1pu in 10 controls in 4 different white matter regions. There is, however, variation with location, presumably associated with the variation in concentration of myelin and other cell types.

Barker *et al* [55] demonstrated significant MTR differences between white matter regions in 10 normal controls. The brain stem, which predominantly comprises white matter, was significantly ($p<0.001$) different from all white matter regions (except for the brain stem vs. left occipital white matter, which was significant at the $p<0.01$ level). In the brain stem the MTR value was 29.1pu vs. 31.9 and 31.7pu for left and right frontal white matter respectively, 29.8 and 30.5pu for left and right occipital white matter respectively and 31.1 and 31.0pu for left and right parietal white matter respectively. The right occipital region showed no significant difference from right parietal white matter, and differed from left parietal white matter only at the $p<0.05$ level. Left parietal vs. right frontal matter MTR difference was also only significant at the $p<0.05$ level.

Engelbrecht *et al* [78] also demonstrated regional MTR values increasing with age in the developing brain, presumably due to increasing myelination. Van Buchem's group then performed MTR histogram analysis in 2001 and found a similar effect [79]. The mean MTR and histogram peak location increased, but the peak height showed a decrease with myelination, which was attributed to the increasing regional variation with myelination.

There are small age-related effects on the MTR, with MTR decreasing with age [80], postulated to be associated with structural changes in brain white matter (similar studies have found a relation between brain atrophy and age [81]), or possibly changes in phospholipids metabolism. Thus, provided that location and age are standardised, reproducibility of MTR values across controls is good.

3.4.2.2 Multiple Sclerosis

Multiple Sclerosis (MS) is primarily a white matter disorder, but affects the entire nervous system. It is predominantly a demyelinating disease, but also involves such pathological processes as inflammation, oedema, gliosis, and axonal damage and/or loss (see section 4.3.2 for a more complete description of MS).

Although MS lesions can be detected and monitored over time using conventional MRI scanning techniques, there is a lack of specificity to the pathological changes occurring in MS lesions. The abnormalities observed are a result of increased water content in tissues, which may be associated with demyelination, axonal dysfunction/loss, oedema, gliosis or inflammation.

MT is potentially a very useful tool for the study of MS because of the changes seen in the white matter: as a lesion is formed, demyelination and axonal damage/loss both take place, thus altering the structure of the brain tissue. This has an effect on the relative sizes of the restricted and free pools, which will cause a reduction in the MTR calculated. These changes have been widely studied both on a longitudinal and cross sectional basis, by the use of region- based analysis and more complex whole brain histogram studies.

Dousset *et al* [66] were the first to use the MTR to characterise MS lesions. They found the MTR in normal human white matter to be 42-44%, with less than 2.5% variation, indicating the high reproducibility of the measurement. In MS patients, all lesions were shown to have a significantly decreased MTR (average 26%), and a reduced MTR in normal-appearing white matter regions was also demonstrated. Since myelin is composed of phospholipid bilayers, a reduction in the amount of MT exchange between macromolecular and free protons would indicate a relative reduction in restricted protons available for exchange, presumably associated with demyelination.

Grossman *et al* [82] demonstrated the differences in MTR between the centre and the outside of the MS lesion, with the lowest MTR values at the centre of lesions, with a ring of gadolinium enhancement around the outside of the lesions, with a higher MTR thought to represent the region of active demyelination. This result was reproduced in a later study performed by Gass *et al* [83].

Similar findings in the cervical cords of MS patients have been observed [84], [85].

The signal intensity decreases observed on T_1 weighted images at lesion sites have been shown to correlate with reductions in the MTR values in those regions [73], [86]. Van Waesberghe *et al* showed a strong correlation between the MTR and the percentage of residual axons and demyelination.

3.4.2.2.1 Correlation of MTR measurements with MR spectroscopy

The metabolite NAA is a marker for axonal integrity and a reduction in the concentration of NAA corresponds to axonal damage or loss. Several studies have demonstrated a decrease in the concentration of NAA in the brain in Multiple Sclerosis [87], [88], [89], [90], and also in other neurological disease processes involving neuronal loss [91].

Decreases in MTR are usually associated with demyelination but other pathological processes may also be relevant. For example, Kimura *et al* were able to demonstrate a positive correlation between the reduction in MTR values and NAA concentration reductions in white matter MS lesions [92]. They postulated that the smaller MTR reductions observed (which did not correlate with NAA/Cr ratio) were due to inflammation and oedema, but that the larger MTR changes, which correlated with decreased NAA/Cr ratios were suggestive of demyelination and irreversible damage in chronic MS plaques.

A study carried out by Davie *et al* [93] detected a marked correlation between a reduced MTR and a reduction in NAA in chronic lesions occurred in patients with progressive disease (SPMS). However, in chronic lesions in patients with the benign form of the disease, it was found that both the NAA concentration and MTR were relatively preserved, suggesting axonal preservation and the possibility that these lesions were never demyelinated or in some way preserved the capacity to remyelinate.

3.4.2.2.2 Animal models of MS

In various demyelinating disease animal models, the lowest MTR values are detected in regions associated with the most extensive demyelination [94]. In Experimental Allergic Encephalomyelities (EAE) in guinea pigs, an animal model for MS, only a slight decrease in MTR values was observed in cerebral lesions. This disease is characterised by only a small amount of demyelination, but more severe inflammation [66].

In a feline model of Wallerian degeneration, Lexa *et al* [95] found a correlation between myelin fragmentation and degradation and MTR changes.

Gareau *et al* [96] found significant reductions in both the mean MTR and myelin water percentage (calculated by performing multi-component T_2 relaxation measurements) in the normal-appearing white matter (NAWM) of EAE guinea pig brain. There is good evidence to suggest that the short T_2 component in NAWM can be attributed to myelin water [97], [98], and is therefore sensitive to tissue myelin content. However, it was found that the two quantities measure different aspects of pathology of NAWM in EAE. It was postulated that the MTR is also affected by changes in inflammatory activity, since the EAE model is inflammatory in nature.

It has previously been shown that MTR increases approximately linearly with RfT_1^A (where R is the exchange rate between the two pools, f is the fraction of protons that are restricted (i.e. $M_0^B/(M_0^A+M_0^B)$) (see also chapter 5), and T_1^A is the T_1 of the free pool in the absence of MT saturation) [99], [100]. An increase in tissue water content (as would be expected in the presence of inflammation) would result in a reduction in the macromolecular proton content f, but also an increase in the T_1^A value, therefore these effects may act to oppose one another.

3.4.2.2.3 Volumetric methods: MTR histograms

The MTR histogram technique was first developed by van Buchem *et al* [101], and involves the generation of whole-brain and segmented white and grey matter (GM) histograms from calculated MT images

Several parameters can be obtained from such analysis, including the peak height and position (i.e. the most common MTR over the whole brain), the average MTR and 25^{th}, 50^{th} and 75^{th} percentiles. The MTR histogram peak height has been shown in several cases to be lower in MS patients than in normal controls [101], [102], [103]. There are also significant differences between the disease subgroups, with a larger reduction in peak height observed in those patients with secondary progressive MS (SPMS) than those with relapsing remitting MS (RRMS) [104], [105].

The histogram peak height is presumed to reflect the residual amount of normal brain tissue (and therefore inversely reflects the global disease burden), and van Buchem *et al* [102] demonstrated a correlation of the peak height with disease duration in MS. However, in this particular study no correlation with clinical disease burden measures such as the EDSS was found.

MTR histograms suggest the presence of diffuse abnormalities, which have been observed in the so-called normal-appearing white matter (NAWM) of MS patients, both at post mortem, and *in vivo*. Dousset *et al* [66] were the first to observe such abnormalities distinct from focal lesions, and MTR histograms have become a useful tool for observation of these irregularities. These diffuse abnormalities modify the relative proportions of free and restricted water protons, and thus alter MTR values, but are too microscopic to be observed on conventional MRI scans. Such abnormalities are thought to originate from diffuse astrocytic hyperplasia, patchy oedema and perivascular cellular infiltration [106]. Several authors have reported such diffuse abnormalities from MTR histogram studies [101], [107], [108], [109].

Pike *et al* [110] demonstrated the appearance of diffuse MTR abnormalities in regions up to two years before MS lesions formed in those regions, thus the method could perhaps be used to predict lesion formation.

The work of Santos *et al* [111] supported previous studies that demonstrated the use of diffuse MTR abnormalities to predict lesion development in MS. The MTR tends to start to decrease when a lesion begins to enhance, then recovers over the subsequent months to varying degrees. Suggested mechanisms include diffuse gliosis and inflammatory activity, small foci of demyelination and axonal damage.

Tortorella *et al* [105] investigated MTR changes in the Normal Appearing Brain Tissue (NABT) as a whole. It was postulated that small cortical lesions may have been missed and thus contributed to the MTR histogram findings. Some variations between clinical phenotypes were also observed, in particular the primary progressive MS (PPMS) patients peak heights were the lowest, but the average MTR and peak position were found to be similar to those of controls, suggesting that that the amount of residual cerebral tissue is lower in this phenotype. RRMS patients had the lowest average MTR and peak position, and the highest peak height, and this was explained as small, discrete lesions beyond the resolution of conventional scanning. In secondary progressive MS (SPMS), patients were found to have a lower MTR histogram peak height than in RRMS. It was hypothesised that a progressive reduction of cerebral tissue with normal MTR may be responsible for the transition from RRMS to SPMS.

Dehmeshki *et al* [112] used principal component analysis and multiple discriminant analysis of MTR histograms, and demonstrated an improvement in the distinction

between MS sub-groups and also found a correlation between a clinical outcome measure (the EDSS score) and the principal components of the histograms. Cercignani *et al* [113] also observed reduced MTR values in NAGM in MS patients, and attributed this discovery to Wallerian degeneration of grey matter neurons secondary to white matter fibre damage.

Kalkers *et al* [114] postulated that MTR histogram abnormalities are capable of indicating the degree of atrophy in addition to the diffuse abnormality in the NABT. Partial volume effects in voxels may affect segmentation results, causing a reduction in the peak MTR if more CSF is present in voxels. This problem could be partially resolved by using smaller voxels, or improvements in the segmentation, but if atrophy were driving disease processes, MTR reductions may still remain correlated with atrophy.

MTR histogram analysis has also been applied in the spinal cord of MS patient [84] and the mean MTR and histogram parameters such as the peak height were lower in MS patients than controls.

3.4.2.3 Dementia

Hanyu *et al* [115] found reduced MTR values in dementia patients, and a correlation with neuropsychological parameters. MTR abnormalities were also observed in Alzheimer's Disease (AD) patients, a finding that was attributed to axonal loss or demyelination. A study performed by Kabani *et al* [116] also demonstrated abnormalities in the grey matter of patients with Mild Cognitive Impairment (MCI). A study performed by Ridha *et al* [117] confirmed previous findings of reduced MTR values in the hippocampal formation in AD patients.

Volumetric MTR histogram analysis of the whole brain, white and grey matter has been performed in dementia patients [118], and abnormalities in the cortical grey matter in the temporal lobe. Van der Flier *et al* [119] also demonstrated significantly lower global MTR histogram measures in MCI and AD disease patients than in controls.

3.4.2.4 Epilepsy

Tofts *et al* [120] showed a significant reduction in MTR in the affected hippocampus of patients with temporal lobe epilepsy.

3.4.2.5 Hydrocephalus

Hahnel *et al* [121] showed a reduction in the MTR in patients with chronic obstructive hydrocephalus when compared with controls.

3.4.2.6 Tumours and abcesses

Gupta *et al* [122], [123] distinguished between different abcesses on the basis of MTR value.

Okumura *et al* [124] found MTR values in human brain tumours to be lower than in normal brain tissue.

3.4.2.7 Miscellaneous

Dousset *et al* [125] found severe MTR decreases in Progressive Multifocal Leukoencephalopathy (PML) patients, a disease characterised by severe demyelination, but only moderate MTR decreases in HIV encephalitis, which is known to cause neuronal damage, but little demyelination.

Silver *et al* [126] demonstrated low MTR values in central pontine myelinolysis (CPM), also characterised by severe demyelination.

In a study of Leber's hereditary optic neuropathy [127], MTR reductions were also observed.

In a recent study, abnormal (elevated) MTR values were observed in the spinal cords of adrenomyeloneuropathy (AMN) patients when compared to healthy controls. A new approach whereby CSF was used as an inter-subject normalisation reference (MTCSF imaging) was exploited [128]. This type of method is unable to remove T_1, T_2 and proton density dependence and is not expected to be able to discriminate between myelination and inflammation effects, but can detect initial changes in myelination when signal alterations are not yet detectable by conventional MRI.

To establish CSF as a suitable normalisation method for MT-weighted imaging, the mean CSF signal/voxel (in the absence of an MT pulse) was measured in six healthy volunteers, in each slice acquired. The SNR was found to be quite invariant for slices superior to C3, but larger deviations were observed for inferior slices, which the authors attributed to B_1 inhomogeneities. Although deviations were still relatively low, the normalisation was performed on a slice-by-slice basis to remove possible B_1 receptivity effects.

SNR calculations were also performed as a function of offset frequency at the C2 level, and showed that MT effects on CSF are negligible, as would be expected, and that the SNR measured was greatly invariant for both the healthy and AMN patient populations, thereby demonstrating that the CSF is appropriate as an internal standard. However, MTCSF imaging is not a perfect internal standard due it its dependence on T_1, T_2 and proton density, therefore its application is expected to be limited to diseases in which inflammation is not yet visible, such as AMN or perhaps spinal cord imaging in the early stages of MS, before inflammation is visible using conventional MRI techniques.

MTR values were also found to correlate with EDSS scores and quantitative tests of vibratory sense and postural sway [129]. It was postulated that axonal degeneration and myelin loss is continuous throughout the course of the disease, but that there is a particular time point at which clinical abnormalities become evident, since MTCSF imaging results in the dorsal column were abnormal even in the youngest patient, who had a normal vibratory sense.

3.4.3 MT-prepared spectroscopy

A molecule freely tumbling in solutions will have a relatively long T_2 relaxation time since intermolecular dipole-dipole interactions contributing to relaxation are largely averaged out, whereas molecules that are motionally restricted (e.g. those that are bound to macromolecules), will experience the dipolar interactions, and will therefore have a relatively short T_2 relaxation time, and exhibit a broader, potentially unobservable MRS signal. However, this property also means that such metabolites will be sensitive to MT saturation.

Therefore, *in vivo* metabolite concentrations measured by MRS may not reflect the actual concentration if the metabolite is 'bound' to slowly tumbling macromolecules, since these may become invisible in conventional MRS due to shortened (T_2) relaxation times. In this situation, it is possible that not all the molecules of a given metabolite present in tissue contribute to the observed MRS signal.

Dreher *et al* observed a reduction in the total creatine (Cr) signal at 3.0ppm for offset frequencies in the range -10 to +10kHz in healthy rat brains at 3.7T [130]. This deficit was attributed to magnetisation transfer between two pools of Cr or phosphocreatine (PCr), one with a long T_2 relaxation time, responsible for the observable signal on conventional MRS, and the other with a reduced T_2, postulated to be caused by binding of protons to slowly tumbling molecules.

Helms & Frahm [131] also made MRS measurements of the total creatine signal in the presence of off resonance saturation, and found that the creatine signal was reduced by 13% in short TE spectra, implying that visible Cr is in exchange with a pool of Cr bound to macromolecules, for example. The other four observable metabolites (i.e. tNAA, choline-containing compounds, Glutamate/glutamine, & myo-Inositol) were unaffected.

Kotitschke *et al* [132] found a deficit in lactate concentration in human brain cells when measured by MRS relative to values obtained using biochemical methods and suggested that binding of lactate spins to macromolecular species could account for this compartment of immobile lactate spins.

Luo *et al* [133] found reductions in MRS measurements of the Lactate methyl proton resonance in rat brain C6 glioma tissue, also using data acquired at a field strength of 4.7T. Again, this effect was attributed to the presence of at least two lactate spin pools in the glioma tumour tissue, coupled via MT exchange, by means of chemical exchange and/or dipolar coupling.

Meyerhoff *et al* [134] observed substantial signal attenuations for Cr-containing compounds in healthy living human brain, in line with the observations of Dreher *et al* [130] in rat brain. They also suggested that spins in Cr-containing metabolites in human brain exist in more than one pool and that dipolar coupling between pools of motionally restricted and more mobile spins causes the signal reduction of the observed Cr signal upon application of off-resonance saturation pulses. However, similar decreases in N-acetyl- and choline-containing metabolites were not observed by Meyerhoff *et al* in human brain. The authors excluded chemical exchange as a possible mechanism for MT exchange because of the high chemical stability of the methyl groups in compounds such as the creatine-containing metabolites. Instead they attributed the Cr signal decrease instead to through-space exchange of methyl magnetisation by direct dipolar coupling of proton-bearing compounds e.g. associated with lipids/proteins, with very short T_2 relaxation times, saturated by the MT pulses.

De Graaf *et al* [135] studied rat brain both *in situ* and *in vivo* and in both cases observed a strong MT effect from the methyl protons of total creatine and all protons from glutamate/glutamine, upon off resonance saturation, and also the methyl protons from lactate post mortem. Other resonances, such as that of N-acetyl aspartate, showed a smaller, but detectable, MT effect. These results were also observed using

both short and long echo time spectroscopy. It was also shown that water protons play an important role in the generation of the observed metabolite MT effects, using low-power off-resonance saturation and selective inversion. There were no large differences between *in vivo* and post mortem results, probably because data were acquired at only 2 hours post mortem, when the decrease in brain temperature was small, and no large changes in the macromolecular network were likely to have occurred. Since the spectral overlap between resonances complicates detection of individual metabolites using 1D spectroscopy, 2D localised Correlation Spectroscopy (COSY) was also performed in this study, and this allowed the detection of low concentration compounds such as taurine, alanine and the neurotransmitter gamma-aminobutyric acid (GABA). It was also demonstrated that the observed effects were not caused by non-specific RF 'bleed-over' of underlying macromolecular compounds with short T_2 relaxation times.

McLean *et al* [136] investigated the MT effect on metabolites, water and macromolecules in human frontal lobes *in vivo*. Three non-selective MT pulses of 0.745μT amplitude and relatively long duration (132ms) were applied prior to a conventional point-resolved spectroscopy (PRESS)-localised single voxel spectroscopy (SVS) technique. The MT pulses were applied with an offset frequency of either 2.5kHz or 30kHz. It was found, in agreement with previous studies, that the MT pulses had the largest consistent effect on the creatine signal (13%). Significant effects were also observed on N-acetyl aspartate (NAA) and N-acetylaspartylglutamate (NAAG), choline, lactate and myo-Inositol, and a trend towards a significant MT effect in glutamate and glutamine. An MT effect was not observed on the MRS-visible macromolecules, which are thought to represent primarily mobile proteins.

4 Basic Neurology, the Nervous System & Multiple Sclerosis

Introduction

A brief review of basic neurology and neurological disease is given here, with a particular emphasis on Multiple Sclerosis (MS). However, the reader should consult the references for a more complete clinical account [137], [138], [139], [140], [141], [142]. The role of magnetic resonance imaging in the diagnosis and monitoring of MS disease pathology will also be discussed, although again, for a more complete review of MRI in MS, the reader is directed to the references [143], [144], [145], [146]. A more complete review of the use of Magnetisation Transfer (MT) MRI in neurological diseases, in particular MS, is given in section 3.4.

4.1 Neuroanatomy and neurophysiology

In this section some basic neuroanatomy and neurophysiology will be discussed in order to introduce some basic terminology and the basic structure and function of the nervous system.

4.1.1 The Nervous System

The nervous system consists of the central nervous system (CNS), composed of the brain and spinal cord, and the peripheral nervous system (PNS), which consists of nerves and ganglia [147]. This thesis is predominantly involved with the imaging of the CNS, in particular the brain. Therefore this section of the chapter will focus on the basic anatomy of the central nervous system. The CNS is composed of two main types of cell, neurons (nerve cells) and glia (glial cells), and three layers of connective tissue that form the meninges (the outermost of which is the dura mater) [141]. The meninges separate the central nervous system from the peripheral nervous system. The CNS and its meningeal covering are then surrounded by bone (the skull and the spinal column) [141].

4.1.2 Organisation of the CNS

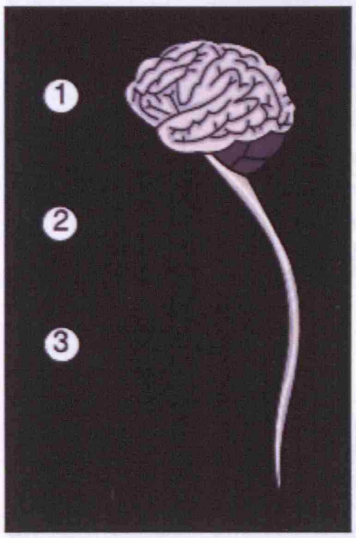

Figure 4.1: Diagram illustrating the main components of the Central Nervous System and their organisation.
(http://en.wikipedia.org/wiki/Central_nervous_system)
1. Brain
2. Central nervous system (brain and spinal cord)
3. Spinal cord

4.1.3 The brain

The brain is a large and highly developed mass of nervous tissue. It forms the upper end of the CNS, and is continuous with the spinal cord below it. It is separated from the PNS by the meninges and is also surrounded by cerebrospinal fluid (CSF) within the skull [148]. The brain controls and co-ordinates most movement, behaviour and homeostatic body functions such as heartbeat, blood pressure, fluid balance and body temperature, and is also responsible for functions such as cognition, emotion, memory, motor and other types of learning. The main components of the human brain are illustrated in figure 4.2.

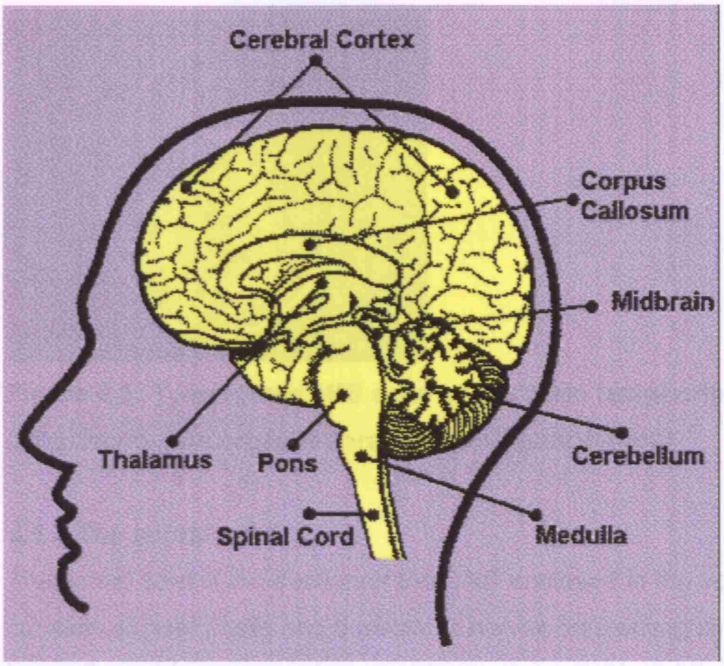

Figure 4.2: Diagram illustrating major components of the human brain (http://faculty.washington.edu/chudler/nsdivide.html)

The two hemispheres of the brain are connected by the corpus callosum, and also by a smaller nerve fibre bundle known as the anterior commissure. The cerebral cortex controls functions such as thought, perception, language and voluntary movement. The cerebellum governs movement, balance and posture, and is located behind the brain stem, which regulates basic functions such as breathing, heart rate and blood pressure. The hypothalamus is a small structure located at the base of the brain, and controls body temperature, emotions, hunger and thirst, among other functions. The thalamus receives sensory information and communicates this information to the cerebral cortex, as well as receiving information from the cerebral cortex which is then transmitted to other areas of the brain and spinal cord. The hippocampus plays an important role in memory and learning, and is part of the limbic system, which controls emotions. The basal ganglia are a group of structures which are important in co-ordinating movement, and the midbrain consists of various structures and controls vision and eye movement and is also involved in body movement.

A T_1-weighted (axial) MRI scan of a human brain is shown in figure 4.3.

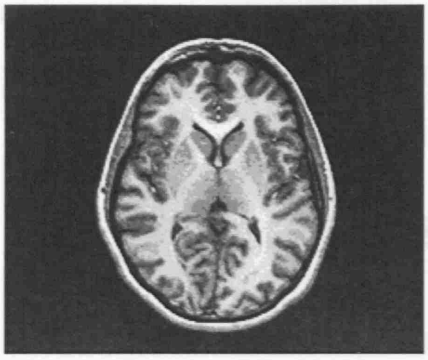

Figure 4.3: T_1-weighted MRI scan of the brain (axial orientation) (http://www.pbs.org/wnet/brain/scanning/mri5.html)

4.1.4 The spinal cord

The spinal cord is the section of the CNS enclosed in the vertebral column, and consists of nerve cells and bundles of nerves connecting all parts of the body with the brain. It contains a core of grey matter surrounded by white matter. Similarly to the brain, it is encased within the meninges. From it the 31 pairs of spinal nerves of the peripheral nervous system connect to the rest of the body, passing out through the spaces between the arches of the vertebrae [148].

4.1.5 Cerebrospinal fluid (CSF)

This clear fluid fills the ventricles and subarachnoid space in the brain and the ventricular system of the brain and spinal cord, and is produced by the choroid plexus, a tissue that partially lines the ventricles, and also by the ependymal lining of the brain's ventricles. The brain floats in the fluid, so that it is cushioned from contact with the skull if the head is moved vigourously [148].

4.2 Cells of the nervous system

4.2.1 The neuron

The basic functional unit of the CNS is the neuron (nerve cell) [140], [142] and there are ~10^{11} neurons in the CNS [141]. Neurons are specialised for rapid communication, via conduction of nerve impulses [140]. Neurons are composed of three components: a soma (cell body) and the processes that extend from the soma; the axon and dendrites (see figure 4.4).

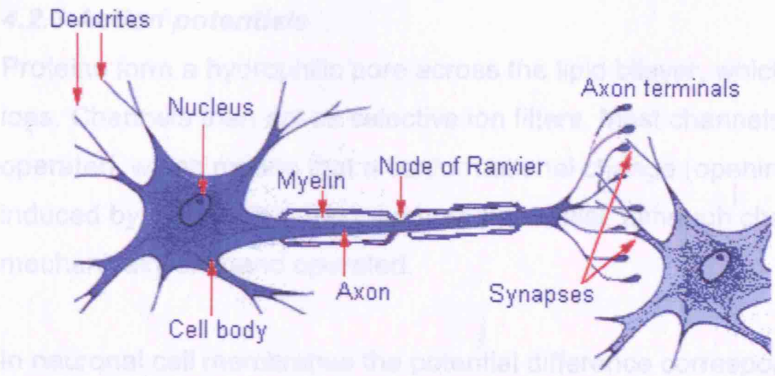

Figure 4.4: Diagram illustrating the main components of a neuron (nerve cell) (http://www.sirinet.net/~jgjohnso/nervous.html)

The central nervous system consists of grey and white matter. Grey matter contains the cell bodies of neurons, each with a nucleus, embedded in a neuropil made up of delicate neuronal and glial processes. White matter consists primarily of long processes (axons) of neurons, the majority of which are surrounded by insulating fatty myelin sheaths [140], and axons typically conduct impulses away from the cell body [141]. Dendrites are usually short branching processes that are specialised to receive signals from other neurons [147]. Each nerve cell usually has a single axon, which can vary greatly in length and type from one type of neuron to another, but may have several dendrites. The nerve fibre consists of the axon and myelin sheath [141]. It has been established that oligodendrocytes are responsible for laying down the myelin sheath around the axon (this process mainly occurs during late foetal development and the first postnatal year). Electron microscopy has shown that myelin consists of many layers of oligodendrocyte plasma membrane, tightly wrapped around the axon [140]. The myelin sheath is interrupted at intervals by nodes of Ranvier, with internode ranges from about 100um to about 1mm, depending on the length and thickness of the fibre [141].

4.2.2 Nerve impulses

Neurons function by the production, propagation and transfer of nerve impulses ('ionic currents'), which are produced by various stimuli 'activating' neurons from their resting state [142]. At rest, a neuron maintains a difference in potential (i.e. a voltage) of ~50mV to -80mV between the inside and outside of its surface membrane [147]. If a stimulus excites a site on the surface membrane, the resting potential at that point drops to zero or even slightly overshoots. Then the so-called action potential propagates along the surface membrane of the neuron.

4.2.3 Action potentials

Proteins form a hydrophilic pore across the lipid bilayer, which is specific for particular ions. Channels then act as selective ion filters. Most channels are voltage "gated" or operated, which means that a conformational change (opening) of the channel is induced by a change in the membrane potential, although channels can also be mechanically or ligand operated.

In neuronal cell membranes the potential difference corresponding to an electrochemical gradient of zero is known as the resting membrane potential. Extracellular fluid has a high concentration of sodium (Na^+) ions and a low concentration of potassium (K^+) ions, whereas in neuronal cytoplasm the reverse is true. For most cells, the permeability to K^+ ions is much larger than that to calcium (Ca^{2+}) ions and the permeability to Na^+ ions is even lower. The resting membrane potential is close to the equilibrium voltage (V_{eq}) for K^+ ions. At the equilibrium potential (or voltage) for a particular ion a residual concentration gradient and a residual charge separation exist across the cell membrane, but at equilibrium the leakage force and electrical force acting on the ions balance each other. The interior of the cells is negative relative to the outside [141]. In the resting state, K^+ ions can leak out of cells due to the concentration difference of K^+ ions in the cells compared to that in the extracellular fluid, but only a small number of Na^+ ions can leak into the cell since Na^+ channels are closed at rest [140].

An action potential is a rapid change in the membrane potential caused by a change in the membrane permeability [147] (see figure 4.5). Such controlled changes in the permeabilities and therefore in the membrane potentials of nerves and muscles are central to their function. The action potential is the basis of the signal-carrying ability of nerves and muscles.

Depolarisation is when the inside of a cell becomes less negative than at resting membrane potential and hyperpolarisation is the opposite, when the inside of the cell becomes more negative than at resting membrane potential [141].

The depolarising phase of the action potential is due to the opening of sodium channels, so that Na^+ ions flow in and the cell becomes more positive. The repolarising phase and hyperpolarisation are due to sodium channels being inactivated and closed, and the opening of a special set of potassium channels (delayed potassium channels) slowly opening. K^+ ions flow from the cell cytoplasm. The action potential is then conducted along the axon as a nerve impulse [147]. This process is illustrated in figure

4.5.

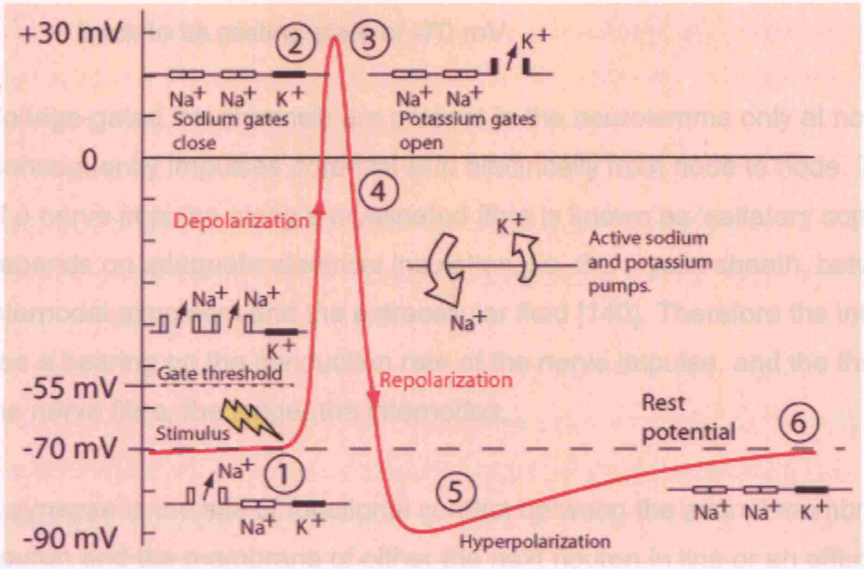

Figure 4.5: Action Potential

(http://members.aol.com/Bio50/LecNotes/lecnot11.html)

A stimulus is received by the dendrites of a nerve cell in figure 4.5. This causes the Na^+ channels to open. If the opening is sufficient to drive the interior potential from -70 mV up to -55 mV, the process continues.

The processes taking place in figure 4.5 are as follows:

1. A stimulus causes more voltage-gated Na^+ channels to open, resulting in an influx of Na^+ ions. This drives the cell membrane potential up to about +30 mV (depolarisation).
2. The Na^+ channels close and the K^+ channels open (much more slowly). If both Na^+ and K^+ channels were open at the same time the system would be driven towards neutrality and prevent the creation of the action potential.
3. With the K^+ channels open, the membrane begins to repolarise back towards its resting potential.
4. The repolarisation typically overshoots the resting membrane potential to about -90 mV. This is called hyperpolarisation and would seem to be counter-productive, but it is actually important in the transmission of information. Hyperpolarisation prevents the neuron from receiving another stimulus during this time, or at least raises the threshold for any new stimulus. Hyperpolarisation prevents any stimulus already sent up an axon from triggering another action potential in the opposite direction. In other words, hyperpolarisation assures that the signal is proceeding in one direction.

5. Following hyperpolarisation, the Na^+/K^+ pumps eventually bring the membrane back to its resting state of -70 mV.

Voltage-gated ion channels are present in the neurolemma only at node positions. Consequently impulses potential skip electrically from node to node. This transmission of a nerve impulse along a myelinated fibre is known as 'saltatory conduction', and depends on adequate electrical insulation, i.e. the myelin sheath, between the internodal axoplasm and the extracellular fluid [140]. Therefore the internodal spacing has a bearing on the conduction rate of the nerve impulse, and the thicker and longer the nerve fibre, the longer the internodes.

A synapse is the site of functional contact between the axonal membrane of one neuron and the membrane of either the next neuron in line or an effector cell (which brings about activity in a muscle or gland). Typical synapses consist of a presynaptic membrane provided by the axonal terminal, a synaptic cleft and a postsynaptic membrane provided by the next cell in line [147]. The arrival of a nerve impulse at the synaptic terminal of the axon releases a stored chemical substance known as a neurotransmitter into the synaptic cleft [141]. The neurotransmitter unites with the chemical receptors on the postsynaptic membrane. There are two types of neurotransmitter. Excitatory neurotransmitters tend to depolarise the cell membrane and excite that cell. They cause the neuron to discharge a nerve impulse or cause an effector to act. Inhibitory neurotransmitters hyperpolarise the next cell in line and inhibit the production of a new impulse by making membrane depolarisation more difficult. Whether a given neuron will generate an impulse or not depends on the summation of the excitatory and inhibitory neurotransmitters acting upon its surface at any particular time [140]. Upon arrival at the axon terminal, the action potential causes the synaptic vesicles to release neurotransmitters into the synaptic cleft. The neurotransmitter molecules then diffuse across the synapse to bind with receptors on the membrane of the second neuron. This is how the excitation is transmitted from one cell to another [140].

4.2.4 Glial cells

Glia are between 5 and 10 times as numerous as neurons and comprise the supporting tissue of the CNS. Not all the functions of glia are known, but are thought to include repair and maintenance, physical support, development and chemical regulation [147]. There are three main types of glial cell; astrocytes, oligodendrocytes and microglia [142].

Astrocytes fill in the spaces that would otherwise exist between neurons and their processes, physically supporting neurons in the brain, and may also be involved in neuronal metabolism, potentially providing nutrients for neurons and possibly taking part in information storage processes [147].

Oligodendrocytes are responsible for forming and maintaining the insulating myelin sheaths surrounding axons within the CNS, thus allowing nerve impulses to propagate more efficiently [147]

Microglia are derived from blood monocytes or macrophages. Resting microglial cells are equivalent to the resident macrophages of other tissues and can acquire phagocytic properties to protect the neurons of the CNS when the central nervous system is afflicted by injury or disease. They can also multiply in case of damage in the brain and may also be involved, although less conspicuously, in protecting the nervous tissue from viruses, microorganisms, and the formation of tumours [147].

Glial cells, especially oligodendrocytes, are often destroyed at the sites of multiple sclerosis (MS) lesions, and this also postpones or even prevents repair of myelin [147].

4.2.5 Blood brain barrier (BBB)

The blood brain barrier (BBB) is the protective layer that isolates the central nervous system from the bloodstream but allows the exchange of substances necessary for it to function. It consists of the cells of the inner lining of blood vessels and other cells behind them pressing together very tightly, preventing diffusion of plasma proteins into the CSF from the extracellular spaces of the choroid plexus and dura mater. It effectively acts as a semi-permeable membrane, controlling the entry of small molecules into the brain via carrier mechanisms within the endothelial cells of the cerebral blood vessels, but preventing larger molecules/solids from passing through. These regulate the transport of glucose, amino acids and other substances from the blood to the neurons and neuroglia [148]. The composition of cerebrospinal fluid is controlled by the choroid epithelial cells.

4.3 Multiple Sclerosis (MS)

Multiple sclerosis (MS) is a chronic autoimmune disorder of the central nervous system. Effectively the body attacks its own (healthy) cells due to an overactive immune response. MS patients can present with a wide variety of neurological symptoms either with isolated attacks, or slow progression over time. Due to its effects on the nervous system it can lead to long-term impaired mobility and disability in the

more severe cases [148], [149].

The MS lesion or plaque is characterised by perivascular infiltration of monocytes and lymphocytes, appearing as indurated areas in pathological specimens [149]. Most evidence suggests that disruption of the blood-brain barrier (BBB) is the initial (or a very early) event in the development of an MS lesion. It is thought that antigen-specific T-cells enter the nervous system, recognise antigen and begin a cytokine cascade that mediates disruption of the blood-brain barrier, which can be observed on contrast enhanced MR images [71], typically using a Gadolinium chelate as a contrast agent (see also section 3.4.1.2). Following the breakdown of the BBB caused by this inflammatory process, the inflammatory response is amplified, causing oedema and activation of macrophages and other cytokines [146], which leads to demyelination, and also some axonal destruction [150].

Lesions with ongoing inflammation and advancing demyelination are described as "active chronic" lesions. It is likely that this stage of lesion development represents a more permanent and irreversible stage of tissue damage.

Remyelination is also thought to play a role, and this is one of the reasons why symptoms tend to have a relapsing-remitting course, especially in the earlier stages of the disease. MRI and pathological studies now indicate that axonal damage and irreversible loss of neurons may occur earlier in lesion development than generally thought. However, due to its plasticity the brain can often compensate for some of the damage. Although the oligodendrocytes which originally formed the myelin sheath are incapable of re-creating the sheath once destroyed, progenitor cells can be recruited by the brain, which then differentiate into mature oligodendrocytes and form a new myelin sheath. However, this new myelin is often not as large or effective as the original.

Permanent disability and progression are probably most closely related to tissue destruction, particularly demyelination and axonal degeneration, and also gliosis, although its role is uncertain [138]. Progression of disability can represent either accumulation of neurological dysfunction as a result of exacerbations that fail to resolve completely or continued pathological damage in existing lesions. The pathological substrate and disease mechanisms for these two aspects may differ. Most evidence points to an immunological process in the initiation and evolution of acute lesions, but progression of old lesions may be independent of immunological mechanisms or may involve mechanisms considerably different than those operating in acute lesions. Possibilities would include persistent, chronic immunological events including antibody

mediated damage due to clonal B-cell activities. In addition, escape for normal regulatory processes such as apoptosis of T-cells or B-cells could have an important role. Progression of damage to partially damaged cells or axons in an immunologically independent manner is possible.

4.3.1 Diagnosis & Clinical features

4.3.1.1 Diagnosis

Diagnosis of MS requires evidence for dissemination of lesions within the CNS both in space and in time [151], [152]. Therefore at least two distinct lesions must exist, either visible on MRI scans or observable via clinical symptoms, and there must also be evidence of new symptoms or lesions with a time interval of at least 30 days. A lumbar puncture (extraction of a sample of CSF) can also be performed in order to confirm the presence of chronic inflammation of the CNS via oligoclonal banding. In MS a mild increase in the level of cellular reaction or protein and an increase in the level of immunoglobin are often observed. The presence of oligoclonal banding in the CSF is associated with the development of clinically definite MS [153], [154] however it is not specific to MS and may be found in many inflammatory and immune-mediated CNS diseases [155]. Nevertheless, since both MRI and CSF oligoclonal banding are both very sensitive, they can be used to completely rule out MS if both tests are negative. Nerve conduction studies can also provide further evidence of MS, since nerve conduction will be impaired/blocked by demyelination [138]. However, MRI is now the principal method used to diagnose and monitor MS.

4.3.1.2 Symptoms

A wide variety of symptoms may be experienced, including vision loss, double vision, nystagmus, speech difficulties, tremor, gait, weakness, spasticity, numbness and bladder, bowel and sexual dysfunction and cognitive impairment.

There are several different clinical phenotypes of MS. Initially most (~85% [156]) patients are diagnosed with a relapsing-remitting course (RRMS) with lesions in many regions of the CNS. After this relapsing-remitting phase, most patients will enter a progressive phase (50% within 10 years [156]). These patients are said to have the secondary progressive form of the disease (SPMS) and will often present with optic neuritis or other sensory disturbances. They may also continue to have remissions superimposed on the progressive disease. There are a few patients who have a progressive decline without the relapse-onset phase of disease. These patients have the primary progressive (PPMS) form of the disease, which in general predominantly affects one part of the CNS. These patients also often present at a much older age

than those with RRMS. There is also a benign form of the disease (BMS), which is characterised by a long disease duration (e.g. 10 years or more) without developing significant disability (score of 3 or less on Kutzke's Expanded Disability Status Scale (EDSS) [157]). However, it is still possible for these patients to enter a progressive disease phase at a later stage.

4.3.2 Multiple Sclerosis pathology

4.3.2.1 Demyelination

Damage to myelin and also to the oligodendrocytes that produce and maintain the myelin (demyelination) is a key feature of the MS lesion [145], [158], [159]. Loss of myelin results in impairment or loss of nerve conduction [138].

Remyelination is also known to occur [160], but may result in myelin of a different composition, but this is not a prerequisite for recovery of function [146].

4.3.2.2 Gliosis

Astrocytes act as the main supporting and structural elements in healthy white matter. They respond to injury of the CNS by proliferation, and this 'CNS repair' mechanism is known as gliosis or astrocytosis [138].

4.3.2.3 Axonal damage/loss

It is likely that irreversible damage to axons occurs in MS, particularly in older lesions, resulting in a permanent functional deficit in most MS patients later on in the course of the disease [161].

4.3.2.4 Observations from Histopathology

The predominant feature observed in histological post mortem studies of MS is demyelination, with associated oedema, inflammation, blood vessel wall changes and gliosis, and axonal damage/loss [150]. Lesions can be found both in grey and white matter, although white matter lesions are observed more frequently. Some purely inflammatory lesions may also be observed, for example in the retina. Some remyelination is also observed [162].

In addition, there is also evidence of astrocytosis, microglial activation, perivascular inflammation and axonal loss in the Normal-Appearing White Matter (NAWM) of MS patients [163], [164].

4.3.3 MRI in MS

MRI is a very sensitive paraclinical tool in the diagnosis and evaluation of MS [152], [165], [166]. Typical observations on a conventional MRI scan of an MS patient include increased T_1 and T_2 values in lesions relative to normal white matter [167].

4.3.3.1 T_2-weighted imaging

T_2-weighted dual-echo conventional spin echo (or FSE) imaging (with a long TR and TE) was previously the most sensitive technique, with MS lesions appearing hyperintense compared to background white matter, but because of the periventricular location of many MS lesions they may be masked on T_2-weighted images by partial volume effects, with lesions tending to blend in with high intensity CSF signal from the adjacent ventricles [146].

Due to this lack of contrast between the CSF and the cortex, FLAIR (or more recently fast FLAIR) has also been used to increase the conspicuity of MS lesions. A long TR and long inversion time TI are used to suppress the signal from CSF, resulting in a heavily T_2-weighted image without the problems caused by the bright CSF signal. Increased lesion-to-brain contrast has been observed using fast FLAIR compared to conventional spin echo imaging [168], [169].

4.3.3.2 T_1-weighted imaging, "black holes" and enhancing lesions

Many MS lesions appear hypointense on T_1-weighted images (so-called "black holes"). The pathology taking place in such lesions is not completely clear, but it is thought that T_1 hypointensities may indicate more severe tissue damage than lesions only visible on T_2-weighted images. Acute/subacute MS lesions tend to manifest as areas of perivascular inflammation, associated with permeability of the blood-brain barrier and also some oedema, but little demyelination. Chronic ("active") lesions appear as T_1 hypointensities reflecting more extensive demyelination and gliosis, and histopathology has also indicated a correlation between the degree of T_1 hypointensity and loss of axons in chronic MS lesions [170]. However, tissue damage can be extremely variable in individual "black holes" [171]. T_1-weighted lesion load has also been shown to correlate with the EDSS in a 3 year period in secondary progressive MS patients, but not relapsing-remitting patients [172]. SPMS patients were also found to have a larger percentage of hypointense T_1 lesions associated with abnormalities visible on T_2-weighted images, suggesting a possible failure of repair processes in these lesions.

4.3.3.3 Contrast enhancement with Gd-DTPA

T_1-weighted MRI in combination with injection of a Gadolinium chelate (the most

commonly used agent is Gd-DTPA; see also section 2.3.6.2) as a contrast agent is a sensitive marker for the breakdown of the blood brain barrier, thought to be the earliest event in the development of an MS lesion [71]. However, the detection of enhancing lesions provides no information regarding the extent and severity of the inflammatory phase [173]; for example it is not possible to distinguish purely oedematous lesions from demyelinating lesions. Such enhancement is thought to be more sensitive than either clinical examination or T_2-weighted images in detecting disease activity [174]. The use of a triple dose of the Gadolinium contrast agent, or a single dose in combination with an MT preparation pulse (which suppresses normal but not enhancing tissue, thus increasing contrast between normal and enhancing tissue regions) results in an increase in the number of lesions detected [175], [176], as does the use of delayed imaging following contrast injection [176].

4.3.3.4 Lack of correlation of disability with conventional MRI

It has been difficult to correlate (quantitative) MRI measures with clinical markers of disease progression [146] such as the Expanded Disability Status Scale (EDSS) [157]. Demyelination, the principal pathological feature of the disease, results in nerve conduction block. However, this may not cause permanent loss of function, and recovery of function is also possible via remyelination. Gliosis also occurs in lesions where demyelination is also observed, but its relationship to axonal damage is unclear [138]. One explanation for this may be the way in which disability is assessed, usually by Kurtzke's Expanded Disability Status Scale (EDSS) [157]. This non-linear scale quantifies a mixture of impairment and disability, and is heavily weighted towards locomotor disability, which is often due to spinal cord disease [177].

Conventional brain MRI sequences also give no information about two of the potentially more disabling aspects of the disease: (1) spinal cord involvement and (2) the amount of demyelination and axonal loss in chronic lesions. The detection of lesions on MR images is related to increased water content and relaxation times, which could result from any of the major pathological features of MS i.e. oedema, inflammation, gliosis, demyelination and axonal loss. The substrates of disability, however, are demyelination (causing persistent conduction block) and axonal loss, but conventional MRI techniques are unable to distinguish between these mechanisms.

It is also possible that the time taken to develop a given lesion load is more relevant than the actual lesion load in determining disability: a slower accumulation may, for example, allow more time for repair and recovery of function.

Pathological studies also reveal remyelination in a substantial number of lesions [162], but the new myelin is morphologically different and it is conceivable that such remyelinated lesions will still produce abnormal MR signal, even though there is no functional deficit.

Therefore it is also important to determine the magnitude and severity of diffuse tissue damage in the normal-appearing white matter (NAWM), which has been demonstrated in histopathological studies [150] and has also been shown to contribute to neurologic impairment [103], [105], [178]. In recent years it has also become apparent that grey matter is not spared in multiple sclerosis [179], [180], [181], and the extent of this pathology should also be examined. Ideally MRI measures used to examine the normal-appearing white and grey matter abnormalities should be quantitative.

4.3.3.5 Spinal Cord imaging

For imaging the spinal cord, sagittal T_1- and T_2-weighted sequences can be used, although it may be difficult to detect "black holes" in the spinal cord, as well as regions such as the optic nerve [182], and fast FLAIR sequences have so far been shown to detect fewer spinal cord lesions than FSE images [183]. If a characteristically elongated lesion without cord swelling, or multiple cord lesions separated by normal areas of cord are observed, then MS is the most likely diagnosis.

Losseff *et al* measured the cord cross-sectional area in MS patients at the C2 level and demonstrated a strong relationship between cord atrophy and disability [184]. Kidd *et al* [185] suggested that atrophy measurements may be important in patients with the progressive form of the disease since these patients have a different disease course and MRI activity pattern, with fewer brain lesions and increasing disability in the absence of obvious changes visible on conventional MR images.

Silver *et al* also demonstrated significant differences between patients and controls using MT imaging in the spinal cord [85].

4.3.3.6 MR Spectroscopy (MRS)

Proton MRS can be used to detect metabolites from selected regions of interest within the brain. Detectable metabolites at long echo times (TE=136 or 272ms) are N-acetyl aspartate (NAA), creatine and phosphocreatine (denoted Cr or tCr for total creatine), choline-containing compounds (Cho), and, under some conditions, lactate (Lac). If a short echo time is used (e.g. TE=30ms), the methyl groups of lipids and other compounds, glutamate and glutamine (Glx), and myo-Inositol (mI) may be observed.

N-acetyl aspartate (NAA) is a sensitive marker for neuronal integrity, and any disease resulting in neuronal loss is therefore associated with a reduction in NAA concentration. The NAA concentration is often expressed as a ratio to creatine (NAA:Cr ratio) or another metabolite such as Cho, but this approach has the disadvantage that an increase in Cr could be interpreted as a decrease in NAA, for example. Miller *et al* demonstrated a reduction of NAA in most MS plaques, and the presence of a lactate peak in some lesions [186]. Very low levels of NAA were found in chronic plaques, consistent with extensive axonal loss. The milder reductions observed in acute plaques might indicate less severe axonal loss, axonal shrinkage secondary to demyelination, inflammatory oedema, or perhaps axonal dysfunction. Reductions in NAA concentration display some reversibility, but not full recovery [89]. Both oedema and vasculitis have been described in new plaques, and it is possible that these mechanisms might result in reduced oxygen delivery to cells and so explain the Lac peak found [186], since lactate is the end product of anaerobic respiration, and the lactate peak is not found in normal adult brains. Acute MS lesions may also demonstrate increased Cho concentrations. This is thought to indicate increased membrane turnover and may therefore result either from the release of choline-containing membrane lipids during active myelin breakdown or from inflammation [187].

Fu *et al* also observed substantial NAA:Cr ratio reductions in the NAWM, although much larger decreases were observed in lesions [178]. However, since the relative volume of the NAWM is so much larger than that of lesions, even modest diffuse pathological changes (e.g. axonal damage or very small foci of inflammation or demyelination) in NAWM could make major contributions to clinical disability. A significantly lower NAA:Cr ratio was observed in the SPMS subgroup, suggesting a greater accumulated load of axonal damage. A correlation between the changes in the EDSS and NAA:Cr ratios was observed in the relaxing-remitting subgroup, probably reflecting the greater disease activity in this subgroup. RRMS patients also showed a larger variation in EDSS over the course of the study. One possible reason for the lack of such a correlation in the secondary progressive subgroup is the fact that there was already more severe damage in the white matter of this group. If the rate of new damage to axons is proportional to the density of existing axons, then new inflammatory foci may lead to less further axonal damage in later stages of the disease when there are fewer axons in close proximity to new inflammatory foci [178].

4.3.3.7 Magnetisation Transfer (MT) imaging

Magnetisation Transfer imaging (MT) (see chapter 3 for definitions and a more

complete review of the use of MT imaging in MS and other neurological diseases) has been used extensively to image MS in recent years, by suppression of background tissue relative to demyelinating regions. One application has been to improve the sensitivity of contrast enhancement on T_1-weighted images with Gadolinium as a contrast agent. The Magnetisation Transfer Ratio (MTR) is significantly decreased in older, chronic MS lesions, probably reflecting the breakdown of myelin. The MTR has also been used to monitor/determine lesion age [110], with acute lesions being predominately oedematous, with inflammation and little demyelination, and demyelination and gliosis present in older lesions [170]. These diffuse abnormalities visible using volumetric MTR analysis are thought to originate from diffuse astrocytic hyperplasia, patchy oedema and perivascular cellular infiltration [106]. MTR histograms have been used in several studies [101], [108], [109] to determine the extent of (diffuse) damage to the normal-appearing white matter (NAWM) and, more recently, normal-appearing grey matter (NAGM) [113], [179]. This type of volumetric analysis demonstrates diffuse abnormalities prior to the formation of lesions visible using conventional MRI techniques [111], even up to 2 years prior to lesion development [110].

5 Quantitative MT (qMT)

Introduction

As discussed in chapter 3, the signal in an MT-weighted image, and hence also MTR values, reflect a complex combination of various biological factors. These include the relative magnitudes of the two proton pools, the relaxation times of both pools (including the observed T_1 of the liquid pool, which is known to be reduced in the presence of MT), the rates of MT exchange between the two pools, and the RF absorption lineshapes of the two components. The MTR is also highly sequence and scanner dependent, therefore more quantitative methods have been developed, in order that more fundamental parameters related to the pathological processes taking place in disease can be obtained. This chapter outlines the development, mathematical modelling and implementation of such techniques, and finally describes some possible further work and potential methods of optimisation of these approaches.

5.1 Quantitative Modelling of Magnetisation Transfer in tissue

Early models for MT in tissue (discussed in chapter 3) assumed complete saturation of the semi-solid pool, an assumption which is not valid in clinical MTR measurements, since it is not possible to completely saturate the restricted proton pool in humans, not least because it would breach RF power deposition restrictions. Some models also assumed that there is no direct saturation effect on the free water pool. Quantitative MT measurements also depend on the particular sequence acquisition parameters used, including the TR' (time between successive MT pulses), TE and excitation pulse flip angle but most importantly the MT pulse shape, amplitude and offset frequency. All of these factors should therefore be taken into consideration in modelling the MT effect.

5.1.1 Henkelman's two-pool model

Henkelman's model for qMT [49] is based on the binary spin bath model, first proposed by Edzes and Samulski [54], and derived from a set of Bloch equations modified to account for the magnetic coupling of the two pools. The basis of the model is illustrated in figure 5.1. In the diagram, the pink shaded areas represent magnetisation not aligned longitudinally (i.e. either aligned transversally, or saturated). R_A and R_B are the longitudinal relaxation rates of the free and restricted pools respectively in the absence of exchange (i.e. $1/T_1^A$ and $1/T_1^B$). The initial populations of the two pools are M_0^A and M_0^B (the longitudinal magnetisation in the absence of any MT saturation). R is the rate constant that determines the rate of MT exchange between the two pools (in both directions) and is weighted by the pool sizes (i.e. the rate of exchange A→B is RM_0^A and the exchange B→A is RM_0^B). However, the liquid pool magnetisation M_0^A has

previously been normalised to a value of 1 in several studies [49], [188], [189]. R_{RFA} and R_{RFB} are the rates of loss of longitudinal magnetisation due to direct saturation of the pools by the RF irradiation, and these depend on the absorption lineshape of the pool and the amplitude and offset frequency of the MT pulse. M_Z^A and M_Z^B represent the longitudinal magnetisation of the free and restricted pools respectively in the presence of MT saturation relative to the equilibriu m magnetisation of each pool i.e. the unshaded areas represent M_Z^A/M_0^A and M_Z^B/M_0^B for the A and B pools respectively.

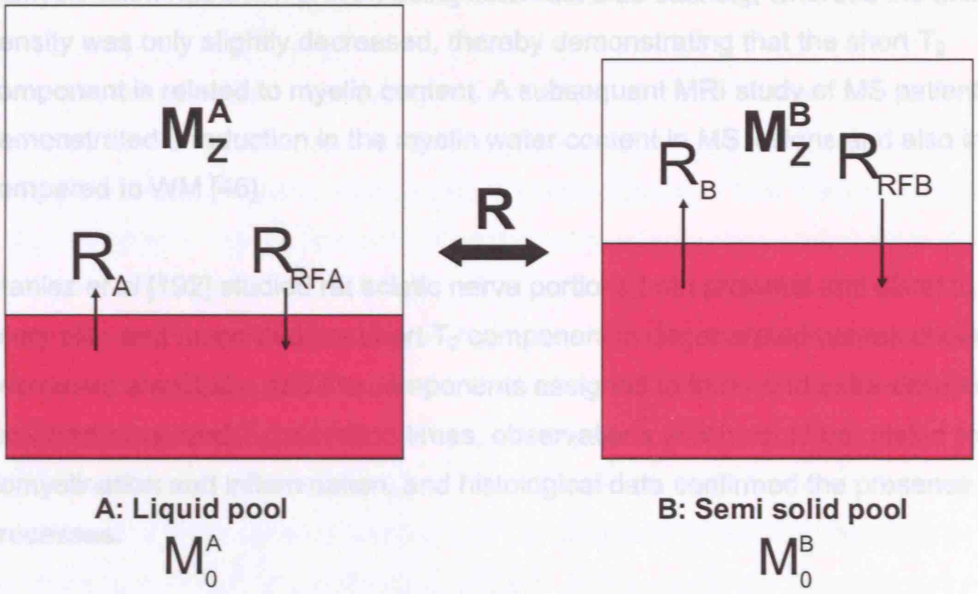

Figure 5.1: The Henkelman two-pool model for qMT [49], as described above.

5.1.2 More realistic models for MT in biological tissue: survey of literature

The free proton component in tissue is known to comprise spins in several different environments, each with a different T_2 relaxation time, and this is not taken into account by the binary spin bath model. Transverse Magnetisation Decay Curve (TMDC) analysis is a technique in which the water in tissue is analysed as a number of compartments. In contrast to MT, the water compartments observed using TMDC are all observable using conventional MRI techniques (the shortest T_2 observed using this technique is typically ~10ms [190]). Previously, three T_2 components have been observed using TMDC in white matter *in vivo*; a short T_2 component at 15-20ms (~15% relative distribution contribution), presumed to be associated with water protons trapped within myelin ("myelin water"), a medium T_2 component at 70-90ms (~85% relative distribution contribution), thought to arise from the intra- and extra-axonal water [97], [98], and also a very small peak with T_2 greater than 1s, assigned to the cerebrospinal fluid (CSF). However, it is not possible to observe species with T_2<1ms

using this type of technique, therefore the restricted pool proton component in the qMT model could not be detected using TMDC, since their T_2 is assumed to be ~10-20μs [47], [48].

Whittall *et al* [98] showed the myelin water component T_2 to be between 15 and 40ms using TMDC analysis. Later Moore *et al* [191] showed that following formalin fixation of MS brain, the component attributed to myelin water was missing in lesions where demyelination had been proven using luxol-fast blue staining, whereas the axonal density was only slightly decreased, thereby demonstrating that the short T_2 component is related to myelin content. A subsequent MRI study of MS patients also demonstrated a reduction in the myelin water content in MS lesions and also in GM compared to WM [46].

Stanisz *et al* [192] studied rat sciatic nerve portions both proximal and distal to the injury site, and found that the short T_2 component in degenerated nerves showed decreased amplitude, and the components assigned to intra- and extra-cellular water exhibited increased T_2 relaxation times, observations which could be related to both demyelination and inflammation, and histological data confirmed the presence of these processes.

In a separate study, Stanisz's group performed a hybrid MT-CPMG experiment [193] in order to study both the MT and T_2 relaxation characteristics of bovine optic nerve tissue. In order to model T_2 relaxation and MT properties, a model consisting of two tissue compartments, each with their own associated liquid and semi-solid pools. Each liquid pool exchanges spins with its associated semi-solid pool (via MT), and the two liquid pools also exchange magnetisation. This formulation resulted in 15 free model parameters, however the experimental data were found not to be sensitive to all of these, such that some remained undetermined or coupled with other parameters. For example, the proton densities of the two semi-solid pools cannot be determined and are therefore coupled with the rates of MT exchange to give pseudo-first order rate constants. The MT-CPMG measured signal originates only from the two liquid components, therefore the sum of the spin populations of these two components was set to 1, as measured immediately following the $\pi/2$ pulse in the MT-CPMG sequence without an MT pulse.

It was shown that this four-pool model for bovine optic nerve (white matter) tissue was sufficient to describe quantitatively all the features of the experimental data collected using the MT-CPMG sequence. The model parameters obtained were all physically

reasonable. It was hypothesized that one compartment represents myelin, whilst the other is associated with intra- and intercellular protons. They postulated that the shorter transverse relaxation times and faster longitudinal relaxation rate observed in the liquid pool B than pool A indicated that the water associated with myelin exhibits decreased translational and rotational motion. The amount of MT exchange taking place in pool B was estimated to be approximately an order of magnitude larger than in pool A. The authors suggested that this indicates that the MT exchange in white matter occurs mainly between water and semi-solid protons associated with myelin.

They also acquired MT data during the transient approach to steady state, but statistical analysis demonstrated that large parameter errors resulted, in addition to strong parameter coupling, and therefore it was concluded that the transient MT data does not provide any additional information not available from steady state data alone.

Li *et al* [194] proposed a quantitative MT model in which the 'restricted pool is divided into protons tightly bound to macromolecules, and those protons at the surface (hydration) layer (see also figure 3.1), exchanging magnetisation via dipolar coupling, with free protons rapidly exchanging with surface layer protons via diffusion (figure 5.2). Harrison *et al* [195] showed that the multiple relaxation species in tissue water experience their own Magnetisation Transfer. In this model the free proton pool is only divided into long (A) and short (A1) relaxation time components. Here the free protons would exchange rapidly with bound protons on the surface of a number of different types of macromolecules (B, C,...), and the MT between the restricted proton pools (B1, C1,...) and the macromolecules would occur more slowly via spin diffusion or chemical exchange. This model is a more realistic representation of the MT exchange taking place in biological tissue, but the complexity of the model would require very large data sets to be acquired in order to constrain all the free parameters of the model. There is a trade-off, therefore, between scanning time and intensive computation and the accuracy of the qMT model.

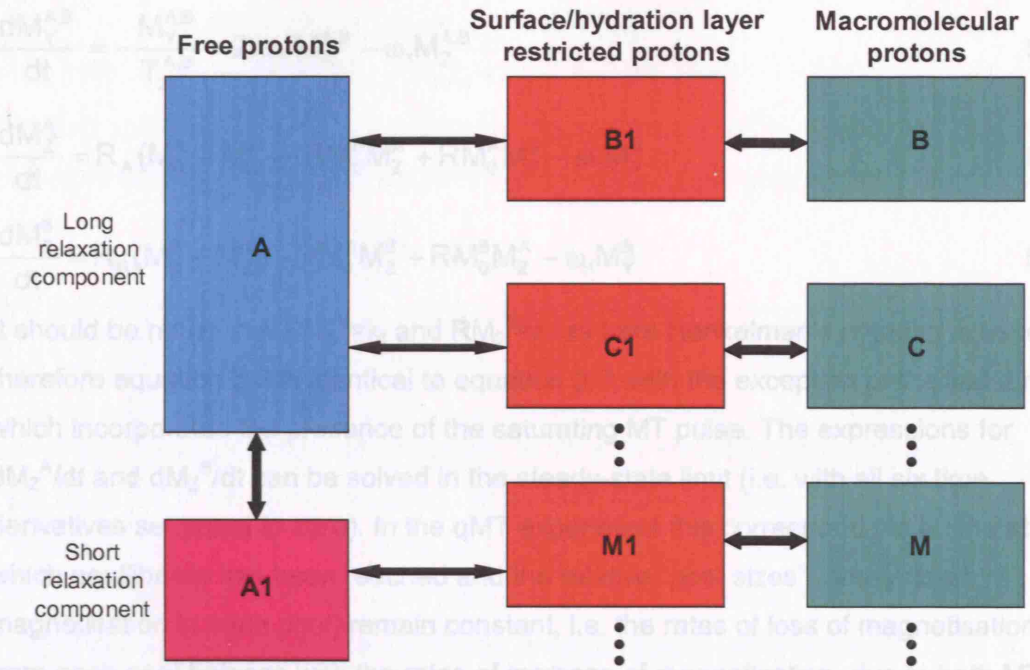

Figure 5.2: A more realistic many-pool model for MT in biological tissue (adapted from Li *et al* [194]). The free proton pool is assumed to comprise at least two pools itself, and these individual pools exchange magnetisation with each of the pools of protons assumed to exist in the surface or hydration layer, which in turn are in exchange with macromolecular protons.

5.1.3 Bloch Equations modified for the coupling of the two pools

The Bloch equations (for a single proton pool) in the x, y and z directions incorporating relaxation terms (equation 2.33) must be modified to include terms to account for the magnetic coupling of the two pools (see also figure 5.1). Equations 5.1 and 5.2 describe the magnetisation behaviour of the free (A) and restricted (B) pools in the x and y directions respectively. Since the restricted pool T_2 relaxation time (T_2^B), is very short, exchange associated with the transverse magnetisation of the two pools is not included in the model. This has previously been shown to be negligible [196], therefore the Bloch equations in the transverse plane are not affected by MT exchange (equations 5.1-5.2). However, in the longitudinal (z) direction the differential equations are modified to include extra terms for the exchange of magnetisation between the two pools, and these are given by equations 5.3 and 5.4 for the free and restricted pools respectively.

$$\frac{dM_X^{A,B}}{dt} = -\frac{M_X^{A,B}}{T_2^{A,B}} - 2\pi\Delta f M_Y^{A,B} \qquad 5.1$$

$$\frac{dM_Y^{A,B}}{dt} = -\frac{M_Y^{A,B}}{T_2^{A,B}} - 2\pi\Delta f M_X^{A,B} - \omega_1 M_Z^{A,B} \quad 5.2$$

$$\frac{dM_Z^{A}}{dt} = R_A(M_0^A - M_Z^A) - RM_0^B M_Z^A + RM_0^A M_Z^B - \omega_1 M_Y^A \quad 5.3$$

$$\frac{dM_Z^{B}}{dt} = R_B(M_0^B - M_Z^B) - RM_0^A M_Z^B + RM_0^B M_Z^A - \omega_1 M_Y^B \quad 5.4$$

It should be noted that $RM_0{}^B=k_f$ and $RM_0{}^B=k_r$ as here Henkelman's notation is used, therefore equation 5.3 is identical to equation 3.3, with the exception of the last term which incorporates the presence of the saturating MT pulse. The expressions for $dM_Z{}^A/dt$ and $dM_Z{}^B/dt$ can be solved in the steady-state limit (i.e. with all six time derivatives set equal to zero). In the qMT experiment this corresponds to a time at which equilibrium has been reached and the relative "pool sizes" (amounts of magnetisation in each pool) remain constant, i.e. the rates of loss of magnetisation from each pool balance with the rates of increase of magnetisation, due to both MT exchange and RF absorption.

The last terms ($-\omega_1 M_Y{}^{A,B}$) in equations 5.3 and 5.4 represent the rates of absorption of RF irradiation ($R_{RFA,B}$) of the free and restricted pools respectively. The Bloch equations by necessity yield a Lorentzian absorption lineshape, which can be written as:

$$g(\omega - \omega_0) = \left(\frac{1}{\pi}\right)\left(\frac{\Gamma_{\frac{1}{2}}}{\left((\omega_1 - \omega_0)^2 + \Gamma_{\frac{1}{2}}{}^2\right)}\right) : \quad 5.5$$

where $g(\omega-\omega_0)$ is the RF absorption lineshape, $\Gamma_{\frac{1}{2}}$, is the FWHM of the Lorentzian lineshape and is equal to $1/T_2{}^{A,B}$, and $(\omega_1-\omega_0)=2\pi\Delta f$ is the difference between the resonant and driving frequencies. Using this expression the Lorentzian absorption lineshape can be written as:

$$R_{RFA,B} = \frac{\omega_1^2 T_2^{A,B}}{\left(1+(2\pi\Delta f T_2^{A,B})^2\right)} = \left(\pi\omega_1^2\right)\left(\frac{1}{\pi}\right)\left(\frac{\left(\frac{1}{T_2^{A,B}}\right)}{\left((2\pi\Delta f)^2 + \left(\frac{1}{T_2^{A,B}}\right)^2\right)}\right) \quad 5.6$$

(or, more generally, $R_{RFA,B}=\pi\omega_1{}^2 g(2\pi\Delta f, T_2{}^{A,B})$, where $g(2\pi\Delta f, T_2{}^{A,B})$ is the absorption lineshape of the particular compartment).

Using this approach, the steady state solution for $M_Z{}^A$ is:

$$M_Z^A = \frac{R_B R M_0^B + R_A R_{RFB} + R_B R_A + R_A R M_0^A}{(R_A + R_{RFA} + R M_0^B)(R_B + R_{RFB} + R M_0^A) - R M_0^A R M_0^B} \quad 5.7$$

In many studies, the free pool equilibrium magnetisation M_0^A is normalised to 1 and is therefore eliminated from this equation [49], [188], [189] to give equation 5.8:

$$M_Z^A = \frac{R_B\left[\frac{R M_0^B}{R_A}\right] + R_{RFB} + R_B + R}{\left[\frac{R M_0^B}{R_A}\right](R_B + R_{RFB}) + \left(1 + \left[\frac{\omega_1}{2\pi\Delta f}\right]^2\left[\frac{1}{R_A T_2^A}\right]\right)(R_{RFB} + R_B + R)} \quad 5.8$$

However, this is dimensionally incorrect. In order to maintain dimensionality, M_0^A should be left in the signal equation. Then there are 6 free parameters: R_A, R_B, R, M_0^B (relative to M_0^A), T_2^A, T_2^B. However, as pointed out by Caines *et al* [197], unique sets of the 6 parameters above cannot be obtained by fitting the steady state longitudinal magnetisation to experimental qMT data because steady state measurements do not contain an explicit reference to the absolute time scale, therefore only particular combinations of these fundamental parameters may be obtained from a qMT experiment.

5.1.4 RF absorption lineshapes for the restricted proton pool

5.1.4.1 Lorentzian

The Lorentzian absorption lineshape (given by equation 5.6) is appropriate for the free proton pool, because liquids experience motional narrowing, where the RF absorption lineshape is narrowed because the rapid motions of free protons cause "averaging out" of dipolar interactions between spins (see also section 5.1.4.3). However it has become apparent [198], [199] that a more complex model may be required for the semi-solid pool.

5.1.4.2 Gaussian

A Gaussian lineshape has also previously been used to characterise the semi-solid pool RF absorption [49]. This lineshape is appropriate for many solids, and is described by:

$$g(2\pi\Delta f, T_2^B) = \left(\frac{T_2^B}{\sqrt{2\pi}}\right)\exp\left(-\frac{2\pi\Delta f T_2^B}{2}\right)^2 \quad 5.9$$

Iino [200] performed qMT experiments on BSA samples of varying concentration. It was demonstrated that a Lorentzian RF absorption lineshape for the semi-solid pool gave the best fit to data for BSA concentrations up to about 6.2mmol/kg, when a transition to a Gaussian lineshape was observed.

This lineshape produces a better agreement between theory and experimental data than the Lorentzian lineshape, but characterises spins that are homogeneously coupled (i.e. solids). Therefore, for biological tissues neither a Lorentzian nor a Gaussian lineshape give acceptable fits of the qMT model to data [201].

5.1.4.3. super-Lorentzian

Morrison and Henkelman [201] performed MT experiments using CW RF irradiation applied to samples of fresh bovine brain tissue, and found that the super-Lorentzian lineshape resulted in improved fits to qMT data compared to either a Lorentzian or Gaussian restricted pool lineshape. The super-Lorentzian lineshape was first observed in potassium laurate [202] and subsequently in lamellar liquid crystals [203] and lipids [204] and is expected to arise from partially ordered materials, such as polymers, liquid crystals, biological membranes, and molecules absorbed on surfaces. Quesson *et al* [205] subsequently used the super-Lorentzian lineshape to model the RF absorption of the restricted proton pool in MT imaging of the rat brain at 4.7T, and also demonstrated a good fit to experimental data.

The spin Hamiltonian is an operator corresponding to the total energy of the spin system, and therefore governs the RF absorption of the spins. In biological tissue, therefore, it is a sum of the Zeeman, chemical shift and dipolar aspects for the particular spin system, describing the interactions between spins and the external and local magnetic fields and other nuclei.

Let us first consider a spin system where spins can assume many different orientations, and where molecular re-orientation causes the spins to jump randomly, with transitional frequency ω. When the correlation time τ_c for the motion of spins is long (such as in solids), these motions cause spectral broadening by an amount of the order $\Delta\omega \sim \tau_c^{-1}$. However, when the τ_c is short (as is the case in liquids), the spectrum collapses to a single doublet with a splitting which corresponds to the average splitting over all of the molecular states between which transitions take place. Therefore, in liquids the dipolar component of the Hamiltonian is approximately zero. This "averaging" of the dipolar interactions between spins is sometimes known as "motional narrowing". For a "free" nucleus (in the liquid state), the Hamiltonian is simply determined by the interaction of the nuclear spin with the static magnetic field $\mathbf{B_0}$ (see also section 2.1), but in tissue the contributions of chemical shift and dipolar interactions between spins must also be considered.

Dipolar, quadrupolar and anisotropic chemical shift interactions are all examples of so-called 'tensor interactions', i.e. they can each be represented as scalar products of two tensors of rank 2. In each case, one of these tensors corresponds to the Wigner rotation matrix, which relates the orientation of the principal axis co-ordinate system for the interaction to the lab reference frame. The other is formed from products of spin operators of neighbouring spins for dipolar interactions, products of spin operators of a single spin for quadrupolar interactions and products of the external magnetic field vector and individual spin operators for anisotropic chemical shift interaction. The problem of motional averaging of dipolar interactions in ^{1}H NMR spectra in biological membranes is different from that of the other tensor interactions. The interaction takes place between pairs of spins rather than single spins (whereas in liquids, the interaction is between single spins), and each member of each pair is then also coupled to many other spins. Here we restrict the discussion to "model" membranes made up of phospholipid molecules, which, because of their amphiphilic nature, form a bilayer structure when dissolved in water. As a result of this, phospholipid molecules form a bilayer structure when dissolved in water. Such membranes usually undergo a well-defined phase transition from a "gel" (solid-like) phase to a higher temperature, "liquid-crystalline" (liquid-like) phase. During the phase transition it can be seen that the molecular motions are much faster above the phase transition than below it, and the molecular motions in the liquid crystalline phase have an axis of symmetry. Rapid diffusion of the molecules parallel to the plane of the membrane effectively averages the intermolecular dipolar interactions to zero in that plane. However, the intramolecular dipolar interactions are only partially averaged due to rapid molecular conformational transitions and molecular rotations. It has been observed that, in the liquid crystalline phase, the phospholipid bilayer normal is an axis of symmetry for the molecular rotations [206].

The overall effect of this is that the dipolar term in the Hamiltonian (and therefore the RF absorption lineshape) is dependent on the angle of orientation θ of the molecule with respect to the bilayer normal. If, as is commonly assumed [188], [201], the lineshape at the angle θ=0 is Gaussian, the super-Lorentzian lineshape is given by:

$$g(2\pi\Delta f, T_2^B) = \int_0^{\frac{\pi}{2}} d\theta \sin\theta \sqrt{\frac{2}{\pi}} \frac{T_2^B}{\left|3\cos^2\theta - 1\right|} \exp\left[-2\left(\frac{2\pi\Delta f T_2^B}{\left|3\cos^2\theta - 1\right|}\right)^2\right] \qquad 5.10$$

where θ is the angle between the external magnetic field and the bilayer normal. The sin θ term is included in order to average the lineshape over all possible angles θ.

The Lorentzian, Gaussian and super-Lorentzian lineshapes are shown in figure 5.3, for MT pulse amplitude ω=896rad s^{-1}, with the restricted pool T_2 relaxation time T_2^B assumed to be 11μs for all three lineshapes. It can be observed that the Lorentzian and Gaussian lineshapes are very similar, but the super-Lorentzian lineshape differs appreciably from the other two, particularly at low offset frequency (the super-Lorentzian lineshape continues to rise at low offset frequency, whereas the other two lineshapes plateau at low frequencies and have longer tails). However, within the likely ranges of offset frequency at which a qMT experiment would be performed (≥1000Hz), the three lineshapes are very similar.

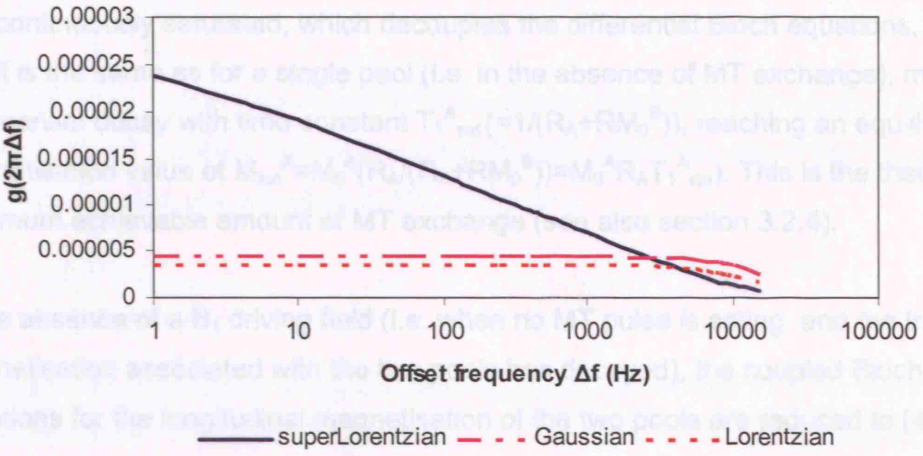

Figure 5.3: Graph illustrating potential 'semi-solid' pool RF absorption lineshapes, as a function of the (logarithmically plotted) MT pulse offset frequency. The restricted proton pool absorption super-Lorentzian, Gaussian and Lorentzian lineshapes g(2πΔf) are illustrated for a B_1 driving field angular frequency (i.e. MT RF pulse amplitude) ω_1=896rad s^{-1}. A T_2^B value of 11μs was assumed for all three lineshapes.

5.1.4.4 Other possible absorption lineshapes

Li *et al* [194] used a method in which the average absorption lineshape could be extracted directly from MT data along with the other parameters that characterise MT exchange in the two-pool model. The fit of the qMT model to data using this "flexible" lineshape was then compared with that obtained using the super-Lorentzian and the Kubo-Tomita [207] lineshapes to model the semi-solid pool RF absorption. The use of such a flexible lineshape significantly improved the fit of the two-pool model to data in various biological tissues and yielded physically realistic results. It was suggested that perhaps biological tissues exhibit a weighted average of the super-Lorentzian and

Kubo-Tomita lineshapes. However, the super-Lorentzian has been widely accepted as the most appropriate lineshape for human white matter *in vivo* [188], [208], [209].

5.1.5 Bi-exponential solutions to the Bloch Equations following the application of an MT pulse

In general, if the magnetisation in either pool is perturbed by the application of RF irradiation, the subsequent recovery of each pool to the equilibrium state is bi-exponential [54]. Thus the observed longitudinal relaxation time constant $T_1^A{}_{sat}$ of the free proton pool is a mono-exponential approximation to the true magnetisation evolution. This is because the restricted pool was previously assumed to be completely and continuously saturated, which decouples the differential Bloch equations, and the result is the same as for a single pool (i.e. in the absence of MT exchange); mono-exponential decay with time constant $T_1^A{}_{sat}(=1/(R_A+RM_0^B))$, reaching an equilibrium magnetisation value of $M_{sat}^A=M_0^A(R_A/(R_A+RM_0^B))=M_0^AR_AT_1^A{}_{sat}$). This is the theoretical maximum achievable amount of MT exchange (see also section 3.2.4).

In the absence of a B_1 driving field (i.e. when no MT pulse is acting, and the transverse magnetisation associated with the two pools has decayed), the coupled Bloch equations for the longitudinal magnetisation of the two pools are reduced to [49], [50]:

$$\frac{dM_Z^A}{dt} = R_A(M_0^A - M_Z^A) - RM_0^AM_Z^B + RM_0^BM_Z^A \qquad 5.11$$

$$\frac{dM_Z^B}{dt} = R_B(M_0^B - M_Z^B) - RM_0^BM_Z^A + RM_0^AM_Z^B \qquad 5.12$$

These differential equations can be solved to yield the eigenvalues (time constants) that describe the bi-exponential recovery of the magnetisation of each pool.

It is assumed that the free pool magnetisation (as a function of time t) is given by:

$$M_Z^A(t) = M_0^A + c_1e^{-\lambda_1 t} + c_2e^{-\lambda_2 t} \qquad 5.13$$

where c_1 and c_2 are constants and the eigenvalues $\lambda_{1,2}$ describing the bi-exponential decay of longitudinal magnetisation are given by:

$$\lambda_{1,2} = \frac{1}{2}\left\{\left[RM_0^A + RM_0^B + R_A + R_B\right] \pm \sqrt{(RM_0^B - RM_0^A + R_A - R_B)^2 + 4R^2M_0^BM_0^A}\right\} \qquad 5.14$$

By substituting for M_z^A in the differential equation for M_Z^B it can also be shown that:

$$M_Z^B(t) = \frac{1}{RM_0^A}\left[RM_0^AM_0^B + c_1\left(RM_0^B + R_A - \lambda_1\right)e^{-\lambda_1 t} + c_2\left(RM_0^B + R_A - \lambda_2\right)e^{-\lambda_2 t}\right] \qquad 5.15$$

and c_1 and c_2 are given by equations 5.16 and 5.17:

$$c_1 = \frac{\left\{\left(M_Z^A - M_0^A\right)\left(R_A + RM_0^B - \lambda_2\right) - RM_0^A\left(M_0^B - M_Z^B\right)\right\}}{\left(\lambda_1 - \lambda_2\right)} \qquad 5.16$$

$$c_2 = \frac{\{RM_0^A(M_0^B - M_Z^B) - (M_Z^A - M_0^A)(R_A + RM_0^B - \lambda_1)\}}{(\lambda_1 - \lambda_2)} \quad 5.17$$

A complete derivation of these results is given in Appendix A. In the liquid pool, a rapid decrease in magnetisation of approximately M_0^B in size is observed, governed by the initial time constant λ_1 as the two pools reach an initial dynamic equilibrium. As time increases, the effect of the λ_1 term diminishes and M_Z^A slowly recovers to its equilibrium value of M_0^A with rate λ_2.

In the ideal case, the minimum value of M_Z^A occurs at a time t_{crit}, given by [62]:

$$t_{crit} = \frac{\ln|\lambda_1 c_1| - \ln|\lambda_2 c_2|}{\lambda_1 - \lambda_2} \quad 5.18$$

The eigenvalue λ_2 (the time constant for the slower phase of magnetisation evolution following an MT pulse) is the observed longitudinal relaxation rate of the free pool R_{Aobs} (which is altered in the presence of MT saturation).

$$R_{Aobs} = \frac{1}{2}\left[RM_0^B + R_A + RM_0^A + R_B - \sqrt{\{(RM_0^B + R_A - RM_0^A R_B)^2 + 4RM_0^A RM_0^B\}}\right] \quad 5.19$$

The observed longitudinal relaxation rate R_{Aobs} must be measured since solving the Bloch equations in the steady state means that no explicit reference to the time dependence of the differential equations is known. R_{Aobs} is therefore related to R_A by:

$$R_A = \frac{R_{Aobs}}{1+\left(\frac{\frac{RM_0^A f}{(1-f)R_A}(R_B - R_{Aobs})}{(R_B - R_{Aobs}) + RM_0^A}\right)} \quad 5.20$$

Since R_B, RM_0^A and $f/R_A(1-f)$ are extracted by fitting the model signal equation to MT data acquired at a number of different combinations of MT pulse amplitude and offset frequency, R_A can be determined by measuring R_{Aobs} (i.e. $1/T_1{}^A{}_{obs}$) experimentally.

5.1.6 Modelling of pulsed MT: modifications to the Henkelman model

5.1.6.1 Dipolar interactions and the semi-solid pool dipolar reservoir: Redfield-Provotorov theory

In 1995 Morrison *et al* [201] reformulated the Henkelman qMT model to include the possibility of the existence of a semi-solid pool dipolar reservoir in addition to its Zeeman reservoir. The liquid pool is modelled using Bloch theory (and is hence characterised by a Lorentzian RF absorption lineshape), but the restricted pool is modelled using Redfield-Provotorov theory. This is because dipolar interactions

between spins are averaged to zero in liquids due to the rapid reorientation of molecules, but this motional averaging does not take place in solids (see also section 5.1.4.3). The dipolar relaxation time T_D characterises the rate of relaxation of dipolar spins back to the Zeeman order ($R_D(=1/T_D)$) and the parameter D depends on the RF absorption lineshape assumed to characterise the RF absorption behaviour of the semi-solid pool. The rate of exchange of magnetisation between the two reservoirs governs the number of spins available for magnetisation transfer with the liquid spins, which is the reason for including this in the mathematical model for qMT.

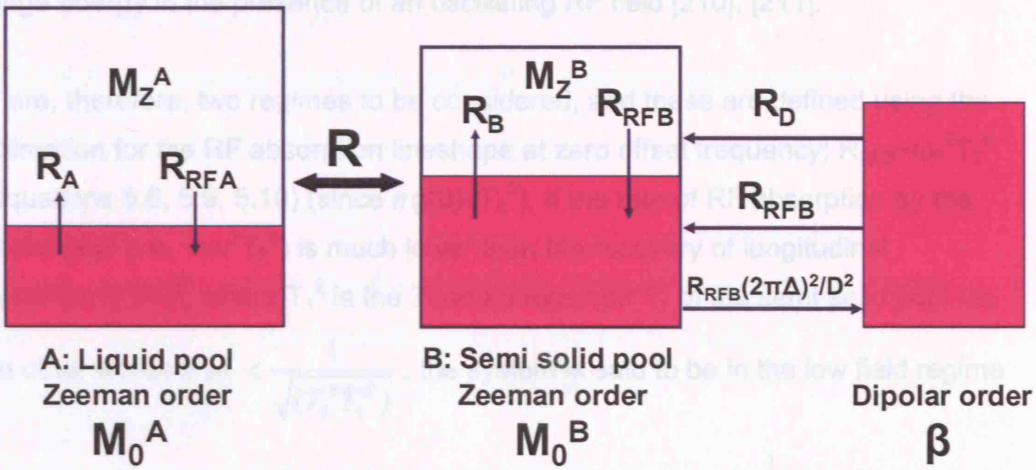

Figure 5.4: Modified spin bath model with dipolar reservoir for the semi-solid pool. R_D is the rate of relaxation of dipolar spins back to the Zeeman reservoir. R_{RFB} is the rate of absorption of RF irradiation by the restricted pool, and $R_{RFB}((2\pi\Delta/D)^2)$ is the rate of loss of RF irradiation to the dipolar reservoir from the Zeeman reservoir.

In the rotating frame of reference, the total spin Hamiltonian **H** (which is usually redefined for convenience as $\mathbf{E}/\hbar$) can be written as a sum of the Zeeman ($\mathbf{H_Z}$) and dipolar ($\mathbf{H_D^0}$) contributions:

$$\mathbf{H} = \mathbf{H_Z} + \mathbf{H_D^0} \qquad 5.21$$

where $\mathbf{H_D^0}$ is the truncated dipolar Hamiltonian (comprising the parts of the dipolar coupling that are unchanged by rotation about the z-axis, and therefore commute with the Zeeman coupling) and $\mathbf{H_Z}$ describes the Zeeman interaction with the magnetic field (as detailed in section 2.1):

$$\mathbf{H_Z} = -\gamma \mathbf{M B_{eff}} \qquad 5.22$$

where the effective field $\mathbf{B_{eff}}$ is given by:

$$\mathbf{B_{eff}} = \left(B_0 - \left(\frac{\omega_0}{\gamma}\right)\right)\hat{\mathbf{k}} + B_1\hat{\mathbf{i}} \qquad 5.23$$

It is assumed that the system is initially at equilibrium, so that the thermal lattice temperature θ_L^L is identical to the temperatures of both the Zeeman (θ_Z^L) and dipolar (θ_D^L) reservoirs in the laboratory (L) frame (i.e. $\theta_L^L=\theta_Z^L=\theta_D^L$). In the rotating frame, since the z-component of the effective field $\mathbf{B_{eff}}'$ is much smaller than the main static field $\mathbf{B_0}$, the Zeeman temperature θ_Z' is much less than the lattice temperature (by Curie's law). The dipolar temperature in the rotating frame $\theta_D'=\theta_D^L$, since the dipolar Hamiltonian $\mathbf{H_D}^0$ is invariant under rotation about the z-axis. In other words, in the rotating frame, the Zeeman reservoir is much cooler than the dipolar reservoir, therefore the two systems exchange energy in the presence of an oscillating RF field [210], [211].

There are, therefore, two regimes to be considered, and these are defined using the approximation for the RF absorption lineshape at zero offset frequency; $R_{RFB}\sim\omega_1^2T_2^B$ (see equations 5.6, 5.9, 5.10) (since $\pi g(0)\sim T_2^B$). If the rate of RF absorption by the semi-solid pool (i.e. $\sim\omega_1^2T_2^B$) is much lower than the recovery of longitudinal magnetisation ($1/T_1^Z$, where T_1^Z is the Zeeman reservoir T_1 of the semi-solid pool i.e. T_1^B), in other words if $\omega_1 < \frac{1}{\sqrt{(T_2^B T_1^Z)}}$, the system is said to be in the low field regime (described by theory due to Provotorov). Alternatively, if $\omega_1 > \frac{1}{\sqrt{(T_2^B T_1^Z)}}$, the system is in the high field regime and Redfield theory is used [210].

5.1.6.1.1 The high field regime (Redfield formulation)

In the high field regime it is assumed that the redistribution of energy is so fast that the spin states are effectively in quasi-equilibrium at all time and the two reservoirs can be assumed to have a common spin temperature θ^*. The RF amplitude of the B_1 field is sufficiently high that the RF-induced transition rate $1/\tau^*$ between the Zeeman and dipolar reservoirs is much greater than the semi-solid pool Zeeman order relaxation rate $1/T_1^Z$ and is given by [210]:

$$\frac{1}{\tau^*} = R_{RFB}\left\{1+\left(\frac{2\pi\Delta f}{D}\right)^2\right\} \qquad 5.24$$

where R_{RFB} is the RF absorption rate of the semi-solid pool as defined previously, and D is related to the linewidth of the dipolar reservoir (see below). In such a state of quasi-equilibrium, the magnetisation vector tends to align with the effective field $\mathbf{B_{eff}}$, and the "quasi-equilibrium" state is characterised by a common spin temperature θ^*, and a thermal relaxation time T_1'.

D depends on the lineshape chosen to describe the RF absorption of the semi-solid pool. For purely dipolar interactions, with D^2 averaged over all orientations (angles), $D^2=1/3(T_2^B)^2$ for a Gaussian semi-solid pool lineshape, and $D^2=1/15(T_2^B)^2$ for a super-Lorentzian lineshape [201].

The spin-lattice interaction can be described by a phenomenological equation for the expectation value of a Hamiltonian $\langle \mathbf{H}^* \rangle$ (or $1/\theta^*$, i.e. the inverse spin temperature):

$$\frac{d}{dt}\left(\frac{1}{\theta^*}\right)=\left(\frac{1}{T_1'}\left\{\left(\frac{1}{\theta^*}\right)_{eq}-\left(\frac{1}{\theta^*}\right)\right\}\right) \qquad 5.25$$

where T_1' is the spin-lattice relaxation time in the rotating frame of reference and $\left(\frac{1}{\theta^*}\right)_{eq}$ is the inverse spin temperature at equilibrium.

Curie's law states that (where M is the magnitude of the magnetisation along the effective field $\mathbf{B}_{eff}$ and M_{eq} is the equilibrium magnetisation) $M \propto \mathbf{B}_{eff}/\theta^*$, therefore:

$$\frac{d}{dt}(M)=\left(\frac{1}{T_1'}\{M_{eq}-M\}\right) \qquad 5.26$$

and T_1' depends on T_1, ω, $2\pi\Delta f$ and D. If it is assumed that nuclear relaxation is caused by random, uncorrelated fields with short correlation times (i.e. $\tau_c << 1/\omega_0$), then:

$$\frac{1}{T_1'}=\frac{(2\pi\Delta f)^2+\omega_1^2+2D^2}{(2\pi\Delta f)^2+\omega_1^2+D^2} \qquad 5.27$$

5.1.6.1.2 The low field regime (Provotorov formulation)

In this case, the RF irradiation is weak enough that the transitions induced by the spin-lattice coupling are much faster than those induced by the RF absorption rate R_{RFB}.

It can therefore no longer be assumed that the Zeeman and dipolar reservoirs have a common spin temperature (where the subscripts Z denote Zeeman (which is in this case synonymous with the z-direction), D the dipolar reservoir and L the lattice, and the superscript L represents the laboratory frame) [198], [210]:

$$\left(\frac{d}{dt}\right)\left(\frac{1}{\theta_Z}-\frac{1}{\theta_Z^L}\right)=-\left[R_{RFB}+\frac{1}{T_1}\right]\left(\frac{1}{\theta_Z}-\frac{1}{\theta_Z^L}\right)+R_{RFB}\left(\frac{1}{\theta_D}-\frac{1}{\theta_D^L}\right)-R_{RFB}\left(\frac{1}{\theta_Z^L}-\frac{1}{\theta_D^L}\right) \qquad 5.28$$

$$\left(\frac{d}{dt}\right)\left(\frac{1}{\theta_D}-\frac{1}{\theta_D^L}\right)=-\left[R_{RFB}\frac{(2\pi\Delta f)^2}{D^2}+\frac{1}{T_D}\right]\left(\frac{1}{\theta_D}-\frac{1}{\theta_D^L}\right)+R_{RFB}\frac{(2\pi\Delta f)^2}{D^2}\left(\frac{1}{\theta_Z}-\frac{1}{\theta_Z^L}\right)+R_{RFB}\frac{(2\pi\Delta f)^2}{D^2}\left(\frac{1}{\theta_Z^L}-\frac{1}{\theta_D^L}\right)$$

but since $\theta_Z^L << \theta_D^L=\theta^L$, $1/\theta_D^L$ can be ignored in the last term.

If the inverse dipolar reservoir spin temperature $1/\theta_D$ is now denoted β, and the difference in spin temperature between the lattice and the spin bath $(1/\theta_D\text{-}1/\theta_D{}^L)=\beta'$ in the rotating frame, the differential equations describing the magnetisation behaviour of the free and restricted pools and the dipolar reservoir can be written as [210], [211]:

$$\frac{dM_Z^A}{dt} = \omega_1 M_y^A + (R_1^A + R)\left(M_A^{ZL} - M_A^Z\right) - \frac{R}{f}\left(M_B^{ZL} - M_Z^B\right) \qquad 5.29$$

(i.e. the free pool magnetisation is unaffected since there is no dipolar reservoir associated with this pool).

$$\frac{dM_Z^B}{dt} = \left[R_{RFB} + R_B + \frac{R^L}{f}\right]\left(M_B^{ZL} - M_B^Z\right) - R_{RFB}\gamma\frac{2\pi\Delta f}{D^2}\beta' - R\left(M_A^{ZL} - M_A^Z\right) - R_{RFB}M_B^{ZL} \qquad 5.30$$

$$\frac{d\beta'}{dt} = R_{RFB}\frac{(2\pi\Delta f)^2}{D^2}\left(M_Z^B - \beta'\right) - \frac{\beta'}{T_D} \qquad 5.31$$

Equations 5.29-30 can be rewritten as [51], [188], [201]:

$$\frac{dM_Z^A}{dt} = R_A(M_0^A - M_Z^A) - RM_0^A M_Z^B + RM_0^B M_Z^A - R_{RFA}M_Z^A \qquad 5.32$$

$$\frac{dM_Z^B}{dt} = R_B(M_0^B - M_Z^B) - RM_0^B M_Z^A + RM_0^A M_Z^B - R_{RFB}M_Z^B + R_{RFB}\beta' \qquad 5.33$$

If the dipolar relaxation time T_D~0 (i.e. the dipolar reservoir relaxes back to the Zeeman order very quickly), these equations reduce back to the usual Bloch equations. The rate and degree of coupling between the Zeeman and dipolar orders depends on the lineshape and linewidth of the semi solid pool and the amplitude and offset frequency of the MT pulse.

5.1.6.2 Approximate solutions for pulsed MT incorporating partial saturation of the semi-solid pool and the free pool (developed by Pike [50])

In 1996 Pike [50] developed some approximate solutions to the pulsed MT problem for a gradient echo acquisition scheme. He first considered the idealised case, where the solution was found to be identical to that for a single pool, i.e. when no MT can take place. Then the more realistic pulsed experiment was examined, and a description of the assumptions underlying his modifications to the theory is given here.

5.1.6.2.1 Idealised pulsed MT

In the case of idealised pulsed MT saturation, it is assumed that the pair of pulses (A pool excitation and B pool saturation) are instantaneous (i.e. both pulse durations<<$T_{1,2}$) and coincident, so that no exchange occurs during the pulses. Therefore $RM_0{}^B=RM_0{}^A=0$ during the pulse, giving $c_1=c_2=M_Z{}^A(0)-M_0{}^A$ and $\lambda_1=\lambda_2=R_A(=1/T_{1A})$, where $c_{1,2}$ and $\lambda_{1,2}$ are as previously defined by Edzes & Samulski in 1977 [54] (see section 5.1.5). This results in the situation where the eigenvalues $\lambda_{1,2}$ of

the matrix solutions of the coupled Bloch equations are repeated. Thus, at the end of the TR,

$$M_Z^A = M_0^A + C_1 e^{-\lambda_1 t} = M_0^A + C_1 e^{-TR/T_1} \quad 5.34$$

The Bloch equations are effectively decoupled and the evolution of magnetisation with time is described by a mono-exponential approximation to the true, bi-exponential magnetisation behaviour. The time constant for the mono-exponential decay is $T_1{}^A{}_{obs}$, the observed T_1 of the free proton pool, and this idealised case gives the maximum amount of MT theoretically achievable in a pulsed sequence.

The equilibrium magnetisation M_Z^* after the application of many excitation pulses is given by:

$$M_Z^* = M_0^A + \left[M_Z^A(0) - M_0^A\right] e^{-TR/T_1} \quad 5.35$$

where $M_Z{}^A(0)$ is taken to be the magnetisation immediately after the previous pulse ($M_Z{}^+$) (i.e. at the beginning of the TR'). The excitation phase is modelled as a simple rotation and contraction of the free pool magnetisation vector and it is assumed that the excitation pulse has no (MT) effect on the restricted pool protons, which is probably a reasonable assumption). The free pool magnetisation immediately following the pulse is therefore given by equation 5.39 and this leads to the result:

$$M_Z^* = M_Z^+ e^{-TR/T_1} + M_0^A(1 - e^{-TR/T_1}) = \cos\alpha M_Z^- e^{-TR/T_1} + M_0^A(1 - e^{-TR/T_1}) \quad 5.36$$

Steady state is attained when $M_Z^- = M_Z^*$ after many TR' periods:

$$M_Z^- = \frac{M_0^A(1 - e^{-TR/T_1})}{(1 - \cos\alpha e^{-TR/T_1})} \quad 5.37$$

Equation 5.37 is the familiar steady state magnetisation equation for a gradient echo sequence.

However, in order to obtain the response after excitation, this should be multiplied by the transverse magnetisation attenuated between excitation and reception (during the echo time TE) due to T_2^* decay, i.e. by $\sin\alpha e^{-TE/T2*}$. The idealised magnetisation response is therefore given by:

$$M_y(TE) = M_0^A \sin\alpha \frac{(1 - e^{-TR/T_1})}{(1 - \cos\alpha e^{-TR/T_1})} e^{-TE/T_2^*} \quad 5.38$$

5.1.6.2.2 Pulsed MT

Here the restricted pool saturation and free pool excitation pulses are again assumed to be instantaneous and coincident, so that no exchange can take place during the pulses. The magnetisation immediately following the pair of instantaneous and

coincident restricted pool saturation and free pool excitation pulses is assumed to be given by:

$$\mathbf{M_Z^+ = SM_Z^-} \quad 5.39$$

Where **S** is a diagonal saturation matrix, with elements S_A and S_B for the free and restricted pools respectively, and the saturation fraction $S_{A,B}$ is between 0 and 1. S_B is assumed to originate only from the saturation pulse. S_A is the fractional direct saturation produced by the MT pulse multiplied by cos α to account for the effect of the excitation pulse (flip angle α).

The sequence was decomposed into different time intervals to describe each stage of the experiment. The equation describing the evolution of magnetisation in the pulsed qMT experiment is given in Appendix B.

Pike performed numerical simulations to solve the coupled Bloch equations without assumptions in order to verify the approximations made. The coupled Bloch equations were evaluated in both RF-on and RF-off periods and to examine the effects of the two pulses not being coincident, the saturation pulse was shifted (by up to half a TR') from the excitation pulse in numerical simulations. However, the Lorentzian lineshape was used to model the restricted pool RF absorption to estimate the restricted pool saturation of various pulses. This assumption resulted in a slight over-estimation of S_B values, but it was shown that the model signal equation was relatively insensitive to alterations in S_B, therefore this was deemed to be an insignificant problem. Agreement between numerical simulations and analytical results was good, and it was also found that the pulse timing assumptions made (i.e. that the two pulses are coincident) resulted in minimal errors.

5.1.6.3 Approximate solutions to the pulsed MT experiment incorporating Redfield-Provotorov theory for the semi-solid pool due to Sled and Pike [51], [208]

In this study the restricted pool was described using Redfield-Provotorov theory, i.e. it was assumed that the irradiation is weak enough and the timescale of the experiment short enough that the Zeeman and dipolar reservoirs have their own associated temperatures.

The time lag in the response of the restricted pool to the MT saturation pulse is very short ($\sim T_2^B$). Therefore in this study this time delay is neglected and it is assumed that the transition rate (i.e. R_{RFB}) is time-varying.

Consistent with previous studies, the on resonance excitation pulse was assumed to have no effect on the restricted pool.

The sequence was decomposed into different time periods, those of free precession in the absence of a pulse, off resonance irradiation of the restricted pool at constant power, and instantaneous (partial) saturation of the free pool by both the imaging and MT pulses. During each of these time periods, the differential equations reduce to first order systems of equations with constant coefficients. The time evolution is periodic with the TR, resulting in a closed form solution for the signal measured when the system has been driven to a steady state. Again, in line with other work [49], the parameter R_B was fixed at a value of $1s^{-1}$ ($\pm 1s^{-1}$).

The approximations presented in this study are very similar to those proposed by Pike [50], with the inclusion of the possibility of partial saturation of the restricted proton pool and direct saturation of the liquid pool, but here a dipolar reservoir associated with the semi-solid pool was also included.

Bi-exponential equations for the magnetisation behaviour following an MT pulse result for each different time interval within the sequence, and during a particular period the matrix (containing the coefficients of the coupled Bloch equations) is constant. The eigenvalues are similar to those obtained by Edzes and Samulski [54], but with additional terms during the particular pulse, and also additional terms to describe the dipolar reservoir. For a specific type of qMT experiment, evaluation of the signal behaviour is then simply a case of combining the results for each stage of the sequence. These approximations are detailed in Appendix C.

Sled and Pike also considered two models for the restricted pool; one in which it experiences continuous wave excitation of equivalent average power (CW approximation) and another in which it experiences a rectangular pulse of equivalent average power and a width equal to the FWHM of the instantaneous pulse power $\omega^2(t)$. The CW approximation was found to be satisfactory for large duty cycles (i.e. τ_{sat}/TR' large so that it approximates CW irradiation more closely), but was inadequate at small duty cycles, or long TR' times. This is because the time constant for equilibration of the two pools is on the order of a few milliseconds, comparable with the duration of the MT pulses.

For the rectangular pulse version of the MT SPGR signal equation the pulse sequence was assumed to have steps of instantaneous saturation of the free pool due to both the

MT and excitation pulses, continuous wave irradiation of the restricted pool for a period t/2, a period TR-t of free precession, and finally another period of continuous wave irradiation of duration t/2. The validity of these approximations was again investigated by performing numerical simulations of the coupled Bloch equations.

Numerical simulations showed that including the dipolar terms resulted in a modest underestimate of the macromolecular pool size ratio F (M_0^B/M_0^A), but in the imaging experiments, neglecting the dipolar terms substantially improved the precision of the estimates of k_f. However, the uncertainty in k_f tends to decrease as F increases and k_f decreases, so this factor is dependent on the particular system being imaged.

The approximate signal equation developed by Sled and Pike, whilst probably the most complete treatment of the qMT experiment, is still complicated and requires a numerical solution of the Bloch equations in order to determine the fractional saturation due to the MT pulse. The complexity of the processing algorithm means that ideally a large number of MT data points would be required to constrain all parameters of the model.

5.1.6.4 Another approximation for pulsed MT (Yarnykh [212])

Yarnykh [212] also divided the sequence into different time intervals; off resonance saturation (due to the MT pulse) of duration τ_{sat}, a delay for the spoiling gradient, the readout (excitation) pulse duration (assumed to be instantaneous), and a delay for signal readout and relaxation.

Only longitudinal magnetisation components are considered, since transverse magnetisation is assumed to disappear through relaxation and spoiling.

Another assumption made in this study was that direct saturation of the free pool is negligible, an assumption that is not reasonable except at very high MT pulse offset frequency.

The imaging pulse is assumed to have no (MT) effect on the restricted pool, but the liquid pool magnetisation is rotated by an angle α.

The MT pulse was modelled as a rectangular pulse of constant amplitude & equivalent duration (i.e. over the MT pulse duration τ_{sat}):

$$\omega_{eff} = \gamma B_{1eff} = \gamma \sqrt{\frac{1}{\tau_{sat}} \int_0^{\tau_{sat}} B_1^2(t)\,dt} \qquad 5.40$$

Simulated Z-spectra were then compared for wide ranges of pulse sequence and spin system parameters with those obtained using the approximate signal equation depending on P, Q and T_2^B. The model provided a close approximation of the experimental data when the MT pulse was applied far from resonance, but underestimated data at low offset frequencies, which is a result of ignoring the direct saturation of the free proton pool. Under conditions of high effective field B_{eff}, long TR', high rate constant k or long pulse duration τ_{sat} the analytical model tended to overestimate the numerical solution in the medium frequency (1-10kHz) range.

5.1.6.5 Simplified 3-parameter model: Yarnykh & Yuan [213]

In a separate study Yarnykh and Yuan [214] reduced the problem to just 3 parameters: T_2^B, and two new parameters P and Q (both independent of the properties of the saturating field) by making various assumptions. These were that all time intervals are very short, the MT pulse is instantaneous, the excitation pulse flip angle is low, and R_B << k/f (this is guaranteed by the small f for most biological materials), therefore R_B can be neglected in sums with a k(1-f)/f term, and also, since (R_B-R_A) << k/f, R_A can be substituted by R_{Aobs}.

The quality of parametric maps obtained appeared to be strongly dependent on the parameter T_2^B, particularly the k and f maps. However, all fixed parameters did affect values of fitted parameters, although the largest effect was seen for T_2^B. Despite this effect, however, parameter estimates were consistent with previous studies [208], [212].

5.1.6.6 Ramani's (CWPE) model for qMT [215] [216]

At our centre, Ramani *et al* [215], [216] developed a very simple model, based on the continuous wave solution of Henkelman *et al* (equation 5.8):

$$M_Z^A = \frac{R_B\left[\frac{RM_0^B}{R_A}\right] + R_{RFB} + R_B + R}{\left[\frac{RM_0^B}{R_A}\right](R_B + R_{RFB}) + \left(1 + \left[\frac{\omega_1}{2\pi\Delta f}\right]^2\left[\frac{1}{R_A T_2^A}\right]\right)(R_{RFB} + R_B + R)} \qquad 5.41$$

To take into account the pulsed behaviour of the RF fields, the MT pulse was treated as having the same effect as a CW irradiation with the same average power (calculated over TR', the time between successive MT pulses). In other words, the frequency ω_1 is replaced by ω_{1CWPE} (where CWPE=Continuous Wave Power Equivalent). The CW power equivalent B_1 (B_{1CWPE}) was defined to be the root mean square (rms.) value of the saturating field:

$$\omega_{1CWPE} = \gamma\sqrt{P_{sat}} = \gamma B_{1CWPE} \qquad 5.42$$

where P_{sat} is the mean square saturating field, averaged over a time TR' (for a 3D FT sequence or single slice 2DFT sequence, TR'=TR, but in the case of multislice 2D FT sequences, TR'=TR/no. of slices, if, as is usually the case, one MT pulse is applied per slice). It should be noted that this approach differs from that of Yarnykh [212], who averages P_{sat} over the pulse duration τ_{sat}.

An arbitrary shaped (amplitude-modulated) RF pulse, applied on resonance, results in an effective excitation flip angle θ radians (a function of the pulse shape e.g. Gaussian, sinc), the pulse duration τ_{sat}, and the maximum amplitude B_{1sat}). From equation 2.21 the flip angle of the MT pulse (in radians) is given by the following relation [76]:

$$\theta = \left(\frac{180}{\pi}\right)\gamma p_1 B_{1sat}\tau_{sat} \qquad 5.43$$

where p_1 is the ratio of the mean amplitude of the saturation pulse to that of a rectangular pulse of the same peak amplitude.

$$P_{sat} = \frac{p_2 B_{1sat}^2 \tau_{sat}}{TR'} \qquad 5.44$$

where p_2 is the ratio of the square of the mean amplitude of the saturation pulse to that of a rectangular pulse of the same amplitude.

The equilibrium free proton pool magnetisation M_0^A was left in this equation for M_Z^A, rather than normalising M_0^A to a value of 1. This also makes the restricted proton pool fraction (given by equation 5.46) more explicit. The equation was also modified to give an explicit expression for the signal S (rather than just M_z^A/M_0^A) that could be fitted to the data in a least squares procedure (by including the factor gM_0^A, with M_0^A the intrinsic proton density of the free proton pool, and g a proportionality constant encompassing various intrinsic scanner-related factors including the 'gain' of the RF amplifier).

$$S = gM_Z^A = gM_0^A\left(\frac{R_B\left[\frac{RM_0^B}{R_A}\right] + R_{RFB} + R_B + RM_0^A}{\left[\frac{RM_0^B}{R_A}\right](R_B + R_{RFB}) + \left(1 + \left[\frac{\omega_{1CWPE}}{2\pi\Delta f}\right]^2\left[\frac{1}{R_A T_2^A}\right]\right)(R_{RFB} + R_B + RM_0^A)}\right) \qquad 5.45$$

This was then rearranged so that the signal S could be expressed in terms of the restricted proton fraction f, where:

$$f = \frac{M_0^B}{M_0^A + M_0^B} \qquad 5.46$$

The restricted proton fraction can be quoted as a dimensionless fraction, or is sometimes expressed as a percentage (often in pu). This parameter gives insight into the biological significance of alterations in the MT parameters in pathologies such as demyelination, since the restricted protons in the qMT model are thought to be attached to macromolecules located for example in myelin.

Substitution of equation 5.46 into equation 5.45 gives:

$$S = gM_0^A \left(\frac{R_B\left[\frac{RM_0^A f}{R_A(1-f)}\right] + R_{RFB} + R_B + RM_0^A}{\left[\frac{RM_0^A f}{R_A(1-f)}\right](R_B + R_{RFB}) + \left(1 + \left[\frac{\omega_{1CWPE}}{2\pi\Delta f}\right]^2 \left[\frac{1}{R_A T_2^A}\right]\right)(R_{RFB} + R_B + RM_0^A)} \right) \quad 5.47$$

Six parameters (some of which are combinations of fundamental parameters) could then be determined by fitting this model signal intensity to qMT signal data collected at various combinations of MT pulse amplitude and offset frequency: R_B, RM_0^A, $f/R_A(1\text{-}f)$, T_2^B (via R_{RFB}), $1/R_A T_2^A$ and gM_0^A.

$$\text{CWPE MTR} = gM_0^A \left(1 - \frac{R_B\left[\frac{RM_0^A f}{R_A(1-f)}\right] + R_{RFB} + R_B + RM_0^A}{\left[\frac{RM_0^A f}{R_A(1-f)}\right](R_B + R_{RFB}) + \left(1 + \left[\frac{\omega_{1CWPE}}{2\pi\Delta f}\right]^2 \left[\frac{1}{R_A T_2^A}\right]\right)(R_{RFB} + R_B + RM_0^A)} \right) \quad 5.48$$

The amount of direct saturation of the free proton pool can be estimated by setting R=0 (i.e. no MT exchange) in the free water signal equation above:

$$\left[\frac{M_Z^A}{M_0^A}\right]_{DS} = \frac{1}{\left[1 + \left(\frac{\omega_{1CWPE}}{2\pi\Delta f}\right)^2 \left(\frac{1}{R_A T_2^A}\right)\right]} \quad 5.49$$

Ramani *et al* [215] compared simulated MTR data using the qMT CWPE model with multi-centre pulsed MTR data [76]. MTR values generated using the CWPE qMT model were consistently higher (or possibly sometimes equal at short TR'(<100ms) [215]) than those measured *in vivo*, and it was concluded that the CWPE MTR (which is defined to occur when B_{1CWPE} is applied continuously for the TR' period) corresponds to the maximum achievable MTR with a pulsed sequence. This was confirmed by the fact that shorter TR' (time between successive MT pulses) (defined in that particular study to be when TR'<100ms) sequences were found to produce higher (closer to the CWPE qMT approximation) MTRs. McGowan *et al* [217] also found increases in MTR values with the duty cycle of the off-resonance irradiation, approaching a maximum corresponding to CW irradiation. This is because the 'semi-solid' spins are unable to recover their equilibrium magnetisation between successive MT pulses if the TR' is short, resulting in a closer approximation to the CW situation. However, in this study a Gaussian RF absorption lineshape was assumed for the semi-solid pool, whereas a

super-Lorentzian lineshape has been shown to be more appropriate to model the behaviour of the macromolecular pool *in vivo* [188], [208].

5.1.6.6.1Investigations of the validity of Ramani's (CWPE) model for qMT:A Preliminary Study performed at our centre

In order to investigate the validity and conditions of applicability of the CWPE approximation, various experiments were performed using Bovine Serum Albumin (BSA) phantoms. The phantoms were prepared at our centre as described later in this thesis in section 7.1.2.2.1 in 50ml plastic tubes. Four samples were scanned (simultaneously), of composition 20 and 25% weight/volume (w/v) BSA dissolved in water, and the same concentrations in physiological concentration (0.9%w/v) saline (NaCl). The reason for this is that it was suggested by Ewing *et al* [218] that this would produce a protein solution more closely representative of the conditions of proteins in biological tissue.

MTR measurements were made using the 2D spoiled gradient echo Euro-MT sequence [63], [219] (with pulse duration τ_{sat}=14.59ms, TR'=27.35ms, MT pulse flip angle 500°, offset frequency 1500Hz), and quantitative MT data were acquired using the 3D qMT protocol developed by Cercignani *et al* [209] (with pulse duration τ_{sat}=14.59ms, TR'=27.35ms) on a 1.5T GE Signa scanner (General Electric, Milwaukee, WI, USA).

In order to test under which conditions the CWPE approximation for B_1, developed by Ramani *et al* [215] is appropriate, various sequence parameters were altered, whilst attempting to keep the CWPE amplitude of the MT pulse constant by altering the MT pulse flip angle accordingly to compensate. The time between successive MT pulses (TR') was varied (the original TR' value (27.35ms) was multiplied by 1.25. 1.5, 1.75 or 2.0). In order to maintain the MT pulse amplitudes, as calculated using the CWPE approximation, the MT pulse flip angles were altered accordingly. A single MTR measurement was performed at each MT pulse flip angle.

An additional experiment was also performed in which the MT pulse shape was varied. There are four different pulses available for use as MT pulses (2 Gaussian, 2 Sinc-shaped) on the 1.5T GE Signa Scanner and their details are given in table 5.1. The Gaussian pulse G3 is the pulse used for the Euro-MT sequence [63], [220], and for the qMT acquisition protocols developed by Ramani *et al* [47] and Cercignani *et al* [209]. Again, the MT pulse flip angle was altered accordingly in each case in order to give an MT pulse amplitude identical to that of the Gaussian G3 pulse, within the assumptions

of the CWPE approximation. Again, a single MTR/qMT acquisition was performed at each MT pulse flip angle.

Table 5.1: Properties of different pulses available to use as MT pulses on the 1.5T GE Signa scanner (see also equations 5.43-5.44 for definitions of p_1 and p_2)

Pulse / Property	G0	S1	S2	G3
Shape	Gaussian	3-lobe apodised sinc	5-lobe apodised sinc	Gaussian
Resolution points	200	800	800	192
Ratio of pulse area to that of a rectangular pulse of the same duration and peak height (p_1) [76]	0.2921	0.2506	0.1245	0.4819
Ratio of mean square amplitude of pulse to that of a rectangular pulse of the same height (p_2) [76]	0.2066	0.2012	0.1127	0.3441

MTR results are shown for just one of the samples (20% w/v BSA dissolved in saline). MTR data is plotted for different TR' values as a function of MT pulse flip angle in figure 5.5 (the nominal MT pulse flip angle for the Euro-MT sequence is 500°), and for different MT pulse types in figure 5.6. MT pulse flip angles for each of the four pulses were altered (using knowledge of the particular pulse p_1 and p_2 values (given in table 5.1)) in order that each resulted in the same B_{1CWPE} value. Theoretical values were calculated using the estimated fundamental qMT parameters obtained for this particular sample (see figures 5.7-5.9). However, it should be noted that these parameters (and therefore the 'theoretical MTRs') were estimated from a qMT acquisition performed at a single TR' (27.35ms) and therefore could show some TR' dependence.

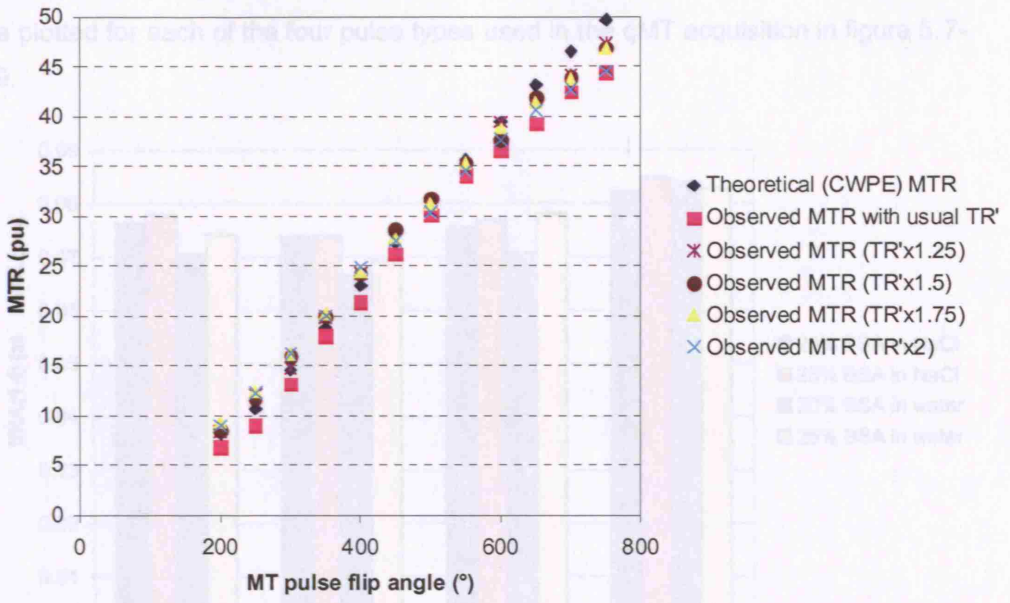

Figure 5.5: MTR values as a function of MT pulse flip angle for 20% w/v BSA dissolved in saline, with MTR data acquired at varying TR' times but the same MT pulse amplitude (as calculated using the CWPE approximation for B_1). Theoretical (CWPE) MTR values are also shown for comparison.

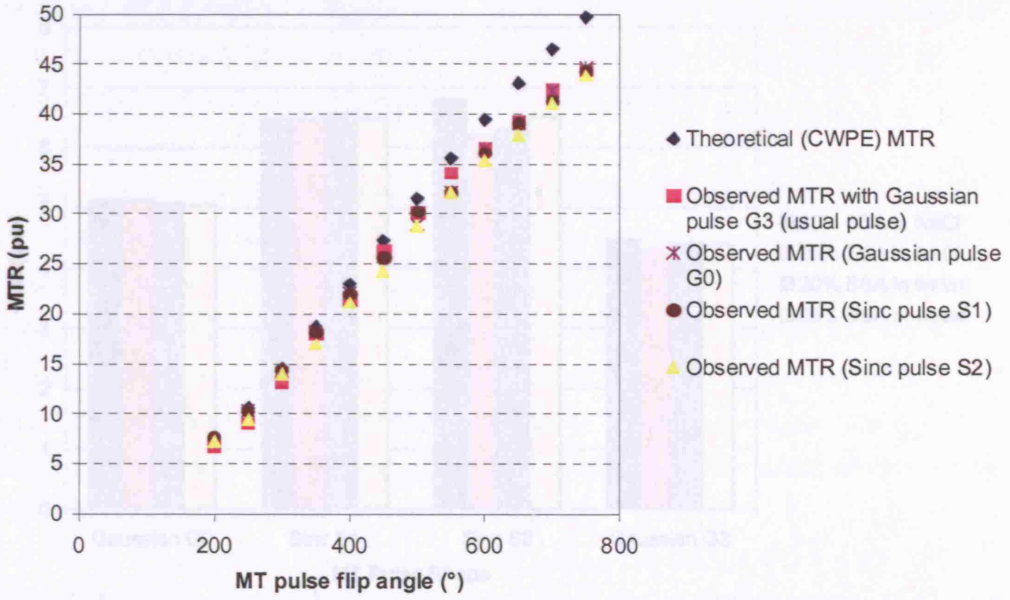

Figure 5.6: MTR values as a function of MT pulse flip angle for 20% w/v BSA dissolved in saline, with MTR data acquired using four different pulse types but the same MT pulse amplitude (as calculated using the CWPE approximation for B_1). Theoretical (CWPE) MTR values are also shown for comparison.

Fundamental qMT parameters estimated for each of the four BSA samples scanned are plotted for each of the four pulse types used in the qMT acquisition in figure 5.7-5.9.

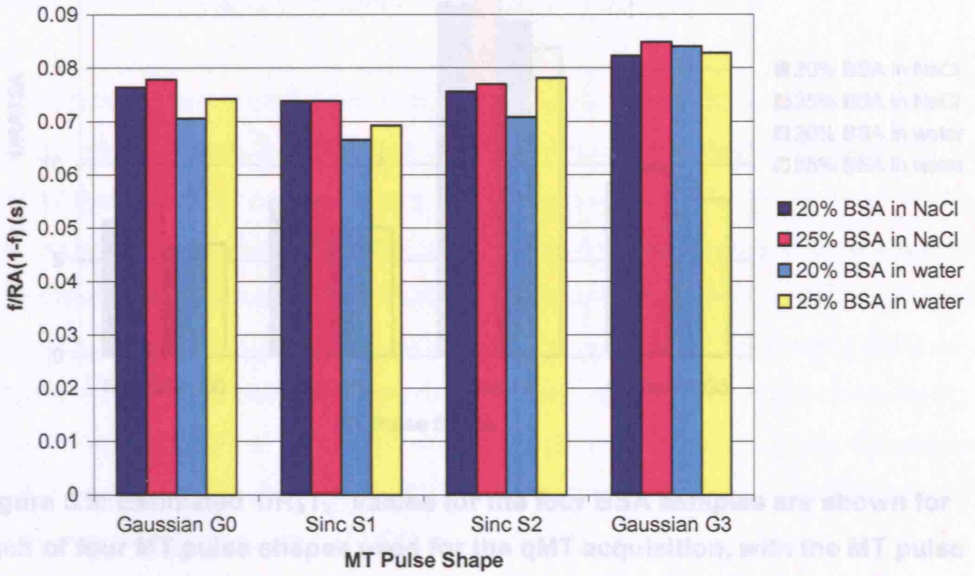

Figure 5.7: Estimated $f/R_A(1-f)$ values for the four BSA samples are shown for each of four MT pulse shapes used for the qMT acquisition, with the MT pulse amplitude (as calculated using the CWPE approximation for B_1) held constant.

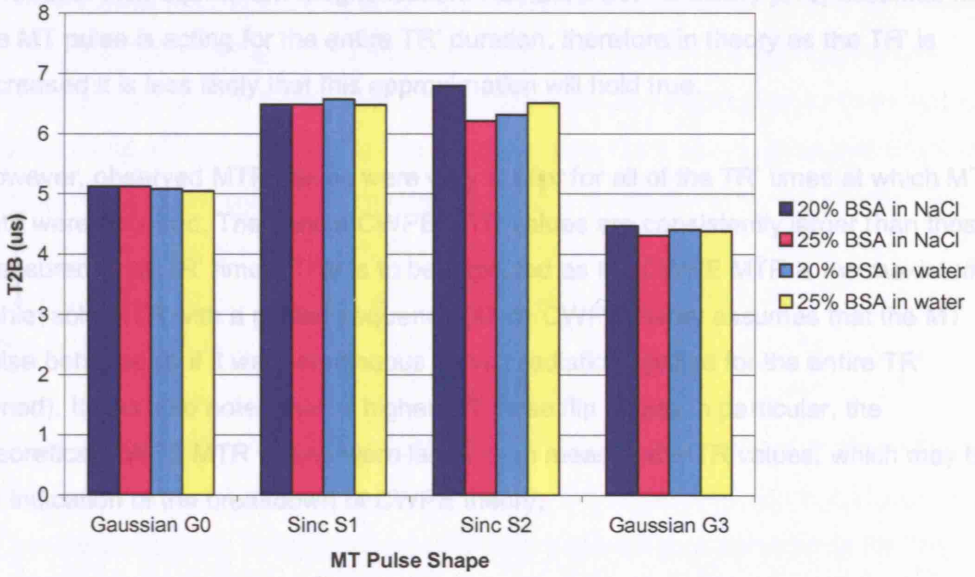

Figure 5.8: Estimated T_2^B values for the four BSA samples are shown for each of four MT pulse shapes used for the qMT acquisition, with the MT pulse amplitude (as calculated using the CWPE approximation for B_1) held constant.

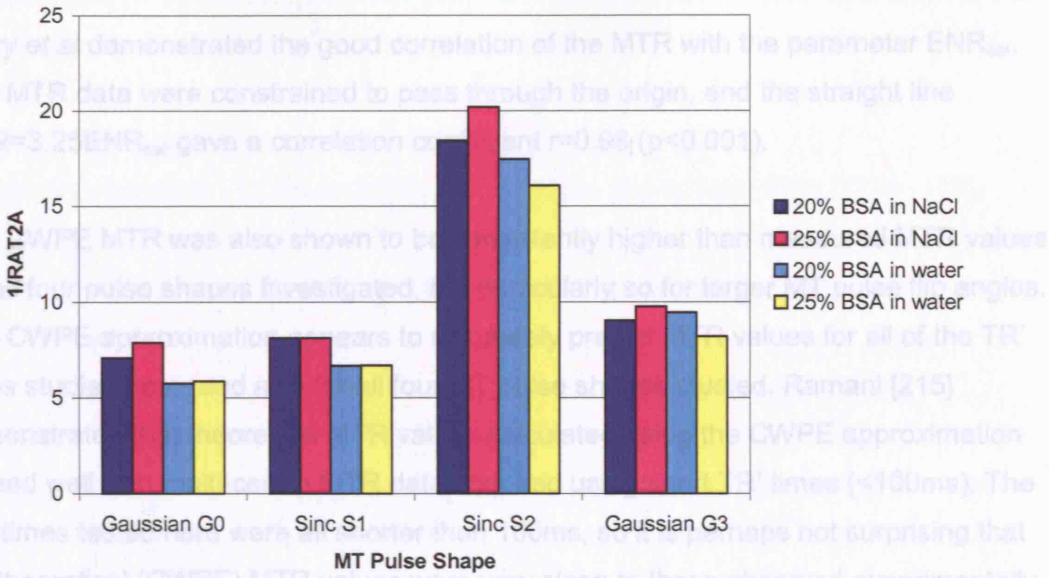

Figure 5.9: Estimated $1/R_A T_2^A$ values for the four BSA samples are shown for each of four MT pulse shapes used for the qMT acquisition, with the MT pulse amplitude (as calculated using the CWPE approximation for B_1) held constant.

Increasing the TR' (time between successive MT pulses) decreases τ_{sat}/TR' (the duty cycle). Therefore there is more time within the pulse sequence for the restricted spins to recover their equilibrium magnetisation. Ramani's CWPE theory [215] assumes that the MT pulse is acting for the entire TR' duration, therefore in theory as the TR' is increased it is less likely that this approximation will hold true.

However, observed MTR values were very similar for all of the TR' times at which MTR data were acquired. Theoretical CWPE MTR values are consistently larger than those measured at all TR' times. This is to be expected as the CWPE MTR is the maximum achievable MTR with a pulsed sequence (since CWPE theory assumes that the MT pulse behaves as if it were continuous wave irradiation applied for the entire TR' period). It was also noted that at higher MT pulse flip angles in particular, the theoretical CWPE MTR values were larger than measured MTR values, which may be an indication of the breakdown of CWPE theory.

The ENR_{sat} (given by equation 7.1) was devised by Berry *et al* [76] and can be thought of as a measure of how 'powerful' the MT pulse is. If the TR' remains constant, but the MT pulse flip angle is increased, the ENR_{sat} value of the MT pulse is increased, but if the TR' (time between successive MT pulses) is increased, the ENR_{sat} value of the MT pulse is decreased.

Berry *et al* demonstrated the good correlation of the MTR with the parameter ENR_{sat}. The MTR data were constrained to pass through the origin, and the straight line $MTR=3.25ENR_{sat}$ gave a correlation coefficient $r=0.98$ ($p<0.001$).

The CWPE MTR was also shown to be consistently higher than measured MTR values for all four pulse shapes investigated, but particularly so for larger MT pulse flip angles. The CWPE approximation appears to accurately predict MTR values for all of the TR' times studied here, and also for all four MT pulse shapes studied. Ramani [215] demonstrated that theoretical MTR values calculated using the CWPE approximation agreed well with multi-centre MTR data acquired using short TR' times (<100ms). The TR' times tested here were all shorter than 100ms, so it is perhaps not surprising that the theoretical (CWPE) MTR values were very close to those observed experimentally. Further investigations with different TR' times and pulse durations should be made in order to test the validity of the CWPE model for qMT.

The fundamental qMT parameters estimated using the four different pulse shapes were shown to be slightly more dependent on the particular pulse shape details used for acquisition than the MTR. In particular, the use of the sinc S2 pulse resulted in a much larger $1/R_AT_2^A$ value than the other 3 pulse shapes (see figure 5.9). The estimated $f/R_A(1-f)$ and f (data not shown) values were highest when estimated using the Gaussian G3 MT pulse, but did not vary widely between pulse shapes (see figure 5.7). T_2^B was lowest when measured using the Gaussian G3 pulse, higher with the Gaussian G3 pulse, and higher still when measured using the two sinc-shaped pulses (See figure 5.8). However, Tyler and Gowland [221] demonstrated the large variability of T_2^B in agar phantoms, and the fact that a large change in T_2^B may only result in a small change in M_0^B.

Since the MT pulse flip angles for each of the four pulses tested were altered in order to achieve the same B_{1CWPE} value in each experiment, it is perhaps surprising that the qMT parameter values obtained here vary with pulse shape, particularly for $1/R_AT_2^A$. However, there may be some coupling of the fundamental qMT parameters estimated here, which could explain this result. T_2^B also appeared to be altered depending on the pulse shape but has only a small effect on M_0^B (and hence f) estimates. However, T_2^B may have a larger effect on other parameters estimated from the fitting process. $1/R_AT_2^A$ can also be used to evaluate direct saturation effects on the free proton pool [47] (see equation 5.49), therefore the larger $1/R_AT_2^A$ value estimated from the fitting

process when the sinc S2 pulse was used for the MT pulses may be as a result of the amount of direct saturation of the free proton pool.

5.1.6.7 Other quantitative models for MT

Three- and four-pool models for MT have also been developed [193], [222], [198], [223], [224] but the complexity of the computation involved and also the amount of data required to constrain all the free parameters make these models impractical for use in clinical imaging.

5.2 Acquisition methods for quantitative MT imaging

Several groups have performed quantitative MT experiments to characterise some or all of the fundamental qMT parameters:

5.2.1 Restricted proton pool size M_0^B(relative to M_0^A)

Gochberg *et al* [225] applied on resonance inversion pulses with pulse separations much longer than the timescale of MT exchange from the free to the restricted pool ($1/k_f$) and pulse durations much shorter than the timescale of exchange. These pulses were applied in order to selectively invert the free pool magnetisation, whilst negligibly affecting the macromolecular protons. They performed numerical simulations and made some approximations to determine the effect of the RF pulse train on the immobile macromolecular proton pool. They used an EPI readout module, and performed a simplified 3-parameter fit to the acquired data to yield a measure of the fractional size (M_0^B/M_0^A) of the semi-solid pool. Experiments were performed on Bovine Serum Albumin (BSA) samples of varying concentration, and as expected, the fractional semi-solid pool size increased linearly with concentration. They assumed a Gaussian lineshape for the semi-solid pool, which may not be appropriate for BSA (see section 7.1.2) and this approach relies heavily on the accuracy of the numerical simulations performed. Despite this simplified approach and the fact that only one MT parameter is obtained using this method, the fractional macromolecular pool size is the fundamental qMT parameter thought to be of most interest biologically.

Lee and Dagher [226] used an off resonance pulsed technique, made the assumption that direct saturation of the free proton pool was low, and measured the MTR and estimated the amount of saturation of the free proton pool. A Lorentzian absorption lineshape was assumed for both pools. Together with a separate measurement of $T_1^A{}_{obs}$ they calculated the fraction of restricted protons relative to free protons using the relation:

$$\frac{M_0^B}{M_0^A} = \frac{MTR}{T_{1obs}^A R_{RFB}} \qquad 5.50$$

However, the approximations made here, and elimination of other fundamental parameters of the model may limit the usefulness of this method.

A technique was employed by Ropele *et al* [227] in which stimulated echoes were used to modulate the phase distribution in a spin ensemble. This 'labelled' spin ensemble is then used as an exogenous tracer, which is diluted due to the MT between the free protons and macromolecular protons. This 'dilution' was used to calculate maps of the restricted proton fraction in BSA and Gd-DTPA doped water phantoms. The pulse sequence compensates for longitudinal relaxation, and requires no T_1 or T_2 measurement and no prior knowledge of the restricted proton pool lineshape. The sequence has an intrinsically low SAR, and low sensitivity to B_1 errors, and was shown to give results for the pool size ratio f which were consistent with other published data [225], and also increased with BSA concentration, as expected.

The use of a stimulated echo is accompanied by an intrinsic loss of SNR, although this effect can be reduced with the use of larger voxels and signal averaging. The advantages of this approach are that that the free pool spins can be labelled exclusively, pool mapping can be achieved efficiently and at a low SAR, and no assumptions regarding the restricted pool lineshape or computationally intensive fitting are required. However, only one of the six possible free parameters can be estimated using this method, providing only a very limited view of the MT process.

In a recent study performed by Tyler & Gowland [221] a train of Gaussian-windowed, sinc-shaped 540° flip angle off resonance MT pulses were applied to agar gel samples (concentration 1-4% by weight) using a 0.5 T scanner, immediately followed by a spoiler gradient to destroy any transverse magnetisation, and an EPI readout module to study the transient approach to steady state. Non MT-weighted images were acquired between each application of the sequence to allow normalisation of the signal intensities (to correct for possible signal drift). M_0^B and T_2^B were quantified using the binary spin bath model, with a Gaussian lineshape to characterise the RF absorption of the semi-solid pool, which is probably accurate in the case of agar gels. Simulations were performed to determine the effects of various parameters on the model (the off resonance pulse chain length, time between pulses, longitudinal relaxation rates of the two pools ($R_{A,B}$), $T_2^A{}_{obs}$, and the MT exchange rate and relative pool sizes. It was determined that R_{Aobs} and $T_2^A{}_{obs}$ are required to describe the system fully, and changes in these parameters have a significant effect on the results output from the model, therefore these were measured independently and entered as constants into the

model. As was found in other studies, results were shown to be relatively insensitive to the exchange rate R of magnetisation between the two pools [47], [228], in the ranges observed for agar [221], and *in vivo* [62], and could therefore be fixed using values obtained from the literature. The results of these simulations also supported previous work [49] in suggesting that results of fitting the model to data are largely insensitive to the actual value of the parameter R_B, hence it is conventionally fixed at $1s^{-1}$. The total acquisition time was 45 minutes to collect the MT-weighted data and 13 minutes for the relaxation time measurements, which is rather long but clinically feasible. Five different pulse chain lengths were acquired, and the experiment was repeated at 6 different offset frequencies.

The binary spin bath model for qMT was assumed both during and after the application of MT pulses such that no assumptions were made regarding the final state of magnetisation, and numerical simulations of the Bloch equations were performed.

M_0^B was also re-fitted alone for different (fixed) values of T_2^B and it was shown that there was a reasonably large range of T_2^B values over which the same M_0^B values were obtained, which may explain the large variation in T_2^B values obtained in qMT experiments. They also showed that if the T_2^B value is known it is possible to fit for just M_0^B using MT data acquired at just a single offset frequency value. They also concluded that better results were likely to be obtained if a model incorporating an arbitrary lineshape was used.

5.2.2 Exchange rate k_f and T_{1sat}

Chai *et al* [229] measured the evolution of the longitudinal magnetisation of the mobile pool in the approach to steady state, using a train of binomial pulses of varying duration and duty cycle, but the acquisition took about 4 minutes per data point, which is clinically unacceptable.

Ropele *et al* [57] used a technique exploiting composite echoes (simultaneous acquisition of a spin echo and a phase-shifted stimulated echo) to measure the $T_1^A{}_{sat}$ from the phase shift of the stimulated echo and also the MTR in order to determine the rate constant k_f using equation 3.7. However, this technique assumes complete saturation of the semi-solid pool, a result not realistically achievable *in vivo*, and also takes no account of the direct saturation of the free pool.

Karampekios *et al* [230] used a 3D spoiled FLASH sequence with and without MT saturation pulses to make MTR measurements, and the T_1^A value in the presence of

MT saturation (i.e. $T_1^A{}_{sat}$) was calculated by fitting the signal intensity obtained from several FLASH imaging sequences acquired at different excitation pulse flip angles in the presence of MT saturation. On a pixel-by-pixel basis, using the measured MTR and $T_1^A{}_{sat}$ values, it was possible to determine k_f, the rate of exchange from the free to the restricted pool, using equation 3.7. The free pool T_1 in the absence of MT saturation (T_1^A) was also calculated using equation 3.5.

However, this approach relies on the assumption of complete saturation of the restricted pool and no direct saturation of the free pool, which not a valid assumption as data were acquired using an offset frequency of just 1.5kHz.

5.2.3 Characterisation of all qMT parameters

There are only a few published methods in which all the fundamental qMT parameters have been successfully estimated.

Sled and Pike [51], [208] applied off resonance saturation pulses, interleaved with on resonance excitation pulses, and acquired data at 60 combinations of MT pulse amplitude and offset frequency. T_1 was measured using a Look-Locker sequence, and T_2 using a 32-echo spin echo sequence. Corrections for B_0 and B_1 inhomogeneity were also made. Data were acquired using two different sequences with differing MT pulse durations (and TR' times) in order to allow better estimation of the cross-relaxation rate k_f, which is thought to depend heavily on pulse timing parameters.

It was found that the rectangular pulse approximation, by taking into account the duty cycle and pulsation frequency, offered extra freedom in designing experiments. They also found that including experimental data from two pulse sequences of different duty cycles improved estimates of k_f beyond that which could be expected from an equivalent increase in SNR.

However, acquisition times were long, and the computation complex. Also, only a single 7mm slice was acquired, although reducing the number of MT weighted data points acquired would allow extension to multi-slice acquisition.

Yarnykh [212] used off-resonance saturation pulses to perform a multi-slice study of MT in biological tissue. Eight 6mm slices were collected, using a 3D gradient echo sequence, taking 2.5 minutes per data point. Nine points were collected at various offset frequencies, but the same saturating amplitude. $T_1^A{}_{obs}$ was measured using a variable flip angle method.

The pulse sequence used by Ramani *et al* [47] at Queen Square involved the application of a Gaussian MT pulse immediately before each excitation pulse of a standard 2D spoiled gradient echo sequence. The excitation pulse flip angle was kept at the optimum value of 25°, to minimise the extent of T_1-weighting in the images (since T_1 is shortened in the presence of MT saturation), whilst sustaining a good SNR. The residual transverse magnetisation was assumed to have been removed by RF spoiling. 28 slices (5mm thick) are collected per acquisition (in a single TR). Quantitative MT data were acquired at ten different "MT weightings" (MT pulse amplitude and offset frequency combinations), then the CWPE qMT model (described in section 5.1.6.6) was fitted to the MT-weighted data to estimate the five fundamental qMT model parameters (RM_0^A, $f/R_A(1-f)$, T_2^B, $1/R_AT_2^A$ and gM_0^A). T_1 maps were also constructed (using the method of Parker *et al* [231]) for determination of R_A.

Yarnykh and Yuan [232] performed what they termed "cross-relaxation imaging" experiments to determine the restricted proton pool fraction f and the rate of cross-relaxation k_f *in vivo*. Sets of images at just four different MT-weighted data points were acquired using a 3D SPGR sequence, and in addition four spoiled gradient echo images at different excitation flip angles were acquired to generate T_1 maps of the whole brain. The total imaging time was less than thirty minutes, which is clinically acceptable. In order to reduce the problem to just two free parameters (f and k_f), the parameter T_2^B was fixed at an "average brain T_2^B value" of 11μs, which was selected on the basis of previous qMT studies [208], [212]. The authors considered this justifiable since T_2^B values have previously been shown not to vary considerably between normal and pathologic human brains [188], [212], [208], [47]. Using previous literature results, they also fixed the product $R_AT_2^A$ at a value of 0.055, and determined T_2^A from this ratio using the independently measured R_A value. However, the limitations of this approach are that the actual variation in a parameter that has been held fixed may then be manifest as variation in a different model parameter or combination of model parameters.

Cercignani *et al* [209] extended the approach of Ramani *et al* [47] to give 3D whole brain coverage, using a fast 3D SPGR sequence to acquire the 10 MT weighted data points. This enabled increased SNR compared with the 2D sequence (for the same resolution) and a reduction of partial volume errors and slice profile artefacts. The potential problems caused by the incidental MT effect in 2D acquisition methods due to excitation of slices adjacent to the slice currently being imaged would also be eliminated by using a 3D sequence. $T_1^A{}_{obs}$ was measured separately by acquiring three sets of SPGR sequence images with different excitation pulse flip angles, resulting in a

total imaging time of less than 20 minutes. MT pulse flip angles were also corrected for B_1 errors using a calibration oil-filled phantom, according to the method of Barker *et al* [233]. The qMT sequence was validated by scanning a post mortem brain slice and comparing data with data acquired using a 2D acquisition scheme. All estimated parameters were found to be within the range of expected values, from comparisons with 2D data sets and published data from other qMT studies.

5.3 Results of *in vivo* applications of qMT

Karampekios *et al* showed that several MS lesions exhibited the same MTR values and were also isointense on T_1-weighted images, but that k_f and T_1^A values differed both in NAWM and in lesions compared with control normal white matter. T_1^A correlated poorly with the MTR in all tissue types studied (normal white matter, NAWM, lesions), and in NAWM k_f measurements correlated poorly with MTR measurements, but correlated well in lesions. However, k_f correlated with T_1^A, but particularly well in severely hypointense lesions. It was concluded that these measurements are more specific than MTR measurements for characterising MS pathology. However, only a small patient group was studied, and Gadolinium-enhancing lesions were not studied, therefore further work would need to be performed in order to support this conclusion.

Fazekas *et al* [234] performed a study of MS patients using the method of Ropele *et al* [235], and demonstrated that the development of new active lesions was preceded by k_f reductions and increases in T_1^A, but found that the increase in k_f was the most pronounced pre-lesional change, and significant changes could be observed as much as four months prior to the appearance of a new lesion.

Ramani *et al* [47] performed qMT experiments both *in vivo* in MS patients and controls, and also *in vitro* on MS patient brains. Regions of interest were defined and the free proton pool model signal intensity was fitted to the quantitative MT data. Tozer *et al* [236] extended the approach to produce quantitative whole-brain parameter maps and histograms from qMT data. The restricted proton fraction map showed the brain structure well and lesions had a reduced f compared with NAWM.

Owing to a pulse sequence error [237], resulting in a systematic deviation of data from the model in the fitting process, it was found that using a Gaussian lineshape to model the semi-solid pool RF absorption gave better fits to *in vivo* data, although the super-Lorentzian lineshape still produced the best results in fitting the model to *in vitro* experimental data, where an increased number of data points were acquired. However, from re-analysis of some previously published clinical data [238], and also in a

subsequent study in a larger cohort of Multiple Sclerosis patients [48], it was observed that a super-Lorentzian lineshape produced much better fits of the quantitative model to data, in line with other work [51], [208].

Davies *et al* [238] demonstrated a small shortening of the T_2^B in MS lesions compared with NAWM, and attributed this change to gliosis, since it indicates that the remaining macromolecular proton fraction is in a more restricted environment. Again, f was reduced in MS lesions when compared with control WM and NAWM. Despite the fact that the data published in this study was affected by the error in the pulse sequence described above [237], the preliminary clinical conclusions drawn from the study remained unchanged. The restricted proton fraction f was shown to be sensitive to MS pathology, both in and distinct from lesions, and T_2^B was shown to be specific for lesion pathology.

Results from a later study of a larger cohort of MS patients supported these preliminary findings [48]. Mean normal frontal white matter parameter values were as follows: f=9.0pu (SD=0.7), T_2^B=10.6μs (SD=0.7). The mean restricted proton fraction f value was reduced from 9.0pu to 4.6pu, and the mean T_2^B value was elevated to 11.5μs in lesions. In NAWM, mean f was reduced to 8.0 pu, but f was not found to be abnormal in deep grey matter or middle cerebellar peduncles. Averaged over the entire cohort T_2^B was not significantly elevated in total NAWM, but in the secondary progressive subgroup T_2^B was elevated compared to controls in the total NAWM, occipital white matter, and the splenium of the corpus callosum. A greater correlation between f and MS disability (measured using the Multiple Sclerosis Functional Composite score (MSFC) [239]) than between T_1 and disability was also observed, demonstrating the clinical relevance of this parameter. The restricted proton fraction f was also shown to correlate with EDSS in the genu of the corpus callosum. The parameter f could be reduced by a decrease in the macromolecular content, either due to demyelination or axonal loss, or by an increase in the free proton component, for example by an increase in water content caused by oedema. The parameter T_2^B is a measure of the motional restriction of the protons in the semi-solid pool, which are assumed to be attached to macromolecules such as proteins or lipids in tissue. Therefore alterations in T_2^B are likely to reflect changes in the structure of the remaining macromolecular content of tissue, which could be caused by damage to myelin or axonal phospholipid bilayers. This parameter was sensitive to lesion pathology, but less sensitive to normal-appearing brain tissue (NABT). The demonstrated increases in T_2^B in lesions and the NAWM of SPMS patients, suggest that the remaining restricted protons attached to macromolecules are "less restricted".

In a pilot study in Alzheimer's Disease patients (performed using the qMT acquisition protocol of Ramani *et al* [47]), Ridha *et al* [240] demonstrated a reduction in the parameter $1/R_A T_2^A$ in the hippocampal formation, which was also shown to correlate with Mini-mental state examination (MMSE) scores. This reduction in $1/R_A T_2^A$ may be due to a lengthening of T_2^A due to membrane breakdown and increase in free water, or a decrease in T_1^A. However, other fundamental qMT parameters were unaffected by AD.

Sled and Pike [208] imaged two healthy volunteers and an MS patient using their qMT method and found the fractional pool size F (M_0^B/M_0^A) to be significantly reduced (from a mean value of approximately 0.16 in control frontal white matter to 0.11 in MS lesions (average from 2 lesions)) and T_2^r to be decreased (from a mean of 12.1μs in control frontal white matter to a mean of 10.6μs) in lesions. The exchange rate k_f from the free to the restricted pool was also decreased in lesions compared to control frontal white matter, and free proton pool relaxation times (T_1^f and T_2^f) were longer in lesions.

Yarnykh [212] acquired qMT data from two healthy subjects, two RRMS patients and one glioma patient at a field strength of 0.5T. Normal control parameter values were in agreement with the results of Sled and Pike [208], with the exception of small discrepancies caused by the cross-relaxation rate, which may be due to assumptions made regarding the direct effect on the free pool (see section 5.1.6.4), or differences in field strength between the two studies. Reductions in the range of restricted proton fraction f values (from 11.0-15.0pu in control white matter, to 2.5-6.5pu in MS lesions) and a shortening of T_2^B from approximately 8.5-10.5μs in white matter to 7.2-9.5μs in MS lesions were observed. The glioma patient also exhibited a reduced f, of approximately 4.0-6.0pu, and oedematous brain tissue in MS patients had a range of f values of 3.0-5.0pu.

Recently a study of the regional variation of qMT parameters in normal control brain tissue was performed [241]. No significant left-right differences were observed, but significant variation between grey and white matter regions was detected. Variations observed were consistent with the hypothesis that the parameters F and PD_r (proton density of the restricted pool) correlated with myelination in white matter. In particular, larger F and PD_r values were observed in the corpus callosum and forceps, which is thought to be due to the tight packing of highly myelinated fibres in those regions. Larger F values were also seen in the frontal lobe compared to the occipital lobe, which corresponds to the high density of myelinated motor fibres in the frontal lobe. The

changes in F also corresponded with changes in axon density. Results of principal components analysis (PCA) suggested a relationship between PD_f and R_{1f} in agreement with increased extracellular water and lengthening T_{1f}. An alternative explanation given by the authors for this regional variation was the alteration of regional rates of exchange between the two proton pools.

Levesque *et al* [242] investigated the nature of T_1 hypointensities observed in the brains of MS patients, using quantitative MT imaging. Histologic studies have demonstrated the association of myelin breakdown and axonal loss with these 'black holes' [170], but it is difficult to characterise such abnormalities in terms of the specific pathological process taking place in the lesion. Hypointensity on T_1 weighted images may reflect a combination of increased water content (despite an associated proton density increase), decreased macromolecular content, and changes in cross-relaxation between the two pools of spins, and these changes could be attributed to a combination of pathological processes, including demyelination, remyelination, inflammation, oedema, and axonal loss. If was found that there was a great range of variation of the parameter F within T_1 black holes, but that F correlated with the observed free pool T_1 ($T_1^A{}_{obs}$) in both T_1- and T_2-weighted lesions. The absolute PD, PD_r of the restricted pool was also highly variable in lesions, and showed a correlation with $T_1^A{}_{obs}$ in lesions abnormal on T_2-weighted scans without an associated T_1 abnormality, i.e. PD_r did not correlate with $T_1^A{}_{obs}$ in chronic lesions. This finding suggested that additional mechanisms such as relaxation may be occurring in this type of lesion. PD_f showed only small variations and it was suggested that increases in extracellular water could be compensated by decreases in intracellular water, which would result in only slightly altered PD_f values but also an increase in $T_2^A{}_{obs}$, although this could not be verified in this study. The MTR was found to correlate with $T_1^A{}_{obs}$, but larger sensitivity to the parameter F was observed. This suggests that the MTR reflects more closely the loss of macromolecular content in tissue than increases in the liquid component. Increases in $T_1^A{}_{obs}$ correlated with a drop in relative and absolute restricted pool sizes, presumably caused by demyelination and axonal damage, and to a lesser extent, with changes in the liquid component density (caused by oedema).

A recent study performed by Kiefer *et al* [243] examined differences in the sub-regions of the hippocampi of schizophrenic patients using quantitative MT imaging. It was shown that differentiation between the hippocampal sub-regions of schizophrenic patients was not possible using the semi-quantitative MTR measure, but significant differences in the parameters T_2^f, T_2^r and T_1 were observed between sub-regions, supporting the assumption that their structural diversity is the basis of the functional

heterogeneity of the hippocampal sub-regions [244]. It was also suggested that structural changes in the hippocampus of schizophrenics could only be detected if corrections for B_0 and B_1 errors are made, since they are very subtle.

Tozer *et al* [190] attempted to correlate the restricted proton fraction, obtained from quantitative MT imaging with the myelin water fraction f_m, obtained from multi-component T_2 analysis (also known as Transverse Magnetisation Decay Curves, or TMDC) in MS patients. Previous studies both in humans and animals [96], [245], [193], [46] have attempted to correlate the MTR with the myelin fraction obtained from TMDC. Gareau *et al* [96] found no correlation between the two measures, but Vavasour *et al* [245] found a significant correlation (r=0.5, P=0.005) in MS lesions but not in WM and GM. Gareau *et al* [96] attributed this finding to the sensitivity of the MTR to processes such as inflammation, as well as myelin content, and suggested that f_m is more specific for myelin, meaning that the two measures are related but still independent. This hypothesis was supported by results of studies performed by Stanisz *et* al [193] and Vavasour *et al* [46], which found that the MTRs of the long and short T_2 proton components differed. The myelin water fraction was defined here to be the fraction of the total signal (i.e. the fraction of the total water content) with a T_2 relaxation time of less than 50ms, observed using a multi-echo sequence and is thought to comprise water trapped between myelin bilayers. However, as stated above, it is not possible to directly observe spin environments with T_2 relaxation times in the ranges assumed for the restricted proton pool in qMT, which may partially explain the lack of correlation between f and f_m. A positive between-subject correlation of f_m and MTR was found in MS lesions and white matter in MS patients, presumably because both measures contain some information relating to myelin content. However a similar correlation was not observed in controls, possibly indicating the presence of other normal biological processes in addition to demyelination affecting one of the parameters at least. However, a negative between-subject correlation was observed in the grey matter of both MS patients and controls. It was suggested that the two quantities to some extent measure the same thing, but that due to other disease processes taking place in MS in addition to demyelination, such as inflammation, gliosis and axonal damage, the two parameters might provide complementary information.

Yarnykh and Yuan [246] performed a two-parameter fit (by fixing the parameters T_2^B and $1/R_A T_2^A$) to yield whole-brain parameter maps for the restricted proton fraction f and cross relaxation rate k_f. These maps showed detailed brain anatomy, with f elevated in white matter regions compared to grey matter, and k_f maps similar to R_1 maps, but with sharper grey-white matter contrast. In particular, f maps provided

identification of white matter fibre tracts confirmed by comparison to diffusion tensor images and these have not been shown to be visible on f maps in any previous qMT study. The f values obtained were consistent with previous studies [208], [212]. However, k_f values were approximately 30% smaller than those obtained by Sled and Pike [208], and the work of Ramani *et al* [47] yielded a very large k_f value independent of brain tissue type and concluded that this parameter is of little diagnostic value (although the model signal equation was parameterised slightly different in that study). It was postulated that perhaps k_f measurements are more sensitive to pulse sequence timings since k_f determines the rate of equilibration of the two pools, and this may explain the failure to reliably extract it from the steady state qMT model.

In the study performed by Cercignani *et al* [209], a post mortem brain slice was scanned using both the 2D acquisition method used by Ramani *et al* [47] and the new 3D sequence, with the same Gaussian MT pulse parameters, and similar MT pulse flip angles and offset frequencies, although the sequences were not exactly matched. It was found that all parameter estimates from the 2D acquisitions approached those estimated using the 3D acquisition when the number of averages (i.e. the SNR) was increased.

Six healthy volunteers were also scanned using this protocol and average estimated parameter values were within the ranges expected from comparison with previous published qMT data. A strong inverse correlation was demonstrated between T_1^A and f, and also between T_2^A and f. T_1^A and T_2^A were also shown to be correlated, although more strongly in grey matter than white matter. Both f and T_2^B average values were consistent with the literature [241], although T_2^B was found to vary widely in white matter, which was attributed to different fibre structures within the white matter. RM_0^A was found to vary widely, although it didn't affect the estimates of other model parameters substantially, as has also been found in a previous study [47]. This was attributed to the quantitative model being unable to accurately take account of pulse sequence timings, as argued by Yarnykh and Yuan [247].

5.4 Future investigations in qMT: Extensions to the Ramani model

The selection of data points (combinations of MT pulse power and offset frequency) should be optimised to minimise uncertainties in fitted parameters of the qMT model. Then either the noise in the calculated parameter maps could be reduced by collecting the optimum set of data points, or less data could be acquired without increasing the noise in images, resulting in a reduction in scanning time.

A thorough investigation of the validity of the CWPE qMT model is required. This could be achieved by increasing the MT pulse duration (whilst the amplitude is decreased in order to maintain the same B_{1CWPE} value for each MT pulse) and/or shortening the TR', and observing the effects on the fitted parameters and the quality of the fit of the qMT model to measured data. The idea behind this approach is to approximate more closely a continuous wave experiment, by increasing the duty cycle (τ_{sat}/TR'), in the hope that the fit of the CWPE model signal values to experimental data would improve.

The theoretical modelling of the qMT technique could be improved. A low excitation pulse flip angle (25° in the current protocol) is usually used in order to minimise T_1 weighting, as T_1 shortening occurs in the presence of MT saturation. However, the use of a low imaging pulse flip angle also results in low SNR images. T_1 weighting could be accounted for in the qMT model, in order that a higher flip angle could be used, which would improve the SNR. The mathematical modelling of the imaging pulse as well as the excitation (MT) pulse should also be investigated as a potential method of improving the accuracy of the model.

6 Magnetisation Transfer Ratio (MTR): A correction for B_1 transmit field inhomogeneities and errors

Introduction

B_1 errors are a problem in MTR measurements, since the measured MTR value is dependent on the amplitude of the MT pulse. B_1 errors can arise from RF non-uniformity (caused by the RF coil, or skin effect and dielectric resonance in the subject's head), and also from inaccurate setting of the transmitter output when compensating for varying amounts of loading of the RF coil. B_1 errors may be as large as 5-10%, and since the MTR is proportional to B_1^2 (see equations 5.42-5.44, 5.48), it may be expected that a 1% error in B_1 would be compounded to give an error of 2% in an MTR measurement. Hence MTR errors may be up to 10-20% in magnitude, and in addition RF non-uniformity may also cause MTR histograms to be broadened.

The MTR depends on a combination of sequence and tissue parameters [76], including the fraction of restricted spins in the tissue (denoted f, where $f=M_0^B/(M_0^A+M_0^B)$; see also section 5.1.6.6). The MTR has been shown to be reduced in many pathological processes, including demyelination [66]. This is because the relative sizes of the two proton pools are altered in many such pathologies, in particular the fraction of restricted protons (f) is often reduced, which may be a result of a reduction in the restricted proton pool size or an increase in the water content of the tissue.

Despite the 'semi-quantitative' nature of MTR measurements and the strong dependence of the measured MTR on sequence acquisition parameters, the MTR has been shown to be highly reproducible and reliable for a particular sequence in an individual centre [76], [55], [77]. Given the good reproducibility of the MTR for a particular sequence, very small changes in the MTR (<1pu) can be relied upon to indicate alterations in tissue structure. There is a wealth of evidence in the literature to show that there are MTR changes of this size, attributable to changes in disease pathology, particularly in MS, some examples of which are given in chapters 3 and 4. There is a very high premium on the ability to undertake multi-centre and serial studies; B_1 errors are a major source of variation in this context and hence there is a great interest in reducing or accounting for such errors.

Volumetric MTR histogram analyses are sensitive to the presence of diffuse abnormalities, which have been observed in the so-called normal-appearing white matter (NAWM) of Multiple Sclerosis (MS) patients, both at post mortem, and *in vivo*

[101], and even preceding the formation of MS lesions by up to two years [110]. In healthy controls, brain tissue MTR histograms are typically characterised by a single sharp peak, suggesting that normal brains are relatively homogeneous with respect to MTR characteristics [248]. In other words, mean white and grey matter MTR values are not distinct enough to result in bimodal histograms (two separate peaks). Several parameters can be derived from MTR histograms, including the peak height, peak location and percentile measures. These measures have also been shown to be highly reproducible and not observer-dependent within a single centre [249], therefore a correction for B_1 errors would be clinically useful in this context. B_1 errors are thought to be the major source of inter-centre discrepancies in MTR measurements, if sequence and pulse-dependent effects have been accounted for [76], [250].

The effect of B_1 errors on MTR measurements was investigated, both theoretically and experimentally, and a method for correcting for B_1 errors was proposed, based on the collection of a B_1 map in addition to MTR data.

The 'Continuous Wave Power-Equivalent' value of B_1 was used (B_{1CWPE}) [47], [215] (see equations 5.42-5.44) to model the effect of the (Gaussian-shaped) MT RF pulses. This is the root mean square (rms) value of the saturating field, averaged over the time between successive MT pulses TR' (which is equal to TR/number of slices in a 2D multi-slice acquisition). The continuous wave approximation for B_1 has been shown to consistently over-estimate measured MTR values since it gives the theoretical maximum achievable MT contrast for a pulsed sequence [215]. However, CWPE theory has been shown to adequately model MT behaviour at large duty cycles [215], in particular if the time between successive MT pulses, TR', is short [215]. In reference [215], a comparison of CWPE theory to multicentre MTR data, it was shown that for MTR sequences with TR'<100ms, CWPE theory gave a good prediction of measured MTR values.

The dependence of MTR on B_1 was modelled, and normalised graphs produced. For B_1 reductions up to 20%, normalised plots for different brain tissue types could be approximated by a single line, indicating that a systematic correction could be applied to MTR measurements with a known B_1 error, regardless of tissue type [251], [252]. On the scanner, B_1 was reduced from its nominal value and the MTR was measured to experimentally determine a correction scheme for B_1 field variations. B_1 field mapping was performed using the Double Angle Method [253] and used to quantify B_1 errors and correct MTR maps and histograms. This work has previously been presented in abstract form [251] and subsequently in Magnetic Resonance Imaging [252].

6.1 B_1 errors, their causes, and their effect on the Magnetisation Transfer Ratio (MTR)

Since the MT effect is produced by partially saturating the restricted protons, errors in the MT RF pulse amplitude directly propagate to errors in the measured MTR. B_1 errors may arise from two sources. Firstly, RF non-uniformity [233] can arise from three effects. These are: a) intrinsic non-uniformity of the transmitter coil, resulting in spins not being equally excited, causing a change in the magnitude of the transverse magnetisation, and therefore signal intensity, b) the skin depth, or RF penetration effect, which attenuates the RF field inside an electrically conducting object resulting in a sample-dependent RF field distortion, and c) dielectric resonance [254] which causes standing waves, thus increasing the RF field inside an object, particularly one containing water (because of its high dielectric constant). This latter problem is more pronounced in phantoms, as electrical conductivity in the brain tissues damps the resonance. Secondly, the pre-scan procedure to adjust the transmitter amplitude for each subject may be imprecise, giving some B_1 error even in the absence of non-uniformity. The effects of B_1 non-uniformity errors may be very important for whole-brain MTR histograms (volumetric analysis), since head coil non-uniformity is often more pronounced in the z-direction (i.e. along B_0).

6.2 Mathematical Modelling of the MTR dependence on B_1

6.2.1 Methods

The binary spin bath model (BSBM) for quantitative MT (qMT) [49] was used to model the dependence of pulsed MTR measurements. Ramani's continuous wave approximation for B_1 (see section 5.1.6.6) [47] was used to model the MTR, given by equation 5.48, (as measured using the Euro-MT sequence [63], [255]) for different brain tissue types (white and grey matter regions) in control subjects and corresponding brain tissue regions in MS patients as well as MS lesions (see table 6.1) for the Euro-MT sequence.

Ramani *et al* demonstrated the small discrepancy between MTR values modelled using CWPE theory (see equations. 5.41-5.47) and those measured in a multi-centre study for MTR measurements made at short TR' (time between successive MT pulses) [215]. This is because the restricted spins cannot significantly recover their magnetisation between successive MT pulses if the TR' (time between MT pulses) is short, and therefore the two-pool system behaves as if it is subjected to continuous wave (CW) RF irradiation. Since the duty cycle of the Euro-MT sequence is high (τ_{sat}/TR'=0.224) and the TR' is short (TR'=34.3ms), CWPE theory was deemed acceptable in this case. A super-Lorentzian RF absorption lineshape was assumed for the restricted proton

pool, as this lineshape has previously been shown to accurately model the behaviour of the restricted pool *in vivo* [188], [208] (although Ramani's study comparing CWPE theory with multi-centre MTR data assumed a Gaussian restricted pool lineshape; see also section 6.7). The tissue parameters required by the model were obtained from previous experimental work [48] and are given in table 6.1.

Table 6.1: Brain tissue qMT parameters used for the CWPE qMT modelling of MTR dependence on B_{1CWPE} Control white (WM) and grey matter (GM) and MS patient normal-appearing white (NAWM) and grey matter (NAGM) and WM lesion $f/R_A(1-f)$, T_2^B and $1/R_AT_2^A$ values are given, with 95% confidence limits (CL) on each estimated parameter in brackets [48].

	Fundamental qMT model parameter		
Brain tissue type	**$f/R_A(1-f)$ (s^{-1})**	**T_2^B (μs)**	**$1/R_AT_2^A$**
Control WM (frontal)	0.063 (±0.015)	10.5 (±3.2)	18.6 (±15.3)
Control WM (centrum semiovale)	0.062 (±0.009)	10.5 (±12.9)	17.0 (±8.7)
Control GM (cerebellar)	0.063 (±0.012)	10.2 (±2.8)	19.1 (±13.0)
Control GM (cortical)	0.057 (±0.013)	10.9 (±3.1)	22.6 (±14.1)
MS patient NAWM (frontal)	0.060 (±0.011)	10.6 (±2.5)	20.5 (±13.8)
MS patient NAWM (centrum semiovale)	0.059 (±0.098)	10.6 (±19.1)	18.2 (±8.8)
MS patient NAGM (cerebellar)	0.062 (±0.010)	10.3 (±2.6)	19.9 (±12.6)
MS patient NAGM (cortical)	0.054 (±0.011)	11.3 (±2.4)	23.8 (±14.7)
MS patient lesion (WM)	0.044 (±0.010)	11.5 (±2.2)	16.7 (±5.0)

[1]

[1]This table gives three of the six parameter values that can be uniquely determined in the qMT experiment, for different control and MS patient brain tissue types; T_2^B, determined via the RF absorption rate of the restricted pool, the restricted proton fraction f, and $1/R_AT_2^A$. R_B, the restricted pool longitudinal relaxation rate (i.e. $1/T_1^B$) has been held fixed at a value of $1s^{-1}$ here, in line with previous qMT experiments [49], [208]. The parameter RM_0^A remained constant at $2000s^{-1}$ (also taken from previous experimental work [48]); it appears to have little diagnostic significance. The RM_0^A value used here differs from those published by other groups (denoted k_r in some other studies), but matches other work performed by Ramani *et al* at the Institute of Neurology [47]. These discrepancies are likely to be due to differences in parameterisation of the model between different groups and the particular value of RM_0^A chosen does not affect the values of the other fitted model parameters or the results of the mathematical modelling of the MTR dependence on B_1. The parameter gM_0^A is a scaling factor dependent on the proton density, RF amplifier gain and other scanner characteristics, but does not affect MTR values and is therefore not given here.

6.2.2 Results

There is a non-linear dependence of the MTR on B_{1CWPE}. At a given B_{1CWPE}, variation is observed between different brain tissue types (see figure 6.1). The largest differences observed were between control frontal white matter and MS lesion tissue, suggesting that the MTR depends most heavily on the restricted proton fraction f (which is likely to be reduced in lesions, due to demyelination), as expected.

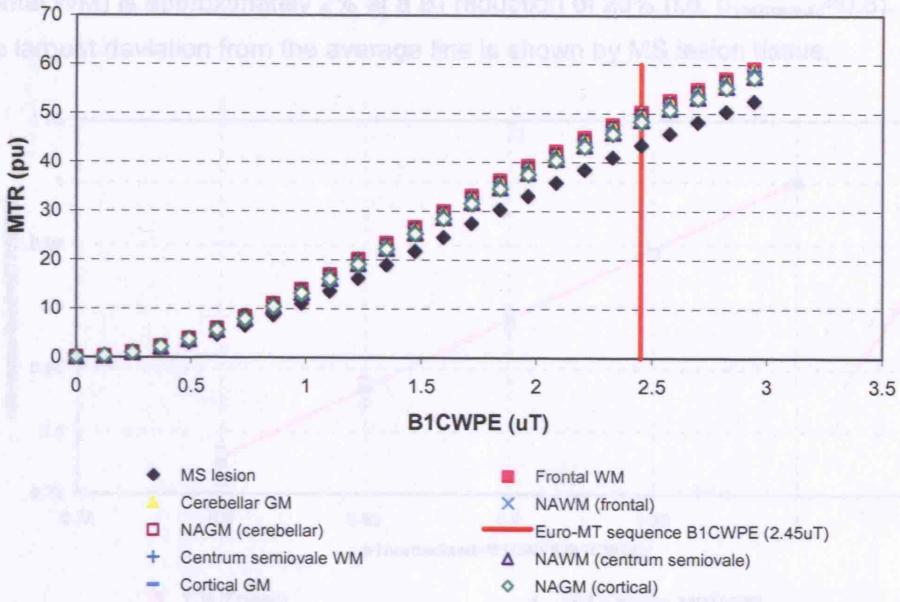

Figure 6.1: Plot showing modelling of the MTR dependence on B_1 for different brain tissue types using Ramani's CWPE approximation based on Henkelman's qMT model [49] (and previous experimental data (see table 6.1)) for the Euro-MT sequence (nominal MT pulse flip angle α=500°, offset frequency=1500Hz (see MR Imaging methods section (6.4) for other sequence parameters)).

A set of theoretical normalised graphs was then plotted (figure 6.2), using the variables $b_{1normalised}$, the B_{1CWPE} normalised to B_{1CWPE0}, which is the nominal B_{1CWPE} for the Euro-MT sequence [63] (i.e. $b_{1normalised}=B_{1CWPE}/B_{1CWPE0}$), and $mtr_{normalised}$, the MTR normalised to MTR_0, the MTR at B_{1CWPE0} (i.e. $mtr_{normalised}=MTR/MTR_0$), the motivation being that for a given sequence a simple relationship between $mtr_{normalised}$ and $b_{1normalised}$ may exist. In other words, each B_{1CWPE} value was divided by B_{1CWPE0} (the B_{1CWPE} value for an MT pulse flip angle of 500°, the nominal FA value for the Euro-MT pulse sequence), and each MTR value was divided by the theoretical MTR value estimated at B_{1CWPE0} for that particular tissue.

It was shown that, for B_1 reductions of up to approximately 20%, the theoretical normalised graphs could be approximated to a straight line for all brain tissue types

(see figure 6.2). This indicated that it would be theoretically possible to apply a simple linear correction to MTR data with a known B_1 error, regardless of tissue type. The linear equation describing the dependence of $mtr_{normalised}$ on $b_{1normalised}$ averaged over all brain tissue types, in the range $b_{1normalised}$=0.8-1.0, was found to be:

$$mtr_{normalised}^{theory} = 1.114b_{1normalised} - 0.112 \qquad 6.1$$

The maximum $mtr_{normalised}$ difference between two brain tissue types (MS lesion and frontal WM) is approximately 2% at a B_1 reduction of 20% (i.e. $b_{1normalised}$=0.8). Again the largest deviation from the average line is shown by MS lesion tissue.

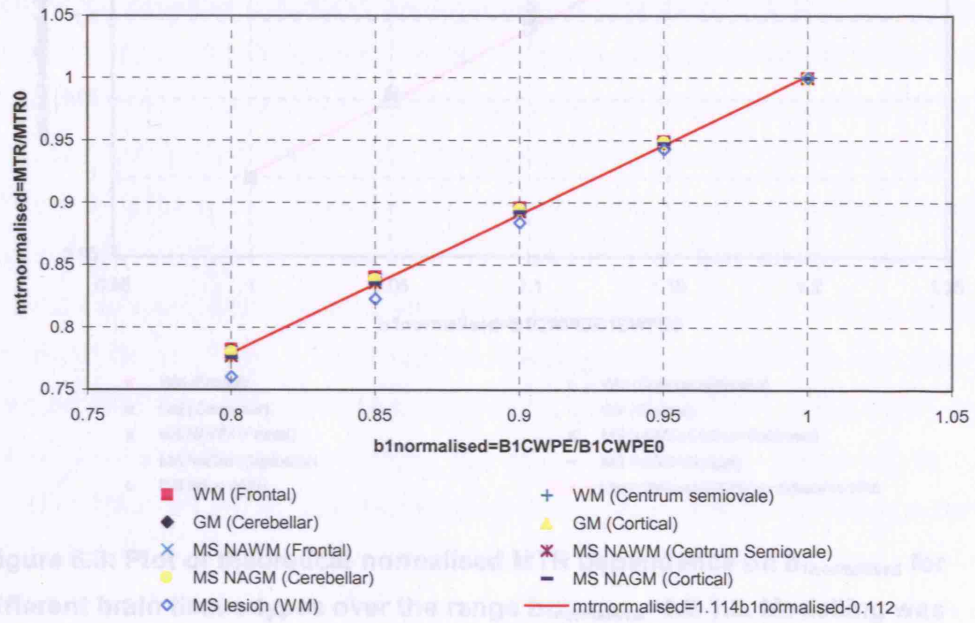

Figure 6.2: Plot of theoretical normalised MTR dependence on $b_{1normalised}$ for different brain tissue types over the range $b_{1normalised}$=0.8-1.0. Modelling was performed using the CWPE qMT model and previous experimental data for brain tissue parameters (see table 6.1) for the Euro-MT sequence (nominal MT pulse flip angle α=500°, offset frequency=1500Hz (see section 6.4 for other sequence parameters)).

It can be seen from figure 6.2 that the large MTR dependence on tissue type has mostly been removed by the normalisation process.

The theoretical dependence of $mtr_{normalised}$ on $b_{1normalised}$>1 was also examined, since B_1 increases in some areas of the brain may also be observed, particularly at higher field strengths, where B_1 field inhomogeneities may be greater. The results are shown in figure 6.3. It can be observed that the direction of spread of different tissue types away from the average line is reversed. Again, the largest deviation is observed for MS

lesion data. The resulting linear equation for the dependence of $mtr_{normalised}$ on $b_{1normalised}$ averaged over all brain tissue types was found to be:

$$mtr_{normalised}^{theory} = 0.923b_{1normalised} - 0.0796 \qquad 6.2$$

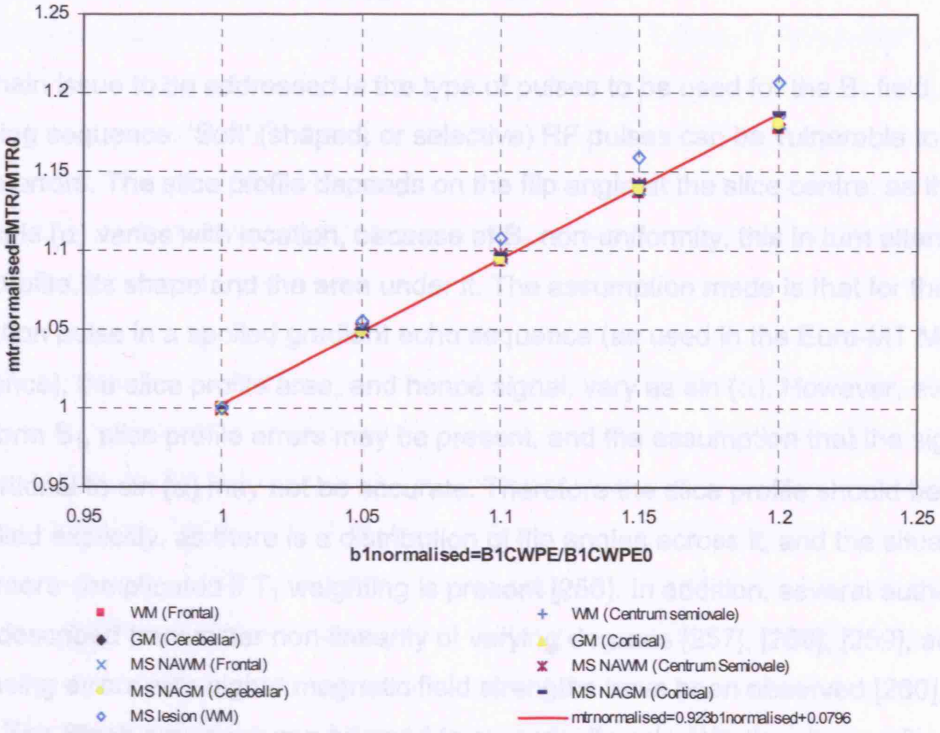

Figure 6.3: Plot of theoretical normalised MTR dependence on $b_{1normalised}$ for different brain tissue types over the range $b_{1normalised}$=1.0-1.2. Modelling was performed using the CWPE qMT model and previous experimental data for brain tissue parameters (see table 6.1) for the Euro-MT sequence (nominal MT pulse flip angle α=500°, offset frequency=1500Hz (see section 6.4 for other sequence parameters)).

For $b_{1normalised}$>1 the slope is <1 (figure 6.3), whereas for $b_{1normalised}$<1, the slope is >1 (figure 6.2). This can be understood as follows. At high $b_{1normalised}$, $mtr_{normalised}$ must level off to a plateau, as the restricted pool approaches maximal saturation; thus the slope decreases as $b_{1normalised}$ increases.

6.3 B_1 field mapping: Methods and Issues

B_1 field mapping could facilitate systematic correction for B_1 errors in quantitative MR measurements such as the MTR, as indicated by the results of the theoretical modelling given in section 6.2. However, there are various issues associated with the implementation of B_1 field mapping in a clinically reasonable time. In addition, such a

method relies on accurate knowledge of the dependence of the MTR on B_1. There is a complex relationship between MTR and B_1 [76], and the MTR is highly dependent on the particular MTR sequence acquisition parameters, and on tissue type, therefore this type of correction scheme could be problematic.

The main issue to be addressed is the type of pulses to be used for the B_1 field mapping sequence. 'Soft' (shaped, or selective) RF pulses can be vulnerable to slice profile errors. The slice profile depends on the flip angle at the slice centre; as the local flip angle (α) varies with location, because of B_1 non-uniformity, this in turn alters the slice profile, its shape and the area under it. The assumption made is that for the excitation pulse in a spoiled gradient echo sequence (as used in the Euro-MT MTR sequence), the slice profile area, and hence signal, vary as sin (α). However, even with a uniform B_1, slice profile errors may be present, and the assumption that the signal is proportional to sin (α) may not be accurate. Therefore the slice profile should be modelled explicitly, as there is a distribution of flip angles across it, and the situation is even more complicated if T_1 weighting is present [256]. In addition, several authors have described transmitter non-linearity of varying degrees [257], [258], [259], and increasing errors with higher magnetic field strengths have been observed [260], [261], [262]. The Bloch equations can be used to numerically calculate the slice profile resulting from a given pulse, of known amplitude and applied in the presence of known field gradients [263], [231]. Firstly the magnetization evolution with time is calculated at many positions within the slice using a Bloch simulator, giving the magnetization vector as a function of position within the slice (values of M_x^s, M_y^s and M_z^s). Then the flip angle $\theta(z)$ at each position in the slice (z) can be calculated (given by $\theta(z)=\tan^{-1}(((M_x^s(z)^2+M_y^s(z)^2)/M_z^s(z)^2)^{1/2})$), and the phase $\Phi(z)$ (direction of the transverse magnetization in the xy plane; $\Phi(z)=\tan^{-1}(M_y^s(z)/M_x^s z)$), i.e. $\Phi=0$ corresponds to the x-axis). These can then be used to calculate the local transverse magnetization (M_x and M_y) taking into account relaxation. Then, via integration over the slice profile, the magnitude signal from the whole slice can be calculated, but with the unknown constants representing the equilibrium magnetization (M_0) and the local gain (signal per unit magnetization and volume) remaining in the expression. The effective slice thickness (ratio of total signal to the signal per unit slab thickness at the slice centre) can be determined and therefore also the variation in slice sensitivity over space.

For the reasons described above, ideally a 'hard' (non-selective) rectangular pulse should be used for the magnetisation preparation stage of the B_1 mapping sequence, but this may make readout difficult, since it gives a large signal from the whole sample, not just from the particular slice of interest. Also, hard pulses may be difficult to

implement as part of an existing sequence, therefore if an existing sequence is to be used, it may be most convenient to use selective pulses.

6.3.1 Double Angle Method (DAM)

The European Magnetic Resonance Network in Multiple Sclerosis (MAGNIMS) group combined B_1/MT project, which was the initial motivation for this study, aimed to account for B_1 errors in MTR measurements and to reduce MTR histogram dispersion using B_1 field mapping [264]. The proposed B_1 field mapping sequence for the study was the Double Angle Method (DAM), which was initially developed by Stollberger *et al* [253] for a spin echo sequence.

In order to minimise acquisition time, a Fast Spin Echo (FSE) sequence was used for B_1 mapping in place of a conventional spin echo sequence in this study. The FSE sequence was performed twice, with the excitation stage of the sequence altered. In the first acquisition the nominal flip angle of the first pulse in the sequence was altered from 90° to α (here α=60°) and in the second acquisition the first flip angle was altered to 2α (i.e. 120° here). The second pulse in the sequence (used for repeated refocusing) remained unchanged (i.e. the two separate acquisitions using the FSE sequence were modified from 90°-180° to be $\alpha - \beta$ for the first acquisition and $2\alpha - \beta$ for the second acquisition, where nominal $\beta \approx 180°$). This approach eliminates any error resulting from the use of selective pulses for the second (readout) pulse, since it is the same in each acquisition; however poor slice profile in the first (α) pulse could result in some error. Sequence acquisition parameters for the FSE sequence are detailed in section 6.4.

Stollberger and Wach showed that the specific (sinc-shaped) amplitude-modulated slice selective pulses used in their study only deviated significantly from the relationship $\alpha = \gamma B_1 \int_{-\tau_{sat}/2}^{\tau_{sat}/2} f(t)dt$ (where τ_{sat}=pulse duration, f(t)=pulse shape) at flip angles α>140° [265]. However, these deviations depend strongly on the RF pulse shape, i.e. the use of a Gaussian pulse would result in greater deviations from this relationship.

The effective flip angle distribution (and therefore the effective B_1) could then be calculated using the signal intensities from the first and second acquisitions. The signal intensity I in each FSE acquisition as a function of position **r** is given by:

$$I(\mathbf{r}) = k\rho(\mathbf{r})S(\mathbf{r})\sin(\alpha(\mathbf{r}))\sin^2\left(\frac{\beta(\mathbf{r})}{2}\right)R_1(\alpha(\mathbf{r}),\beta(\mathbf{r}),TR,TE,T_1(\mathbf{r}))\exp\left(\frac{-TE}{T_1(\mathbf{r})}\right) \qquad 6.3$$

where $\alpha(\mathbf{r})$ is the excitation flip angle, $\beta(\mathbf{r})$ is the flip angle of the refocusing pulse (i.e. $\beta \approx 180°$), $\rho(\mathbf{r})$ is the spin density, k is a system constant, $S(\mathbf{r})$ is the coil receive sensitivity, and $R_1(\alpha_1(\mathbf{r}),\beta(\mathbf{r}),TR,TE,T_1(\mathbf{r}))$ is a term describing the longitudinal relaxation of the system.

The effective flip angle distribution (and therefore the effective B_1) can therefore be calculated using the ratio of the signal intensities resulting from the first and second acquisitions. Provided that the TR of the sequence is sufficient for complete longitudinal relaxation of all tissue types within the region to be imaged, longitudinal relaxation terms in the signal equation are unity, and transverse relaxation terms for the two acquisitions cancel out. The ratio of signals then depends only on the flip angles α_1 and α_2 of the first and second acquisitions respectively (the transverse magnetisation after the first pulse depends on sin α).

If the additional condition that $\alpha_2(\mathbf{r})=2\alpha_1(\mathbf{r})$ is then imposed, then using the expression:

$$\frac{I_2}{I_1} = \frac{\sin(2\alpha_1)}{\sin(\alpha_1)} = 2\cos(\alpha_1) \qquad 6.4$$

where I_1 and I_2 are the signal intensities resulting from the first and second acquisitions respectively, the effective flip angle α_1 (as a function of position $\mathbf{r}$) can be calculated using the simple relation:

$$\alpha_1(\mathbf{r}) = \cos^{-1}\left(\frac{I_2(\mathbf{r})}{2I_1(\mathbf{r})}\right) \qquad 6.5$$

This is only an approximation for slice selective pulses, but, as stated above, from numerical simulations it has been shown that for flip angles<140° and non-Gaussian pulses (which result in poorer ('less rectangular') slice profiles than sinc-shaped pulses), no serious errors should arise [266].

The T_1 in CSF is very long (approximately 4s [39]); thus to achieve complete longitudinal relaxation in CSF regions would require a very long TR (for approximately 99% recovery, $TR=5T_1$ is required, i.e. ~20s here), and hence acquisition time. In fact the maximum TR limit on the 1.5T GE Signa scanner for the FSE sequence used at our centre (15s) is not long enough to allow complete CSF relaxation. This led to errors in B_1 maps acquired using this technique and partial volume errors in the regions around the CSF.

The WM and GM regions of the brain are of most interest in neurological research, and MTR measurements in the CSF regions are not necessarily required. Thus the TR of the B_1 field mapping sequence could be reduced such that complete longitudinal

recovery takes place in the WM and GM, but not in the CSF, in order to reduce scanning time. It may then be possible to apply a simple correction for incomplete longitudinal recovery to the signal intensity calculated for the CSF, using knowledge of the signal intensity dependence on T_1. An alternative solution would be to completely eliminate the signal from CSF (and this approach would also allow a much shorter TR to be used), since in general this information is not of interest. Both of these possible solutions to the problem of CSF relaxation are discussed below.

6.3.2 Incomplete longitudinal relaxation in the CSF

The signal intensity for a gradient echo or spin echo sequence (assuming that the flip angle of the first pulse in the spin echo sequence is not 90° [40], that complete longitudinal relaxation has not yet taken place, and that either there are no errors in the second (180°) pulse or that a CPMG sequence is used to remove the effects of such errors) is given by (see also section 2.10.2):

$$\text{signal} = \frac{C\sin(\alpha)e^{-TE/T_2}(1-e^{-TR/T_1})}{1-\cos(\alpha)e^{-TR/T_1}} \qquad 6.6$$

where α is the flip angle of the excitation pulse and C is a factor depending on the intrinsic proton density (PD) of the object/subject being imaged and scanner receiver gain. The term $e^{-TE/T2}$ takes account of the attenuation of signal due to T_2 relaxation during the pulse delay TE. It should be noted, however, that this signal attenuation would result from T_2^* effects (rather than T_2) for a gradient echo sequence, as the effects of B_0 field inhomogeneities cannot be removed using a gradient echo sequence. B_1 errors may also be present in the second pulse of a spin echo sequence, but these could be removed through the use of a CPMG sequence (see section 2.5). The sequence acquisition details used in this study are given in section 6.4.

The signal intensity for completely (longitudinally) relaxed tissue is given by:

$$\text{fully relaxed signal} = C\sin(\alpha)e^{-TE/T_2} \qquad 6.7$$

Therefore, the fractional signal loss in a single image caused by incomplete T_1 recovery in a particular tissue region (which would result in the assumptions of the DAM being violated and lead to errors in measured B_1 maps) is given by:

$$\text{fractional signal loss} = C\sin(\alpha)e^{-TE/T_2}\left(\frac{\left(\frac{1-e^{-TR/T_1}}{1-\cos(\alpha)e^{-TR/T_1}}\right)-1}{C\sin(\alpha)e^{-TE/T_2}}\right) \qquad 6.8$$

$$= \frac{(1-\cos(\alpha))e^{-TR/T_1}}{(1-\cos(\alpha)e^{-TR/T_1})}$$

The theoretical percentage signal losses due to incomplete T_1 recovery in a spin echo or gradient echo sequence (calculated using equation 6.8) are shown in figure 6.4.

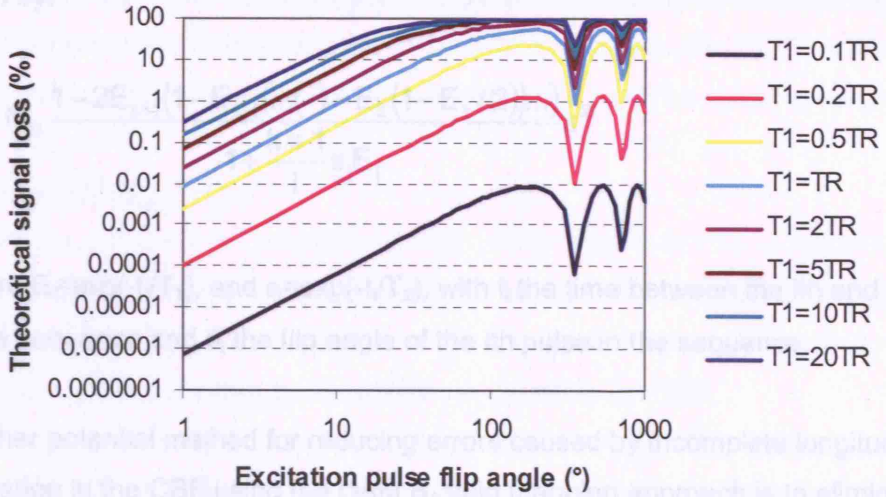

Figure 6.4: A logarithmic plot of the theoretical percentage signal losses due to incomplete T_1 relaxation in data acquired using a gradient echo or spin echo sequence, for various T_1 values (as a function of the repetition time TR of the sequence).

By using equation 6.8 to calculate the signal loss observed following each of the first and second acquisitions in the DAM B_1 mapping technique (i.e. for flip angles of α and 2α respectively), it is theoretically possible to calculate the effective flip angle distribution that would result in the signal intensity distribution observed. In other words, the fractional increase in the effective α observed due to this effect (the estimated effective B_1 is increased due to this problem) can be calculated and using this a correction could be applied to the effective flip angle calculated using this method.

It should be noted that the treatment above (in particular equation 6.6) of losses due to T_1 relaxation is not strictly true for the fast spin echo sequence due to interferences between successive echoes in the train and a rather more complicated analysis is necessary. Bakker *et al* [267] performed a theoretical analysis of the response of the

magnetisation of a spin system to various RF pulse sequence designs using the Bloch equations, and these were then tested in a phantom study. Mono-exponential relaxation and ideal RF pulses were assumed that in all cases. It was also assumed that if short RF pulses were used, the effective field in the rotating frame lies along the x-axis and relaxation during pulses could be neglected. By combining the cases of precession around the effective field during a particular pulse and free induction decay following the RF pulse, a steady state solution for any pulse sequence could be obtained. For a FSE sequence with k echoes the result for the steady state signal is given by:

$$S_i \approx M_0 \frac{1-2E_{k+1}\left(1-E_{k-i}\left(...\left(\ \right)-E_2\left(1-E_1/2\right)\right)...\right)}{1+\frac{k+1}{i}\varepsilon_j E_j}\varepsilon_1^{2i} \qquad 6.9$$

Where $E_i=\exp(-t_i/T_1)$, and $\varepsilon_i=\exp(-t_i/T_2)$, with t_i the time between the ith and (i+1)th pulse in the sequence and θ_i the flip angle of the ith pulse in the sequence.

Another potential method for reducing errors caused by incomplete longitudinal relaxation in the CSF using the DAM B_1 field mapping approach is to eliminate the signal from CSF completely. A new B_1 field mapping technique was investigated, based on the principles of the DAM, but using an optimised fast Fluid Attenuated Inversion Recovery (FLAIR) sequence [268], where the signal from CSF is nulled, in place of the FSE sequence. Errors caused by incomplete longitudinal recovery in brain regions containing CSF could be removed using such a method, and acquisition time could also be reduced, since WM and GM exhibit much shorter T_1 relaxation times than CSF; therefore a shorter TR is required for complete longitudinal relaxation in these regions. The sequence still requires a reasonably long TR to account for the longest possible T_1 occurring in the brain; here the longest T_1 value observed in MS lesions (approximately 1.7s [269]) was assumed to calculate the TR required, since this is likely to be the longest T_1 observed in patients scanned at this centre.

In FLAIR sequences the inversion recovery time TI required to null the CSF signal is long enough to allow complete recovery of longitudinal magnetisation in all other brain tissue structures, and the sequence could therefore be used for PD- or T_2-weighted imaging of other structures in the brain. FSE-based versions of the basic FLAIR sequence (Fast FLAIR) have been developed, resulting in shorter acquisition times [270].

In this study, an FSE-based fast FLAIR sequence [268] was used in place of the FSE sequence to acquire the two sets of images at nominal flip angles α and 2α. This sequence is a "hybrid" (2D-3D), multi-slab sequence where thick slabs consisting of 8 slices are excited during a relatively long TR and then sub-divided using phase encoding. This is based on the 2D Optimised Interleaved (OIL) FLAIR sequence developed by Listerud *et al* [271], in which the inversion pulse for a particular slice is played out several readout periods before that slice is acquired, possibly during the previous TR period. The minimum time between the inversion pulse and the following readout period (TJ) is limited only by the duration of the inversion pulse itself and the time needed to switch the associated gradients. However, the TR, TI and number of slices are inter-dependent in this type of sequence, with the relationship given by:

$$TI=(N_{skip}(TR/N_{slices}))+TJ \qquad 6.10$$

Where N_{skip} is the number of slices 'skipped' between the inversion pulse and data acquisition, and N_{slices} is the number of slices collected within a TR period. (i.e. if collecting 28 slices, but in two acquisitions, 14 slices per TR)

Most multi-slice sequences are implemented using spin-warp encoding. Such 2D sequences (including OIL FLAIR) use frequency selective RF pulses to define scan planes, which are then divided into pixels by in-plane phase and frequency-encoding gradients.

$$\text{Scan time} = TR * NEX * N \qquad 6.11$$

$$SNR \propto V \sqrt{(NEX\ N/BW)} \qquad 6.12$$

Where NEX = number of excitations (signal averages), N = number of phase encode steps, V = voxel volume, and BW=receiver bandwidth.

For a true 3D sequence, a second phase-encoding gradient is used to define the scan planes, and the scan time and SNR are thus given by:

$$\text{scan time} = TR\ NEX\ N_1\ N_2 = TR\ NEX\ N_1\ (N_{slices} + N_{discarded}) \qquad 6.13$$

$$SNR \propto V \sqrt{(NEX\ N_1N_2\ /BW)} \qquad 6.14$$

Where N_1 = number of in-plane phase encode steps, N_2 = number of through-plane phase-encoding steps, N_{slices} = number of slices discarded to reduce wrap-around artefact.

The hybrid sequence used here was implemented with thick slabs being excited in the usual multi-slice manner of a 2D sequence, during a relatively long TR. Phase encoding is used to sub-divide each slab into much thinner slices, with the multiple phase encodes within each echo train being used to reduce the total scan time. For such a sequence the SNR is still given by equation 6.13, but with N_2 greatly reduced (8 here). The scan time, however, becomes:

$$\text{scan time} = (N_{acqs}\ TR\ NEX\ N_1\ N_2)/ETL = (N_{acqs}\ TR\ NEX\ N_1\ (N_{slices}/N_{slab}) + N_{discarded})/ETL \quad 6.15$$

where N_{acqs} = number of acquisitions required for slice interleaving (typically 2), N_{slices} = number of slices per acquisition, N_{slab} is the number of slabs and ETL = echo train length.

Thus, with suitable choices for e.g. ETL and N_{slabs}, a hybrid 3D FSE sequence can give a scan time comparable to that of a true 3D sequence with a much shorter TR. Therefore this method combines the benefits of 3D encoding (thin slices and high SNR per unit time), and those of 2D FSE (relatively long TR and thus high inherent SNR, T_2 weighting and minimal susceptibility effects). Note that this sequence is also less susceptible to inflow effects, since the CSF signal is suppressed from a complete slab, rather than a slice.

This sequence was employed in place of the FSE sequence in the DAM B_1 mapping method in the same way; i.e. the sequence was acquired twice sequentially, once with the flip angle of the first pulse in the sequence altered to 60° (α) and the second time with the first pulse flip angle altered to 120° (2α). The same method for calculation of the effective flip angle was used. The sequence acquisition parameters used are detailed in section 6.4.

It should also be noted that a much lower image resolution could be used for B_1 mapping, which could significantly reduce acquisition time. However, this may not be straightforward to implement, depending on intrinsic limits set by the manufacturer.

6.4 MR Imaging Methods

The aim of this experiment was to simulate B_1 errors (reductions) in the measurement of the MTR, to perform corrections for these errors using the results of theoretical modelling (section 6.2), and finally to compare theoretical predictions with experimental MTR data acquired at a known B_1 error.

All MTR and B_1 field mapping data were acquired using a 1.5T GE Signa scanner (General Electric, Milwaukee, WI, USA) with a birdcage transmit/receive head coil. Five controls were imaged using the 2D spoiled gradient echo (SPGR) Euro-MT sequence [63], [272], and one of these was scanned 4 times to investigate reproducibility. The parameters of the Euro-MT sequence are: TR=960ms (TR'=34ms), echo time TE=12 ms, flip angle=20°, acquisition matrix 256x128, reconstructed matrix 256x256, field-of-view (FOV)=25x25cm with ¾ FOV in the phase direction. This was implemented on 28 5mm slices for whole brain coverage. A Gaussian MT pulse, flip angle=500°, duration τ_{sat}=7.68ms (FWHM=3.51ms, bandwidth=250Hz) was applied prior to the acquisition of each slice at an offset frequency of 1500Hz on the opposite side of the water resonance to fat. The p_1 value for the Gaussian MT pulse (the ratio of the mean amplitude of the saturation pulse to that of a rectangular pulse of the same amplitude [76]) is 0.4819, and the p_2 value is 0.3441 (the ratio of the square of the mean amplitude of the saturation pulse to that of a rectangular pulse of the same amplitude). These values are used to calculate the B_{1CWPE} (and hence the pulse amplitude ω_{1CWPE}) for the MT pulse (see equations 5.43-5.44). For an MT pulse flip angle of 500°, the B_{1CWPE} is 2.45μT and ω_{1CWPE} is 655rads^{-1}.

B_1 transmit coil non-uniformity was simulated by decreasing the MT pulse from its nominal flip angle (FA) value of 500° down to 400° in 20° steps. The imaging pulse FA was not reduced, as would be the case with a true B_1 reduction. Assuming that the excitation pulse flip angle is small enough that its MT effect is negligible, which is an assumption usually made in qMT modelling [50], [208], alteration of the imaging pulse would not affect the MTR values, as MTR calculation involves a ratio of two proton density weighted images. Since T_1 is known to be reduced in MT, the imaging flip angle (20°) of the SPGR sequence was selected so as to minimise any T_1 weighting in the resulting images, whilst producing images with an acceptable signal-to-noise ratio (SNR).

B_1 field mapping of 4 subjects (and 8 additional subjects on three occasions as part of the scanner upgrade quality assurance programme) was performed using the FSE

DAM [253] in order to quantify the size of typical B_1 errors, and thus provide accurate MTR values over the whole brain.

Acquisition parameters used for the FSE DAM technique were: TR=15s, TE=14ms, echo train length (ETL)=8, bandwidth=16.63kHz, Acquisition matrix 256x128, reconstructed matrix 256x256, FOV 25x25cm with ¾ FOV in the phase direction, 28 5mm slices. This gave a total imaging time of exactly 3 minutes for each of the two scans.

B_1 field mapping was also performed on two controls using the fast FLAIR implementation of the DAM. The sequence parameters used for the optimised fast FLAIR DAM B_1 field mapping sequence were TR=8.5s, TE=17ms, 'skip time' TJ (minimum time between the inversion pulse and the following readout) =150ms, ETL=16, bandwidth=16.63kHz, acquisition matrix 256x128, reconstructed matrix 256x256, FOV 36x36cm with ½ FOV in phase direction, 28 5mm slices, 2 acquisitions, 1 NEX, with an acquisition time of 2:16 minutes for each of the two scans required.

6.5 Image Analysis

A set of 18 regions of interest (ROIs) was generated, each region corresponding to a normal tissue in the brain. For each tissue, the normalised MTR (i.e. $mtr_{normalised}$) was plotted against normalised B_1 (i.e. $b_{1normalised}$) and linear regression was used to determine the linear relationship between $mtr_{normalised}$ and $b_{1normalised}$ for each individual tissue type. Data were averaged over all controls and tissue types to give a single line approximating all tissue types (equation 6.16).

This tissue-independent equation was applied to measured MTR values from each tissue region and their (reduced) B_1 values to estimate MTR values at 100% B_1, and compared with results obtained by correcting measured MTRs using equation 6.1. MTR histograms were generated; M_0 and M_S images were co-registered using the Mutual Information algorithm [273]. Segmentation was performed using SPM2 (The Wellcome Department of Imaging Science, UCL, London, UK) and whole-brain and segmented white and grey matter MTR histograms were generated. These were smoothed and then normalised by dividing all values by the total number of voxels, resulting in a fractional value of the whole brain volume (such that the area under the histogram is equal to unity). These could then be multiplied by 100 to give results in percent units (pu), and the generation of fully normalised histograms allows comparison of data between sites.

Fully normalised, smoothed whole-brain, white and grey matter (GM) B_1 histograms were also produced for each control using the FSE DAM B_1 mapping technique, which would facilitate comparison of B_1 data across sites

6.6. Results

6.6.1 Theoretically and experimentally derived B_1 correction schemes

6.6.1.1 Experimental results

Averaging normalised data over all controls and tissue types gave:

$$mtr^{expt}_{normalised} = 0.812b_{1normalised} + 0.193 \qquad 6.16$$

The experimental normalised data used to calculate this equation, averaged over all controls and brain tissue types, are shown in figure 6.5. The error bars indicate the 95% CL on average normalised MTR measurements. It can be observed that the data does not fit a perfect straight line (see also section 6.2.2); in fact it appears to curve slightly downwards, levelling off as $b_{1normalised}$ tends towards 1 (i.e. as B_1 tends towards its nominal value) and the MTR tends towards its correct value. This is an indication of the true MTR dependence on B_1 and matches theory (see also figures 6.2 & 6.3). The correlation coefficient (R) for fitting the curve $mtr_{normalised}=1.005b_{1normalised}^{0.793}$ is 0.9986, very close to that resulting from the linear regression (0.9982). However, within the likely ranges of B_1 error, the graph can be approximated to a straight line, which is the basis for this simple linear correction method.

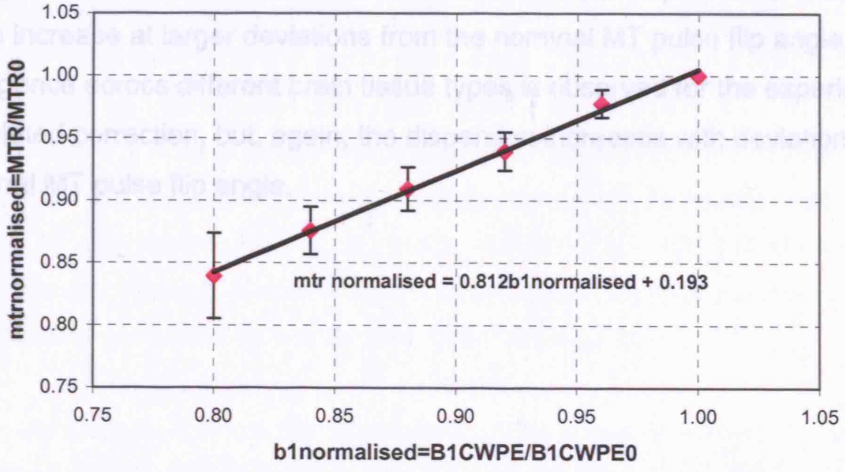

Figure 6.5: Plot of average experimentally measured normalised MTR dependence on normalised B_{1CWPE} for different brain tissue types. Data were acquired using the Euro-MT sequence (nominal MT pulse flip angle=500°, offset frequency=1500Hz (see section 6.4 for other sequence parameters)).

The standard deviation (SD) of an individual MTR measurement was calculated for frontal WM using the Bland-Altman method [274] for 6 repeated pairs of measurements, and was found to be approximately 0.41pu. This method involves making repeated pairs of measurements, and calculating the SD of the differences between each pair of measurements s. The SD of a single measurement is then given by $SD=s/\sqrt{2}$. The difference between the repeats in pairs of measurements is normally distributed with $SD= s*\sqrt{2}$. The SD of the differences between each pair of measurements (s) is also known as the within-subject variability, and the coefficient of repeatability can also be foundfrom this ($1.96*s*\sqrt{2}$), assuming that there is no bias between the first and second measurements. Therefore for a biological change to be detected in a single subject with 95% confidence, it must exceed the repeatability.

The minimum detectable MTR difference in an individual pair of measurements, with 95% confidence limits (CL), is 0.81pu. One control was scanned four times and the standard deviation for the mean in a frontal white matter ROI in this subject was found to be 0.70 pu.

6.6.1.2 Comparison with theoretical results

The theoretically (eqn 6.1) and experimentally (eqn 6.9) derived corrections were applied to control frontal WM MTR data and the results are shown in figure 6.6. The divergence of the theoretical model from data and the dispersion of different tissue types increase at larger deviations from the nominal MT pulse flip angle. A smaller divergence across different brain tissue types is observed for the experimentally calculated correction, but, again, the dispersion increases with deviation from the nominal MT pulse flip angle.

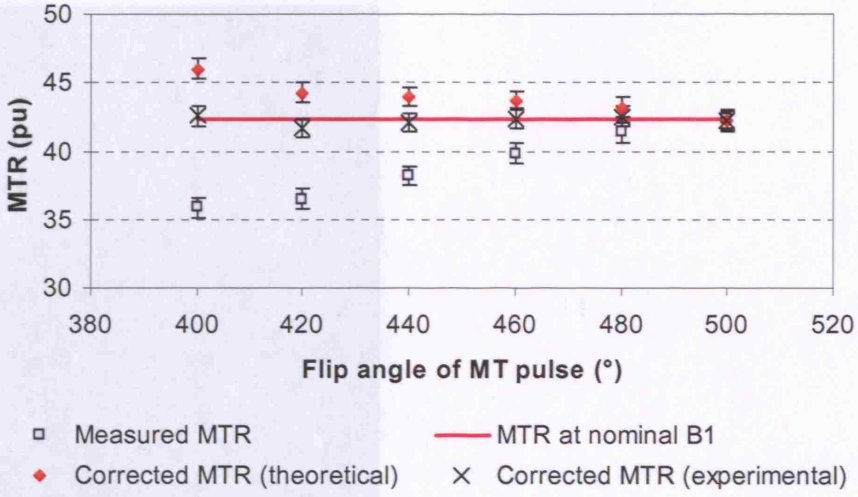

Figure 6.6: Plot of theoretically (eqn 6.1) and experimentally (eqn 6.9) derived B_1 corrections applied to control frontal WM (Euro-MT sequence (nominal MT pulse flip angle=500°, offset frequency=1500Hz (see section 6.4 for other sequence parameters))) MTR data, averaged over 4 scans. The error bars represent the 95%CLin estimating the MTR, estimated using the Bland-Altman method [274].

6.6.2 B_1 Field Mapping

Figures 6.7(a) and 6.7(b) illustrate the FSE DAM B_1 mapping results obtained on the 1.5T GE Signa scanner. This B_1 map (showing B_1 as a fraction of the nominal B_1 for the sequence) was acquired using the DAM with TR=15s. Some inherent tissue structure can be observed throughout the B_1 map, possibly caused by incomplete CSF relaxation and partial volume errors in and around regions of CSF in the brain. This would result in the terms relating to longitudinal relaxation in equation 6.3 not cancelling each other out in the two acquisitions, thereby causing errors in the calculated effective B_1. Figure 6.7(b) is a horizontal profile across the B_1 map in figure 6.7(a) (taken where the lines are shown). The lack of smoothness is probably due to partial volume errors in voxels containing some CSF as well as other brain tissue types.

For comparison, a B_1 map for segmented CSF is shown in Figure 6.7(c) and its corresponding profile in figure 6.7(d). It can be seen that many of the regions of tissue structure in Figure 6.7(a) correspond to regions in and around the CSF, suggesting that this is the cause of the lack of smoothness observed in the B_1 maps. However, the calculated fractional B_1 is correct in brain tissue regions and would also be correct in lesions, which are known to have an increased T_1 relaxation time compared with healthy brain tissue, but still well below the T_1 of CSF (for example, the longest T_1

Multiple Sclerosis (MS) lesions have been shown to have a T_1 of approximately 1.7s [269]).

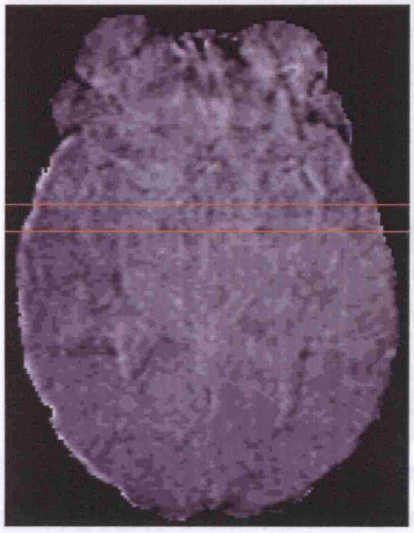

Figure 6.7(a): FSE DAM method fractional B_1 field map (B_1 as a fraction of the nominal value), acquired with TR=15s.

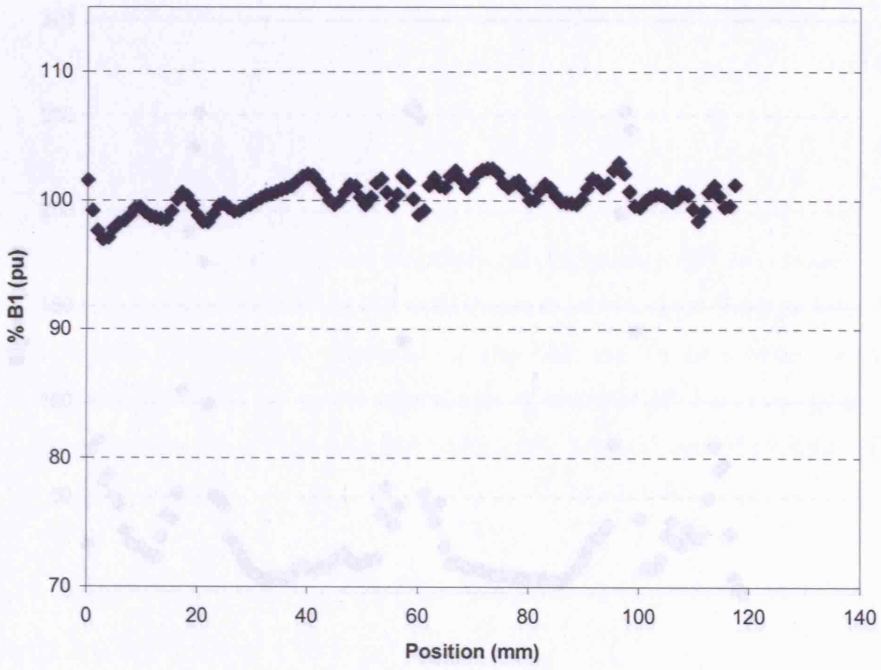

Figure 6.7(b): Profile across FSE DAM-acquired fractional B_1 map shown in figure 6.7(a) (taken where the lines are shown).

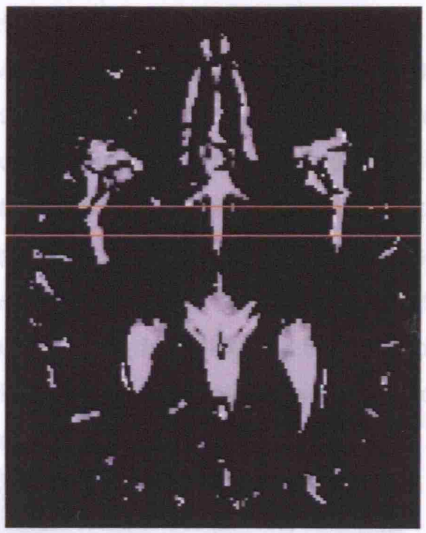

Figure 6.7(c): CSF image (segmented using SPM2 from the first FSE DAM image (i.e. with α=60°) used to calculate the B_1 map in 6.7(a)). It can be seen that many of the regions of non-uniformity in Figure 6.7(a) correspond to regions of the CSF, where partial volume errors may have occurred.

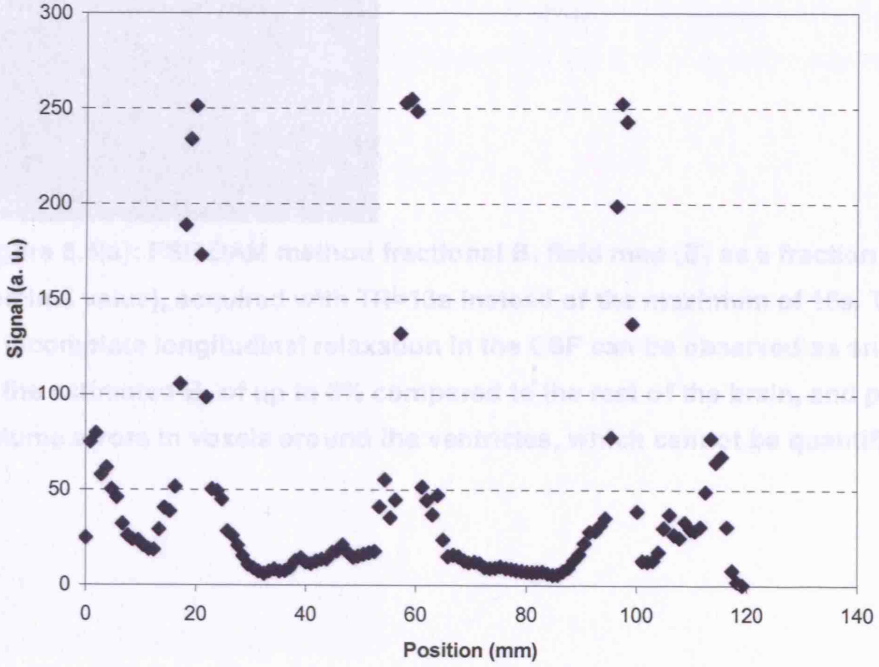

Figure 6.7(d): Profile across the CSF segmented image shown in figure 6.7(c). Some of the CSF regions correspond to positions where a lack of uniformity is observed in profile 6.7(b), indicating that this non-uniformity can be attributed to CSF partial volume errors.

6.6.3 CSF correction scheme

An example of the application of the correction scheme described in section 6.3.2 is shown in figure 6.8. Firstly, a fractional B_1 map collected using the FSE DAM with a TR of 13s instead of the maximum (15s) to demonstrate the effects of using a TR that is too short for complete CSF relaxation is shown in figure 6.8(a), and the corresponding profile (taken where the lines are shown in figure 6.8(a)) in figure 6.8(b). The correction scheme was then applied to this data set and the resulting B_1 map is shown in figure 6.8(c), and its profile in 6.8(d). It is obvious that partial volume errors are present in the B_1 map, causing the simple correction scheme to fail in some regions, particularly around the ventricles.

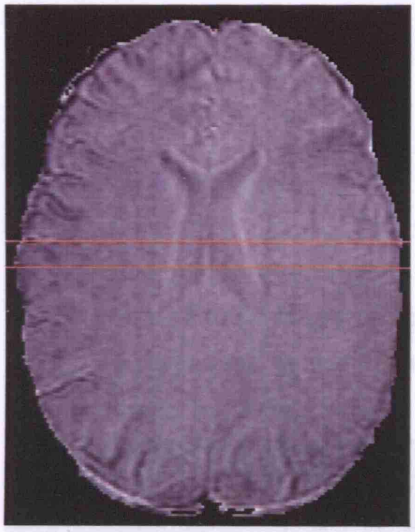

Figure 6.8(a): FSE DAM method fractional B_1 field map (B_1 as a fraction of the nominal value), acquired with TR=13s instead of the maximum of 15s. The effects of incomplete longitudinal relaxation in the CSF can be observed as an increase in the estimated B_1 of up to 5% compared to the rest of the brain, and partial volume errors in voxels around the ventricles, which cannot be quantified.

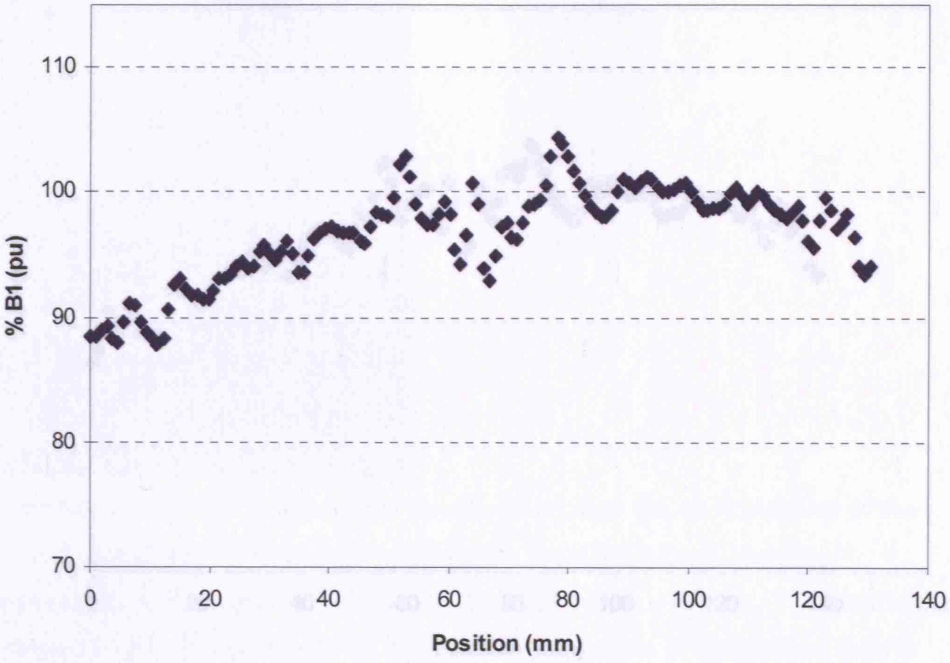

Figure 6.8(b): Profile across fractional B_1 map shown in figure 6.8(a). B_1 is artificially enhanced in and around regions of the CSF due to incomplete longitudinal relaxation.

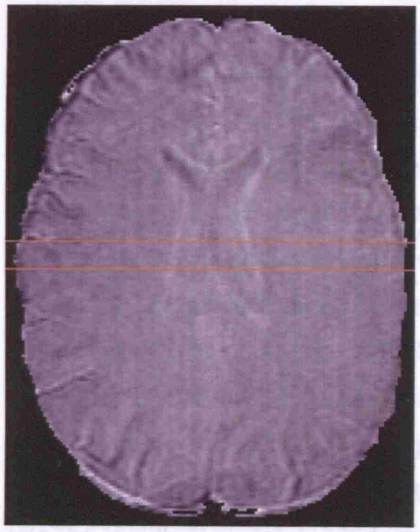

Figure 6.8(c): Example B_1 map showing correction applied to B_1 mapping data exhibiting incomplete longitudinal relaxation in the CSF (acquired with the DAM B_1 mapping technique, using a TR of 13s for each FSE sequence). Partial volume errors are present, due to the occupation of voxels by more than one tissue type, causing the correction method to fail, for example at the edges of the ventricles.

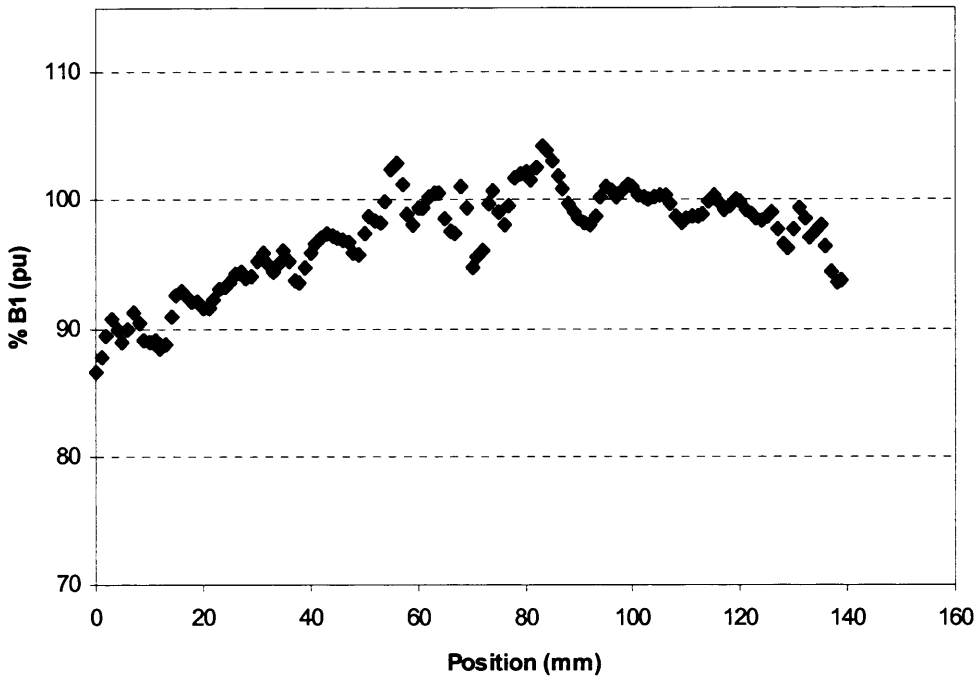

Figure 6.8(d): Profile across corrected fractional B_1 map shown in figure 6.8(c). Enhancement of B_1 can still be observed in and around regions of the CSF due to partial volume errors in those regions.

6.6.4 Fast FLAIR DAM B_1mapping

A fractional B_1 map obtained using the fast FLAIR-based DAM technique is shown in figure 6.9(a), and the corresponding profile (taken where the lines are shown) in figure 6.9(b). Since the CSF signal is suppressed using this type of sequence, errors due to incomplete CSF longitudinal recovery and partial volume effects could potentially be eliminated. Acquisition time could also be reduced, since WM and GM exhibit shorter T_1 relaxation times than the CSF. The sequence still requires a reasonably long TR, however, to account for the longest possible T_1 values occurring in MS lesions (approximately 1.7s [269]). T_1 weighting resulting from relaxation during the inversion time TI is the same in both acquisitions, and therefore does not introduce any errors into the resultant signal, but it does result in a reduction of signal-to-noise ratio (SNR) in images compared with those acquired using the FSE-based version. There is also a loss of resolution since a larger FOV was used to reduce scan time, which may account for some of the blurriness in the image. This sequence also has a longer echo train than the original FSE DAM, which may have caused some blurring in the resulting images. It is also possible that the lack of T_2 contrast in this image could have resulted in registration interpolation errors.

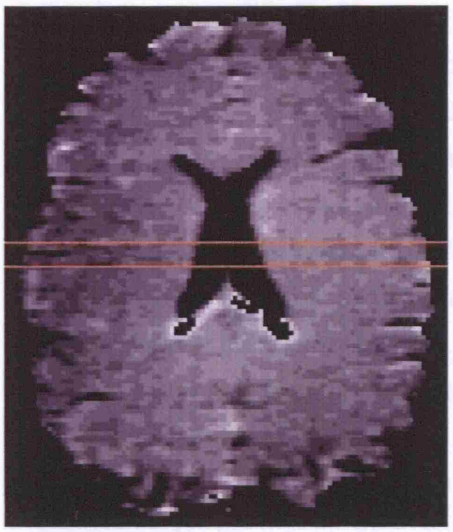

Figure 6.9(a): Control whole-brain fractional B_1 map (B_1 as a fraction of the nominal value) acquired using FLAIR DAM. The CSF signal has been suppressed, reducing errors caused by partial volume effects. The blurring observed in this image could be explained by the loss of resolution due to increased FOV with respect to the FSE DAM, and also the lack of T_2 contrast in this image, giving rise to registration interpolation errors.

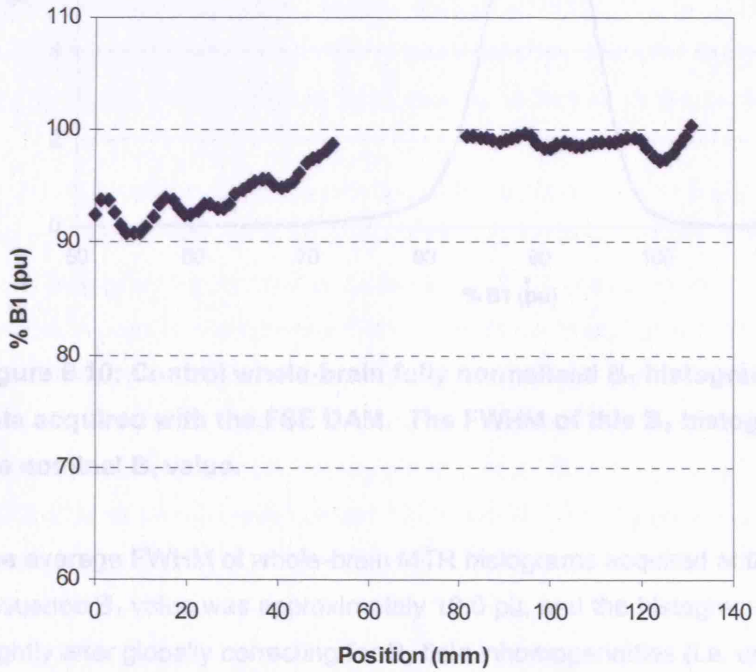

Figure 6.9(b): Profile across FLAIR DAM-acquired fractional B_1 map shown in figure 6.9(a). The CSF signal has been suppressed using this method, reducing errors caused by partial volume effects. Again, this profile is very smooth in comparison to those in Figures 6.7 and 6.8.

6.6.5 B_1 Histograms

A fully normalised control subject whole-brain B_1 histogram, acquired using the FSE DAM is shown in figure 6.10. The DAM technique was used to quantify the B_1 non-uniformity errors and correct for B_1 errors in MTR maps and histograms. B_1 errors in the birdcage head coil in the 1.5T GE Signa scanner were found to be rather small (the average whole-brain B_1 histogram FWHM (using data acquired from 4 subjects) is just 9.1pu (i.e. 9.1% of the nominal B_1 value for the sequence). B_1 histograms were fully normalised (such that the area under the histogram is 100%) to enable comparison of histogram metrics such as peak height, location etc with other sites.

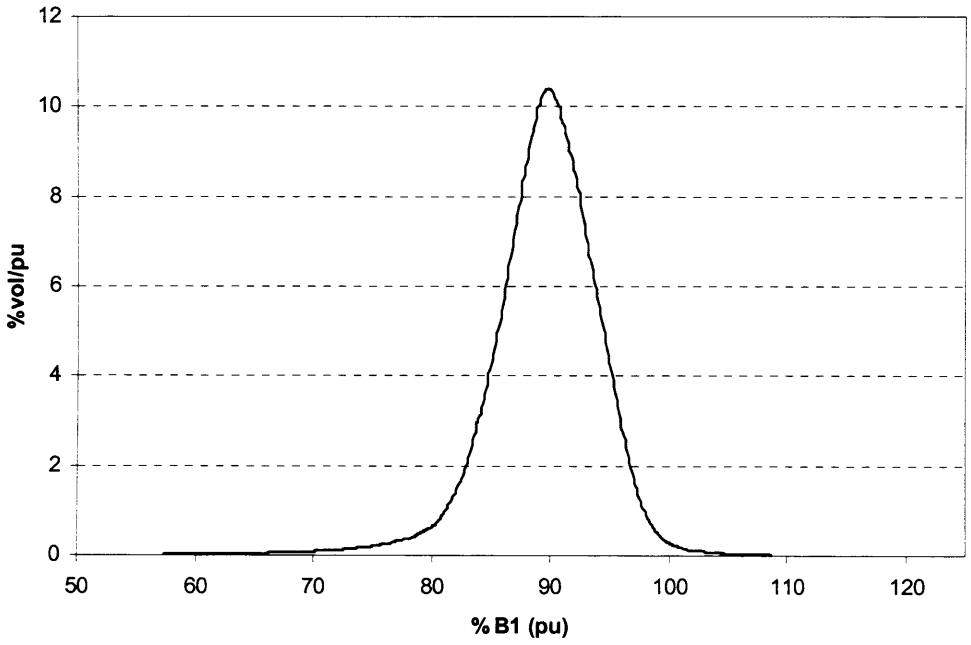

Figure 6.10: Control whole-brain fully normalised B_1 histogram produced using data acquired with the FSE DAM. The FWHM of this B_1 histogram is just 8.7% of the nominal B_1 value.

The average FWHM of whole-brain MTR histograms acquired at the nominal Euro-MT sequence B_1 value was approximately 10.0 pu, and the histograms were narrowed only slightly after globally correcting for B_1 field inhomogeneities (i.e. using the same correction scheme for all tissue types), which may be explained by the good homogeneity of the birdcage coil (B_1 histograms were found to be very narrow). A control WM MTR histogram corrected using the experimentally calculated B_1 correction is shown in figure 6.11. A small shift in peak position to lower MTR values is observed

(approximately 0.8pu), and very slight FWHM reduction (just 0.5pu) of the histogram peak.

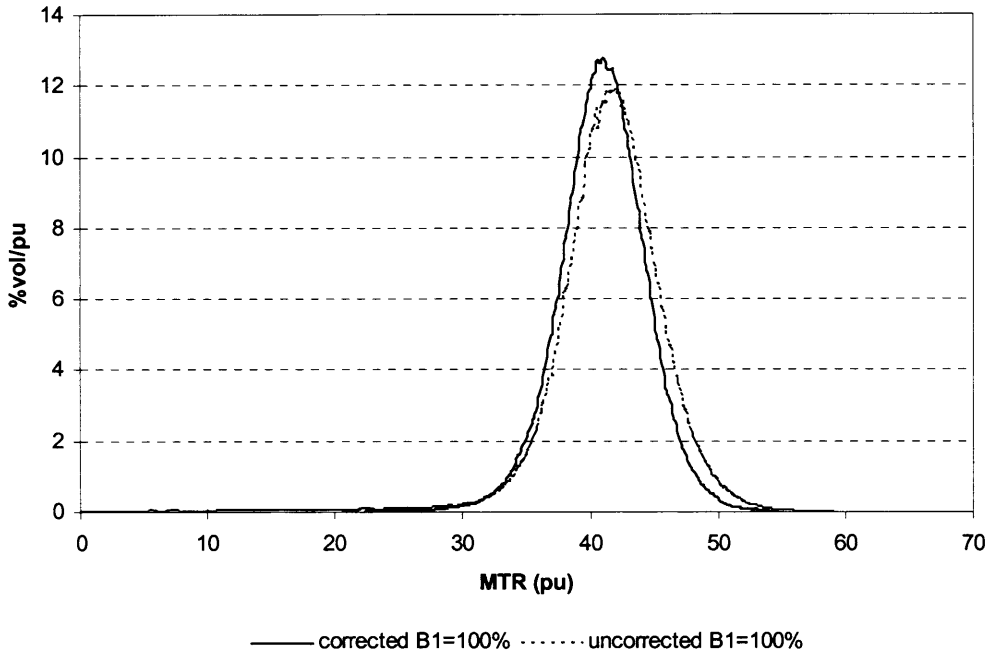

Figure 6.11: Control WM MTR histogram (acquired using a birdcage transmit/receive head coil) before and after correcting for B_1 errors. A very small shift (approximately 0.2pu) of the peak location towards lower MTR values and slight reduction of FWHM (0.1pu) can be observed in the corrected histogram.

As a demonstration of the application of the B_1 correction scheme, figure 6.12 shows fully normalised WM MTR histograms of data acquired at 80% MT pulse FA, 100% FA, and a histogram for the data acquired at 80% FA corrected for a 20% B_1 error. The histogram peak is shifted towards the correct position, but suffers some broadening (and therefore reduction of peak height). The FWHM of the uncorrected histogram acquired at 80% FA is 7.8pu, and this is increased to 9.2pu on applying the correction (the FWHM of the 100% B_1 histogram is 7.0pu). This could have been caused by the application of a non-tissue specific correction to a single brain tissue type, and possibly by noise present in the B_1 map used to apply the correction to MTR data.

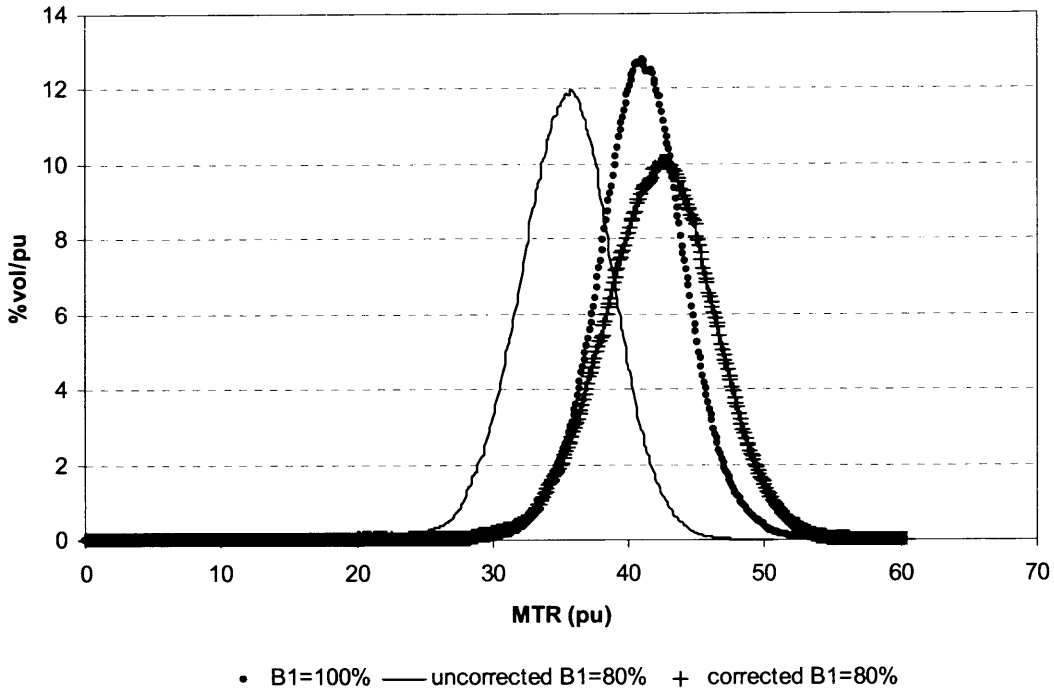

Figure 6.12: Example of application of the B_1 correction scheme to white matter MTR data acquired with 80% MT pulse FA. For comparison the WM MTR histogram acquired at B_1=100% is also shown. The corrected histogram shows almost the correct peak position (0.9 pu too high), but histogram broadening (and also therefore reduction of peak height) is also present, probably due to the variation in tissue types included in the correction scheme.

6.7 Discussion

The experimentally calculated B_1 correction equation (eqn. 6.2) differs from the average linear equation derived theoretically (eqn. 6.1), which may be explained by limitations in the CWPE qMT model (see also figure 6.6). CW methods are more efficient than pulsed schemes; thus the CWPE MTR is the maximum achievable MTR with a pulsed sequence [215]. The two-pool model is also only an approximation to the true in vivo situation. The free proton pool alone is known to comprise at least three pools [190] and three- or four-pool models for qMT have been developed [193], [222] but the increased acquisition time required in order to determine all the parameters involved, and computational complexity make these models difficult to apply clinically. In addition, it is possible that some T_1 weighting was introduced into the MTR measurements, since the excitation pulse flip angle used for the Euro-MT sequence is rather high (20°) in order to give a high SNR in the resulting images, and the TR is 960ms. This could have the effect of increasing the tissue dependence of the B_1 sensitivity of MTR measurements, thus increasing differences between brain tissue types.

The comparison made by Ramani *et al* [215]of multi-centre data to simulated MTR data, modelled using the CWPE approximation was made using a Gaussian RF absorption lineshape for the semi-solid pool, and the modelling was performed using parameters obtained using the Gaussian lineshape for the macromolecular pool in fitting (white matter MT parameters used were from a study performed by Morrison *et al* [188]). In the study by Morrison *et al*, it was shown that a super-Lorentzian semi-solid pool lineshape is more appropriate for human white matter tissue. However, it may be possible that the use of the super-Lorentzian lineshape to model the RF absorption of the semi-solid pool results in the best fit to qMT data, but that the Gaussian lineshape predicts measured multi-centre MTR data, perhaps due to T_1 weighting effects. This may provide a possible explanation for the discrepancies observed between the theoretical and experimental data in this study.

It was assumed that terms due to longitudinal relaxation in equation 6.3 are equal to unity (since complete longitudinal relaxation was assumed to take place for all tissue types) for both acquisitions in the DAM B_1 mapping technique. However, since a FSE sequence (with ETL=8) was used to acquire the DAM data rather than a simple spin echo, it is difficult to define the repetition time TR precisely. Therefore it is also possible that some T_1 weighting may have been introduced into the images which would be different for the two sets of images acquired (at α=60° and α=120°).

In Figure 6.6, both the theoretically (equation 6.1) and experimentally (equation 6.9) derived correction schemes have been applied to control frontal WM MTR data. The divergence of the theoretical model from data and the dispersion of data from different tissue types both increase at larger deviations from the nominal MT pulse FA for the Euro-MT sequence. The divergence from the experimentally fitted line is obviously smaller, but a similar spread of differences between tissue types is observed, again with the dispersion increasing with deviation from the nominal MT pulse flip angle.

The almost linear dependence of $mtr_{normalised}$ on $b_{1normalised}$ (equation 6.9) is interesting, as it contradicts the widely held belief that the MTR depends on the square of the B_1, and supports earlier work [76], which also indicated a linear, rather than quadratic dependence.

The improvement to the MTR histogram (see Figure 6.10) was not particularly dramatic, as the RF uniformity is good for the birdcage coil (see Figure 6.9). However work on other scanners [275] has shown that RF non-uniformity can be a significant source of histogram broadening, and in such cases this method will probably be

valuable. We attribute this to the fact that a global correction scheme for all tissue types is being applied to a single brain tissue type. A second contributing cause of the broadening may be that at the higher MT pulse flip angle values, white and grey matter converge to similar MTR values (this is supported by the fact that the FWHM of the MTR histogram is less at 100% B_1 than at 80% B_1). However, this may not be the case for a true B_1 reduction, as the imaging flip angle would then also be affected which might affect the (tissue dependent) T_1 weighting of the resulting images.

A correction for incomplete CSF T_1 recovery was applied to FSE DAM B_1 mapping data (in order that a shorter TR could be used to reduce acquisition time), but tended to fail where voxels contained more than one tissue type, for example at the edges of the ventricles, due to partial volume effects.

A new B_1 field mapping technique was also investigated, based on the principles of the DAM, but using a fast FLAIR sequence to remove CSF contributions and thus eliminate partial volume errors, and to reduce acquisition time. The SNR was reduced, however, as was the resolution since the FOV used in the fast FLAIR DAM was larger. The fast FLAIR DAM-acquired B_1 maps did not display the sharp artifacts observed in the FSE DAM B_1 maps, caused by incomplete longitudinal recovery in regions containing CSF.

This technique can readily be implemented on other scanners. If the Euro-MT sequence is available, the data in this paper and equation 6.9 can be used directly. However, it should be noted that the MTR is highly dependent on sequence parameters, therefore a new dataset will be required if any of the details of the MTR sequence are altered, in particular, the MT pulse flip angle or offset frequency, but also the MT pulse shape, duration τ_{sat} and repetition time TR' between successive MT pulses. The MT pulse flip angle can be reduced from its nominal value, as performed in this study, or alternatively (and perhaps more realistically) the B_1 value can be progressively reduced (i.e. the imaging pulse flip angle could be reduced in line with the MT pulse flip angle). This approach has the advantage that no assumptions regarding T_1 weighting are made. If present, such (tissue-dependent) T_1 effects would be altered with B_1.

In reference [264], linear regression was performed on segmented white matter data sets in healthy controls, and from this a non-tissue specific correction was derived. This was independently verified using a method similar to that presented in this paper. However, pixels from all white matter regions were included in the regression analysis,

regardless of position. There are several lines of evidence to show that there are regional variations within and between different white matter structures.

Barker *et al* [55] demonstrated significant MTR differences between white matter regions in 10 normal controls. The brainstem, which predominantly comprises white matter was significantly ($p<0.001$) different from all white matter regions (except for the brain stem vs. left occipital white matter, which was significant at the $p<0.01$ level). A pair-wise comparison of each region with every other showed that most differences were significant at the $p<0.001$ level. The brain stem exhibited an MTR of 29.1pu vs. 31.9 and 31.7pu for left and right frontal white matter respectively, 29.8 and 30.5pu for left and right occipital white matter respectively and 31.1 and 31.0pu for left and right parietal white matter respectively. The right occipital region showed no significant difference from right parietal white matter, and differed from left parietal white matter only at the $p<0.05$ level. Left parietal vs. right frontal matter MTR difference was also only significant at the $p<0.05$ level.

Similar variations of T_1 in white matter of healthy controls have also been observed [269], [276], and the MTR is also known to depend on the observed T_1 of the tissue/object being imaged. Under conditions of complete saturation of the restricted pool protons (not realistically achievable *in vivo*), it has been shown that the first order rate constant for MT from the free to the restricted pool, k_f (RM_0^B using the notation of Henkelman *et al* [49]) is given by $k_f = \frac{MTR}{T_{1sat}^A}$, where $T_1{}^A{}_{sat}$ is the longitudinal relaxation time of the free proton pool (reduced from its value $T_1{}^A$ in the presence of MT) [53], [36]. Lee and Dagher [226] also proposed a method for quantifying the restricted proton fraction f from a single MTR measurement, a $T_1{}^A{}_{obs}$ measurement, and a measurement of the amount of saturation of the restricted protons. The relationship between these quantities is $\frac{M_0^B}{M_0^A} = \frac{MTR}{T_{1obs}^A R_{RFB}}$, from which f can be calculated. This approximation holds under conditions of low MTR and low direct saturation of the free pool (i.e. the offset frequency should be > 3-5kHz for white and grey matter [277]).

Additionally, a recent study by Sled *et al* [241] showed regional variations in qMT parameters in normal brain. A two-way ANOVA demonstrated that all parameters apart from the proton density (PD) of the free water pool showed highly significant ($p<0.0005$) differences between all white matter anatomical regions. For example, the ratio of restricted to free protons M_0^B/M_0^A (which Sled *et al* denote as F) was measured as 12.7% in frontal white matter vs. 12.0% in occipital white matter and the first order

rate constant k_f was $4.3s^{-1}$ in frontal white matter and $3.7\ s^{-1}$ in occipital white matter. There was a smaller difference inT_2^B, the transverse relaxation time of the restricted pool (11.0μs vs. 11.2μs in frontal and occipital white matter respectively), and a small difference in the free proton pool longitudinal relaxation rate R_A was also observed ($1.73s^{-1}$ vs. $1.70s^{-1}$ in frontal and occipital white matter respectively).

Since the correction proposed by Ropele *et al* [264] was calculated using all white matter pixels regardless of position, we suggest that positional changes in MTR may have been confounded with B_1 changes, which are additionally known to vary across the subject's head. Furthermore, a white matter-specific correction was derived from segmented white matter data and this was then extrapolated to calculate a different, non tissue-specific correction, rather than using pixels from all brain tissues in the brain. However, this non tissue-specific correction was shown to be in fairly good agreement with the correction determined from numerical simulations.

In the work presented here, the theoretical linear correction scheme was calculated using previously measured quantitative MT parameter values for 9 different brain tissue types [48], including control white (WM) and grey (GM), corresponding regions in the normal-appearing white matter (NAWM) and normal-appearing grey matter (NAGM) of MS patients, and in MS lesions. The experimentally derived correction was calculated by altering B_1 in a controlled way and measuring the MTR in normal controls. Averaged data from 18 different tissue regions in the brain were used, thus eliminating the possibility of confounding positional MTR changes with those caused by changes in B_1. Our correction scheme is therefore applicable to all brain tissue types.

The B_1 of the MTR sequence was decreased from its nominal value by up to 20%, and MTR values were corrected using both the theoretically and experimentally derived correction schemes. Whilst it has been shown that the CWPE qMT theory does not accurately match experimental MTR data, the MTR expressed as a fraction of its nominal value has been shown to depend linearly on the fractional B_1 for B_1 reductions up to 20% in size, allowing a simple correction scheme to be applied to MTR data. We showed that, even for B_1 errors as large as 20%, the deviation of the MTR from its true value could be significantly decreased. In figure 3 of reference [264], the MTR deviated from its mean value as a function of the B1 error by as much as 10pu (mean deviation ~5pu) even at low B_1 error values. Following correction using the scheme proposed in that study by the authors this level of scatter from the mean MTR value would remain. In our study, using our experimentally derived correction scheme, the mean MTR value for the 18 tissue types was 7.0 pu (i.e. ~16%) below the correct value for a 20%

reduction in B_1. After correction using the single equation above for all tissue types, all MTR values were within 1.5pu of their correct value (rms error 0.7pu). There is a slight over-correction of MTR data (see figure 6.5) since the true MTR dependence on B_1 is not strictly linear. However, after correction using our experimentally derived correction scheme for all brain tissue types, all MTR values were within 1.5pu of their correct value (rms error 0.7pu).

Future areas of work might include refining the CWPE qMT model (see chapter 5), to attempt to match theoretical predictions to experimental data better, an extension of the approach both to other MTR sequences and other modality sequences (e.g. T_1, T_2 etc.), and finally an investigation of alternative possible B_1 mapping methods (although the FSE DAM approach works well, a faster method is desirable to reduce acquisition time).

6.8 Conclusions

In conclusion, it has been shown that a simple correction scheme can be applied to MTR maps with a known B_1 error, regardless of tissue type. There is some discrepancy between results obtained from numerical simulations and experimental data, which can be explained by limitations of the CWPE qMT model.

The DAM B_1 field mapping technique has been implemented and used to quantify and correct for B_1 errors in MTR maps and histograms, taking only 6 minutes to acquire data for a whole-brain B_1 map. Whole-brain normalised B_1 field maps were found to exhibit FWHM's ranging from just 6.8 – 11.5% of the nominal B_1 value for the birdcage head coil in a 1.5T GE Signa scanner. However, an increased TR (and hence acquisition time) would be preferred in order to eliminate errors observed in regions containing CSF caused by the incomplete longitudinal relaxation of CSF.

7 Quality Assurance (QA), Phantoms and Internal Thermometry

Introduction

Quality assurance (QA) testing is the method by which the scanner is assessed continuously in order to ensure that it is working satisfactorily. In order to perform quantitative MR measurements satisfactorily, a QA programme implemented by the user (i.e. rather than the manufacturer's regular servicing programme) should involve making quantitative measurements of various MRI parameters both in phantoms (test-objects) and control subjects, in addition to checks of SNR, temporal fMRI stability etc. This allows the observation of any changes in equipment operation that may affect the validity of results and may also facilitate correction for errors caused by such changes.

In the first section of this chapter two protein gels (Bovine Serum Albumin (BSA) and agarose) are assessed for use as potential MT phantoms, the objective being to develop a QA phantom with qMT properties similar to those of human brain *in vivo*. A brief literature review will be given first, followed by sections detailing the investigations performed on each type of gel, their results and a discussion.

The second section of the chapter describes the development of internal thermometry in MRI phantoms. One possible source of systematic error in phantom QA measurements is the dependence of many quantitative MR properties on temperature, and not accounting for such errors may limit the accuracy of phantom QA measurements, which will, in turn, have an impact on the interpretation of quantitative changes observed in long-term clinical studies. Phantoms are much more readily available than human controls, therefore QA measurements are often performed in phantoms. It is therefore desirable to be able to measure test-object temperature when performing quantitative phantom QA measurements, but many traditional thermometry methods are unsuitable for use in an MRI scanner. Here a simple, readily available method of internal thermometry is developed for use in MRI phantoms.

7.1 Phantoms (test objects) used for MT

Phantom measurements have the advantages of availability, potentially high accuracy for the MR quantity being measured, possibly stability (although some gels/liquids can be chemically unstable) and uniformity (especially in liquids). However, phantoms are unrealistic of true *in vivo* situations, where such confounding factors as subject motion and partial volume effects due to tissue heterogeneity also occur. Another major issue

is that many quantitative MR properties, such as T_1, T_2, diffusion and also MT (probably due to its T_1 dependence), are temperature dependent, varying by about 2-3% per °C [6].

Here agarose gels and the cross-linked protein gel Bovine Serum Albumin (BSA) are evaluated for their potential use as MT phantoms. Agarose gels are widely used as test-objects for different MRI modalities because their T_1 and T_2 values can be manipulated independently to mimic closely those observed *in vivo*, BSA protein gels have previously been reported to have higher MTR values and less narrow Z-spectra by Mendelson *et al* [278].

7.1.1 Agarose gels

7.1.1.1 Literature review

Agarose gels have been successfully used as test-objects in many MRI studies to model tissue [4], [5], [6], [7], [8], [9], [279]. These polysaccharide gels have previously been used because the relaxation properties of water protons in agarose can be made similar to those of tissue in the MRI field strength range through the use of doping (using for example paramagnetic ions). Many different types of gels can be produced that match the relatively long T_1 values characteristic of biological tissue, but agar-based gels also have the appropriate T_2:T_1 ratio, with the gel concentration dictating the T_2 value of the gel [20], whilst leaving the T_1 value relatively unaffected by changes in T_2 value. In other words it is possible to achieve $T_2 << T_1$ (as is the case *in vivo*) in agar gels, making short T_2 values accessible without shortening T_1. Tyler and Gowland also demonstrated a linear increase of the restricted proton pool size ratio M_0^B/M_0^A with concentration in agar gel [221].

It has been demonstrated [280] that the rotational correlation time τ_c of ^1H nuclei increases by a factor of 6.3×10^5 when a water molecule binds to agarose, presumably by multiple hydrogen bonds, and therefore these binding sites contribute significantly to relaxation processes (see also figure 2.14; when protons are in a more "solid-like" environment, with a longer τ_c, their T_2 is very short). It has been inferred that such water binding sites are related to the extent of cross-linking in BSA [280]. Given that the rotational correlation time of 2% weight/volume (w/v) agarose gel has been shown to be in the microsecond range (as has the τ_c for cross-linked BSA [281]), and that Kellar *et al* [282] demonstrated significant transfer of magnetisation from solvent to agarose, a relationship between the degree of cross-linking and the number of water binding sites, and therefore also the amount of MT exchange, seems a reasonable assumption.

7.1.1.2 Methods

7.1.1.2.1 Production of agarose gels

To test their suitability as MT phantoms, 2% w/v agarose gels were produced, using the Sigma-Aldrich recommended protocol (www.sigma-aldrich.com), as follows: Agarose was dissolved either in de-ionised water, or, for comparison, in a buffer solution (TBE buffer = 1.0M solution of 1.0M Tris, 0.9M Boric Acid and 0.01M EDTA). 40ml distilled water/TBE buffer was placed in a beaker with a stir bar, and the agarose powder slowly sprinkled into the liquid while stirring to prevent clumping. The stir bar was then removed and the beaker containing the agarose solution was weighed before heating, in order to control the volume (and hence concentration) of gel. The beaker was covered with clingfilm with holes pierced in the wrap for ventilation, then placed in a microwave and heated on high power for 1-2 minutes, before removing from the microwave and swirling gently to re-suspend any remaining agarose particles. The solution was then reheated on high power for a minute or so or until the solution came to a boil, and then boiled again for 1 more minute or until it became clear and the agarose was completely dissolved. The beaker plus solution was re-weighed and, while on the scales, enough hot distilled water was added to return the contents to the initial weight (and therefore volume) before heating. The solution was then poured into the 50ml test tubes, sealed using plastic (Whatman) sealing film to prevent dehydration, and allowed to cool at room temperature over a period of a few hours. The gels were then stored in a refrigerator (i.e. at approximately 4°C) in order to preserve the gels. Fungicide was not added as a preservative to these gels since the fungicide Sodium Azide (added to the BSA proteins as described in section 7.1.2.2.1) can become explosive on heating.

7.1.1.2.2 MRI acquisition methods

MTR data were acquired using both the Euro-MT gradient echo sequence (described in section 5.2.2 [63], [283]) (3 acquisitions were performed) and a 32-echo interleaved dual Spin Echo MTR sequence [55] (performed once). The acquisition parameters for the two MTR sequences are given in table 7.1.

Table 7.1: Acquisition parameters for the Euro-MT 2D spoiled gradient echo and 2D interleaved spin echo MTR sequences

Acquisition Parameter	2D Euro-MT Spoiled Gradient Echo MTR Sequence	2D Interleaved Dual Echo Spin Echo MTR Sequence
TR (ms)	960	1730
TR' (ms) (=TR/number of slices for a multislice acquisition)	34.3	123.6
TE (ms) or TE1/TE2 (ms) for spin echo sequence	12	31/80
Flip Angle (°) of gradient echo imaging pulse	20	N/A
Acquisition matrix	256 x 128	256 x 128
Reconstructed matrix	256 x 256	256 x 256
FOV (cm) (with ¾ FOV in the phase direction in both cases)	25 x 25	25 x 25
Number of slices	28	28 (interleaved dual echo: 14 slices in each acquisition)
Slice thickness (mm)	5	2.5
Inter-slice spacing (mm)	0	2.5
MT pulse shape	Gaussian	3-lobe Hamming apodised Sinc
Effective MT pulse flip angle θ_{sat} (°)	500	1430
ENR_{sat}[1] (°/ms)	14.6	11.6
MT pulse duration (ms)	7.68	16
MT pulse offset frequency (Hz)	1500	1000

[1]ENR_{sat} is the Effective Nutation Rate of the MT saturation pulse used in the sequence [76]. It is given by:

$$ENR_{sat} = \frac{\theta_{sat}}{TR'} \qquad 7.1$$

where θ_{sat} is the effective flip angle of the MT pulse, and TR' is the time between successive MT pulses. This is a measure of the 'degrees of saturation applied per unit time' and can be thought of as a simple measure of how 'powerful' the MTR sequences are. The total acquisition time for the Euro-MT sequence is just 3 minutes (approximately) whereas for the interleaved dual echo spin echo MTR sequence the acquisition time is approximately 19 minutes. The spin echo sequence is very long due

to time spent waiting for the free pool to reach equilibrium, and in addition, some T_1 weighting may be present since a short TR is required in order to minimise acquisition time. Some direct saturation of the free proton pool may also occur when using this sequence for MT imaging, since the offset frequency of the MT pulse is only 1kHz. This would have the effect of reducing the free pool signal and hence the MTR. Published normal white matter MTR values for the Euro-MT sequence and interleaved spin echo MTR sequence are 41.7 pu [284] and 39.2 pu [76] respectively.

qMT data were also acquired for the agarose phantoms, using the method developed by Ramani *et al* [47], (described in section 5.2.3) for comparison with BSA phantom qMT data.

7.1.1.3 Results

7.1.1.3.1 MTR data

The average Euro-MT MTR for the 2% w/v agarose gel dissolved in water was found to be 25.1±0.3pu (n=3), and the agarose dissolved in the TBE buffer was found to have an MTR of 24.9±0.8pu (n=3).

The interleaved spin echo MTR sequence yielded quite different results from the MTRs measured using the Euro-MT sequence for the agarose system; an MTR of just 14.4pu was measured with the agarose dissolved in water and 14.9pu when dissolved in the TBE buffer (n=1). This is likely to be due to differences in the two acquisition methods, in particular the MT pulse shape, amplitude and offset frequency, and the fact that a spin echo acquisition sequence was used rather than a gradient echo sequence. The Effective Nutation Rate (ENR_{sat}, given by equation 7.1) [76] of the Euro-MT gradient echo MTR sequence is a little higher than that of the interleaved spin echo MTR sequence (see table 7.1), i.e. the Euro-MT sequence is 'more powerful', in that it provides 'more degrees of saturation per unit time', therefore the lower MTR measured with the interleaved spin echo MTR sequence is unsurprising. The differences observed between measurements made using the two sequences are larger than would be expected from published values for both sequences in normal human white matter, however this can be attributed to the differences between the agarose system and human white matter. In particular, agarose is thought to be more "solid-like" than white matter, probably resulting in a larger restricted proton pool size and different absorption lineshape characteristics (see also section 7.1.1.3.2). Since the MTR depends on the reduction in restricted proton pool magnetisation due to the MT pulse, which is then transferred to the free pool via MT, in addition to any direct saturation of

the free pool signal which occurs, this might account for the larger differences observed between MTRs measured using the two different sequences.

However, it would be possible to increase the MTR of the agarose system from the values measured in this study by increasing the concentration of the gel, since the MT exchange in proteins is thought to be related to the degree of cross-linking, and therefore the number of water proton binding sites [282]. It was relatively easy to dissolve the agarose at this low concentration, and previous studies have used higher concentration agar-based gels [221], therefore it is likely that agarose samples of higher concentration could be easily prepared.

7.1.1.3.2 qMT data

qMT measurements performed on the 2% w/v agarose system, using the acquisition protocol developed by Ramani *et al* [47] yielded very different results for some of the qMT model function parameters depending on the particular lineshape used to model the RF absorption of the semi-solid pool (see table 7.2). The residual sum of squares (SSQ) divided by the degrees of freedom (dof) was much larger when a super-Lorentzian lineshape was used to model the restricted proton pool RF absorption, indicating that a Gaussian lineshape may be more appropriate for the agarose system. T_2^B and f values obtained using both lineshapes differed from typical values estimated from *in vivo* qMT experiments, but those obtained using the super-Lorentzian restricted proton pool lineshape were closer to those quoted for *in vivo* white matter than values obtained using a Gaussian lineshape. Table 7.2 gives the qMT parameters obtained for the two agarose samples. Z-spectra are also shown for the two different lineshapes, with experimental signal data points and theoretical lines calculated using fitted parameters on the same plots.

Table 7.2: Comparison of 2% w/v agarose gel (dissolved in TBE buffer) qMT parameters (data from a single acquisition) analysed using a Gaussian or a super-Lorentzian lineshape to model the RF absorption of the semi-solid pool.

Semi-solid pool absorption lineshape	Gaussian	Super-Lorentzian
Fundamental qMT Parameter		
RM_0^A (s^{-1})	2000	2000
$f/R_A(1-f)$ (s^{-1})	0.660	0.027
T_2^B (μs)	0.32	1.28
$1/R_A T_2^A$	79.6	45.7
gM_0^A	340.9	340.9
$T_1^A{}_{obs}$ (ms)	2197	2197
f (%)	18.1	1.20
SSQ/dof	98.8	209.8

The sum of squares residual (SSQ) divided by the degrees of freedom (dof) was used here as a measure of the "goodness-of-fit" of the qMT model to experimental data. This parameter is closely related to the reduced X^2, which is the sum of squares of ratios of the deviation at each data point of the model from the data to its 'error' (95% CL), subsequently divided by the degrees of freedom (number of data points minus the number of free ("adjustable") model parameters). Here, however, the parameter SSQ/dof was examined as the individual 'errors' at each data point are unknown since data are acquired only once at each data point in the qMT experiment, performed using the method of Ramani *et al* [285] (see also section 5.2.3).

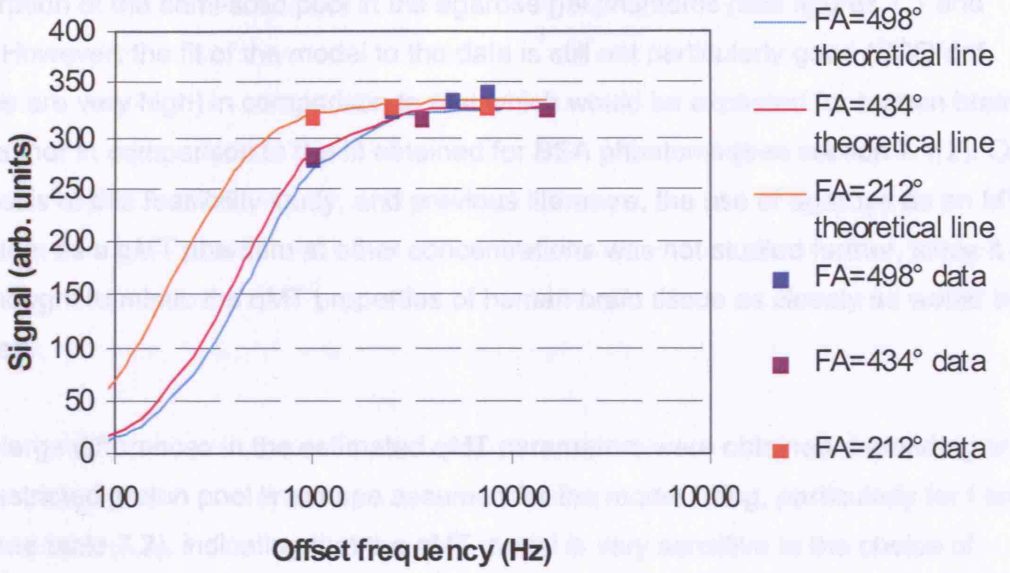

Figure 7.1: Z-spectra (plotted using fitted qMT model parameter values) using a Gaussian lineshape to model the RF absorption of the 'semi-solid' pool, and experimentally measured data points for 2% w/v agarose gel dissolved in TBE buffer.

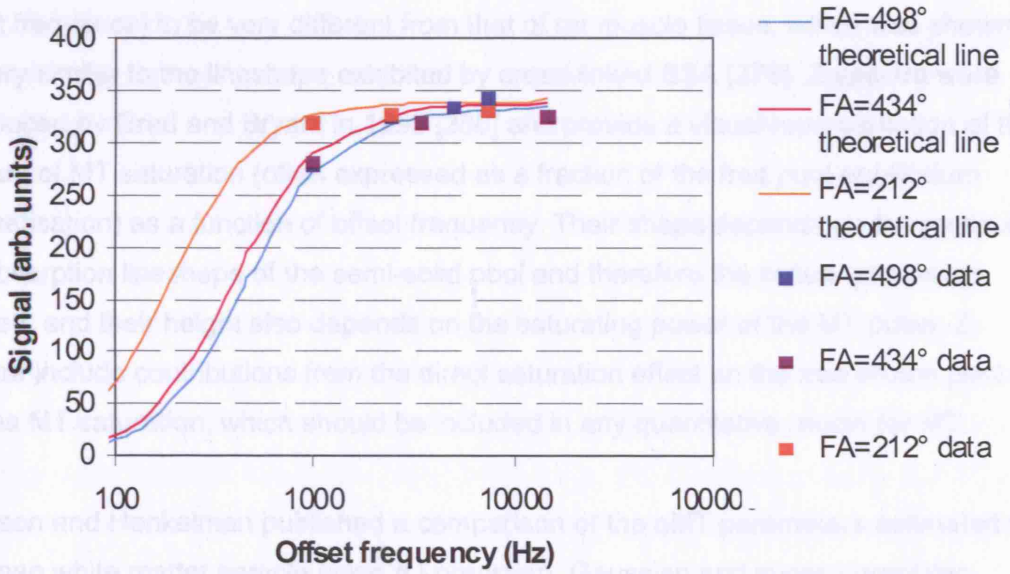

Figure 7.2: Z-spectra (plotted using fitted qMT model parameter values) using a super-Lorentzian lineshape to model the RF absorption of the 'semi-solid' pool, and experimentally measured data points for 2% w/v agarose gel dissolved in TBE buffer.

As expected from SSQ/dof values (see Table 7.2), a better quality of fit was obtained when a Gaussian rather than a super-Lorentzian lineshape is used to model the

absorption of the semi-solid pool in the agarose gel phantoms (see figures 7.1 and 7.2). However, the fit of the model to the data is still not particularly good (SSQ/dof values are very high) in comparison to that which would be expected for human brain tissue, nor in comparison to the fit obtained for BSA phantoms (see section 7.1.2). On the basis of this feasibility study, and previous literature, the use of agarose as an MT phantom as a qMT phantom at other concentrations was not studied further, since it is not thought to mimic the qMT properties of human brain tissue as closely as would be desired.

Very large differences in the estimated qMT parameters were obtained depending on the restricted proton pool lineshape assumed for the model fitting, particularly for f and T_2^B (see table 7.2), indicating that the qMT model is very sensitive to the choice of semi-solid pool RF absorption lineshape. The agarose system is thought to be "solid-like" hence it is unsurprising that a Gaussian restricted pool lineshape results in a better fit to data than a super-Lorentzian (see also sections 5.1.4.2-3), which is thought to be more appropriate to characterise human brain tissue. Mendelson *et al* demonstrated the shape of the agarose Z-spectrum (plot of magnetisation against offset frequency) to be very different from that of rat muscle tissue, which was shown to be very similar to the lineshape exhibited by cross-linked BSA [278]. Z-spectra were introduced by Grad and Bryant in 1990 [286] and provide a visual representation of the amount of MT saturation (often expressed as a fraction of the free pool equilibrium magnetisation) as a function of offset frequency. Their shape depends on the particular RF absorption lineshape of the semi-solid pool and therefore the tissue type being imaged, and their height also depends on the saturating power of the MT pulse. Z-spectra include contributions from the direct saturation effect on the free proton pool as well as MT saturation, which should be included in any quantitative model for MT..

Morrison and Henkelman published a comparison of the qMT parameters estimated for a human white matter sample using a Lorentzian, Gaussian and super-Lorentzian lineshape to represent the RF absorption behaviour of the semi-solid pool. They found that all estimated parameters varied depending on the semi-solid pool lineshape; in particular T_2^B was estimated to be much larger when a Gaussian semi-solid pool lineshape was used compared to the estimate obtained using a super-Lorentzian, and $1/R_A T_2^A$ was also much larger. R and RM_0^B/R_A did not vary much with lineshape; these were reduced when a Gaussian lineshape was used instead of a super-Lorentzian but less markedly [188]. A Lorentzian semi-solid lineshape yielded a very large T_2^B from the fit, unsurprisingly, as a long T_2 is required in order for the Lorentzian lineshape to be narrow.

7.1.2 Bovine Serum Albumin (BSA)

7.1.2.1 Literature review

Mendelson *et al* [278] demonstrated the much broader Z-spectrum of cross-linked BSA compared to agarose gels. The BSA system was found to exhibit similar qMT characteristics to rat muscle. The shape of the Z-spectrum is related to the spin-relaxation properties of the macromolecule spin system and cannot simply be adjusted by changing the concentration of the protein, whereas adjusting the concentration directly affects the T_1 and T_2 relaxation times, and the restricted proton fraction f.

A major contribution to the longitudinal relaxation rate $1/T_1$ of water protons involves transfer of longitudinal magnetisation (Zeeman energy) between the solvent and protein proton ensembles, which depends on the molecular rotational or translational mobility. For highly mobile protein protons, diffusion of Zeeman energy is accompanied by relaxation of magnetisation and only the outer shell of the protein is important in MT. However, for relatively immobile protein systems, magnetisation can diffuse through the protein with proton relaxation occurring at particular sites, which are generally assumed to be the rotationally immobile methyl groups within the protein [287]. The overall rotational motion of the protein molecules is slowed or stopped (leading to an increase in the correlation time), and there is little/no averaging of the proton dipole-dipole interactions. The immobilisation (cross-linking) of proteins causes increased magnetisation transfer at these sites in addition to an increase in the correlation time for MT. Protein-water interfacial interactions that couple the proton Zeeman energy reservoirs of solvent and BSA protein proton ensembles have been demonstrated to be very strong in cross-linked protein gels, increasing the range of transport of Zeeman energy within protons (and therefore the Zeeman reservoir), and the correlation times for interfacial contributions to relaxation rates [218], [280]. The spin population in this type of system is easier to saturate using MT pulses, and therefore cross-linked BSA has good potential for use as a phantom in MT imaging experiments.

Cross-linking can be achieved either thermally or chemically. It has been shown that, as the BSA cross-links and enters a solid phase, the relaxation times of the protein decrease irreversibly, T_1 by about 20%, and T_2 by approximately 80%, resulting in very short T_2 times, closely approaching those observed *in vivo* [218].

7.1.2.1.1 Thermal cross-linking

Two structural changes take place in BSA gels on heating; the first (up to ~65°C) is reversible, but the second (above ~65°C) is irreversible, although it does not necessarily involve complete destruction of the ordered structure of the protein. The

first stage of conformational changes begins at 58.1°C, but denaturation takes place between approximately 62 and 67°C [288].

7.1.2.1.2 Chemical cross-linking

Chemical cross-linking (e.g. using glutaraldehyde) [280] [289] entails denaturing by pH, and is caused by ionisation of side chains, but many molecules (i.e. rather than protons) may affect both the side chains and backbone of molecule. Zhou and Bryant [290] measured MT in chemically cross-linked (using glutaraldehyde) BSA proteins, and found that the pseudo first order magnetisation transfer rate constant increased as a function of the degree of cross-linking (using the glutaraldehyde concentration as an indicator of the extent of cross-linking).

Thermal cross-linking has previously been shown to produce more homogeneous gels than chemical cross-linking methods [291], [286].

Ewing *et al* also suggested dissolving the BSA in (physiological concentration) saline rather than water, since this would produce a protein solution more closely representative of the conditions of proteins in tissue [218].

Koenig and Brown showed the amount of MT exchange (as measured by the MTR) to be proportional to the BSA protein concentration, as expected [280]. Ewing *et al* also demonstrated that the BSA concentration is inversely proportional to the reduced T_1 of the protein (i.e. $T_1^A{}_{sat}$), and also confirmed that $1/T_1^A{}_{sat}$ is sensitive to the molecular mobility (i.e. whether or not the BSA is cross-linked) within the sample [218]. However, in this study it was assumed that the macromolecular pool is completely saturated, and that the direct saturation effect on the free proton pool was negligible, such that equation 3.7 holds true, which may have been true for their study but is not a valid assumption here since in any qMT experiment designed to be used clinically, complete saturation of the restricted protons is not viable.

Gochberg *et al* [225] demonstrated a linear increase in the pool size ratio (M_0^B/M_0^A) with BSA concentration, with a slope of approximately 1/3.

7.1.2.2 Methods

7.1.2.2.1 Production of BSA samples

BSA was dissolved in either distilled water or physiological concentration (0.9%) saline. On the basis of results of a feasibility study (see table 7.3), samples of concentration

20 and 25% BSA by weight were prepared, since these exhibited MTR values closest to those observed in human brain white matter (approximately 40pu).

The samples were sealed in 50ml plastic tubes with Whatman plastic sealing film after closing the lids firmly, to prevent evaporation and also contact with air, which may accelerate decomposition of the gels. The BSA samples were repeatedly weighed to ensure that no evaporation took place from the sample tubes.

Dissolving the BSA was difficult for the high concentration samples, even after using both a vortex mixer and spiramix, therefore the samples were heated in the oven at 45˚C in order to help them dissolve (denaturation occurs at 62-67˚C therefore the samples were not heated up to these temperatures until completely dissolved, in order to cross-link the BSA proteins).

The fungicide sodium azide was added to the BSA gels at a concentration of 0.01%, to prevent possible decomposition due to bacterial growth, which would affect the gel stability.

The samples were then thermally cross-linked by heating in a water bath at 80°C for about 10 minutes, and then left at room temperature for a few hours to allow the cross-linking reaction to continue. Finally they were sealed and placed in a refrigerator for storage (at ~4°C), also to prevent potential decomposition of the gels.

7.1.2.2.2 MRI acquisition methods

The BSA samples were scanned repeatedly over a period of a few months, using the modified Euro-MT sequence described previously (section 7.1.1.2.2), with the MTR sequence acquisition repeated three times at each time point.

For the feasibility study, samples of concentration 5-20% BSA were scanned on 5 separate occasions. On the basis of that feasibility study, samples of concentration 20% and 25% by weight dissolved either in water and in saline,were prepared and then scanned repeatedly using the Euro-MT sequence. qMT analysis was also performed on two occasions (although results from only one acquisition are shown in figures 7.3-7.6).

7.1.2.3 Results

Repeated weighing of the initial set of BSA samples showed that, to within 0.1g (compared to a total mass of 50g), no evaporation took place over a time period of several months.

7.1.2.3.1 MTR data

BSA MTR data are given in tables 7.3 (feasibility study using 4 different BSA concentrations) and 7.4 (2 BSA samples of higher concentration), with 95% CL given in brackets (i.e. 1.95SD). MTR data are also plotted as a function of BSA sample concentration for the feasibility study in figure 7.3, with error bars showing the 95% CL for each measurement. It was necessary to remove the BSA samples from the fridge and place them in the scanner room a few hours before scanning, to allow them to reach room temperature (since both T_1 and MTR depend on sample temperature). It was found that the 20% concentration BSA gels gave the most realistic (i.e. closest to those observed *in vivo*) MTR values, around 40 pu (as stated above, the average normal WM MTR value obtained using the Euro-MT sequence in a multi-centre study was 41.7pu on a GE scanner [292]). Thus, for subsequent experiments, BSA gels with concentrations of 20 and 25% both with and without the fungicide sodium azide were produced, again dissolved both in saline and distilled water. 0.01% concentration by weight sodium azide was used to preserve the phantom material. 25% concentration BSA gel gave even higher MTR values than 20% w/v BSA, but dissolving the BSA became progressively more difficult with increasing concentration.

Table 7.3: Mean MTR values obtained for BSA samples in feasibility study, measured using the Euro-MT gradient echo MTR sequence (data from 5 acquisitions)

Sample	MTR (± 95% CL) (pu)
5% w/v dissolved in water	18.5 (± 0.3)
10% w/v dissolved in water	31.5 (± 1.0)
15% w/v dissolved in water	37.5 (± 1.7)
20% w/v dissolved in water	41.4 (± 1.7)
5% w/v dissolved in saline	25.0 (± 0.6)
10% w/v dissolved in saline	33.5 (± 0.5)
15% w/v dissolved in saline	38.8 (± 1.6)
20% w/v dissolved in saline	42.1 (± 1.7)

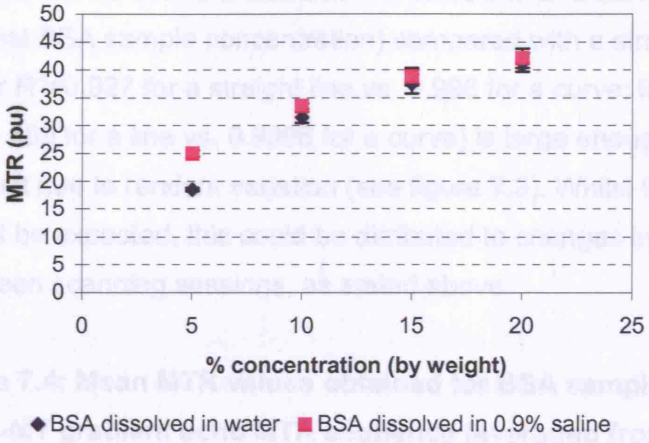

Figure 7.3: BSA sample MTR values as a function of sample concentration. Error bars indicate the 95% CL for each measured MTR value (data from 5 acquisitions; see table 7.3)

The samples dissolved in saline exhibit slightly higher MTR values than those dissolved in water, suggesting that these samples may be more appropriate to mimic human white matter *in vivo*. 95% CL on these measures larger than might be expected, which may be due to temperature changes between scanning sessions. From equation 3.7, it can be seen that the MTR scales with T_1, which is known to vary with temperature by about $2.4\%K^{-1}$ [293], therefore the MTR could be expected to vary similarly.

Previous work [280] indicated that MTR values increase with BSA concentration. However, previously the MTR was found to increase linearly with protein concentration. Here it was found that, whilst the MTR data plotted against protein concentration could be approximated by a straight line, a curve fitted the data better and gave a higher correlation coefficient than a straight line, for BSA dissolved in water or in saline (see also figure 7.3). There are a few possible explanations for this (see also section 7.1.2.3.2 regarding the trends in BSA qMT data with sample concentration). In addition to the MTR, $1/T_1{}^A{}_{sat}$ has also previously been shown to be proportional to the BSA protein concentration, and has also been shown to be sensitive to the degree of molecular mobility (i.e. cross-linking) [218], which may not increase linearly with concentration. Kellar *et al* [282] also suggested that the amount of MT exchange is related to the extent of cross-linking, and that the cross-linking itself depends on specialised water binding sites, where the exchange is assumed to take place (thought to be hydrogen bonding sites) [281].

The difference in size of correlation coefficient for a curve (of MTR value plotted against BSA sample concentration) compared with a straight line (for BSA dissolved in water R^2=0.927 for a straight line vs. 0.996 for a curve; for BSA dissolved in saline R^2=0.959 for a line vs. 0.9996 for a curve) is large enough to suggest that the trend is not just due to random variation (see figure 7.3). Whilst 95% CL may be larger than might be expected, this could be attributed to changes in scanner bore temperature between scanning sessions, as stated above.

Table 7.4: Mean MTR values obtained for BSA samples, measured using the Euro-MT gradient echo MTR sequence (averaged from 9 acquisitions)

Sample	MTR (± 95% CL) (pu)
20% w/v dissolved in water	40.4 (± 2.3)
25% w/v dissolved in water	41.7 (± 2.1)
20% w/v dissolved in saline	40.5 (± 2.7)
25% w/v dissolved in saline	43.1 (± 2.0)

Table 7.5: Mean MTR values obtained for BSA samples, measured using the interleaved spin echo MTR sequence (see table 7.1 for sequence details) (averaged from 4 acquisitions)

Sample	MTR (± 95% CL) (pu)
20% w/v dissolved in water	29.0 (± 0.7)
25% w/v dissolved in water	32.8 (± 0.5)
20% w/v dissolved in saline	28.9 (± 2.1)
25% w/v dissolved in saline	33.6 (± 1.6)

As for agarose, lower MTR values were obtained using the interleaved spin echo MTR sequence than when using the gradient echo Euro-MT sequence, because of differences between the two sequences (the Euro-MT sequence is more powerful).

7.1.2.3.2 qMT data

The BSA phantoms were also scanned using the qMT protocol developed by Ramani *et al* [47] (see also section 5.2.3), in order that, based on both qMT and MTR data, the optimum BSA concentrations (i.e. those with MT properties most similar to those observed in human brain tissue) could be selected for further investigations. The qMT parameter estimates for the BSA samples dissolved in saline, using the Gaussian and super-Lorentzian lineshapes to model the restricted proton pool, are shown in tables 7.6 and 7.7 respectively. However, it should be noted that the acquisition protocol of Ramani *et al* [47] was not fully optimised, therefore ideally these experiments should be

repeated using an optimal acquisition scheme (combination of MT pulse amplitudes and offset frequencies). The issue of optimising the qMT sequence acquisition will be addressed in chapter 8.

Table 7.6: qMT results for BSA samples dissolved in saline (data from a single acquisition), analysed using a Gaussian RF absorption lineshape to model the semi-solid pool

Fundamental qMT parameter	5% w/v BSA dissolved in saline	10% w/v BSA dissolved in saline	15% w/v BSA dissolved in saline	20% w/v BSA dissolved in saline
RM_0^A (s^{-1})	2000	2000	2000	2000
$f/R_A(1-f)$ (s^{-1})	0.012	0.031	0.040	0.041
T_2^B (μs)	30.14	18.10	19.23	22.94
$1/R_AT_2^A$	14.8	28.7	32.9	34.0
gM_0^A	434.1	410.5	394.8	312.2
$T_1^A{}_{obs}$ (ms)	1296	579	565	569
f (%)	0.88	5.3	6.8	7.0
SSQ/dof	14.2	11.1	15.1	18.4

Table 7.7: qMT results for BSA samples dissolved in saline (data from a single acquisition), analysed using a super-Lorentzian RF absorption lineshape to model the semi-solid pool.

Fundamental qMT parameter	5% w/v BSA dissolved in saline	10% w/v BSA dissolved in saline	15% w/v BSA dissolved in saline	20% w/v BSA dissolved in saline
RM_0^A (s^{-1})	2000	2000	2000	2000
$f/R_A(1-f)$ (s^{-1})	0.0178	0.046	0.057	0.063
T_2^B (μs)	9.59	4.77	5.48	6.50
$1/R_AT_2^A$	5.68	13.43	11.33	8.04
gM_0^A	434.9	411.4	385.9	314.5
$T_1^A{}_{obs}$ (ms)	1296	579	565	569
f (%)	1.28	7.56	9.50	10.36
SSQ/dof	12.9	8.7	8.1	3.1

Various trends in the BSA qMT data (tables 7.6-7.7) can be observed. Literature [280] indicated that MTR values increase linearly with BSA concentration, and $1/T_1^A{}_{sat}$ has also previously been shown to be proportional to the BSA protein concentration, which was additionally shown to be sensitive to the molecular mobility (i.e. cross-linking)

[218]. The qMT results from this study, however, indicate that the increase in f is not linear with concentration as might perhaps be expected.

As stated above, Gochberg *et al* [225] found that M_0^B/M_0^A (or k_f/k_m) increased linearly with BSA concentration (weight/volume), with a slope of approximately 1/3. They converted the x-axis from a weight ratio to a proton mole ratio, resulting in a slope of approximately 2/3. They suggested that if all free protons participate in spin exchange via diffusion, then at all BSA concentrations, effectively 2/3 of the macromolecular proton sites may exchange with free protons, and this result is consistent with exchange being limited to an outer layer of the macromolecular BSA complex.

In Ramani's qMT model, M_0^A is not normalised to unity, and the restricted proton fraction $f=M_0^B/(M_0^A+M_0^B)$, which could partially explain the non-linear increase in f with protein concentration; however, since $f<<1$ this is an unlikely explanation for this discrepancy.

Kellar *et al* [282] demonstrated that the rotational correlation time τ_c of ^1H nuclei increases by a factor of $6.3x10^5$ when a water molecule binds to agarose, and reasoned that these specialised water binding sites (assumed to be multiple hydrogen bonds [281]) are related to the extent of cross-linking. Since the correlation time for agarose was found to be in the microsecond range, similarly to BSA, they inferred that water exchange takes place at these sites and therefore that the extent of cross-linking of the protein must be related to the amount of MT exchange.

Koenig and Brown argued that particular hydration sites, with long-lived water molecules (~1μs), about 1% of a hydration monolayer, dominate relaxation behaviour [280], and that for relatively immobile systems, this rather long lifetime becomes the dominant correlation time for interfacial effects. They found by comparison of data and theory that there also exists a second class of hydration sites, with lifetimes ~23ns at 293K, and interpreted the proton $1/T_1$ profiles of cross-linked BSA in terms of magnetic dipolar interactions at these two classes of sites. Therefore, the relaxation profiles (and hence MT properties) of these systems depend on the surface densities of these sites, the residence lifetimes of the respective bound waters and the extent of coupling of the protons of these waters to protein protons. Changes in the relaxation (T_1 and T_2) profiles of the BSA system could potentially, therefore, have an impact on the restricted proton fraction estimated using the qMT model for fitting and would therefore not necessarily be expected to be directly proportional to the protein concentration.

The restricted proton pool T_2^B relaxation time does not appear to follow a particular trend with concentration, regardless of the lineshape assumed for fitting. T_2^B is thought to reflect the geometry and structure of the restricted pool, indicating how 'tightly bound' the protons are to macromolecules, therefore this result is surprising. Tyler and Gowland demonstrated a linear increase of M_0^B relative to M_0^A with concentration in agar gel, and their M_0^B measurements were consistent with previous estimates from the literature [221]. However, they found no trend in T_2^B values with concentration, and also found that this parameter showed large variability. By re-fitting for M_0^B alone at various T_2^B values, they were able to show that when plotted against T_2^B, the fitted M_0^B values described a broad minimum in M_0^B, and therefore that varying T_2^B around this minimum in M_0^B led to very small changes in M_0^B, which may explain this large variability in T_2^B.

Interestingly, the fit of the model to data improves with increasing BSA concentration (i.e. SSQ/dof decreases) when a super-Lorentzian lineshape is used to model the semi-solid pool RF absorption (table 7.7). This could be explained by hypothesising that with increasing concentration the BSA system appears to be approaching more closely the qMT model for biological tissue, incorporating the super-Lorentzian restricted pool absorption lineshape (the restricted proton fraction f in healthy human white matter is of the order of 9-15% [48], [208], [212]). The parameter RM_0^A appears to give little meaningful physical information. It does not fluctuate greatly from the initial starting value input into the fitting routine, however if the parameter is set to a value much lower/higher than this, the other free parameters of the qMT model are relatively unaffected. Fixing this parameter when performing the fitting routine may prove to be more effective, and may allow a more accurate estimation of the remaining qMT model parameters. gM_0^A (a factor related to the scanner receiver 'gain', and the apparent PD of the sample) decreases with increasing sample concentration, which may seem surprising, but this may also depend on other factors such as the extent of cross-linking of the protein. The restricted proton fraction f increases with concentration, but not linearly as may be expected. This may be partly a result of the reduction of the free pool longitudinal relaxation time T_1^A with increasing concentration, as spins become less "free", and the gel becomes more "solid-like".

It should also be noted that SSQ/dof values obtained from fitting the qMT model to experimental data for agarose gels (table 7.2) were much larger than those obtained for the BSA gels (tables 7.6-7), indicating that the qMT model is more appropriate to describe BSA protein than for agarose, and since the qMT parameters extracted for

BSA are closer to those of human brain tissue than agarose, it could be suggested that BSA more closely mimics the properties of human brain tissue.

qMT results for the BSA gels that exhibit qMT parameters closest to those of human brain white matter (i.e. 20 and 25% w/v) are given below, analysed using a Gaussian restricted pool absorption lineshape (table 7.8) and a super-Lorentzian lineshape (table 7.9). 95 % CL are given in brackets.

Table 7.8: qMT parameter values for BSA gels (from 3 acquisitions), analysed using a Gaussian restricted pool absorption lineshape

Fundamental qMT Parameter	20% BSA dissolved in water	25% BSA dissolved in water	20% BSA dissolved in saline	25% BSA dissolved in saline
RM_0^A (s^{-1})	2000.0 (± 0.02)	2000.0 (± 0.01)	2000.0 (± 0.01)	2000.0 (± 0.02)
$f/R_A(1-f)$ (s^{-1})	0.044 (± 0.008)	0.043 (± 0.005)	0.037 (± 0.008)	0.050 (± 0.004)
T_2^B (μs)	23.5 (± 5.9)	22.8 (± 1.9)	24.9 (± 6.4)	21.0 (± 3.1)
$1/R_AT_2^A$	38.4 (± 4.0)	44.1 (± 3.4)	39.0 (± 6.3)	44.7 (± 10.7)
gM_0^A	326.7 (± 70.4)	272.4 (± 64.2)	311.0 (± 92.7)	291.8 (± 85.7)
$T_1^A{}_{obs}$ (ms)	564.6 (± 121.5)	510.0 (± 219.6)	531.1 (± 73.7)	479.1 (± 67.8)
f (%)	7.63 (± 4.46)	8.28 (± 2.36)	6.80 (± 2.23)	10.05 (± 1.73)

Table 7.9: qMT parameter values for BSA gels (from 3 acquisitions), analysed using a super-Lorentzian restricted pool absorption lineshape

Fundamental qMT Parameter	20% BSA dissolved in water	25% BSA dissolved in water	20% BSA dissolved in saline	25% BSA dissolved in saline
RM_0^A (s^{-1})	2000.0 (± 0.02)	2000.0 (± 0.01)	2000.0 (± 0.02)	2000.0 (± 0.02)
$f/R_A(1-f)$ (s^{-1})	0.067 (± 0.020)	0.063 (± 0.012)	0.056 (± 0.0087)	0.072 (± 0.0052)
T_2^B (μs)	6.57 (± 0.765)	6.79 (± 0.211)	7.31 (± 1.84)	6.29 (± 1.31)
$1/R_AT_2^A$	11.4 (± 8.3)	16.4 (± 5.0)	14.4 (± 4.98)	14.3 (± 13.6)
gM_0^A	329.3 (± 72.0)	274.1 (± 65.0)	313.0 (± 92.7)	293.3 (± 86.4)
$T_1^A{}_{obs}$ (ms)	564.7 (± 121.5)	509.8 (± 219.6)	531.1 (± 73.7)	479.1 (± 67.8)
f (%)	11.27 (± 5.65)	11.87 (± 2.75)	9.98 (± 2.81)	14.07 (± 1.94)

It can be seen from tables 7.8 and 7.9 that very different results are obtained for the parameter T_2^B depending on the lineshape chosen to model the RF absorption of the semi-solid pool when fitting the qMT model to data. There are also substantial differences in other parameters depending on the lineshape, in agreement with previous work (see section 7.1.1.3.2). It is also noted that the samples dissolved in saline rather than water exhibit larger f values, which may indicate that these samples

exhibit qMT properties closer to those of human brain white matter. The parameter $1/R_AT_2^A$ also differs considerably depending on the restricted pool absorption lineshape assumed for fitting the qMT model to data. $1/R_AT_2^A$ can also be used to estimate the amount of direct saturation, which depends on the MT pulse amplitude ω_{1CWPE}, the offset frequency Δf and the fitted values of $1/R_AT_2^A$, which varies with tissue type [47].

Since tables 7.8-7.9 comprise data obtained from 3 separate qMT experiments, residual sums of squares divided by the degrees of freedom are not shown, but these were of the order of 4-28 (mean 13.3, SD 6.4) when using a Gaussian lineshape to model the RF absorption of the restricted proton pool, and ~2-9 (mean 5.0, SD 2.1) when using a super-Lorentzian restricted pool absorption lineshape. This indicated that the BSA system is much more appropriate to mimic the MT characteristics of human brain tissue, for which a super-Lorentzian restricted pool lineshape has been shown to be more appropriate [188], [208]. The SSQ/dof values obtained when fitting the qMT model to data obtained for the 20 or 25% concentration BSA samples were also much lower than those obtained for lower concentrations, indicating that the MT properties at these higher concentrations are closer to those observed *in vivo* (see tables 7.6-7.7 and 7.8-7.9).

Example Z-spectra from a single experiment for 20% w/v BSA dissolved in water and in saline, also both analysed using a Gaussian and a super-Lorentzian restricted pool absorption lineshape are shown in figures 7.4–7.7.

BSA samples Z-spectra – results from a single experiment

The Z-spectra below are for the 20% w/v BSA dissolved in water and then in saline. Results from fitting the model to data using both the Gaussian and the super-Lorentzian lineshape for the restricted proton pool are shown in both cases, to demonstrate the better quality of fit obtained using the Gaussian lineshape.

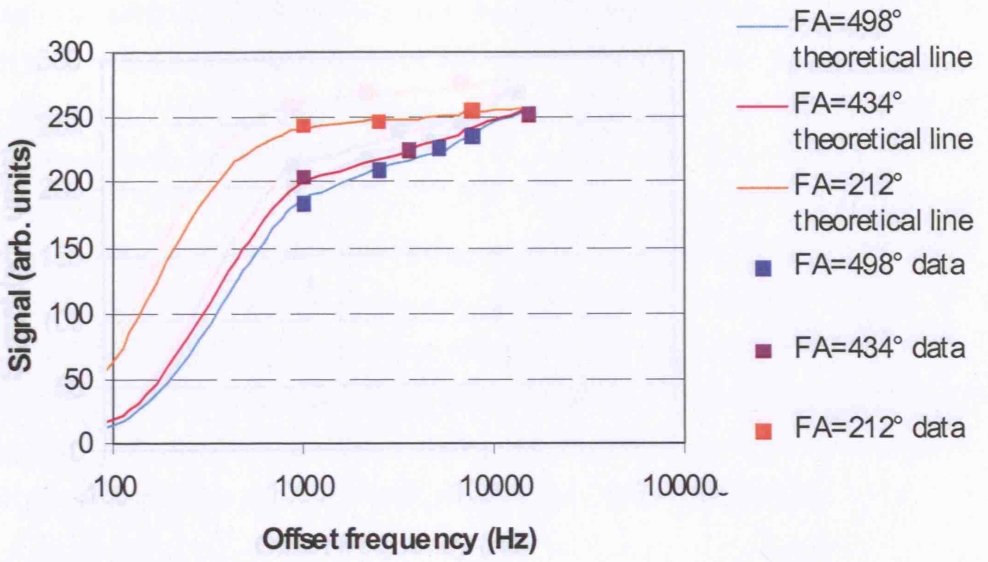

Figure 7.4: Z-spectrum for 20% w/v BSA gel dissolved in water, using a Gaussian lineshape to model the semi-solid pool RF absorption

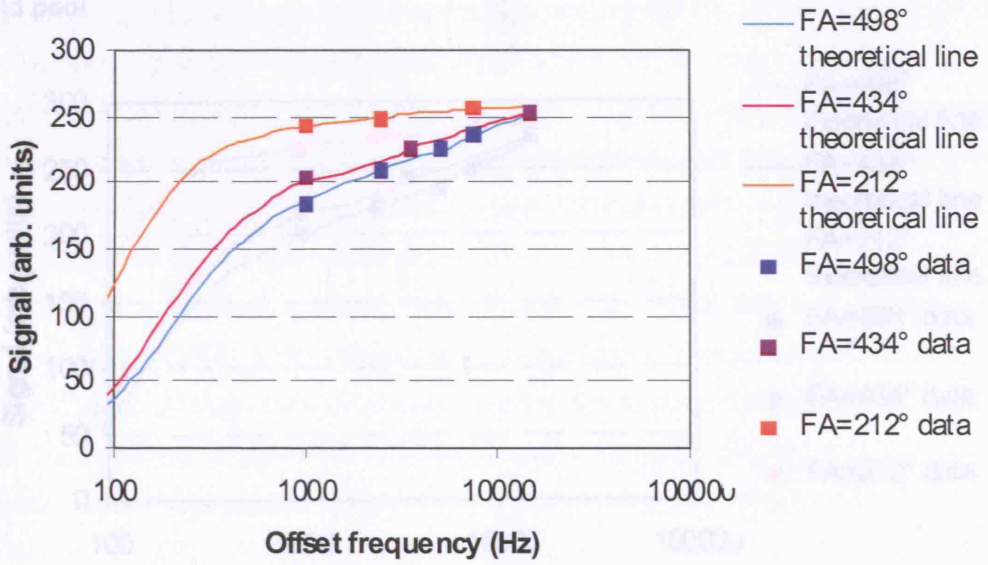

Figure 7.5: Z-spectrum for 20% w/v BSA gel dissolved in water, using a superLorentzian lineshape to model the semi-solid pool RF absorption

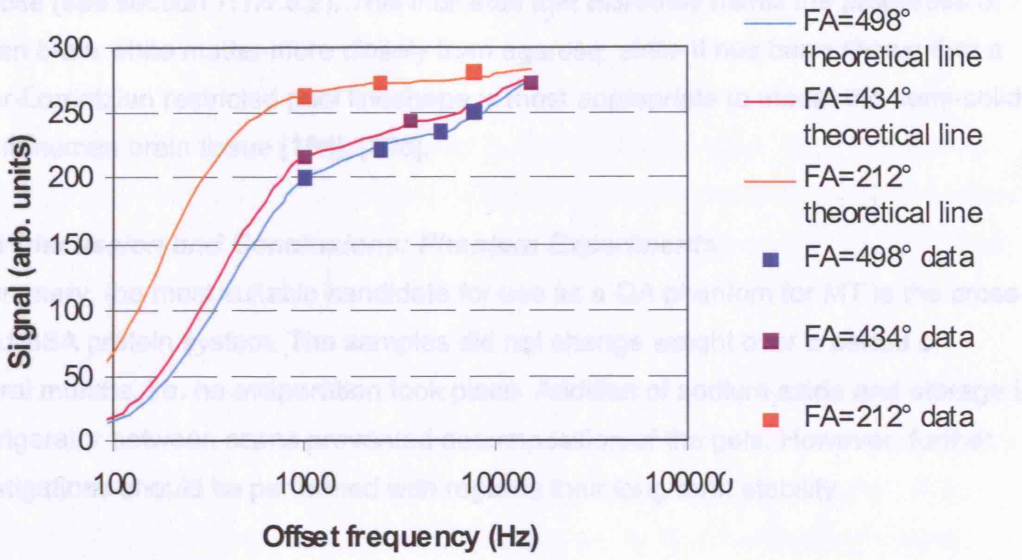

Figure 7.6: Z-spectrum for 20% w/v BSA gel dissolved in normal physiological concentration saline, using a Gaussian RF absorption lineshape for the semi-solid pool

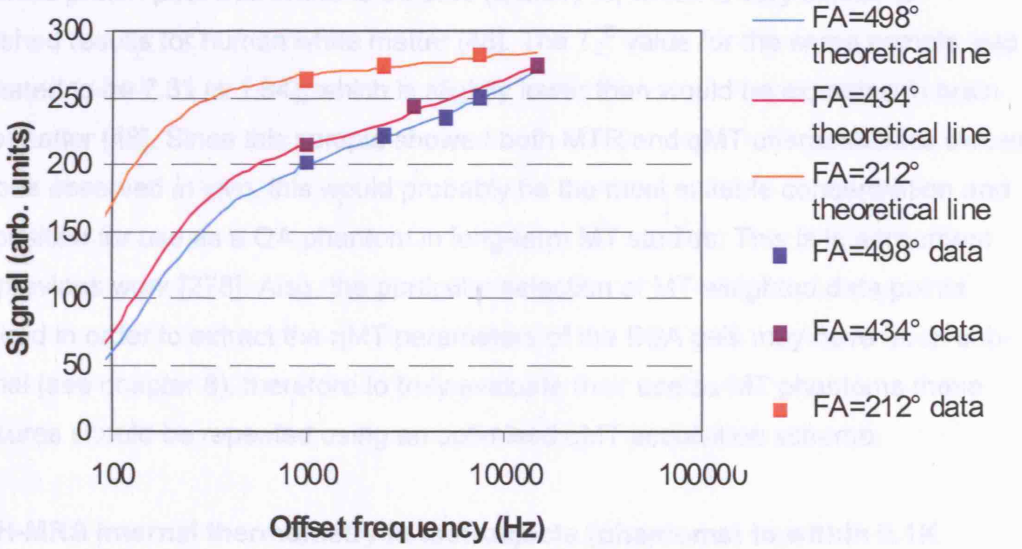

Figure 7.7: Z-spectrum for 20% w/v BSA gel dissolved in normal physiological concentration saline, using a superLorentzian RF absorption lineshape for the 'semi-solid' pool

It can be observed from figures 7.4 - 7.7 that a slightly better fit of the qMT model to experimental data is obtained when using a super-Lorentzian lineshape to model the semi-solid pool, rather than a Gaussian, which was found to be more suitable for

agarose (see section 7.1.1.3.2). This indicates that BSA may mimic the properties of human brain white matter more closely than agarose, since it has been shown that a super-Lorentzian restricted pool lineshape is most appropriate to model the semi-solid pool in human brain tissue [188], [208].

7.1.3 Discussion and Conclusions: Phantom Experiments

In summary, the most suitable candidate for use as a QA phantom for MT is the cross-linked BSA protein system. The samples did not change weight over a period of several months, i.e. no evaporation took place. Addition of sodium azide and storage in a refrigerator between scans prevented decomposition of the gels. However, further investigations should be performed with regards their long-term stability.

BSA samples of 20% w/v concentration were shown to exhibit MTR values of around 40pu, which is very close to those observed in human white matter, using the Euro-MT MTR sequence [63], [294]. The restricted proton fraction f for a 20% w/v concentration BSA sample, using the super-Lorentzian lineshape to model the RF absorption of the restricted proton pool was found to be 9.98 (± 2.81) %, which is very similar to published results for human white matter [48]. The T_2^B value for the same sample was estimated to be 7.31 (± 1.84), which is slightly lower than would be expected in brain white matter [48]. Since this sample showed both MTR and qMT characteristics closest to those observed *in vivo*, this would probably be the most suitable concentration and composition for use as a QA phantom in long-term MT studies. This is in agreement with previous work [278]. Also, the particular selection of MT-weighted data points acquired in order to extract the qMT parameters of the BSA gels may have been sub-optimal (see chapter 8), therefore to truly evaluate their use as MT phantoms these measures should be repeated using an optimised qMT acquisition scheme.

7.2 ^{1}H-MRS internal thermometry in test-objects (phantoms) to within 0.1K

Long-term clinical MRI studies require scanners to be stable over time. Stability (long-term reproducibility) can sometimes be established by making measurements in normal control subjects, however these are likely to vary at least a small amount during studies which may extend for several years or decades. A more attractive option is to use stable test-objects (phantoms) to perform serial QA measurements. The quantitative Magnetic Resonance (qMR) properties of phantoms (e.g. T_1, self-diffusion coefficient D, MTR) often vary with temperature; thus the phantom temperature must be known at the time of data collection. At our MR facility, the scanner bore temperature commonly varies by ~2 – 5 K over a timescale of weeks, and if not accounted for, such variations limit the minimum detectable size of changes in phantom qMR parameters or in

scanner performance, and this will have an impact on the interpretation of quantitative changes observed in long-term clinical studies.

Multi-centre studies require that measured quantities be accurate (i.e. in close proximity to true values). Phantoms are needed to establish this, and these can either be a single object sent between centres, or a set of identical phantoms can be made from a standard substance (e.g. alkanes for D measurements [295]).

After a property has been measured at a known temperature, and given knowledge of how its property varies with temperature, the measurement can be used in one of two ways. Firstly, the difference between the measured value and the true value, at the measurement temperature, can be reported, probably as a percentage difference. Secondly, the measurement can be converted to that at a standard reference temperature (e.g. 295K); this can then be compared with measurements made at other times or at other centres. However, many traditional thermometry methods are unsuitable for use in the scanner. Here a simple, readily available thermometry method is developed for use in MRI phantoms.

Proton magnetic resonance spectroscopy (^{1}H-MRS) has previously been used to estimate accurately absolute tissue temperature *in vivo*, based on the linear temperature dependence of the chemical shift difference between water and temperature-stable reference metabolites such as *N*-acetylaspartate (NAA). In this study, the applicability of this method to accurately determine the temperature of QA test-objects was investigated, and in particular the value of DSS (sodium 3-(trimethylsilyl)propane-1-sulphonate)) as a chemical shift reference was demonstrated. This work has been published in abstract form [296] and subsequently in NMR in Biomedicine [297].

7.2.1 Temperature Dependence of MR Properties

If the test-object temperature is known, it is possible to account for uncontrolled changes in the test-object quantitative MR properties. Conventional thermometry techniques are unsuitable for use in MRI scanners, and may result in image artefacts. Alternative thermometry methods, such as MR-compatible thermocouples, are expensive and may complicate experiments. However, if the absolute temperature (T) dependence of a particular qMR measure is robustly defined, an internal estimate of the test-object temperature can be made, and could be used to correct qMR measurements performed in the same session.

Venkatesan *et al* measured a change in signal amplitude in PD-weighted images of -0.32% K^{-1} in a water phantom [293]. The same group also measured a T_1 temperature coefficient of +2.4% K^{-1} in water [293], and the T_1 temperature coefficients of the Eurospin gels ($GdCl_3/LaCl_3$ doped agarose) are reported to be +2.6% K^{-1} at 1.5 Tesla (T) and 294K [6]. The T_2 temperature coefficient for the Eurospin gel closest to brain tissue is -1.5% K^{-1} [6]. The temperature coefficient for D in free water is approximately +2.5% K^{-1} [298] and D has been proposed for non-invasive MR temperature mapping [298], [299], although this method has fallen out of use. However, instrumental imperfections, such as gradient miscalibration, static field drift, off-resonance operation, errors in RF calibration or slice profile are likely to produce systematic errors in estimates of all these quantities, confounding their use to correct for sample temperature.

Since temperature coefficients of MR quantities are ~2-3% K^{-1}, to provide a QA measurement accurate e.g. to within 1% of a previous calibration, temperature should ideally be known to within 0.3K [6].

The ^1H chemical shift of water (δ_{H2O}) is linearly dependent on temperature between 273K and 313K, due to thermally driven changes in the hydrogen bonding in water molecules [300], [301], [302]. δ_{H2O} has therefore been proposed as an MR temperature probe, initially exploited in the proton resonant frequency phase-sensitive gradient echo imaging technique [303]. This method provides reliable estimates of temperature changes relative to a baseline acquisition, but does not provide a measure of absolute temperature as would be required for correction of QA measurements. This can be achieved with ^1H-MRS using a suitable temperature-stable internal chemical shift reference. For *in vivo* applications, the chemical shift of N-acetyl aspartate (NAA) ($C_6H_9NO_5$), δ_{NAA}, has been proposed as a reference, since σ_{NAA} (= δ_{H2O} - δ_{NAA}) has also been shown to be stable with respect to pH and ionic strength fluctuations within the ranges encountered physiologically [301], [304].

This ^1H-MRS thermometry technique appears promising for incorporation in QA protocols, because of the linear temperature dependence of δ_{H2O}, its ease of measurement, and because absolute temperature values are available from a single measurement. Additionally, assuming that the temperature is uniform throughout the sample, the chemical shift difference between δ_{H2O} and a suitable reference peak may be obtained independently of gradient errors, RF miscalibration, or off-resonance errors.

In order to explore the applicability of "self-referenced" ^{1}H-MRS thermometry in QA test-objects, we aimed first to determine a suitable temperature-stable chemical shift reference suitable for incorporation into QA phantoms and secondly to explore the accuracy and precision with which temperature could be determined using this method.

7.2.2 Methods

7.2.2.1 Selection of a suitable Reference Compound

In terms of potential for use in everyday test-objects, NAA is cost effective, demonstrates good solubility, has an intrinsic T_2 of about 0.5s, and σ_{NAA} (= δ_{H2O} - δ_{NAA}), which is of the order of 2.7 ppm around room temperature, and exhibits minimal pH dependence [305]. Each NAA molecule only has one methyl group; therefore the methyl group proton mass fraction in NAA is 0.017, resulting in a fairly low intrinsic signal-to-noise ratio (SNR) at low concentrations, although this could obviously be improved by increasing the concentration (with an associated increase in cost) of the phantom solution (see also table 7.10). NAA is also partially biodegradable, rendering it unsuitable for use in long-term studies, whereas the alternative reference species considered in table 7.10 are all thought to be non-biodegradable (http://www.sigmaaldrich.com).

Alternative reference compounds for use in internal thermometry were considered and, based on several factors (see table 7.10), DSS sodium salt (sodium 3-(trimethylsilyl)propane-1-sulphonate or $(CH_3)_3SiCH_2CH_2SO_3Na$), a standard NMR chemical shift reference, was selected as the most suitable candidate. DSS is very hygroscopic, and thus exhibits good solubility. The methyl group proton mass fraction is 0.041, resulting in a fairly high intrinsic SNR. The T_2 of DSS is also rather long, resulting in a relatively narrow spectral linewidth. The chemical shift difference between DSS (δ_{DSS}) and δ_{H2O} (σ_{DSS} (i.e. $\delta_{H2O} - \delta_{DSS}$) =4.742ppm at 300K) is much larger than σ_{NAA} (≈2.7ppm at 300K), which may reduce the effect of the sloping water peak baseline on estimates of the DSS peak position in comparison to NAA peak position estimates [306].

An alternative choice for test-objects comprising organic solvents might be Tetramethylsilane (TMS or $(CH_3)_4Si$) but this was eliminated because it is only very sparingly soluble in water, is toxic, and is usually dissolved in a deuterated chloroform ($CDCl_3$) solvent, which itself should only be handled in a fume hood. Another potential chemical shift reference, TSP sodium salt (sodium 3-(trimethylsilyl) propanoate, or $C_6H_{14}O_2SiNa$) was also considered unsuitable since it is also toxic and very expensive,

and its chemical shift has also been shown to exhibit some pH dependence (see table 7.10) [306].

Table 7.10: Properties of temperature-stable compounds for potential use as reference substances (in order of desirability)

Property	Potential reference compound			
	DSS (sodium-3-(trimethylsilyl-1-propane sulphonate))	**TMS (Tetramethyl silane)**	**NAA (N-acetyl aspartate)**	**TSP (sodium 3-(trimethyl silyl) propanoate)**
Molecular formula	$(CH_3)_3SiCH_2CH_2SO_3Na$	$(CH_3)_4Si$	$C_6H_9NO_5$	$C_6H_{14}O_2SiNa$
Compound – water chemical shift (ppm)	4.8	4.8	2.7	4.8
Formula Weight	218.33	88.22	175.14	168.25
Methyl Group Proton Mass Fraction	0.041	0.136	0.017	0.054
Solubility	Good; hygroscopic[a]	Poor in water, good in organic solvents[a]	Good[a]	Good; hygroscopic[a]
(Temporal) Chemical Stability	Stable[a]	Unstable[a]	Stable [307]	Unstable[a]
Bio-degradability	Non-biodegradable[a]	Non-biodegradable[a]	Biodegradable[a]	Non-biodegradable[a]
pH dependence	0ppm (pH 2-11) [306]	-	change <0.01ppm (pH 3 – 9) [305]	$\delta_{TSP} = \delta_{TSPobs} - 0.019 * (1+10^{(5.0-pH)})^{-1}$ (at 25°C, pH 7.0) [308]
Approximate Cost/5g Euros *(USD)*	44 *(59)*[a]	41 *(54)*[a]	128 *(171)*[a]	183 *(245)*[a]
Biohazard	Non-toxic[a]	Toxic[a]	Non-toxic[a]	Toxic[a]

[a]Sigma-Aldrich online catalogue: http://www.sigmaaldrich.com

7.2.2.2 Insulating "Isothermal Enclosure"

A cylindrical insulating "passive isothermal enclosure" was designed (by P. S. Tofts at the Institute of Neurology) to hold the cylindrical bottle containing DSS solution, in order that its temperature remained as constant as possible throughout the experiment. This was constructed from phenolic foam (Kingspan Kooltherm K7 board), with thermal conductivity $\kappa=0.022 Wm^{-1}K^{-1}$, and was shown to be capable of maintaining a constant temperature to within 0.2K for 100 minutes (which should be adequate for a typical QA experiment), whereas in comparison, the loading ring (used to ensure correct loading when scanning a phantom rather than a human head) temperature increased by 1.0K [309]. The cylindrical 'enclosure' was designed to fit closely inside the birdcage head coil (diameter 18cm) of the GE Signa 1.5T scanner (General Electric, Milwaukee, WI, USA).

7.2.2.3 Calibration Experiment: Temperature Dependence of σ in DSS

To regulate pH, aqueous solutions of 60 mM DSS were prepared in a phosphate buffer solution consisting of 72mM K_2HPO_4, 28mM KH_2PO_4, and 200mM sodium formate (recommended LCModel metabolite solvent) in 150ml cylindrical bottles (which were then heated/cooled to different temperatures). The solutions were titrated carefully using 1M Sodium Hydroxide (NaOH) to pH neutral in order to control for any potential pH dependence of the reference compound chemical shift.

The bottles (diameter 50mm x height 104mm, neck internal diameter 26mm) were encased individually in the phenolic foam insulating cylinder as described. Using the birdcage head coil on the 1.5T GE Signa scanner, single voxel ^{1}H-MRS PRESS spectra without water suppression were acquired with a repetition time (TR) = 3s, echo time (TE)=30ms, voxel size 2.30cm x 2.02cm x 1.50cm. Twelve sets of eight averages (total number of signal averages (N_{av}) =96) were collected, giving a total acquisition time for each spectrum of 4 minutes 48s, which is half the N_{ax} acquired in *in vivo* SVS PRESS studies. For an extension to a routine QA experiment, this was deemed an acceptably short scanning time and the resulting spectra had a good SNR. 2048 data points were collected with a spectral width of 2500Hz, giving a spectral resolution of 1.22Hz/point.

Data were acquired at five different temperatures, ranging from 286K to 309K. The solutions were heated or cooled in water baths for several hours prior to the experiment in order to achieve a uniform temperature throughout each sample. The temperatures of the solutions were measured using a K-type thermocouple (accurate to within 0.1K), to ensure that there was no temperature change during the acquisitions. Two spectra

were acquired at each temperature (without voxel re-positioning, shimming or other pre-scan adjustments between measurements). The chemical shift difference between δ_{H2O} and δ_{DSS} (σ_{DSS}) was estimated using two different analysis software packages (see section 7.2.2.6). From the 5 pairs of measurements, the SD of the signed difference between each pair of repeated measurements was used to estimate the SD of a single σ measurement [274]. Linear regression was performed using the mean σ_{DSS} at each temperature in order to quantify the relationship between T and σ_{DSS}.

7.2.2.4 Reproducibility Experiment in DSS

The objective here was to characterise the reproducibility of thermometry measurements under conditions of stable temperature with a realistic pre-scan setup procedure before each repeated data collection. In this case measurements were made using a 250mM DSS solution held in a 39ml volume plastic bottle (diameter 33mm x height 61mm, neck internal diameter 19mm). To enable the use of the insulating enclosure, these were submerged in a cylindrical water bath (volume 250ml, diameter 60mm x height 145mm) at room temperature (and these were placed in the scanner room several hours before the experiment in order to ensure that they reached thermal equilibrium). The time for each experiment was short (<5 minutes), and the delay between experiments was minimal, therefore it could safely be assumed that there were no changes in temperature between individual experiments, especially as the solution temperature was approximately equal to room temperature (i.e. any temperature gradient would be very small). Ten acquisitions were made, the sample being removed, repositioned and re-shimmed between each acquisition and the SD of a single temperature measurement was estimated from these 10 acquisitions (using the same size voxel as for the calibration experiment). The whole procedure was repeated for 5 different values of N_{av} ranging from 32 to 96, and the temperature was checked (using the thermocouples previously described) between successive sets of 10 experiments. The SDs obtained from each set of 10 experiments were assumed to be a measure of the reproducibility of the temperature measurement at each NEX value.

7.2.2.5 Feasibility study in aqueous gels

The possibility of dissolving the DSS reference compound in aqueous gel-based phantom materials was also investigated. The concern here was to determine if the reference compound had undesired effects on the phantom material, or vice versa. Preliminary investigations were performed in agarose and BSA. 2% w/v agarose gel and 20% w/v BSA were made up in 50ml test tubes, both containing 60mM DSS. Non water-suppressed ^{1}H-MRS data were acquired using the PRESS sequence as

previously described and the linewidths of the DSS and water peaks measured using the SAGE (Spectroscopy Analysis by General Electric) software package (version 2003.1) (General Electric Medical Systems, Milwaukee, WI, USA).

7.2.2.6 Data analysis methods

For comparison, results for both the calibration and reproducibility experiments were analysed using two different spectroscopy analysis software packages (table 7.11).

Using the SAGE software, the time domain data having been averaged, then zero filled 8 times (i.e. expanded by a factor of 256) prior to Fourier transformation. Preliminary experiments demonstrated that, for the quality of data obtained in these acquisitions, automatic peak picking (in the frequency domain) gave a more reproducible estimation of chemical shift difference than fitting model line shapes to the spectra, therefore zero filling improved the precision of peak location measurements. Automatic zeroth order phasing was performed, with small first order manual adjustments where necessary. Maximum precision was obtained with SAGE software configured to report results in Hz (where the 'digital precision' is 0.01Hz, i.e. 0.000157 parts per million (ppm), corresponding to 15.1mK) rather than in chemical shift units. The software displayed the same number of significant figures using either units, and therefore compared to ppm, the 'digital precision' was higher in Hz. The σ difference between water and the DSS reference peak was then calculated and the results reported in ppm. The reproducibility calculated for data analysed using SAGE with the same procedure but without zero filling is also indicated for comparison.

Data were also analysed using the AMARES [310] algorithm implemented using the non-proprietary jMRUI (java-based Magnetic Resonance User Interface) analysis software (version 2.1) [311]. Peak positions (and therefore the water-reference peak σ difference) were obtained by fitting exponentially damped sinusoids to time domain data (equivalent to fitting Lorentzian lineshapes in the frequency domain). The zeroth and first order phase corrections for each peak were determined automatically, and no advantage is obtained by zero-filling prior to analysis; this software also reported peak positions with a digital precision of 0.01Hz or 15.1mK when set to report results in Hz rather than ppm.

Table 7.11: Reproducibility measured using the two different spectroscopy analysis software packages.

Software	SAGE*	jMRUI
Pooled SD (±95% CL) (mK))	50 (±10)	184 (±36)

*If no zero filling was performed the reproducibility obtained using the SAGE software was 930 (±183) mK.

7.2.3. Results

7.2.3.1 Calibration Experiment: Temperature dependence of σ

SAGE software analysis

The temperature dependence of σ_{DSS} ($\delta_{H2O} - \delta_{DSS}$) is shown in figure 7.8. Linear regression yielded the relationship:

$T = 764.55\ (\pm 5.05) - 97.72\ (\pm 1.05)\ \sigma_{DSS}$ K 7.2

where standard errors on the slope and intercept of the results of regression analyses are given in brackets, and the regression correlation coefficient r=0.999. The root mean square (rms) residual in fitting the straight line to data was 0.14K. The SD obtained using SAGE software for analysis (with 95% CL on estimating the SD in brackets) was estimated to be 0.14 (±0.13) K. The 95% confidence limits on the SD (i.e. $1.95s_{SD}$, where s_{SD} is the uncertainty on the SD, were calculated using the relation $s_{SD} = SD/\sqrt{2(n-1)}$, where n=number of samples [312]).

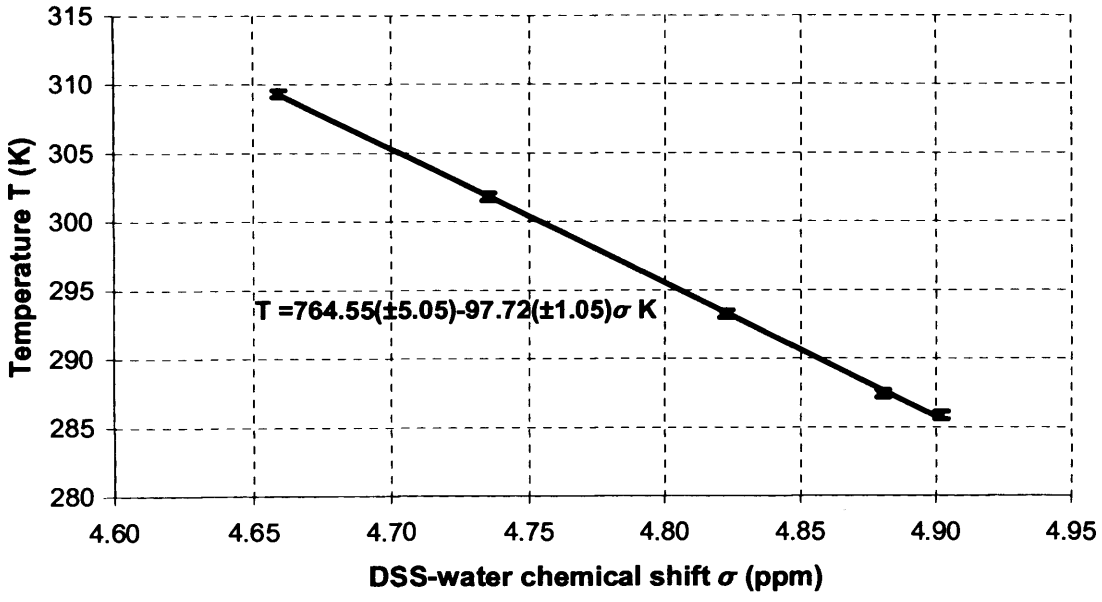

Figure 7.8: Calibration experiment: Dependence of the DSS-water chemical shift on temperature (analysed using SAGE software). The error bars represent the 95% CL on temperature measurements.

jMRUI software analysis

Linear regression yielded the relationship:

$T = 758.59\ (\pm\ 4.04) - 96.21\ (\pm\ 0.84)\ \sigma_{DSS}\ K$ 7.3

with a regression correlation coefficient r=0.999, and an rms residual of 0.09 (data not shown for conciseness). The SD for data fitted in the time domain using jMRUI software was estimated to be 0.13 (±0.13) K. Average linewidths for both the water and DSS peaks were approximately 2.5Hz (measured using both software analysis packages).

7.2.3.2 Reproducibility Experiment

SAGE software analysis (figure 7.9)

The SD values obtained using the SAGE software were all low (30-70mK) and did not exhibit a $N_{av}^{-1/2}$ dependence (see figure 7.9), as would be expected if the variance of results were caused by intrinsic (thermal) noise alone. Therefore the 'pooled' (rms) SD for any number of signal averages is quoted here. 10 acquisitions of the 250mM DSS sample at room temperature yielded a collective SD of 50 (± 10) mK (minimum detectable temperature difference 100 (±20) mK). The 95% confidence limits on the SD (i.e. $1.95 s_{SD}$, where again, s_{SD} is the uncertainty on the SD, calculated using the relation $s_{SD} = SD/\sqrt{2(n-1)}$, where n=number of samples [312]) are shown as error bars in figure 7.8. The predicted rms rounding error ($'resolution'/\sqrt{12}$ [6]) attributable to the intrinsic software 'digital resolution' is just 4.5mK and is indicated on the graph as an equivalent SD, to demonstrate its relative size to measured SDs. The analysis was also repeated without performing zero filling prior to reconstruction, and the reproducibility obtained in this case was 930 (± 180) mK.

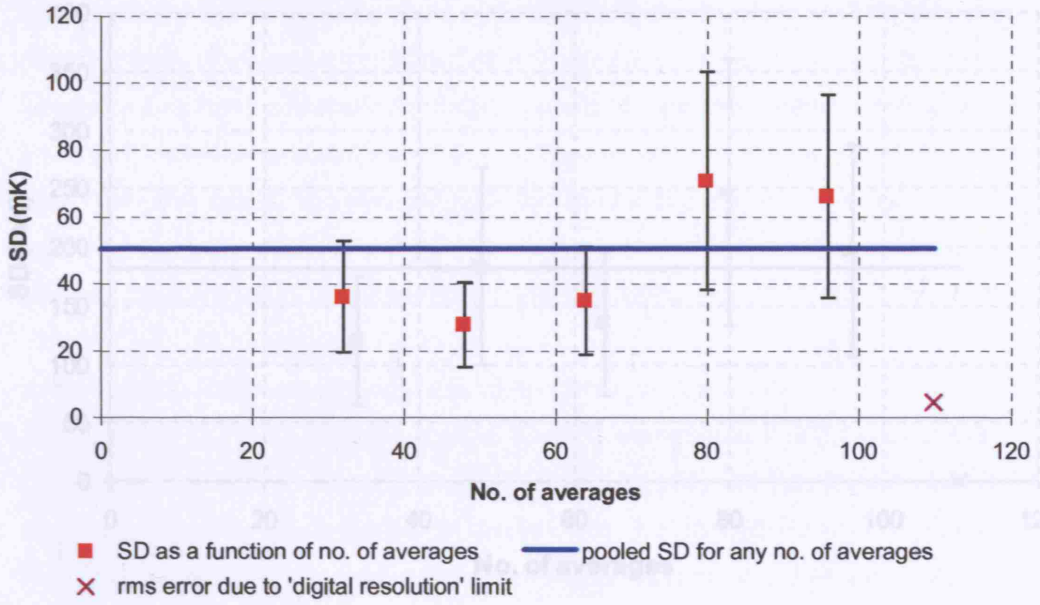

Figure 7.9: Reproducibility of temperature measurements as assessed from 10 repeat scans for each number of averages N_{av} (analysed using SAGE software with zero filling as described in section 7.2.2.6). The error bars indicate the 95% CL in estimating a SD. The rms rounding error due to the limit of the intrinsic software resolution (4.5mK) is also shown for comparison.

jMRUI software analysis (figure 7.10)

Again, SDs did not exhibit the expected proportionality to $N_{av}^{-1/2}$ (see figure 7.10); the collective SD calculated using this software for any number of averages is 182 (± 36) mK (minimum detectable temperature difference 354mK). The rms rounding error due to the intrinsic software 'digital resolution' is the same as for the SAGE software and is indicated on the graph as an equivalent SD.

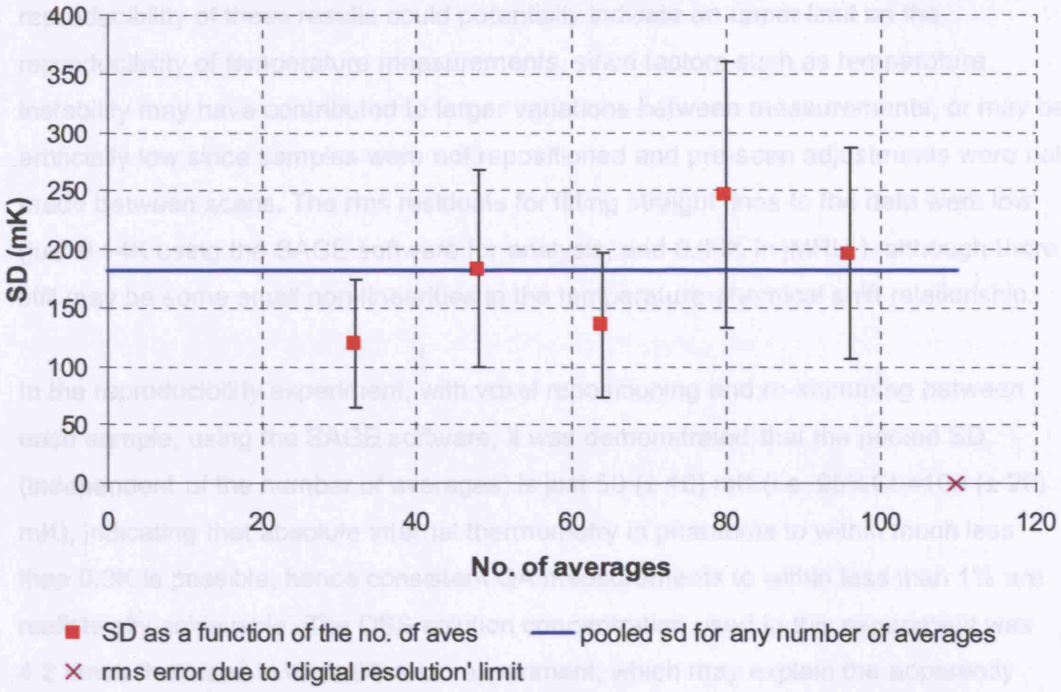

Figure 7.10: Reproducibility of temperature measurements as assessed by repeat scans (analysed using jMRUI software as described in section 7.2.2.6). The error bars reflect the 95% CL in estimating a SD. The rms error due to the limit of the intrinsic software resolution (4.5mK) is also shown for comparison.

7.2.3.3 Preliminary investigations in gel phantoms

In the agarose phantom, the linewidths of both the water and DSS peaks were very large (~20Hz) compared with those observed in aqueous solutions (~2.5Hz). In the BSA phantom, the water peak Full-Width-Half-Maximum (FWHM) was just 4Hz, and the DSS peak was absent.

7.2.4 Discussion: Internal Thermometry in MRI Phantoms

The temperature dependence of the water-DSS chemical shift difference (calibration experiment, sections 7.2.2.3, 7.2.3.1) was investigated *without* voxel re-positioning, shimming and other pre-scan adjustments, allowing the effects of the intrinsic noise upon temperature precision to be determined. The reproducibility experiment (sections 7.2.2.4, 7.2.3.2) then addressed the precision with which temperature measurements can be estimated *with* the additional variability introduced by such inter-scan adjustments, in order to determine a realistic measure of the thermometric precision possible.

In the calibration experiment, a marked linear dependence of chemical shift difference upon temperature was demonstrated; the relationships given by equation 7.2 for SAGE

software analysis, and equation 7.3 for jMRUI software were very similar. The reproducibility of these results could potentially indicate an upper limit on the reproducibility of temperature measurements, since factors such as temperature instability may have contributed to larger variations between measurements, or may be artificially low since samples were not repositioned and pre-scan adjustments were not made between scans. The rms residuals for fitting straight lines to the data were low (just 0.14K using the SAGE software for analysis, and 0.09K in jMRUI), although there still may be some small non-linearities in the temperature-chemical shift relationship.

In the reproducibility experiment, with voxel repositioning and re-shimming between each sample, using the SAGE software, it was demonstrated that the pooled SD (independent of the number of averages) is just 50 (± 10) mK (i.e. 95%CL=100 (± 20) mK), indicating that absolute internal thermometry in phantoms to within much less than 0.3K is possible, hence consistent QA measurements to within less than 1% are realistically achievable. The DSS solution concentration used in this experiment was 4.2 times that used in the calibration experiment, which may explain the apparently higher precision obtained here compared with the calibration study.

Using jMRUI, exponentially damped sinusoids were fitted to the time domain data and peak positions determined automatically. In this case the pooled SD (independent of the number of averages) was found to be 180 (± 36) mK, (i.e. 95%CL=350 (± 70) mK). The predicted rms SD caused by rounding errors due to the 'digital resolution' of each software package (see figures 7.9, 7.10) is the same, and much less than the measured SDs for both software types, indicating that in both cases this is unlikely to have been the limiting factor in the reproducibility of temperature measurements (although in the case of data analysed using SAGE without zero filling, the reproducibility was much worse as expected (table 7.11)). Peak-picking using SAGE software performed better than either time domain fitting using jMRUI, or frequency domain fitting attempted in SAGE. This suggested that in this specific case of well shimmed, high SNR spectra, simple peak picking of zero-filled spectra may provide a more robust estimate of peak separation than more sophisticated peak fitting algorithms, or that the interpolation method used by the peak fitting algorithms may not be optimal. Errors may be introduced using the fitting methods if the spectral lineshapes obtained are not truly Lorentzian, and also the ultimate precision of frequency estimation using these methods may be determined by an arbitrary convergence criterion internal to the software. Using either software analysis method, the SDs did not exhibit the expected proportionality to $N_{av}^{-1/2}$ (see figures 7.9, 7.10) for normally distributed data, indicating that the DSS concentration used here was

sufficiently high that the SD was not determined by intrinsic noise. Instead, variations introduced by e.g. temperature fluctuations, voxel re-positioning and shimming probably limited the precision more than intrinsic noise, suggesting that with the reference compound concentrations used here, few signal averages are needed for reproducible temperature measurements.

In order to investigate the applicability of internal thermometry in gel-based MRI test-objects, preliminary investigations were performed in agarose and BSA. In the agarose phantom, the linewidths of both the water and DSS peaks were markedly increased (20Hz vs. ~2.5Hz) compared with that obtained in aqueous solutions. There are three possible causes of this; (1) susceptibility effects due to the geometry of the container of the gel, (2) a binding effect between the DSS and agarose causing a reduction in the T_2 value of the DSS peak, and (3) variations in the gels on a microscopic level (presence of microbubbles due to the rapid cooling of the gel, or other local inhomogeneities). Since the linewidths of both the water and DSS peaks in the agarose gel were much larger than was observed in aqueous solutions (in the same type of container), geometric effects (i.e. cause 1) can be eliminated as a possible cause. It should also be noted that the lineshape for a gel phantom is unlikely to be truly Lorentzian, and in fact may approach a Gaussian function. Binding of DSS to the agarose (cause 2) can also be eliminated as both peaks were affected equally by the line broadening, therefore the broadening cannot be explained simply by a reduction in the DSS peak T_2. It is therefore hypothesized that microbubbles (cause 3) produced during cooling of the gel caused local susceptibility gradients and are responsible for the line broadening observed within the agarose phantoms.

In the BSA samples, the DSS peak was absent, although the linewidth of the water peak was acceptable (FWHM ~3-4Hz), and the SNR of the water peak was high (~550 at TE=30ms) (calculated by estimating the water peak signal and baseline signal (noise) and taking a ratio), although reduced in comparison to experiments in solutions (partly due to the increased linewidth of the water peak). It is likely that interactions between the DSS molecules and the BSA may have caused line broadening (i.e. T_2 shortening) of the DSS peak greater than that for water, resulting in a low peak height causing the DSS peak to be hidden by baseline noise.

Therefore, in order to avoid loss of precision due to these types of line-broadening effects in gel test-objects, the ideal situation (in terms of cost, possible effects on the phantom material and optimal spectroscopic conditions) would probably be to insert a small, highly concentrated (e.g. 250mM), sealed sample of aqueous DSS solution

inside existing QA phantoms. This would enable absolute spectroscopic temperature monitoring whilst maintaining the original phantom properties. The equipment and experimental procedure (including the thermal insulation) and quality of data obtained in this study demonstrate that this approach is viable for use in MRI test-objects. Some additional optimisation of software analysis techniques may improve the precision of temperature measurements further.

7.2.5 Conclusions: Internal thermometry in MRI Phantoms

We have shown that using localised ^{1}H-MRS acquisition sequences routinely available on clinical MRI scanners, and commonly available analysis packages, internal thermometry to within much less than 0.3K in phantoms using DSS as a chemical shift reference is realistic. The minimum detectable temperature difference was shown to be 100 (±20) mK, which would typically correspond to changes in MR quantities of less than 0.3%. this enables the identification and correction of systematic errors in quantitative QA measurements caused by temperature variation and therefore provides confidence in changes observed in quantitative MR properties in long-term clinical studies. Accuracy for multi-centre studies can also be measured. Our method avoids the additional experimental complexity of using standard thermometry techniques (e.g. thermocouples) during QA measurements, and possible image artefacts caused by the close proximity of such thermometer probes. Small containers filled with highly concentrated reference compound solutions could be inserted into existing phantoms to enable internal thermometry to be performed without otherwise compromising the QA measurement. Further optimisation of acquisition parameters and automated spectral processing strategies [313] may improve the precision of this method further.

8 Optimisation of qMT sequence acquisition parameters

Introduction

The aim of this study was to optimise the quantitative MT sequence acquisition parameters (i.e. the selection of "MT weightings", each a combination of MT pulse amplitude and offset frequency), in order to increase the precision of the estimated fundamental qMT model parameters. In a clinical setting there is a limit on patient scan time, which restricts the number of qMT data points that can be collected; therefore optimising the selection of sampling points is an important aspect of the design of a qMT experiment. Compared to a conventional acquisition, the optimisation enables less data to be acquired, reducing acquisition time without compromising uncertainties in estimated parameters. Alternatively, for the same number of MT-weighted data points, the map noise could be reduced, thereby minimising uncertainties in estimated parameter maps. A novel approach was used, involving the minimisation of the Cramer-Rao minimum variance bound (CRMVB) by altering the combination of MT pulse amplitudes and offset frequencies at which data are acquired. This analytical approach was verified numerically, through the use of Monte Carlo simulations, thereby providing two independent measures of the uncertainties in fitted parameters.

Firstly an introduction to non-linear least squares fitting is given. Next there is a brief description of possible quantification methods (to fit the qMT model function to experimental data to yield sets of fundamental qMT parameters), and the fitting routine used in this study is discussed. An introduction to Maximum Likelihood (ML) estimation theory is then given, followed by the principles of Cramer-Rao theory. The numerical Monte Carlo method used to validate the approach, by providing a separate measure of the uncertainties in fitted parameters, is also discussed.

The CRMVB approach to optimising the selection of qMT data points was validated by comparing results from numerical simulations with theoretical predictions (for the estimation of just two fundamental qMT parameters). Then a description of the minimisation procedures used to optimise the qMT acquisition scheme is given. Optimal acquisition schemes were also verified experimentally and this is discussed in section 8.6.3.

8.1 Quantification Method

The existing qMT acquisition scheme employed at this centre [47] involves acquiring "MT-weighted" data at 10 combinations of MT pulse amplitude and offset frequency. The qMT model signal equation is then fitted to the measured signal data at each data point via least squares minimisation. Here the Marquardt-Levenberg method, implemented using routines adapted from Numerical Recipes in C [314] was used.

Firstly the general approach and some concepts involved in non-linear least squares fitting are discussed, followed by a more detailed description of the Marquardt-Levenberg method which was used in this study.

8.1.1 Non-linear least squares fitting: Least squares method

If the noise distribution at the nth data point x_n is assumed to be Gaussian, the likelihood or probability function is given by equation. 8.8, where $\boldsymbol{\theta}$ is the vector of parameters θ_i to be estimated, x_n is the nth data point at which the signal values s_n is measured, σ is the uncertainty in each signal measurement (assumed to be the same for each data point here so that $\sigma=\sigma_n$) and $s(x_n)$ is the theoretical model function value calculated at the nth data point x_n. The likelihood is maximised with respect to the parameters by minimising the exponent (i.e. the log likelihood or 'goodness-of-fit parameter' X^2):

$$X^2 = \sum \left\{ \frac{1}{\sigma_n^2} [s_n - s(x_n)]^2 \right\} \qquad 8.1$$

The optimum parameter value θ_i' for each of the i parameters can be obtained by minimising X^2 simultaneously with respect to each parameter (i.e. by setting the derivative of X^2 with respect to each of the parameters equal to zero) [315]:

$$\frac{\partial X^2}{\partial \theta_i} = \frac{\partial}{\partial \theta_i} \sum_{n=0}^{N-1} \left\{ \frac{1}{\sigma_n^2} [s_n - s(x_n)]^2 \right\} = -2 \sum_{n=0}^{N-1} \left\{ \frac{1}{\sigma_n^2} [s_n - s(x_n)] \frac{\partial s(x_n)}{\partial \theta_i} \right\} = 0 \qquad 8.2$$

Taking partial derivatives of X^2 with respect to each of the j parameters yields j coupled equations in the unknown parameters θ_i. If these equations are not linear in all the parameters, X^2 is treated as a continuous function of the j parameters, describing a "hypersurface" in j-dimensional space [315]. That space is then searched for the appropriate minimum X^2 value. In order to find the value of each of the parameters θ_i that yields a minimum for X^2, the j coupled non-linear equations must be solved, and there are several ways of accomplishing this.

8.1.1.1 Other considerations in non-linear least squares fitting

For any non-linear fitting routine, the speed of convergence toward a solution may depend upon the choice of the method for finding solutions, starting values for the parameters, and the iterative step size for each individual parameter, in addition to the convergence criteria selected to terminate the routine [314].

An unfortunate choice of starting values for parameters may drive the solution towards a local minimum rather than the absolute minimum. It can, therefore, be useful to search the parameter space to locate all minima and identify the desired range of parameter values over which to refine the search.

Some routines allow constraints to be imposed on fitted parameter values in order to prevent the search converging towards solutions that are physically unreasonable, e.g. negative results.

The parameter step sizes (the amount by which each parameter is altered between successive iterations) must also be carefully chosen. Small step sizes result in slow convergence, whereas step sizes that are too large may miss local minima.

There are several ways to define convergence criteria for termination of the fitting process when an acceptable solution has been reached. The change in X^2 between two iterations, the change in the actual parameter value between successive iterations, and the maximum number of iterations allowed are all potential termination criteria. In order to validate a particular quantification method, the stringency of the convergence criteria should be tested.

8.1.2 Grid-search method

If the X^2 variation with each parameter θ_i is not very sensitive to the values of other parameters (i.e. there is no correlation between X^2 variation for different fitted parameters), the optimum parameter values can be obtained by simply minimising X^2 with respect to each parameter individually [314], [315]. This is a very simple approach, but its main disadvantage is that if the X^2 variation of different parameters is correlated, convergence to a solution may be very slow [315].

8.1.3 Gradient search (steepest descent) method

One alternative to the grid search method is the gradient search method, where all parameters are incremented simultaneously, with relative magnitudes (and signs) adjusted so that the resultant direction of travel in parameter space is always down the

direction of maximum variation (i.e. highest gradient) of X^2. Partial derivatives are estimated numerically in order to determine the gradient [314], [315].

However, it is difficult to approach the bottom of the minimum asymptotically because the gradient of X^2 tends to 0 at the minimum, and the search therefore becomes inefficient. Therefore it may be advantageous to use a different method to locate the minimum once the gradient search has approached it sufficiently closely. These methods are known as expansion methods and two possible approaches are those of parabolic expansion (where the X^2 hypersurface is approximated by a parabolic surface) and Taylor expansion of the fitting function to give an analytical description of the hypersurface.

8.1.4 The Marquardt-Levenberg method

One disadvantage of the analytical methods of expanding either the fitting function s(x) or X^2 is that although they converge quite rapidly to the point of minimum X^2 from points nearby, they cannot be relied on to approach the minimum with any accuracy from a point outside the region where the X^2 hypersurface is approximately parabolic [314], [315]. Conversely, the gradient search method is ideally suited for approaching a minimum from far away, but does not converge rapidly near the minimum [314], [315]. An algorithm that behaves like a gradient search far away from the solution, and behaves more like an analytical solution as the search converges would be ideal, and there is a routine known as the Marquardt-Levenberg method [316] that meets these requirements. The Marquardt-Levenberg method is a combination of the methods of expanding the fitting function and the gradient search method, varying smoothly between the extremes of the two. The gradient method is used far from the minimum, and the algorithm switches continuously to expansion of the fitting function as the minimum is approached. The first order expansion of the analytical method is sufficient here because the expansion only needs to be valid in the immediate neighbourhood of the minimum. Therefore to calculate the curvature matrix only first order derivatives are required.

The method can be problematic if the gradient close to the minimum is small in magnitude, resulting in a very small pivot, consequently generating a large correction which is then rejected and may result in the optimisation becoming trapped in "flat valleys" [314]. Taking this into consideration, terminating the routine on the first or second occasion that X^2 decreases by negligibly small amount; for example some fractional amount like 10^{-3} is probably reasonable.

The Marquardt-Levenberg method finds the best fit of the model function to experimental data most directly and efficiently of the routines discussed above, and has become the "standard" of non-linear fitting [314]. It has the advantage of being reasonably insensitive to the starting values of the parameters, although it may have difficulties when the starting parameters of the function for the peak are outside reasonable ranges, resulting in termination at local minima. The Marquardt-Levenberg method also has the advantage over the grid and gradient search methods of providing an estimate of the full error matrix [315].

8.2 The Maximum Likelihood (ML) Method

In Maximum Likelihood estimation theory it is assumed that there exists a (known) joint probability distribution function (pdf) for the noise contribution to observed data, and that the model function (which describes the data in the absence of noise) is also known [317].

The most commonly used joint pdf (here denoted $\mathbf{p}(\mathbf{x},\boldsymbol{\sigma},\boldsymbol{\theta})$) is the distribution valid for uncorrelated, Gaussian noise, given by:

$$p(\mathbf{x},\boldsymbol{\sigma},\boldsymbol{\theta}) = \prod_{n=0}^{N-1}\left(\frac{1}{2\pi\sigma_n^2}\right)^{\frac{1}{2}} \exp\left[\frac{-1}{2\sigma_n^2}\{s_n - \hat{s}_n(\boldsymbol{\theta})\}^2\right] \qquad 8.3$$

where $\mathbf{x}$ is the vector of data points, $\boldsymbol{\sigma}$ is the vector of the noise standard deviations σ_n, $s_n(\boldsymbol{\theta})$ is the model function value at the nth data point, and $\boldsymbol{\theta}$ is a vector containing the model function parameters.

For a set of data points $\mathbf{x}$, the ML estimation of the model function parameters $\boldsymbol{\theta}$ simply amounts to maximising the joint pdf. For Gaussian distributed noise (distribution function given by equation 8.1), it is convenient to maximise the natural logarithm of the distribution function, rather than the distribution function itself. Therefore, if an estimated model parameter ("estimator") maximises the logarithm of the likelihood (probability) function, it is by definition the Maximum Likelihood estimator [317], [318].

If it is assumed that the SDs of all noise contributions (i.e. at all data points) are equal to a value σ, then the quantity to be maximised at the nth data point is given by:

$$\text{constant} - \frac{1}{2\sigma^2}\sum_{n=0}^{N-1} | s_n - \hat{s}_n |^2 \qquad 8.4$$

This implies that in case of uncorrelated, Gaussian-distributed, noise the ML method amounts to applying the least squares method [317].

The ML method exhibits some important statistical properties; for a sufficient number of data points, the variances of the estimated parameters approach certain fundamental lower bounds (the so-called Cramer-Rao Minimum Variance Bounds (CRMVBs)) [317], [318], [319], [320]. Also, assuming that the correct model function is used, the estimated model function parameters have no systematic errors, i.e. they are unbiased (and this implies that the expectation values asymptotically approach the true parameter values as the number of samples approaches infinity).

8.3 Analytical Method: The Cramer-Rao minimum variance bound (CRMVB)

There is a minimum variance known as the Cramer-Rao Minimum Variance Bound (CRMVB) which can be attained by any estimated model parameter quantified using a specific set of data points [318], [321], and is limited by the noise in the data. Irrespective of the method used to quantify the parameters from the data, this lower bound on the precision of the parameters cannot be improved upon. An estimator that achieves this bound is said to be efficient, and is by definition the ML estimator [317], [319]. CRMVBs can therefore be used to optimise sample positions (data acquisition parameters), via minimisation of the theoretical uncertainties in fitted parameters [322]. CRMVBs could also be used to test the particular quantification method (e.g. fitting routine) used to estimate the model parameters, since a maximum likelihood quantification method would be expected to attain (or approach asymptotically) this minimum bound on the uncertainty in an estimated parameter.

Let us assume that the signal measured at the nth data point s_n can be described by:

$$s_n = \hat{s}_n + \varepsilon_n \qquad 8.5$$

where $\hat{s}_n$ is the model function value and ε_n is the noise contribution of the nth data point. The noise contribution at each data point has its own (known) pdf, and it is also assumed that the noise contributions of successive data points are uncorrelated. Here, for simplicity, it is assumed that the noise contribution is the same for each data point.

If $\boldsymbol{\theta}$ is a vector of unknown parameters to be estimated, with each individual parameter labelled θ_i, then $\hat{\boldsymbol{\theta}}$ is the (vector) estimate of $\boldsymbol{\theta}$, and $\hat{\theta}_i$ (the estimator) is the ith element of $\hat{\boldsymbol{\theta}}$.

The Cramer-Rao inequality [318], [319] (equation. 8.4) states that any unbiased estimator $\hat{\boldsymbol{\theta}}$ (with pdf (or likelihood function) $\mathbf{p}(\mathbf{x},\boldsymbol{\theta})$ and noise SD at each data point x_i equal to σ) has a variance that is bounded from below by the corresponding element

of the inverse of the Fisher information matrix **F**. An unbiased estimator that achieves this lower bound is a minimum variance (or maximum likelihood) estimator.

It can be shown [317], [318], [319] that for any unbiased estimate $\hat{\boldsymbol{\theta}}$ of $\boldsymbol{\theta}$:

$$\mathrm{Var}(\hat{\theta}_i) \geq F_{ii}^{-1}(\boldsymbol{\theta}) \qquad 8.6$$

where $F_{ii}^{-1}(\boldsymbol{\theta})$ is the ith diagonal element of the inverse of the Fisher information matrix $\mathbf{F}(\boldsymbol{\theta})$.

The elements of the Fisher information matrix are given by the second derivative of the log likelihood function, evaluated at the true parameter values, and describe the degree of curvature of the average log likelihood:

$$F_{ij}(\boldsymbol{\theta}) = -E\left[\frac{\partial^2 \ln \mathbf{p}(\mathbf{x};\boldsymbol{\theta})}{\partial\theta_i \partial\theta_j}\right] \qquad 8.7$$

The Fisher information matrix could be interpreted as a measure of the sensitivity of the data to the parameters being estimated, taking into account the noise.

8.3.1 CRMVB for a Gaussian Noise Distribution

Let us consider the estimation of a parameter from a measured signal corrupted by white Gaussian noise. If the signal s_n (at the nth data point) is assumed to be given by equation 8.3, where ϵ_n is white Gaussian noise (at the nth data point) with $\varepsilon_n = N(0,\sigma^2)$, the likelihood function (pdf) is given by:

$$\mathbf{p}(x_0,\ldots,x_{N-1};\boldsymbol{\theta}) = \frac{1}{(2\pi)^N \sigma^N} \exp\left(-\frac{1}{2\sigma^2}\sum_{n=0}^{N-1}(s_n - \hat{s}_n(\boldsymbol{\theta}))^2\right) \qquad 8.8$$

Using equations 8.4 and 8.5, it can be shown that the theoretical lower bound on the variance for a set of estimators $\hat{\boldsymbol{\theta}}$ of the true model function parameter set $\boldsymbol{\theta}$, estimated from a set of N signals $s_0,..,s_{N-1}$ corrupted by Gaussian noise, is given by the inequality [319]:

$$\mathrm{Var}(\hat{\boldsymbol{\theta}}) \geq \frac{\sigma^2}{\sum_{n=0}^{N-1}\left(\frac{\partial \hat{s}_n(\boldsymbol{\theta})}{\partial\theta_i}\right)^2} \qquad 8.9$$

Elements of the Fisher information matrix are therefore given by [319], [322]:

$$F_{ij}(\boldsymbol{\theta}) = \frac{1}{\sigma^2}\left[\sum_{n=0}^{N-1}\frac{\partial \hat{s}_n(\boldsymbol{\theta})}{\partial\theta_i}\frac{\partial \hat{s}_n(\boldsymbol{\theta})}{\partial\theta_j}\right] \qquad 8.10$$

where i, j=1, 2, ..., J, for each of the J model function parameters θ_i to be estimated; the CRMVBs for each estimated parameter are the diagonal elements of the inverse of the

Fisher information matrix and therefore the CRMVB SD $\sigma_{\theta i}$ for each parameter θ_i is given by the square root of equation 8.10 for the theoretical minimum variance of an estimated parameter $\hat{\theta}_i$:

$$\sigma_{\theta_i} \geq \sqrt{CRMVB_{\theta_i}} = \sqrt{F_{ii}^{-1}(\boldsymbol{\theta})} \qquad 8.11$$

It can be seen therefore, that for Gaussian, uncorrelated noise the CRMVBs are proportional to the variance of the noise distribution at each data point, σ^2 [322]. Theoretical CRMVBs should be calculated using the true parameter values.
It should be noted that noise in magnitude MR images follows a Rician distribution [323], rather than a Gaussian distribution, as was used to model the noise here. This is because the non-linear mapping of each pixel in the real and imaginary images to the magnitude images results in a noise distribution that is no longer Gaussian. A special case of the Rician distribution is observed in regions where only noise is present, known as the Rayleigh distribution. Therefore at low signal-to-noise ratio (SNR) (SNR $\leq$ 5 [324]) the noise distribution tends towards a Rayleigh distribution, but at higher SNR, the noise distribution approaches a Gaussian function. Since the SNR can be assumed to be higher than 5 in the images acquired for this study, this issue is ignored here and a Gaussian noise distribution is assumed.

8.4 Numerical method: Monte Carlo Simulations

The quantification method used to estimate the model function parameters could equally be tested using a Monte Carlo study. This is a numerical method performed by means of statistical simulations, and could also be used to verify the CRMVBs for the model. It has previously been stated [325] that any study using a random number generator is called a Monte Carlo study, in homage to the famous casino. The physical process is simulated, using the true parameter values to generate model signal values. The physical system must be described by probability density functions (and for validation of the CRMVB theory, these should be identical to the pdfs assumed for CRMVB calculations), and the simulations proceed by random sampling from these pdfs. In our case, random, computer-generated Gaussian noise is superimposed on a set of simulated signals. The model function is then fitted to the synthetic data sets corrupted by Gaussian noise using the usual quantification method, and each simulation yields a set of fitted parameters. Many simulations (known as Monte Carlo "realisations"), each with a different amount of random noise superimposed on the model signal value (although using the same Gaussian noise distribution mean and SD) are performed. Each of these yields a set of fitted model parameters, and the desired result is taken as an average over all the realisations [326], [327]. This process is illustrated in figure 8.1.

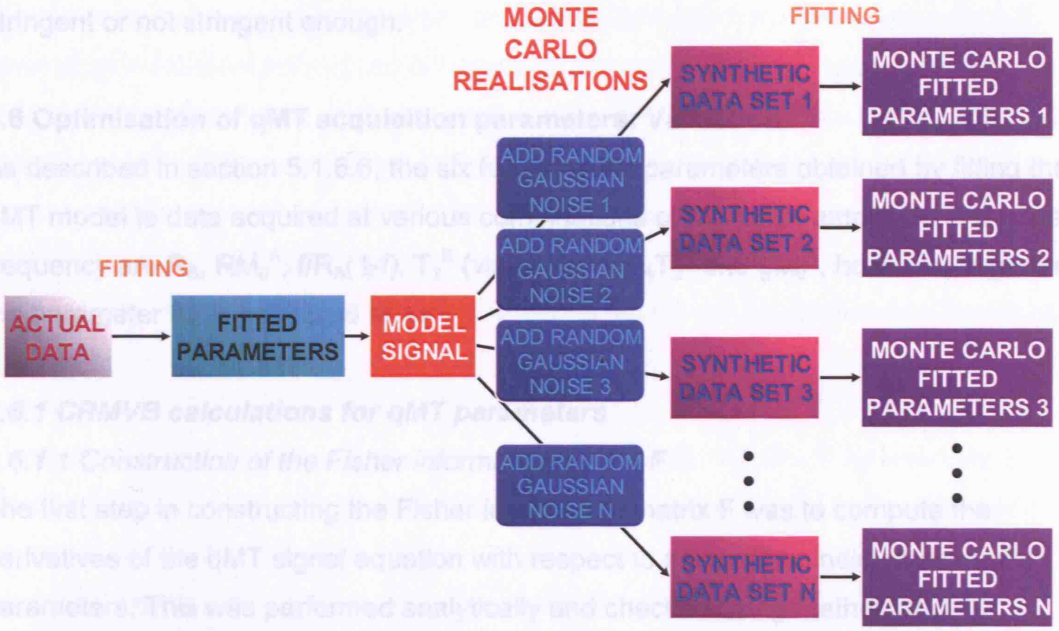

Figure 8.1: Schematic of the Monte Carlo Simulation method. Firstly real data are fitted to give a set of fitted parameters. The physical process is simulated using this set of fundamental model parameters to give the model (noise-free) signal data. Several "Monte Carlo realisations" are performed, where random, computer-generated Gaussian-distributed noise (with zero mean and a known SD) is superimposed on the model signal data, resulting in several synthetic data sets. Each synthetic data set is then fitted in the usual manner, yielding several sets of fitted model parameters.

If the quantification method used to estimate the fundamental parameters of the model has the ML property, the mean estimated parameters should be equal to the true parameter values (to within the 95% confidence limits (CL)), and the variances should be approximately equal to the CRMVBs.

8.5 Validation and testing of the fitting routine used for quantification

During initial experiments, the starting conditions for each parameter were varied (by ±20%) in order to check that the final results of the fitting routine were independent of the starting values. All analytically derived first derivatives (gradients) were checked numerically by calculating the model signal at the starting value, incrementing each parameter value individually, re-calculating the model signal at this new parameter value and dividing the difference by the increment. The convergence criteria were also

varied to ensure that results were not affected by termination conditions that are too stringent or not stringent enough.

8.6 Optimisation of qMT acquisition parameters: Validation

As described in section 5.1.6.6, the six fundamental parameters obtained by fitting the qMT model to data acquired at various combinations of MT pulse amplitude and offset frequency are R_B, RM_0^A, $f/R_A(1-f)$, T_2^B (via R_{RFB}), $1/R_AT_2^A$ and gM_0^A, however, in general the parameter R_B is held fixed at $1s^{-1}$.

8.6.1 CRMVB calculations for qMT parameters

8.6.1.1 Construction of the Fisher information matrix ***F***

The first step in constructing the Fisher information matrix **F** was to compute the derivatives of the qMT signal equation with respect to each of the indidvidual model parameters. This was performed analytically and checked using Mathematica (www.wolfram.com/products/webmathematica/) but an additional step was included in the CRMVB calculation program to check the derivatives numerically, by incrementing each parameter individually by 1%, recomputing the model signal, subtracting the original model signal from the incremented signal and dividing by the increment.

Firstly the precision with which just two parameters could be measured (whilst holding the other parameters fixed) was investigated. This idea could have important implications since it is possible that certain parameters give a greater insight than others into the biological mechanisms taking place in disorders such as MS. Potentially, therefore, more relevant information could be extracted from just two parameters if they were characterised with maximum precision, despite it being at the expense of the other parameters of the model. However, it should also be noted that by fixing certain parameters, some information may be lost and there is also the danger that this could be reflected as 'false' variation in the unfixed parameters.

It is necessary to extract the intrinsic signal intensity gM_0^A (depending on factors such as the scanner receiver gain g as well as the free pool signal intensity in the absence of exchange); the second parameter chosen to be extracted was either $f/R_A(1-f)$, or T_2^B, the T_2 relaxation time of the restricted pool. These parameters were selected on the basis of the information they are thought to provide with regards the pathological processes taking place in disease.

A reduction in f could be caused by either a decrease in the macromolecular content in tissue (resulting from demyelination or axonal loss in Multiple Sclerosis, for example),

or an increase in the free water proton component, as is observed in oedema. Correlations between the parameter f and disability in MS have been observed [48], indicating the clinical relevance of changes in this parameter. T_2^B has been shown to be very sensitive to lesion pathology, but less so to changes outside lesions. It is likely to reflect changes in the structure of the remaining macromolecular content of tissue, and has been shown to be increased in lesions and in the normal-appearing white matter (NAWM) of SPMS patients, suggesting that a disruption in the myelin and/or axonal tissue has caused the macromolecular environment to become less 'restricted' [48].

Firstly it was necessary to construct the Fisher information matrix **F** for each set of fundamental parameters to be estimated. For a two-by-two matrix, computation of the inverse Fisher matrix could be checked manually or using Excel, but in general, matrix inversion was performed using a Gauss-Jordan elimination routine adapted from Numerical Recipes [314].

CRMVB coefficients of variation (CVs; defined as the SD divided by the mean parameter value, expressed as a percentage) for each parameter were computed using previously measured qMT parameter values for control white matter [48]. The parameters not fitted in this instance were held fixed at their "true" values, and the same parameter values were used to simulate model signals for the Monte Carlo simulations. Firstly this was performed for an existing qMT sequence used at this centre [47] for a range of Noise-to-Signal Ratio (NSR) values (1% $\leq$NSR $\leq$10%) and graphs were plotted of the CRMVB CV values obtained. 95 % confidence limits (CL) were calculated from the uncertainty in each SD measurement (σ_{SD}), from σ_{SD}=SD/(2(n-1))$^{1/2}$ [312], where n is the number of samples, i.e. it is given by the total number of pixels in each ROI multiplied by the number of samples).

8.6.2 Monte Carlo simulations

Model signal data were generated for the 10 combinations of MT pulse amplitude and offset frequency in the existing sequence [47], using previously measured control white matter qMT parameter values [48]. This existing acquisition scheme has been successfully applied in several studies of normal control subjects and Multiple Sclerosis patients to provide reliable estimates of qMT parameters in clinically feasible times [47], [48], [328], [238]. Random, computer generated Gaussian noise was then superimposed on the signals at each data point, again using the Box-Muller algorithm [329] (implemented using Numerical Recipes [314]) to generate normal deviates, which were then transformed to have a mean given by the model signal value at each data

point and a noise SD value set by the user. The same NSR value was input to generate the normal deviates for all signals, and the same NSR values were used for CRMVB calculations for comparison.

10000 MC realisations were performed for each NSR value (1% $\leq$NSR $\leq$10%) and the synthetic data sets were then fitted using the Marquardt-Levenberg fitting routine, implemented using Numerical Recipes [314] (described in section 8.4.4). Again, it was verified that the distributions of random deviates were Gaussian for each NSR value. Mean parameter values from 10000 MC realisations and parameter SDs at each NSR value were calculated, and the numerically calculated CVs were plotted as a function of the NSR value. The mean parameter values were compared with the true parameter values, and the CVs compared with theoretically predicted (CRMVB) CVs for each fitted parameter.

This procedure was performed for just two estimated parameters for validation of the technique; either gM_0^A and $f/R_A(1-f)$ or gM_0^A and T_2^B.

8.6.3 Validation Results

Theoretical (CRMVB) and numerical (Monte Carlo) coefficients of variation are plotted as a function of NSR value for $f/R_A(1-f)$ (figure 8.2) (for estimation of just $f/R_A(1-f)$ and gM_0^A). Results obtained for the estimation of T_2^B with gM_0^A instead of $f/R_A(1-f)$ are not shown.

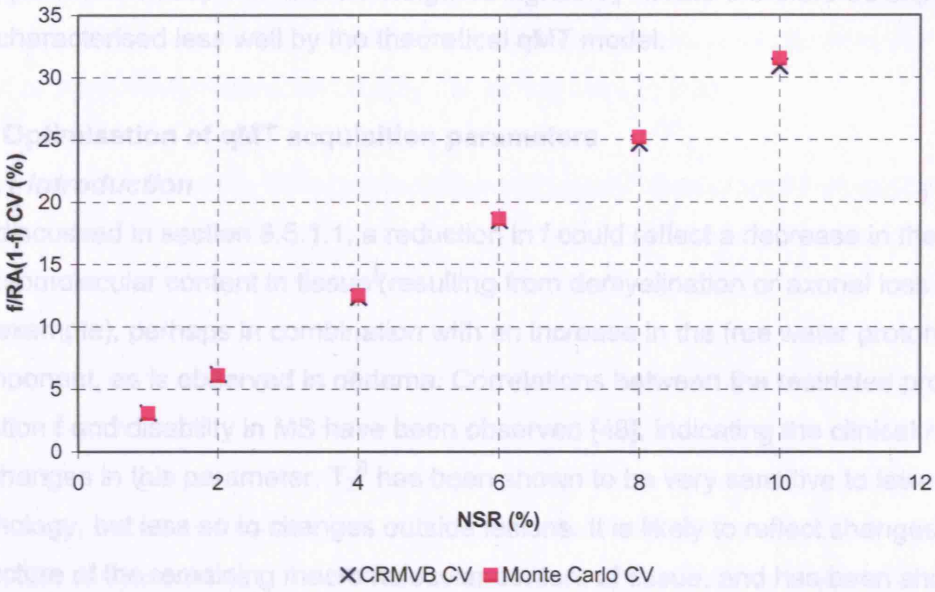

Figure 8.2: Coefficients of variation for the parameter $f/R_A(1-f)$ resulting from 10000 Monte Carlo realisations are compared with theoretical results. Error bars indicate the 95% CL in estimating the CV numerically.

8.6.4: Discussion: Validation of CRMVB approach

- Theoretical (CRMVB) and numerically simulated SDs agreed well for both gM_0^A and $f/R_A(1-f)$ (see figure 8.2; gM_0^A data not shown).
- At higher NSR values, linear CR theory begins to break down and SD's are under-estimated by theory (figure 8.2).
- For conciseness the graphs of numerical and theoretical CVs as a function of NSR for the estimation of T_2^B with gM_0^A instead of $f/R_A(1-f)$ are not shown, but similar results were obtained.
- By examining fractional differences between numerical and theoretical data (data not shown), it was apparent that theoretical data was more consistent with experimental data for the parameter gM_0^A than for $f/R_A(1-f)$ or T_2^B. It was also noted that fractional differences between numerical and theoretical CVs were much smaller for $f/R_A(1-f)$ estimation than for T_2^B estimation. This is attributed to the relationship between qMT signal measurements at each MT data point with the particular parameter. In Ramani's qMT model signal equation (equation 5.47), gM_0^A is simply a scaling factor. The parameter $f/R_A(1-f)$ appears twice in the signal equation (both in the numerator and the denominator of the fraction), therefore it is not surprising that this parameter behaves more "badly". T_2^B is characterised via the RF absorption lineshape of the semi-solid pool (the super-Lorentzian function, given in equation. 5.10) and therefore has the most

complex relationship with the MT-weighted signal. T_2^B would therefore be expected to be characterised less well by the theoretical qMT model.

8.7 Optimisation of qMT acquisition parameters

8.7.1 Introduction

As discussed in section 8.5.1.1, a reduction in f could reflect a decrease in the macromolecular content in tissue (resulting from demyelination or axonal loss in MS, for example), perhaps in combination with an increase in the free water proton component, as is observed in oedema. Correlations between the restricted proton fraction f and disability in MS have been observed [48], indicating the clinical relevance of changes in this parameter. T_2^B has been shown to be very sensitive to lesion pathology, but less so to changes outside lesions. It is likely to reflect changes in the structure of the remaining macromolecular content of tissue, and has been shown to be increased in lesions and in the normal-appearing white matter (NAWM) of Secondary Progressive MS patients, suggesting that a disruption in the myelin and/or axonal tissue has caused the macromolecular environment to become more 'restricted' [48]. Also, the normal-abnormal ranges of RM_0^A and $1/R_AT_2^A$ values *in vivo* are both fairly narrow [47], [48]. It was also found in preliminary calculations that CRMVB coefficients of variance are very high for these parameters, even when estimated with gM_0^A alone (data not shown). The value of RM_0^A as estimated using the particular formulation of the qMT model used here (Ramani's model [47]) appears to be of little diagnostic value, and has virtually no effect on the model signal or the estimation of other model parameters even if it is altered greatly. However, ideally it is desirable to be able to estimate all parameters of the model, and RM_0^A may give some insight into exchange processes taking place in tissue if this were possible. It has previously been suggested that RM_0^A cannot be determined with confidence in some qMT experiments since they are performed in the steady state rather than the transient regime (where experiments have no specific reference to absolute time scales [330]). It was also shown by Tyler and Gowland that the qMT model is relatively insensitive to the value of R within the ranges observed in agar, and within the ranges observed *in vivo* by Graham and Henkelman [62]. It was also found that CRMVB CVs are very high for these parameters, even when estimated with gM_0^A alone. Based on previous observations in MS patients using this modification of the Henkelman qMT model [47], [48], the parameters f and T_2^B have been shown to give the best insight into the particular disease processes taking place. It can be assumed (see section 2.5) that the measurement of the observed T_1 of the free proton pool does not introduce large uncertainties into the estimation of f from $f/R_A(1-f)$, and since $f=M_0^B/(M_0^A+M_0^B)$, this parameter is dependent on tissue macromolecular content, and is hence likely to be

related to the myelin content in tissue in MS patients. This optimisation method also relies heavily on the assumption that the model parameters not estimated are held fixed at their "true" values, which may not be the case *in vivo*.

Other constraints on the data points acquired in a qMT experiment include SAR limitations and limits on the offset frequency of the MT pulses, which should not be too low in order to avoid direct saturation of the free proton pool.

The two-pool model for qMT is the most widely used but is only an approximation to the true *in vivo* situation. The free proton pool alone is known to comprise at least three pools [190] and three- or four-pool models for qMT have been developed [193], [222] but the increased acquisition time required in order to determine all the parameters involved, and computational complexity make these models difficult to apply clinically. There is a trade-off, therefore, between scanning time and intensive computation and the accuracy of the qMT model. It is also possible that the introduction of many more free parameters in the model might result in the fitting routine used to constrain all the free parameters producing physically unrealistic or meaningless solutions.

8.7.2 Optimisation methods

Following validation of the analytical approach to optimisation (via CRMVBs), which was performed for two combinations of just two qMT parameters (either gM_0^A and $f/R_A(1-f)$ or gM_0^A and T_2^B), optimisation of the acquisitions parameters to yield higher precision parameter sets was performed, using a single NSR value of 2.22 (± 0.07)% (although the actual NSR value selected is irrelevant since it is simply a scaling factor). This "optimisation" was performed for data sets consisting of 10 MT pulse amplitude-offset frequency pairs (i.e. the length of MR examination was fixed) for a 1.5T scanner. It should be noted that qMT acquisition parameters are also constrained by SAR limitations, and also by the restriction that no MT-weighted data points should be too close to the free proton pool resonance, since direct saturation of the free proton pool should ideally be minimised.

The NSR value selected is the average measured NSR (from 3 subjects) using uniform regions of right and left frontal WM and cerebellar grey matter (GM) in an image with little/no signal attenuation due to MT (i.e. zero power, high offset frequency data point) to measure the signal, and uniform regions of interest (ROIs) in the absence of any signal (i.e. in air) for the noise SD measurement, using the method of Edelstein *et al* [331] to compute the noise SD value.

The estimation of different combinations of fundamental qMT parameters was investigated:

a) $f/R_A(1-f)$ & gM_0^A
b) T_2^B & gM_0^A
c) $f/R_A(1-f)$, T_2^B & gM_0^A

As described earlier, it is necessary to extract the intrinsic signal intensity gM_0^A. When just two parameters were to be estimated, the second parameter chosen to be extracted was either $f/R_A(1-f)$ (a) or T_2^B (b). In situation (c) all 3 parameters were estimated. These parameters were selected on the basis of the information they are thought to provide with regards the pathological processes taking place in disease (see section 8.6.1).

Acquisition schemes were optimised for the different combinations of parameters above using methods described in the next section, and CRMVB CVs compared with those calculated for an existing protocol [47].

8.7.2.1 Minimisation of CRMVBs: Powell's quadratically convergent direction set method

To minimise a function of just one variable, a simple line minimisation is possible, but in order to perform a minimisation in multiple dimensions, it is important to carefully select the directions in which to perform the minimisation. Gradient information can be incorporated into a minimisation routine to improve the efficiency of the optimisation routine (otherwise a very inefficient routine could result, cycling endlessly through all possible directions). It is desirable to perform the successive line minimisations along so-called conjugate directions, so that minimisation along one direction is not "spoiled" by a subsequent minimisation along another direction.

The algorithm tries to find a few good directions along narrow valleys rather than N necessarily conjugate directions. The basic idea of this new method is to discard the old direction along which the function f made the largest decrease, despite the fact that this is effectively the best direction of that iteration. This is because it is likely to be a major component of the next direction to be added, therefore discarding it reduces the chances of linear dependence of subsequent directions.

This particular variation on Powell's method was implemented using a routine from Numerical Recipes [314], using a one dimensional line minimisation routine by constructing a function of one variable, which is the value of the function along the direction of a line going through the particular point the routine is at. This one

dimensional function is minimised using inverse parabolic interpolation (Brent's method), also incorporating derivative information.

8.7.2.2 Methods: MR Imaging

qMT data were acquired for three healthy volunteers on a 1.5T GE Signa scanner (General Electric, Milwaukee, WI, USA) using optimal acquisition parameters for estimation of each combination of parameters, and also using an existing scheme [47] for comparison. The qMT model was then fitted to all data sets using a Marquardt-Levenberg algorithm, implemented using Numerical Recipes [314] to obtain sets of parameter estimates. Coefficients of variation were calculated in regions of interest (ROIs) in GM and WM and compared with theoretical values.

8.7.3 Results of optimisation

8.7.3.1 Experimental validation of optimal sampling schemes

Optimal sampling strategies for different combinations of estimated parameters are given in Table 8.1, and CRMVB CVs for WM and GM (for NSR=2.22 (± 0.07)%) are compared with those for an existing protocol (and with experimentally measured values using each particular sampling strategy) in Table 8.2. Proposed schemes 1A and 1B were designed for use in situation (a), i.e. the acquisition schemes were optimised for estimation of $f/R_A(1-f)$ (along with gM_0^A). Scheme 2 was optimised for estimation of T_2^B (with gM_0^A), and scheme 3 was designed to allow reasonably precise estimation of both $f/R_A(1-f)$ and T_2^B with gM_0^A, but was specifically optimised for T_2^B estimation since the optimisation method used here can only be performed with respect to a single parameter at any one time.

Ranges of parameter values in normal white (WM) & grey matter (GM) & normal-appearing white matter (NAWM) in MS patients were examined [48]. The WM-NAWM range of T_2^B values *in vivo* is much less than the range of $f/R_A(1-f)$ values [48], therefore in MS patients it may be more important to achieve a lower SD on T_2^B than on the parameter $f/R_A(1-f)$, although this will depend on the particular clinical application. Hence in situation (c) (scheme 3), the sequence parameters were optimised for T_2^B (see table 8.1).

Table 8.1: Optimal qMT acquisition schemes

Acquisition Scheme	MT pulse Flip Angle (°)	Offset frequency (kHz)
Existing scheme	212	1.0, 2.5, 7.5
	434	1.0, 3.5, 15.0
	843	1.0, 2.5, 5.0, 7.5
Proposed Scheme 1A	0	2.75, 2.80, 2.85, 2.90, 2.95
	900	2.75, 2.80, 2.85, 2.90, 2.95
Proposed Scheme 1B	0	2.80, 2.85, 2.90
	900	2.80, 2.85, 2.90
Proposed Scheme 2	500	1.0, 1.25, 1.5, 12.5, 15.0
	900	1.5, 1.75, 2.0, 12.5, 15.0
Proposed Scheme 3	0	1.0, 2.0, 10.0
	500	1.0, 1.5, 2.0
	900	2.5, 7.5, 10.0, 12.5

Measured CVs from (left and right averaged) regions of WM (frontal) and GM (cerebellar) were compared with theoretical (CRMVB) values (see table 8.2). Theoretical CVs are proportional to the particular NSR value assumed.

Tissue heterogeneity was demonstrated not to be a limiting factor in determining the appropriate NSR value, by varying the ROI size and observing the change in SD (see Figure 8.3). SD values within GM regions are larger than those observed in WM, and show a larger dependence on ROI size. This is likely to be due to the greater heterogeneity of cerebellar GM tissue than frontal WM. However, it can be seen that ROI area is unlikely to be a limiting factor in the estimation of CVs at the ROI size used experimentally (53mm^2).

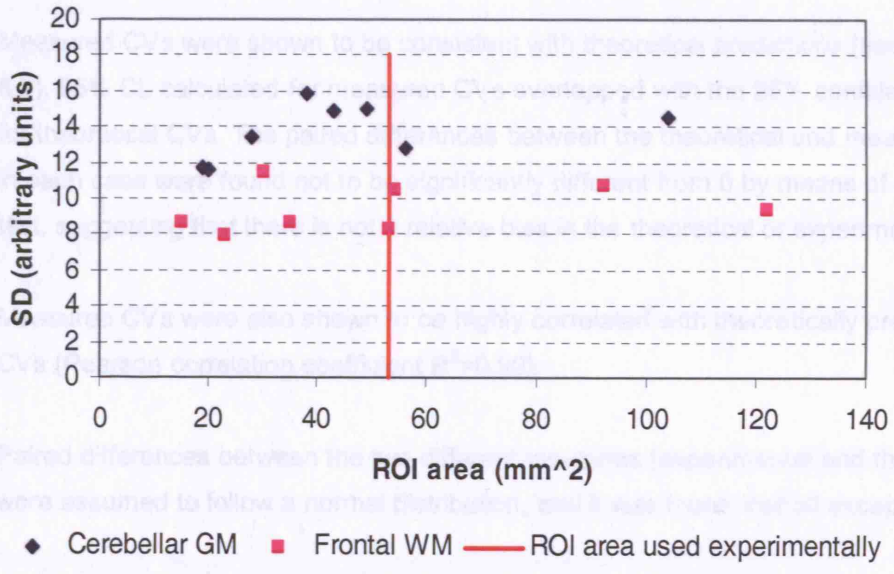

Figure 8.3: Variation of SDs in regions of white (frontal) and grey matter (cerebellar) with ROI area

It was shown that experimentally measured CVs for parameters estimated using the new proposed schemes were reduced in comparison to those estimated using the existing scheme [47] for GM and WM regions, verifying theoretical calculations (see table 8.2). CRMVB values for the parameter gM_0^A were consistently low and did not vary by large amounts depending on the particular acquisition scheme used (the optimisation was not performed to improve the estimation of gM_0^A for those reasons), therefore for brevity these data are not shown here.

Table 8.2: Theoretical (CRMVB) and measured (n=3; averaged right and left) coefficients of variation (CV) for optimal sampling schemes are compared with those for an existing protocol used in several previous studies of MS patients [47], [48], [332].

Parameters to be estimated	Acquisition Scheme	Theoretical Coefficients of variation (CV)				Measured Coefficients of variation (CV) (%)			
		White Matter		Grey Matter		White Matter		Grey Matter	
		f/RA(1-f)	T2B	f/RA(1-f)	T2B	f/RA(1-f)	T2B	f/RA(1-f)	T2B
f/RA(1-f)	Proposed Scheme 1	4.9 (± 0.3)	-	5.1 (± 0.4)	-	5.3 (± 0.2)	-	5.6 (± 0.2)	-
	Proposed Scheme 1B	6.4 (± 0.5)	-	6.2 (± 0.4)	-	6.9 (± 0.2)	-	6.1 (± 0.2)	-
	Existing Scheme	6.9 (± 0.5)	-	7.3 (± 0.5)	-	7.0 (± 0.3)	-	7.0 (± 0.3)	-
T2B	Proposed Scheme 2	-	6.2 (± 0.4)	-	6.9 (± 0.5)	-	6.4 (± 0.5)	-	6.6 (± 0.5)
	Existing Scheme	-	12.4 (± 0.9)	-	13.7 (± 1.0)	-	11.5 (± 1.0)	-	11.8 (± 1.0)
f/RA(1-f), T2B	Proposed Scheme 3	6.2 (± 0.4)	7.0 (± 0.5)	7.2 (± 0.5)	8.3 (± 0.6)	6.6 (± 0.6)	7.2 (± 0.6)	7.3 (± 0.6)	8.4 (± 0.7)
	Existing Scheme	7.5 (± 0.5)	13.7 (± 1.0)	8.1 (± 0.6)	15.1 (± 1.1)	7.3 (± 0.9)	11.3 (± 0.6)	8.1 (± 1.2)	14.3 (± 0.7)

95% confidence limits in measuring an SD from 6 samples (3 subjects, averaged right and left) for each CV measurement are also given in table 8.2 in brackets.

95% confidence limits for the NSR measurement (which dictate the uncertainties in theoretical CV estimates) were calculated using the uncertainty of the noise SD estimate, again taking into account the total number of pixels over which the ROI noise estimates were made.

Measured CVs were shown to be consistent with theoretical predictions (see Table 8.2). 95% CL calculated for measured CVs overlapped with the 95% confidence limits for theoretical CVs. The paired differences between the theoretical and measured CVs in each case were found not to be significantly different from 0 by means of a paired t-test, suggesting that there is not a relative bias in the theoretical or experimental data.

Measured CVs were also shown to be highly correlated with theoretically predicted CVs (Pearson correlation coefficient R^2=0.99).

Paired differences between the two different measures (experimental and theoretical) were assumed to follow a normal distribution, and it was found that all except one of

the paired differences lie within the 95% CL of the mean difference, suggesting good agreement of the two measures (measured and theoretical CRMVBs).

The paired differences were found to be inversely correlated (R^2=0.69) with the paired means of the theoretical and measured CVs, indicating that the variance in the theoretical CV is not equal to that observed in measured CV values.

As a proof of concept, a reduced sampling scheme (1B) (see table 8.1) was also tested for estimation of $f/R_A(1-f)$. It was shown that, compared to an existing scheme, the number of MT-weighted data points could be reduced by 40% for estimation of $f/R_A(1-f)$ without compromising uncertainties in estimated parameters (see table 8.2).

8.7.3.2 Extraction of f: propagation of uncertainties in $T_1^A{}_{obs}$ measurement into the restricted proton fraction

In order to determine the theoretical precision of an estimation of the restricted proton fraction f itself, rather than the parameter $f/R_A(1-f)$, the coefficient of variation for the estimation of R_A (i.e. $1/T_1^A$) (measured separately from the qMT experiment) is required.

Propagation of errors can then be used to determine the predicted CRMVB SD for f. The theoretical (CRMVB) SDs (or CVs) for $f/R_A(1-f)$ can be determined from parameter maps (see Table 2 for both theoretically and experimentally calculated CVs). The restricted proton fraction f can be estimated from $f/R_A(1-f)$ and the longitudinal relaxation rate $R_A(=1/T_1^A)$ of the free proton pool (since $R_A=1/T_1^A$). R_A is obtained from the separate R_{Aobs} measurement using equation 5.19. Using the theory of propagation of errors [312], it can be shown that the fractional uncertainty (i.e. coefficient of variation) in a measurement of f (σ_f) is given by (since $f/R_A(1-f)=fT_1^A/(1-f)$), assuming that there is no coupling between the individual parameters:

$$\sigma_f = \sqrt{\sigma^2_{f/R_A(1-f)} + \sigma^2_{T_{1A}}} \qquad 8.12$$

where $\sigma_{f/R_A(1-f)}$ is the CV in an estimate of $f/R_A(1-f)$, and $\sigma_{T_{1A}}$ is the CV in an estimate of T_1^A.

Strictly one should take into account uncertainties in the parameters RM_0^A, R_B and $f/R_A(1-f)$ when evaluating the uncertainty in T_1^A, since it is calculated from the observed relaxation rate R_{Aobs} (i.e. $1/T_1^A{}_{obs}$) using equation 5.19 [47], [208].

(to within the 95% CL), as would be expected, demonstrating that the use of the new proposed scheme does not introduce systematic errors into fitted parameter values.

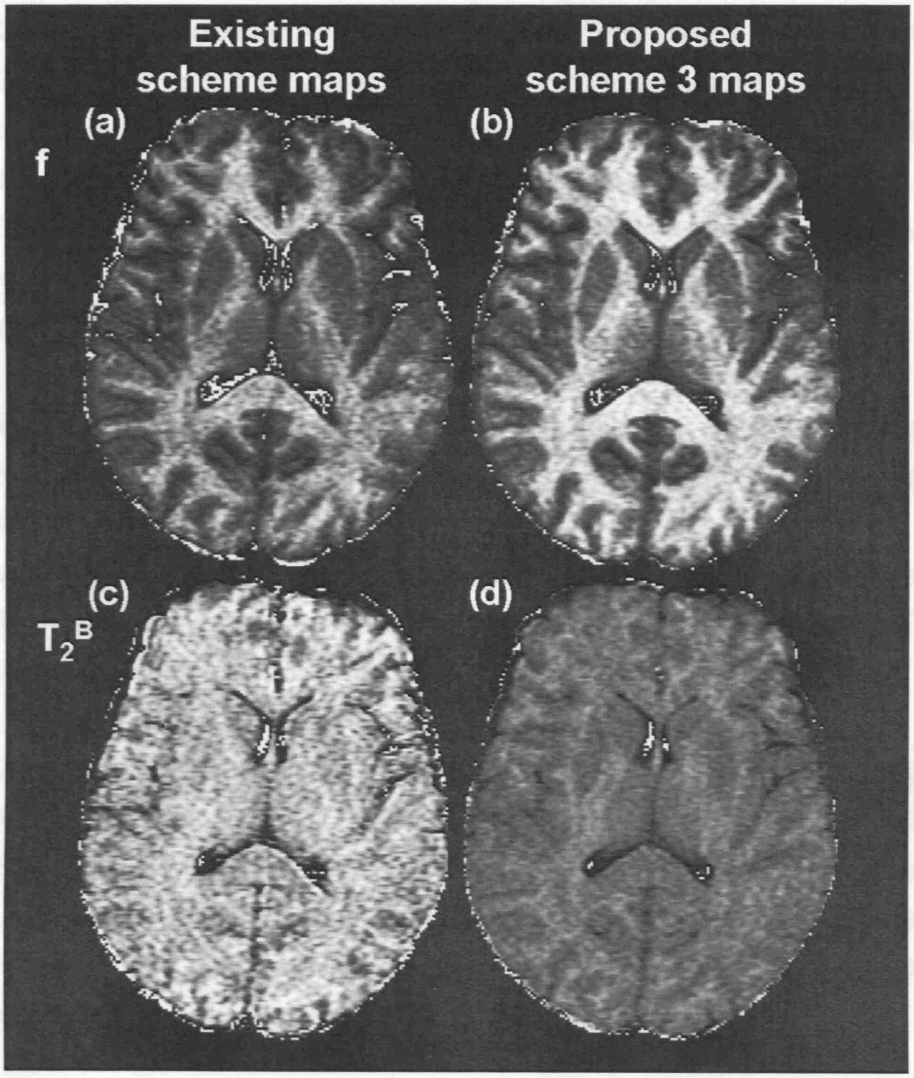

Figure 8.4: Comparison of qMT parameter maps obtained using the new proposed scheme and an existing scheme [47] (displayed using the same window level). The restricted proton fraction f map estimated using the existing scheme is shown in 8.4(a) and compared with that obtained using scheme 3 in 8.4(b), and T_2^B maps estimated using the existing scheme and scheme 3 are shown in 8.4(c) and 8.4(d) respectively.

8.7.4 Discussion and Conclusions: Optimisation

95% CL of theoretically predicted CVs all overlap with those of measured values. The NSR value assumed for theoretical calculations and numerical simulations may also have been under/over-estimated, although 95% confidence limits for the NSR measurement was low (~0.16% of the NSR value). Potential sources of error in

measured CV measurements may include large uncertainties in measurements of SDs in regions of interest (due to the small ROI size or small number of samples).

One potential drawback of this method is that fixing some MT parameters may influence the estimated values of the remaining free parameters, if there is coupling between these parameters. These possible effects and methods for dealing with them are beyond the scope of this study. However, the parameter maps obtained (see figure 8.4) are significantly improved relative to those obtained using the original acquisition scheme, therefore it is assumed that this effect is not large for the particular parameters estimated here.

We have produced a set of optimal qMT data collection schemes which substantially reduce uncertainties in parameter estimates, and are applicable to a range of brain tissues (see table 8.2). Although abnormal brain was not studied here, it is important to accurately characterise normal brain tissue in order to determine its expected variation. This increase in precision could alternatively be traded off to reduce qMT acquisition time, by acquiring less 'MT-weighted' data points.

Using scheme 3, for estimation of both T_2^B and $f/R_A(1-f)$, a theoretical improvement of 48.8% (± 3.7) in the WM T_2^B CV and 44.9% (± 4.0) in the GM T_2^B CV, and a 17.6% (± 5.3) (WM) or 11.0% (± 6.2) (GM) improvement in $f/R_A(1-f)$ CV were observed when using our new optimised scheme, compared to an existing acquisition scheme [47] (where 95% CL are given in brackets). Experimental data was shown to be consistent with theoretical predictions.

Parameter maps obtained for both f and T_2^B were considerably improved in terms of spatial homogeneity and grey-white matter contrast when using scheme 3 for acquisition in comparison to using the existing scheme. It was also demonstrated (see section 8.7.3.3) that the use of the new proposed scheme (3) to estimate f and T_2^B did not result in systematic errors in fitted parameter values (estimated values using this scheme agreed with those estimated using the existing scheme to within 95% CL).

It was demonstrated theoretically, using CRMVB theory combined with the theory of propagation of errors, that the separate measurement of T_1^A does not contribute large uncertainties to the estimation of the restricted proton fraction f. This was confirmed by estimating coefficients of variation in white and grey matter regions in calculated f maps.

It is not possible to say whether the proposed schemes would be directly applicable for use at different field strengths. SAR calculations are scanner dependent, therefore to optimise qMT sampling schemes for use at higher field strengths would probably involve first determining the maximum allowed SAR and constraining the optimisation using this limit.

This approach could easily be extended to other quantitative MRI techniques in which particular quantities are estimated by fitting a quantitative model to a set of MRI measurements collected with different acquisition parameters. Examples include T_1 and T_2 mapping, diffusion imaging (mapping of the apparent diffusion coefficient (ADC)), and perfusion imaging. In all of these cases it may be possible to reduce acquisition time by avoiding collection of unnecessary data, or to increase the precision of estimation of these MR parameters by acquiring data using optimal acquisition schemes.

9 Discussion and Conclusions

Results associated with each individual chapter in this thesis were discussed at the end of each chapter, therefore this final chapter aims to briefly summarise these findings and to consider possible future work in the field of quantitative MT.

9.1 Introduction

Magnetisation Transfer Imaging is widely used both to characterise normal and pathological tissue, often via measurement of the MTR, and also to manipulate tissue contrast. The most commonly used measure of MT is the Magnetisation Transfer Ratio (MTR).

MTR abnormalities have been demonstrated in MS patients in several studies [66], [73], [82], [83], [84], [85], [86], and are thought to be related to demyelination, axonal dysfunction/loss, oedema, gliosis or inflammation. Reductions in MTR values have also been found in dementia patients [115], Alzheimer's Disease (AD) patients [117], the affected hippocampi of temporal lobe epilepsy patients [120] and brain tumours [124], amongst other neurological disorders.

However, the MTR measure reflects a complex combination of various biological and acquisition-dependent factors. Quantitative MT imaging techniques allow us to probe fundamental MT parameters which are thought to give a better insight to changes occurring in tissue in the presence of pathology. In particular, the fraction of macromolecular protons relative to the sum of the pool sizes (f), and the T_2 relaxation time of the semi-solid pool (T_2^B) are thought to be of particular interest in the study of changes occurring in Multiple Sclerosis (MS), since the macromolecular component is likely to be related to myelin content.

In a study of MS patients [48], the mean restricted proton fraction f value was reduced, and the mean T_2^B value was elevated in lesions. In NAWM, mean f was reduced but less markedly, but T_2^B was not significantly elevated in total NAWM. A greater correlation between f and MS disability (measured using the Multiple Sclerosis Functional Composite score (MSFC) [239]) than between T_1 and disability was also observed, demonstrating the clinical relevance of this parameter. The parameter f could be reduced by a decrease in the macromolecular content, either due to demyelination or axonal loss, in combination with an increase in the free proton component, for example by an increase in water content caused by oedema. T_2^B is a measure of the motional restriction of the protons in the semi-solid pool, which are assumed to be attached to macromolecules such as proteins or lipids in tissue.

Therefore alterations in T_2^B are likely to reflect changes in the structure of the remaining macromolecular content of tissue. Other studies have also demonstrated similar changes in fundamental qMT parameters in MS patients [208], [212], [242].

Ridha *et al* [240] demonstrated a reduction in the parameter $1/R_A T_2^A$ in the hippocampal formation in Alzheimer's Disease patients, and it was also shown to correlate with Mini-mental state examination (MMSE) scores. This reduction in $1/R_A T_2^A$ may be due to a lengthening of T_2^A due to membrane breakdown and increase in free water, or a decrease in T_1^A. However, other fundamental qMT parameters were unaffected by AD.

Kiefer *et al* [243] demonstrated significant abnormalities in the parameters T_2^B and T_2^A in the sub-regions of the hippocampi of schizophrenic patients using quantitative MT imaging, supporting the assumption that their structural diversity is the basis of the functional heterogeneity of the hippocampal sub-regions [244].

These preliminary findings demonstrate the potential of quantitative MT imaging for use to diagnose and monitor the pathological changes taking place in many neurological disorders.

9.2 A simple correction for B_1 errors in MTR measurements

B_1 errors, caused by RF non-uniformity and/or inaccurate setting of the transmitter output when compensating for varying amounts of loading of the RF coil, are a problem in MTR measurements, since the measured MTR value is dependent on the amplitude of the MT pulse. This could lead to large errors in MTR measurements, and may also cause MTR histogram dispersion.

The dependence of the MTR on B_1 was modelled using the CWPE model [47], [215] for qMT, and normalised graphs were produced. For B_1 reductions up to 20%, normalised plots for different brain tissue types could be approximated by a single line, indicating that it may be possible to systematically correct for B_1 errors in MTR measurements [251], [252].

On the scanner, B_1 was reduced from its nominal value and the MTR was measured to experimentally determine a correction scheme for B_1 field variations. B_1 field mapping using the Double Angle Method was performed in order to quantify B_1 errors and correct MTR maps and histograms [251], [252].

It was shown that a simple correction scheme can be applied to MTR maps with a known B_1 error, regardless of tissue type. There is some discrepancy between results obtained from numerical simulations and experimental data, which can probably be explained by limitations of the CWPE qMT model.

9.3 Quality Assurance (QA), Phantoms and Internal Thermometry

Bovine Serum Albumin (BSA) was assessed for use as a quality assurance (QA) test-object for MT. It was found that at a concentration of 20% weight/volume, BSA samples both exhibited MTR values close to those of human white matter (around 40pu, when measured using a modified Euro-MT sequence [333], [252]), and also qMT parameters mimicking those observed *in vivo*. The restricted proton fraction f for a 20% w/v concentration BSA sample, using the super-Lorentzian lineshape to model the RF absorption of the restricted proton pool was found to be 9.98 (± 2.81) %, which is very similar to published results for human white matter [48]. The T_2^B value for the same sample was estimated to be 7.31 (± 1.84) μs, which is a little lower than would be expected in brain white matter [48].

One possible source of systematic error in phantom QA measurements is the dependence of many quantitative MR properties on temperature, and not accounting for such errors may limit the accuracy of phantom QA measurements, which will, in turn, have an impact on the interpretation of quantitative changes observed in long-term clinical studies. It is therefore desirable to be able to measure test-object temperature when performing quantitative phantom QA measurements, but many traditional thermometry methods are unsuitable for use in an MRI scanner. A simple, readily available method of internal thermometry was developed for use in MRI phantoms. Using localised ^{1}H-MRS acquisition sequences routinely available on clinical MRI scanners, and commonly available analysis packages, internal thermometry in phantoms using DSS (sodium 3-(trimethylsilyl)propane-1-sulphonate)) as a chemical shift reference was demonstrated to be feasible. The minimum detectable temperature difference was shown to be 100 (±20) mK, which would typically correspond to changes in MR quantities of less than 0.3% [334].

9.4 Optimisation of qMT sequence acquisition parameters

The quantitative MT sequence acquisition parameters (i.e. the selection of 'MT weightings', each a combination of MT pulse amplitude and offset frequency) were optimised, in order to increase the precision of the fundamental qMT model parameters estimated. Compared to a previously published acquisition scheme [47] used in several studies of healthy volunteers and Multiple Sclerosis patients at our centre [48], [335],

[238], the optimisation enables less data to be acquired, reducing acquisition time without compromising uncertainties in estimated parameters. Alternatively, for the same number of MT-weighted data points, the parameter map noise could be reduced, thereby minimising uncertainties in estimated parameter maps. A novel approach was used, involving the minimisation of the Cramer-Rao minimum variance bound (CRMVB) by altering the combination of MT pulse amplitudes and offset frequencies at which data are acquired. This analytical approach was also verified numerically, through the use of Monte Carlo simulations, and experimental data were shown to be consistent with theoretical predictions.

A set of optimal qMT data collection schemes (for estimation of f, T_2^B or both) were produced which substantially reduce uncertainties in parameter estimates, and are applicable to a range of brain tissues. Parameter maps obtained for both f and T_2^B were considerably improved in terms of spatial homogeneity and grey-white matter contrast when using the new proposed scheme for estimation of both parameters for acquisition in comparison to using the existing scheme [336].

This approach could easily be extended to other quantitative MRI techniques in which particular quantities are estimated by fitting a quantitative model to a set of MRI measurements collected with different acquisition parameters. Examples include T_1 and T_2 mapping, diffusion imaging (mapping of the apparent diffusion coefficient (ADC)), and perfusion imaging. In all of these cases it may be possible to reduce acquisition time by avoiding collection of unnecessary data, or to increase the precision of estimation of these MR parameters by acquiring data using optimal acquisition schemes.

9.5 Future work: qMT

An investigation of the validity of the CWPE qMT model is required. This could be achieved by increasing the MT pulse duration (whilst the pulse amplitude is decreased in order to maintain the same B_{1CWPE} value for each MT pulse) and/or shortening the TR' in order that the experiment more closely approaches a continuous wave MT experiment, and observing the effects on the fitted parameters and the quality of the fit of the qMT model to measured data.

In 1995 Morrison *et al* [201] reformulated the Henkelman qMT model to include the possibility of the existence of a semi-solid pool dipolar reservoir in addition to its Zeeman reservoir. The liquid pool is modelled using Bloch theory (and is hence characterised by a Lorentzian RF absorption lineshape), but the restricted pool is

modelled using Redfield-Provotorov theory. It should be investigated whether the inclusion of this additional compartment combined with the CWPE model for qMT results in an improvement of the fit of the model to experimental data (although the fit of the model to data has previously been shown to be very good [337]). A comparison of the model adopted by Sled and Pike [51], and also the 3-parameter approximation made by Yarnykh and Yuan [338] with the CWPE qMT model [47] should also be made. The two-pool model for MT is only an approximation for biological tissue. Three- and four-pool mathematical models to describe MT in tissue have been developed [193], [198], [222], [223], [224] but the complexity of the computation involved, and also the amount of data required to determine all the free parameters make these models difficult to apply in a clinical setting.

A low excitation pulse flip angle is usually used in order to minimise T_1 weighting, as T_1 shortening occurs in the presence of MT saturation. However, the use of a low imaging pulse flip angle also results in low SNR images. T_1 weighting could be accounted for in the qMT model, in order that a higher flip angle could be used, which would improve the SNR. The mathematical modelling of the imaging pulse as well as the excitation (MT) pulse should also be investigated as a potential method of improving the accuracy of the model.

References

1. Haacke EM, Brown RW, Thompson MR, Venkatesan R. Magnetic Resonance Imaging. Physical principles and sequence design. 1st ed. Wiley; 1999.

2. Purcell EM. Electricity and Magnetism. 3rd ed. McGraw-Hill; 1965.

3. Bloch F. Nuclear Induction. Physical Review 1946 Oct;70(7):460-74.

4. Bloch F. Nuclear Induction. Physical Review 1946 Oct;70(7):460-74.

5. Bloch F, Hansen WW, Packard M. The Nuclear Induction Experiment. Physical Review 1946 Oct;70(7):474-85.

6. Tofts PS. Quantitative MRI of the Brain. Measuring Changes Caused by Disease. John Wiley & Sons; 2003.

7. Bottomley PA. Spatial localization in NMR spectroscopy *in vivo*. Annals of the New York Academy of Science 1987;508:333-48.

8. Bloch F. Nuclear Induction. Physical Review 1946 Oct;70(7):460-74.

9. Bloch F, Hansen WW, Packard M. The Nuclear Induction Experiment. Physical Review 1946 Oct;70(7):474-85.

10. Bloembergen N, Purcell EM, Pound RV. Relaxation Effects in Nuclear Magnetic Resonance Absorption. Physical Review 1948 Apr;73(7):679-712.

11. Bloembergen N, Purcell EM, Pound RV. Relaxation Effects in Nuclear Magnetic Resonance Absorption. Physical Review 1948 Apr;73(7):679-712.

12. Bloembergen N, Purcell EM, Pound RV. Relaxation Effects in Nuclear Magnetic Resonance Absorption. Physical Review 1948 Apr;73(7):679-712.

13. Bloembergen N, Purcell EM, Pound RV. Relaxation Effects in Nuclear Magnetic Resonance Absorption. Physical Review 1948 Apr;73(7):679-712.

14. Gadian DG. Nuclear Magnetic Resonance and its Applications to Living Systems. Clarendon Press 1982.

15. Harris RK. Nuclear Magnetic Resonance Spectroscopy: a Physiochemical View. Longman 1986.

16. Brasch RC. Work in progress: methods of contrast enhancement for NMR imaging and potential applications. A subject review. Radiology 1989;171:273-6.

17. Ordidge RJ, Gorell JM, Deniau JC, Knight RA, Helpern JA. Asessment of relative brain iron concentrations using T2-weighted and $T2^*$-weighted MRI at 3 Tesla. Magnetic Resonance in Medicine 1994;32:335-41.

18. Gillis P, Koenig SH. Transverse relaxation of solvent protons induced by magnetised spheres: application to ferritin, erythrocytes, and magnetite. Magnetic Resonance in Medicine 1987;5:323-45.

19. Proctor WG, Yu FC. The Dependence of a Nuclear Magnetic Resonance Frequency upon Chemical Compound. Physical Review 1950 Jan;77:717.

20. Walker PM, Lerski RA, Mathur-de Vre R, Binet J, Yane F. VI. Preparation of agarose gels as reference substances for NMR relaxation time measurement. Magnetic Resonance Imaging 1988;6:215-22.

21. Damadian R. Tumor detection by Nuclear Magnetic Resonance. Science 1971;171(3976):1151.

22. Bottomley PA. In vivo Tumor Discrimination in a Rat by Proton Nuclear Magnetic Resonance Imaging. Cancer Research 1979;39(2):468-70.

23. Hahn EL. Spin Echoes. Physical Review 1950 Nov;80(4):580-94.

24. Hahn EL. Spin Echoes. Physical Review 1950 Nov;80(4):580-94.

25. Carr HY, Purcell EM. Effects of Diffusion on Free Precession in Nuclear Magnetic Resonance Experiments. Physical Review 1954 May;94(3):630-8.

26. Meiboom S, Gill D. Modified Spin-Echo Method for Measuring Nuclear Relaxation Times. Review of Scientific Instruments 1958;29(8):688-91.

27. Haacke EM, Brown RW, Thompson MR, Venkatesan R. Magnetic Resonance Imaging. Physical Principles And Sequence Design. 1st ed. 1999.

28. Lauterbur PC. Image formation by induced local interactions: examples employing Nuclear Magnetic Resonance. Nature 1973;242:190-1.

29. Lauterbur PC, Kramer DM, House WV, Jr., Chan C. Zeugmatographic High Resolution Nuclear Magnetic Resonance Spectroscopy, Images of Chemical Inhomogeneity within Macroscopic Objects. Journal of the American Chemical Society 1975 Nov;97(23):6866-8.

30. Mansfield P, Maudsley AA, Baines T. Fast scan proton density imaging by NMR. Journal of Physics E: Scientific Instruments 1975 Nov;9:271-8.

31. Blackman RB, Tukey JW. Particular Pairs of Windows. The Measurement of Power Spectra. From the point of View of Communications Engineering. 1st ed. New York: Dover; 1959. p 98-9.

32. Kumar A, Welti D, Ernst RR. NMR Fourier Zuegmatography. Journal of Magnetic Resonance 1975;18:69-83.

33. Edelstein WA, Hutchison JMS, Johnson G, Redpath TW. Spin warp NMR imaging and applications to human whole-body imaging. Physics in Medicine and Biology 1980 May;25:751-6.

34. Mansfield P, Maudsley AA, Baines T. Fast scan proton density imaging by NMR. Journal of Physics E: Scientific Instruments 1975 Nov;9:271-8.

35. Tweig DB. The k trajectory formulation of the NMR imaging process with applications in analysis and synthesis of imaging methods. Medical Physics 1983;10:610-21.

36. Wolff SD, Balaban RS. Magnetization Transfer Contrast (MTC) and Tissue Water Proton Relaxation *in vivo*. Magnetic Resonance in Medicine 1989;10(1):135-44.

37. Dixon WT, Engels H, Castillo M, Sardashti M. Incidental Magnetization Transfer Contrast In Standard Multislice Imaging. Magnetic Resonance Imaging 1990;8:417-22.

38. Hennig J, Nauerth A, Friedburg H. RARE Imaging: A fast method for clinical MR. Magnetic Resonance Imaging 1986;6:391-5.

39. Clare S, Jezzard P. Rapid T1 Mapping Using Multislice Echo Planar Imaging. Magnetic Resonance in Medicine 2001;45 :630-4.

40. Ernst RR, Anderson WA. Application of Fourier transform spectroscopy to magnetic resonance. Review of Scientific Instruments 1966;37:93.

41. Wang HZ, Riederer SJ. A Spoiling Sequence for Suppression of Residual Transverse Magnetization. Magnetic Resonance in Medicine 1990;15 :175-91.

42. Harris RK, Becker ED, Caqbral de Menezes SM, Goodfellow R, Granger P. NMR Nomenclature: Nuclear Spin Properties and Conventions for Chemical Shifts. IUPAC Recommendations 2001. Solid State Nuclear Magnetic Resonance 2002;22:458-83.

43. Frahm J, Merboldt KD, Hanicke W. Localized proton spectroscopy using stimulated echoes. Journal of Magnetic Resonance 1987;72:502-8.

44. Frahm J, Michaelis T, Merboldt KD, Bruhn H. Improvements in localized proton NMR spectroscopy of human brain. Water suppression, short echo times, and ml resolution. Journal of Magnetic Resonance 1989;90:464-73.

45. Eng J, Ceckler T, Balaban RS. Quantitative 1H magnetization transfer imaging in vivo. Magnetic Resonance in Medicine 1991;17(2):304-14.

46. Vavasour IM, Whittall K, Li DK, MacKay A. Different magnetization transfer effects exhibited by the short and long T2 components in human brain. Magnetic Resonance in Medicine 2000;44(6):860-6.

47. Ramani A, Dalton C, Miller DH, Tofts PS, Barker GJ. Precise estimate of fundamental in-vivo MT parameters in human brain in clinically feasible times. Magnetic Resonance Imaging 2002;20 :721-31.

48. Davies GR, Tozer DJ, Cercignani M, Ramani A, Dalton C, Thompson AJ, Barker GJ, Tofts PS, Miller DH. Estimation of the macromolecular proton fraction and bound pool T2 in multiple sclerosis. Multiple Sclerosis 2004;10:607-13.

49. Henkelman RM, Huang XM, Xiang QS, Stanisz GJ, Swanson SD, Bronskill MJ. Quantitative Interpretation of Magnetization-Transfer. Magnetic Resonance in Medicine 1993;29(6):759-66.

50. Pike GB. Pulsed magnetization transfer contrast in gradient echo imaging: A two-pool analytic description of signal response. Magnetic Resonance in Medicine 1996;36(1):95-103.

51. Sled JG, Pike GB. Quantitative interpretation of magnetization transfer in spoiled gradient echo MRI sequences. Journal of Magnetic Resonance 2000;145(1):24-36.

52. McConnell HM. Reaction rates by nuclear magnetic resonance. Journal of Chemical Physics 1958;28:430-1.

53. Forsen S, Hoffman RA. Study of moderately rapid chemical exchange reactions by means of nuclear magnetic double resonance. Journal of Chemical Physics 1963;39(11):2892-901.

54. Edzes HT, Samulski ET. The measurement of cross-relaxation effects in the proton NMR spin-lattice relaxation of water in biological systems: hydrated collagen and muscle. Journal of Magnetic Resonance 1978;31:207-29.

55. Barker GJ, Tofts PS, Gass A. An interleaved sequence for accurate and reproducible measurement of magnetization transfer ratio. Magnetic Resonance Imaging 1996;14(4):403-11.

56. Ropele S, Stollberger R, Hartnung HP, Fazekas F. Fast multislice T(1) and T(1sat) imaging using a phase acquisition of composite echoes (PACE) technique. Journal of Magnetic Resonance Imaging 1999;42(65):1089-97.

57. Ropele S, Stollberger R, Kapeller P, Hartnung HP, Fazekas F. Estimation of magnetization transfer rates from PACE experiments with pulsed RF saturation. Journal of Magnetic Resonance Imaging 2000;12(5):749-56.

58. Hu BS, Conolly SM, Wright GA, Nishimura DG, Macovski A. Pulsed saturation transfer contrast. Magnetic Resonance in Medicine 1992;26(2):231-40.

59. Pachot-Clouard M, Darasse L. Optimization of T2-selective binomial pulses for Magnetization Transfer. Magnetic Resonance in Medicine 1995;34:462-9.

60. Pike GB, Hu BS, Glover GH, Enzmann DR. Magnetization transfer time-of-flight magnetic resonance angiography. Magnetic Resonance in Medicine 1992;25(2):372-9.

61. Pike GB, Glover GH, Hu BS, Enzmann DR. Pulsed Magnetization Transfer Spin-Echo Mr-Imaging. Jmri-Journal of Magnetic Resonance Imaging 1993;3(3):531-9.

62. Graham SJ, Henkelman RM. Understanding pulsed magnetization transfer. Journal of Magnetic Resonance Imaging 1997;7(5):903-12.

63. Barker GJ, Schreiber W, Gass A, Ranjava JP, Campi A, van Waesberghe JH. Standardising magnetisation transfer ratio measurements between MR scanners from different manufacturers. Proceedings of the International Society of Magnetic Resonance in Medicine 1997;5:1556.

64. Barker GJ, Schreiber WG, Gass A, Ranjeva JP, Campi A, van Waesberghe JHTM, Franconi JM, Watt HC, Tofts PS. A standardised method for measuring magnetisation transfer ratio on MR imagers from different manufacturers - The EuroMT sequence. Magnetic Resonance Materials in Physics Biology and Medicine 2005 May;18(2):76-80.

65. Barker GJ, Schreiber WG, Gass A, Ranjeva JP, Campi A, van Waesberghe JHTM, Franconi JM, Watt HC, Tofts PS. A standardised method for measuring magnetisation transfer ratio on MR imagers from different manufacturers - The EuroMT sequence. Magnetic Resonance Materials in Physics Biology and Medicine 2005 May;18(2):76-80.

66. Dousset V, Grossman RI, Ramer KN, Schnall MD, Young LH, Gonzalez-Scarano F, Lavi E, Cohen JA. Experimental Allergic Encephalomyelitis and Multiple Sclerosis: lesion characterization with magnetization transfer imaging. Radiology 1992;182 :483-91.

67. Dehmeshki J, Barker GJ, Tofts PS. Classification of disease subgroup and correlation with disease severity using magnetic resonance imaging whole-brain histograms: application to magnetization transfer ratios and multiple sclerosis. IEEE Trans Medical Imaging 2002;21(4):320-31.

68. Finelli DA, Hurst GC, Amantia P, Jr., Gullapali RP, Apicella A, . Cerebral white matter: technical development and clinical applications of effective magnetization transfer (MT) power concepts for high-power, thin-section, quantitative MT examinations. Radiology 1996;199(1):219-26.

69. Tozer DJ, Tofts PS. Removing Spikes Caused by Quantization Noise From High-Resolution Histograms. Magnetic Resonance in Medicine 2003;50:649-53.

70. Edelmann RR, Ahn SS, Chien D, Wei L, Goldmann A, Mantello M, Kramer J, Kleefield J. Improved time-of-flight Magnetic Resonance Angiograpy of the brain with Magnetisation Transfer Contrast. Radiology 1992 Aug;184:395-9.

71. Kermode AG, Thompson AJ, Tofts PS, MacManus D, Kendall BE, Kingsley DPE, Moseley IF, Rudge P, McDonald WI. Breakdown of the blood-brain barrier precedes symptoms and other MRI signs of new lesions in multiple sclerosis. Pathogenetic and clinical implications. Brain 1990;113 :1477-89.

72. Tanttu JI, Sepponen RE, Lipton MJ, Kuusela T. Synergistic enhancement of MRI with Gd-DTPA and magnetization transfer. Journal of Computer Assisted Tomography 1992;16(1):19-24.

73. van Waesberghe JH, Castelijns JA, Scheltens P, Truyen L, Nijeholt GJ, Hoogenraad FG, Polman CH, Valk J, Barkhof F. Comparison of four potential MR parameters for severe tissue destruction in multiple sclerosis lesions. Magnetic Resonance Imaging 1997;15(2):155-62.

74. Mehta RC, Pike GB, Haros SP, Enzmann DR. Central nervous system tumor, infection and infarction: detection with gadolinium-enhanced magnetization transfer MR imaging. Radiology 1995;195 (1):41-6.

75. Finelli DA, Hurst GC, Gullapali RP, Bellon EM. Improved contrast of enhancing brain lesions on post gadolinium, T1-weighted spin-echo images with use of magnetization transfer. Radiology 1994;190 :553-9.

76. Berry I, Barker GJ, Barkhof F, Campi A, Dousset V, Franconi JM, Gass A, Schreiber W, Miller DH, Tofts PS. A multicenter measurement of magnetization transfer ratio in normal white matter. Journal of Magnetic Resonance Imaging 1999;9(3):441-6.

77. Silver NC, Barker GJ, Miller DH. Standardization of magnetization transfer imaging for multicenter studies. Neurology 1999;53(5):S33-S39.

78. Engelbrecht V, Rassek M, Preiss S, Wald C, Modder U. Age-dependent changes in magnetization transfer contrast of white matter in the pediatric brain. American Journal of Neuroradiology 1998;19:1923-9.

79. van Buchem MA, Steens SCA, Vrooman HA, Zwinderman AH, McGowan JC, Rassek M, Engelbrecht V. Global estimation of myelination in the developing brain on the basis of magnetization transfer imaging: a preliminary study. American Journal of Neuroradiology 2001;22:762-6.

80. Silver NC, Barker GJ, MacManus DG, Tofts PS, Miller DH. Magnetisation transfer ratio of normal brain white matter: A normative database spanning four

decades of life. Journal of Neurology Neurosurgery and Psychiatry 1997;62(3):223-8.

81. Good CD, Johnsrude IS, Ashburner J, Henson RN, Friston KJ, Frackowiak RS. A voxel-based morphometric study of ageing in 465 normal adult human brains. NeuroImage 2001;14:21-36.

82. Grossman RI, Kapouleas I, Kessler DB, Lexa FJ, Boorstein JM, Cohen JA. Clinical-Application of Lesion Quantitation in Multiple- Sclerosis. Radiology 1992;185:219.

83. Gass A, Davie CA, Barker GJ, McDonald WI, Miller DH. Demonstration of plaque development in multiple sclerosis using magnetisation transfer imaging and short echo time proton spectroscopy. Neurology 1997;68(12):996-1001.

84. Filippi M, Bozzali M, Horsfield MA, Rocca MA, Sormani MP, Iannucci G, Colombo B, Comi G. A conventional and magnetization transfer MRI study of the cervical cord in patients with MS. Neurology 2000;54(1):207-13.

85. Silver N, Barker GJ, Gawne-Cain ML, MacManus D, Thompson AJ, Miller DH. Magnetization transfer ratio measurement in the cervical spinal cord: a preliminary study in multiple sclerosis. Neuroradiology 1996;39 :441-5.

86. Hiehle JF, Lenkinski RE, Grossman RI, Dousset V, Ramer KN, Schnall MD, Cohen JA, Gonzalez-Scarano F. Correlation of Spectroscopy and Magnetization Transfer Imaging in the Evaluation of Demyelinating Lesions and Normal Appearing White Matter in Multiple Sclerosis. Magnetic Resonance in Medicine 1994;32 :285-93.

87. Arnold DL. Magnetic resonance spectroscopy: imaging axonal damage in MS. Journal of Neuroimmunology 1999;98 :2-6.

88. Matthews PM, Pioro E, Narayan S, De Stefano N, Fu L, Francis GS, Antel JP, Wolfson C, Arnold DL. Assessment of lesion pathology in multiple sclerosis using quantitative MRI morphometry and magnetic resonance spectroscopy. Brain 1996;119 :715-22.

89. Davie CA, Hawkins CP, Barker GJ, Brennan A, Tofts PS, Miller DH, McDonald WI. Serial Proton Magnetic-Resonance Spectroscopy in Acute Multiple-Sclerosis Lesions. Brain 1994;117:49-58.

90. De Stefano N, Matthews PM, Fu L, Narayan S, Stanley J, Francis GS, Antel JP, Arnold DL. Axonal damage correlates with disability in patients with relapsing-remitting multiple sclerosis. Results of a longitudinal magnetic resonance spectroscopy study. Brain 1998;121 :1469-77.

91. De Stefano N, Narayan S, Matthews PM, Mortilla M, Teresa Dotti M, Federico A, Arnold DL. Proton MR spectroscopy to assess axonal damage in multiple sclerosis and other white matter disorders. Journal of Neurovirology 2000;6 (Supplement 2) :S121-S129.

92. Kimura H, Grossman RI, Lenkinski RE, Gonzalez-Scarano F. Proton MR spectroscopy and magnetization transfer ratio in multiple sclerosis: Correlative findings of active: versus irreversible plaque disease. American Journal of Neuroradiology 1996;17(8):1539-47.

93. Davie CA, Silver NC, Barker GJ, Tofts PS, Thompson AJ, McDonald WI, Miller DW. Does the extent of axonal loss and demyelination from chronic lesions in

multiple sclerosis correlate with the clinical subgroup? Journal of Neurology Neurosurgery and Psychiatry 1999;67(6):710-5.

94. Brochet B, Dousset V. Pathological correlates of magnetization transfer imaging abnormalities in animal models and humans with multiple sclerosis. Neurology 1999;53 (Supplement 3)(S12):S17.

95. Lexa FJ, Grossman RI, Rosenquist AC. MR of Wallerian Degeneration in the Feline Visual-System - Characterization by Magnetization-Transfer Rate with Histopathologic Correlation. American Journal of Neuroradiology 1994;15(2):201-12.

96. Gareau DF, Rutt BK, Karlik SJ, Mitchell JR. Magnetization transfer and multicomponent T2 relaxation measurements with histopathologic correlation in an experimental model of MS. Journal of Magnetic Resonance Imaging 2000;11(6):586-95.

97. MacKay A, Whittall K, Adler RS, Li D, Paty D, Graeb D. In vivo visualization of myelin water in brain by magnetic resonance. Magnetic Resonance in Medicine 1994;37(6):673-7.

98. Whittall K, MacKay A, Graeb D, Nugent RA, Li DK, Paty D. In vivo measurement of T2 distributions and water contents in normal human brain. Magnetic Resonance in Medicine 1997;37(1):34-43.

99. Henkelman RM, Stanisz GJ, Graham SJ. Magnetization transfer in MRI: a review. NMR in Biomedicine 2001;14(2):57-64.

100. Stanisz GJ, Webb S. Understanding the MT, T1 and T2 changes during demyelination and inflammation. Proceedings of the International Society of Magnetic Resonance in Medicine 2002;10:183.

101. van Buchem MA, McGowan JC, Kolson DL, Polansky M, Grossman RI. Quantitative volumetric magnetization transfer analysis in multiple sclerosis: estimation of macroscopic and microscopic disease burden. Magnetic Resonance in Medicine 1996;36(4):632-6.

102. van Buchem MA, Grossman RI, Armstrong C, Polansky M, Miki Y, Heyning FH, Boncoeur-Martel MP, Wei L, Udupa JK, Grossman M, Kolson DL, McGowan JC. Correlation of volumetric magnetization transfer imaging with clinical data in MS. Neurology 1998;50(6):1609-17.

103. Filippi M, Tortorella C, Bozzali M. Normal-appearing white matter changes in multiple sclerosis: the contribution of magnetic resonance techniques. Multiple Sclerosis 1999;5(4):273-82.

104. Filippi M, Iannucci G, Tortorella C, Minicucci L, Horsfield MA, Colombo B, Sormani MP, Comi G. Comparison of MS clinical phenotypes using conventional and magnetization transfer MRI. Neurology 1999;52(3):588-94.

105. Tortorella C, Viti B, Bozzali M, Sormani MP, Rizzo G, Gilardi MF, Comi G, Filippi M. A magnetization transfer histogram study of normal-appearing brain tissue in MS. Neurology 2000;54(1):186-93.

106. Filippi M, Tortorella C, Rovaris M, Bozzali M, Possa F, Sormani MP, Iannucci G, Comi G. Changes in the normal appearing brain tissue and cognitive impairment in multiple sclerosis. Journal of Neurology, Neurosurgery and Psychiatry 2000;68 :157-61.

107. Ge Y, Grossman RI, Udupa JK, Babb JS, Mannon LJ, McGowan JC. Volume and magnetization transfer ratio of normal adult brain tissues: Quantitative MR imaging. Radiology 2000;217:212.

108. Dehmeshki J, Silver NC, Leary SM, Tofts PS, Thompson AJ, Miller DH. Magnetisation transfer ratio histogram analysis of primary progressive and other multiple sclerosis subgroups. Journal of the Neurological Sciences 2001;185(1):11-7.

109. Leary SM, Silver NC, Stevenson VL, Barker GJ, Miller DH, Thompson AJ. Magnetisation transfer of normal appearing white matter in primary progressive multiple sclerosis. Multiple Sclerosis 1999;5(5):313-6.

110. Pike GB, De Stefano N, Narayanan S, Worsley KJ, Pelletier D, Francis GS, Antel JP, Arnold DL. Multiple sclerosis: Magnetization transfer MR imaging of white matter before lesion appearance on T2-weighted images. Radiology 2000;215(3):824-30.

111. Santos AC, Narayanan S, De Stefano N, Tartaglia MC, Francis SJ, Arnaoutelis R, Caramanos Z, Antel JP, Pike GB, Arnold DL. Magnetization transfer can predict clinical evolution in patients with multiple sclerosis. Journal of Neurology 2002;249(6):662-8.

112. Dehmeshki J, Ruto AC, Arridge S, Silver N, Miller DH, Tofts PS. Analysis of MTR histograms in multiple sclerosis using principal components and multiple discriminant analysis. Magnetic Resonance in Medicine 2001;46 :600-9.

113. Cercignani M, Bozzali M, Iannucci G, Comi G, Filippi M. Magnetisation transfer ratio and mean diffusivity of normal appearing white and grey matter from patients with multiple sclerosis. Journal of Neurology Neurosurgery and Psychiatry 2001;70(3):311-7.

114. Kalkers NF, Hintzen RQ, van Waesberghe JH, Lazeron RHC, van Schijndel RA, Ader HJ, Polman CH, Barkhof F. Magnetization transfer histogram parameters reflect all dimensions of MS pathology, including atrophy. Journal of the Neurological Sciences 2001;184 :155-62.

115. Hanyu H, Asano T, Sakurai H, Imon Y, Iwamoto T, Takasaki M, Shindo H, Abe K. Diffusion-weighted and magnetization transfer imaging of the corpus callosum in Alzheimer's disease. Journal of the Neurological Sciences 1999;167 :37-44.

116. Kabani NJ, Sled JG, Chertkow H. Magnetization Transfer Ratio in Mild Cognitive Impairment and Dementia of Alzheimer's Type. NeuroImage 2002;15 :604-10.

117. Ridha BH, Symms MR, Lewis EB, MacManus DG, Boulby PA, Barker GJ, Tofts PS, Rossor MN, Fox NC. Magnetization Transfer Imaging of the Hippocampal Formation: Application to Alzheimer's Disease. Neurobiology of Aging 2004;25(Supplement 2):270.

118. Bozzali M, Franceschi M, Falini A, Pontesilli S, Cercignani M, Magnani G, Scotti G, Comi G, Filippi M. Quantification of tissue damage in AD using diffusion tensor and magnetization transfer MRI. Neurology 2001;57 :1135-7.

119. van der Flier WM, van den Heuvel DMJ, Weverling R, Bollen ELEM, Westendorp RGJ, van Buchem MA, Middelkoop HAM. Magnetization Transfer

Imaging in Normal Aging, Mild Cognitive Impairment, and Alzheimer's Disease. Annals of Neurology 2002;52 :62-7.

120. Tofts PS. Novel MR Image-Contrast Mechanisms in Epilepsy. Magnetic Resonance Imaging 1995;13(8):1099-106.

121. Hahnel S, Munkel K, Jansen O, Heiland S, Reidel M, Friston KJ, Aschoff A, Sartor K. Magnetization Transfer Measurements in the Normal-Appearing Cerebral White Matter in Patients with Chronic Obstructive Hydrocephalus. Journal of Computer Assisted Tomography 1999;23 (4):516-20.

122. Gupta RK, Vatsal DK, Husain N, Chawla S, Prasad KN, Roy R, Kumar R, Jha D, Husain M. Differentiation of tuberculous from pyogenic brain abcesses with *in vivo* proton MR spectroscopy and magnetization transfer MR imaging. American Journal of Neuroradiology 2001;22:1503-9.

123. Gupta RK, Husain N, Kathuria MK, Datta S, Rathore RK, Husain M. Magnetization transfer MR imaging correlation with histopathology in intracranial tuberculomas. Clinical Radiology 2001;56:656-63.

124. Okumura A, Takenaka K, Nishimura Y, Asano Y, Sakai N, Kuwata K, Era S. The characterization of human brain tumor using magnetization transfer technique in magnetic resonance imaging. Neurological Research 1999;21:250-4.

125. Dousset V, Armand JP, Lacoste D, Mieze S, Leteneur L, Dartigues JF, Caille J. Magnetization transfer study of HIV encephalitis and progressive multifocal leukoencephalopathy. American Journal of Neuroradiology 1997;18:895-901.

126. Silver NC, Barker GJ, MacManus DG, Miller DH, Thorpe JW, Howard RS. Decreased magnetisation transfer ratio due to demyelination: A case of central pontine myelinolysis. Journal of Neurology Neurosurgery and Psychiatry 1996;61(2):208-9.

127. Inglese M, Rovaris M, Bianchi S, La Mantia L, Mancardi G, Ghezzi A, Mantagna P, Salvi F, Filippi M. Magnetic resonance imaging, magnetization transfer imaging and diffusion weighted imaging correlates of optic nerve, brain and cervical cord damage in Leber's hereditary optic neuropathy. Journal of Neurology Neurosurgery and Psychiatry 2001;70:444-9.

128. Smith SA, Golay X, Fatemi A, Jones CK, Raymond GV, Moser HW, van Zijl PCM. Magnetization Transfer Weighted Imaging in the Upper Cervical Spinal Cord Using Cerebrospinal Fluid as Intersubject Normalization Reference (MTCSF Imaging). Magnetic Resonance in Medicine 2005;54:201-6.

129. Fatemi A, Smith SA, Dubey P, Zackowski KM, Bastian AJ, van Zijl PCM, Raymond GV, Golay X. Magnetization transfer MRI demonstrates spinal cord abnormalities in adrenomyeloneuropathy. Neurology 2005;64:1739-45.

130. Dreher W, Norris DG, Liebfritz D. Magnetization transfer affects the proton creatine/phosphocreatine signal intensity: in vivo demonstration in the rat brain. Magnetic Resonance in Medicine 1994;31:81-4.

131. Helms G, Frahm J. Magnetization Transfer attenuation of creatine resonances in localized proton MRS of human brain. NMR in Biomedicine 1999;12:490-4.

132. Kotitschke K, Jung H, Nekolla S, Haase A, Bauer A, Bogdahn U. High-resolution one-dimensional and 2-dimensional 1H-MRS of human brain tumour and normal glial cells. NMR in Biomedicine 1994;7(3):111-20.

133. Luo Y, Rydzewski J, de Graaf RA, Gruetter R, Garwood M, Schleich T. In Vivo Observation of Lactate Methyl Proton Magnetization Transfer in Rat C6 Glioma. Magnetic Resonance in Medicine 1999;41:676-85.

134. Meyerhoff DJ. Proton Magnetization Transfer of Metabolites in Human Brain. Magnetic Resonance in Medicine 1999;42:417-20.

135. de Graaf RA, van Kranenburg A, Nicolay K. Off-resonance Metabolite Magnetization Transfer Measurements on Rat Brain In Situ. Magnetic Resonance in Medicine 1999;41(4):1136-44.

136. McLean MA, Simister RJ, Barker GJ, Duncan JS. Magnetization Transfer Effect on Human Brain Metabolites and Macromolecules. Magnetic Resonance in Medicine 2005;54:1281-5.

137. McDonald WI, Silberberg DH. Multiple sclerosis. Butterworths; 1986.

138. McDonald WI. The pathophysiology of multiple sclerosis. In: Compston A, Ebers GC, Lassmann H, McDonald I, Matthews B, Wekerle H, editors. 3rd ed. Edinburgh: Churchill Livingstone; 1997.

139. Kandel ER, Schwartz JH, Jessell TM. Principles of Neural Science. 4th ed. McGraw-Hill; 2000.

140. Kiernan JA. Barr's The Human Nervous System: An Anatomical Viewpoint. 7th ed. Philadelphia: Lippincott-Raven Publishers; 1998.

141. Kingsley RE. Concise Text of Neuroscience. 2nd ed. Baltimore: Lippincott Williams & Wilkins; 2000.

142. Gertz SD. Liebman's Neuroanatomy made easy and understandable. 5th ed. Maryland: Aspen Publishers Inc; 1996.

143. Miller DH, Ormerod IEC, Du Boulay EPGH, McDonald WI, Rudge P, Kendall BE, Moseley IF, Halliday AM, Scaravilli F, Tofts PS, Zilkha KJ. A summary of the present contribution of magnetic resonance imaging to diagnosis and understanding of multiple sclerosis. Magnetic Resonance Imaging 1995;121-5.

144. Filippi M, Miller DH. Magnetic resonance imaging in the differential diagnosis and monitoring of the treatment of multiple sclerosis. Current Opinion in Neurology 1996;9(3):178-86.

145. Miller DH, Frank JA. Magnetic resonance imaging techniques to monitor short term evolution of multiple sclerosis and to use in preliminary trials. Journal of Neurology Neurosurgery and Psychiatry 1998;64:S44-S46.

146. Miller DH, Grossman RI, Reingold SC, McFarland HF. The role of magnetic resonance techniques in understanding and managing multiple sclerosis. Brain 1998;121:3-24.

147. De Myer W. Neuroanatomy. 1st ed. Williams & Wilkins; 1988.

148. Martin EA. Oxford Concise Medical Dictionary. 6th ed. 2002.

149. Dangond F. Multiple Sclerosis. eMedicine Neurology . 2005.
Ref Type: Electronic Citation

150. Trapp BD, Peterson J, Ransohoff RM, Rudick RA, Mork S, Bo L. Axonal transection in the lesions of multiple sclerosis. The New England Journal of Medicine 1998;338 :278-85.

151. Poser CM, Paty DW, Scheinberg L, McDonald WI, Davis FA, Ebers GC, Johnson KP, Sibley WA, Silberberg DH, Tourtellotte WW. New diagnostic criteria for multiple sclerosis: guidelines for research protocols. Annals of Neurology 1983;13:227-31.

152. McDonald WI, Compston A, Edan G. Recommended diagnostic criteria for multiple sclerosis: guidelines from the International Panel on the Diagnosis of Multiple Sclerosis. Annals of Neurology 2001;50:121-7.

153. Tourtellotte WW, Tumani H. Multiple Sclerosis: cerebrospinal fluid. In: Raine CS, McFarland HF, Tourtellotte WW, editors. Multiple Sclerosis: clinical and pathogenetic basis. 1st ed. London: Chapman and Hall; 1997. p 57-79.

154. Cole SR, Beck RW, Moke PS, Kaufman DI, Tourtellotte WW. The predictive value of CSF oligoclonal banding for MS 5 years after optic neuritis. Neurology 1998;51(3):885-7.

155. McLean BN, Miller DH, Thompson AJ. Oligoclonal banding of IgG in CSF, blood-brain barrier function, and MRI findings in patients with sarcoidosis, systemic lupus erythematosus, and Behcet's disease involving the nervous system. Journal of Neurology Neurosurgery and Psychiatry 1995;58:548-54.

156. Runmarker B, Andersen O. Prognostic factors in a multiple-sclerosis incidence cohort with 25 years of follow-up. Brain 1993;116(1):117-34.

157. Kurtzke JF. Rating Neurological Impairment in Multiple Sclerosis - An Expanded Disability Status Scale (EDSS). Neurology 1983;33(11):1444-52.

158. Miller DH, Albert PS, Barkhof F, Francis G, Frank JA, Hodgkinson S, Lublin FD, Paty DW, Reingold SC, Simon J. Guidelines for the use of magnetic resonance techniques in monitoring the treatment of multiple sclerosis. Annals of Neurology 1996;39(1):6-16.

159. Miller DH. Biomarkers and Surrogate Outcomes in Neurodegenerative Disease: Lessons from Multiple Sclerosis. The Journal for the American Society for Experimental NeuroTherapeutics 2004;1:284-94.

160. Bruck W, Kuhlmann T, Stadelman C. Remyelination in multiple sclerosis. Journal of the Neurological Sciences 2003;206 :181-5.

161. Davie CA, Barker GJ, Webb S, Tofts PS, Thompson AJ, Harding AE, McDonald WI, Miller DH. Persistent functional deficit in multiple sclerosis and autosomal dominant cerebellar ataxia is associated with axon loss. Brain 1995;118(6):1583-92.

162. Prineas JW, Barnard RO, Kwon EE, Sharer LR, Cho E-S. Multiple Sclerosis: Remyelination of Nascent Lesions. Annals of Neurology 1993;33:137-51.

163. Evangelou N, Esiri MM, Smith S, Palace J, Matthews PM. Quantitative pathological evidence for axonal loss in normal appearing white matter in multiple sclerosis. Annals of Neurology 2000;47:391-5.

164. Allen IV, McKeown SR. A histological, histochemical and biochemical study fo the macroscopically normal white matter in multiple sclerosis. Journal of the Neurological Sciences 1979;41:81-9.

165. Fazekas F, Barkhof F, Filippi M, Grossman RI, Li DKB, McDonald WI, McFarland HF, Paty DW, Simon JH, Wolinsky JS, Miller DH. The contribution of magnetic resonance imaging to the diagnosis of multiple sclerosis. Neurology 1999;53(3):448-56.

166. Frohman EM, Goodin DS, Calabresi PA, Corboy JR, Coyle PK, Filippi M, Frank JA, Galetta SL, Grossman RI, Hawker K, Kachuck NJ, Levin MC, Phillips JT, Racke MK, Rivera VM, Stuart WH. The utility of MRI in suspected MS. Report of the Therapeutics and Technology Assessment Subcommittee of the American Academy of Neurology. Neurology 2003;61:602-11.

167. Stark DD, Bradley Jr. WG. Magnetic Resonance Imaging. 3rd ed. Mosby; 1999.

168. Filippi M, Yousry T, Baratti C, Horsfield MA, Mammi S, Becker C, Voltz R, Spuler S, Campi A, Reiser MF, Comi G. Quantitative assessment of MRI lesion load in multiple sclerosis: a comparison of conventional spin-echo with fast fluid-attenuated inversion recovery. Brain 1996;119:1349-55.

169. Rydberg JN, Hammond CA, Grimm RC, Erickson BJ, Jack CR, Huston J, Riederer SJ. Initial clinical experience in MR imaging of the brain with a fast fluid-attenuated inversion-recovery pulse sequence. Radiology 1994;193:173-80.

170. van Walderveen MAA, Kamphorst W, Scheltens P, van Waesberghe JHTM, Ravid R, Valk J, Polman CH, Barkhof F. Histopathologic correlate of hypointense lesions on T1-weighted spin-echo MRI in multiple sclerosis. Neurology 1998;50(5):1282-8.

171. Bitsch A, Kuhlmann T, Stadelmann C, Lassmann H, Lucchinetti C, Bruck W. A longitudinal study of histopathologically defined hypointense multiple sclerosis lesions. Annals of Neurology 2001;49:793-6.

172. Truyen L, van Waesberghe JH, van Walderveen MAA, van Oosten BW, Polman CH, Hommes OR, Ader HJ, Barkhof F. Accumulation of hypointense lesions ('black holes') on T1 spin-echo MRI correlates with disease progression in multiple sclerosis. Neurology 1996;47:1469-76.

173. Tofts PS. Modeling tracer kinetics in dynamic Gd-DTPA MR imaging. Journal of Magnetic Resonance Imaging 1997;7:91-101.

174. Miller DH, Barkhof F, Nauta JJP. Gadolinium enhancement increases the sensitivity of MRI in detecting disease activity in multiple sclerosis. Brain 1993;116 :1077-94.

175. Filippi M, Yousry T, Campi A, Kandziora C, Colombo B, Voltz R, Martinelli V, Spuler S, Bressi S, Sotti G, Comi G. Comparison of triple dose versus standard dose gadolinium-DTPA for detection of MRI enhancing lesions in patients with MS. Neurology 1996;46:379-84.

176. Silver NC, Good CD, Barker GJ, MacManus DG, Thompson AJ, Moseley IF, McDonald WI, Miller DH. Sensitivity of contrast enhanced MRI in multiple sclerosis - Effects of gadolinium dose, magnetization transfer contrast and delayed imaging. Brain 1997;120:1149-61.

177. Filippi M, Horsfield MA, Tofts PS, Barkhof F, Thompson AJ, Miller DH. Quantitative assessment of MRI lesion load in monitoring the evolution of multiple sclerosis. Brain 1995;118 :1601-12.

178. Fu L, Matthews PM, De Stefano N, Worsley KJ, Narayan S, Francis GS, Antel JP, Wolfson C, Arnold DL. Imaging axonal damage of normal-appearing white matter in multiple sclerosis. Brain 1998;121 :103-13.

179. Davies GR, Ramio-Torrenta L, Hadjiprocopis A, Chard DT, Griffin CM, Rashid W, Barker GJ, Kapoor R, Thompson AJ, Miller DH. Evidence for grey matter MTR abnormality in minimally disabled patients with early relapsing-remitting multiple sclerosis. Journal of Neurology Neurosurgery and Psychiatry 2004;75:998-1002.

180. Davies GR, Altmann DG, Rashid W, Chard DT, Griffin CM, Barker GJ, Kapoor R, Thompson AJ, Miller DH. Emergence of thalamic magnetization transfer ratio abnormality in early relapsing-remitting multiple sclerosis. Multiple Sclerosis 2005;11:276-81.

181. Kidd D, Barkhof F, McConnel R, Algra PR, Allen IV, Revesz T. Cortical lesions in multiple sclerosis. Brain 1999;122:17-26.

182. Gass A, Filippi M, Rodegher M, Schwartz A, Comi G, Henerici MG. Characteristics of chronic MS lesions in the cerebrum, brain stem, spinal cord and optic nerve on T1-weighted MRI. Neurology 1998;50:548-50.

183. Filippi M, Yousry T, Alkadhi H, Stehling MK, Horsfield MA, Voltz R. Spinal cord MRI in multiple sclerosis with multicoil arrays: a comparison between fast spin echo and fast FLAIR. Journal of Neurology Neurosurgery and Psychiatry 1996;61:632-5.

184. Losseff NA, Webb SL, ORiordan JI, Page R, Wang L, Barker GJ, Tofts PS, McDonald WI, Miller DH, Thompson AJ. Spinal cord atrophy and disability in multiple sclerosis - A new reproducible and sensitive MRI method with potential to monitor disease progression. Brain 1996;119:701-8.

185. Kidd D, Thorpe JW, Kendall BE, Barker GJ, Miller DH, McDonald WI, Thompson AJ. MRI dynamics of brain and spinal cord in progressive multiple sclerosis. Journal of Neurology Neurosurgery and Psychiatry 1996;60(1):15-9.

186. Miller DH, Austin SJ, Connelly A, Youl BD, Gadian DG, McDonald WI. Proton magnetic resonance spectroscopy of an acute and chronic lesion in multiple sclerosis. The Lancet 1991;337 :58-9.

187. Brenner RE, Munro PMG, Williams SCR, Bell JD, Barker GJ, Hawkins CP, Landon DN, McDonald WI. The proton NMR-spectrum in acute EAE - The significance of the change in the Cho-Cr ratio. Magnetic Resonance in Medicine 1993;29:737-45.

188. Morrison C, Henkelman RM. A Model for Magnetization-Transfer in Tissues. Magnetic Resonance in Medicine 1995;33(4):475-82.

189. Graham SJ, Henkelman RM. Pulsed magnetization transfer imaging: Evaluation of technique. Radiology 1999;212(3):903-10.

190. Tozer DJ, Davies GR, Altmann DR, Miller DH, Tofts PS. Correlation of Apparent Myelin Measures Obtained in Multiple Sclerosis Patients and Controls From

Magnetization Transfer and Multicompartmental T2 Analysis. Magnetic Resonance in Medicine 2005;53:1415-22.

191. Moore GRW, Leung E, MacKay A, Vavasour IM, Whittall K, Cover KS, Li DKB, Hashimoto SA, Oger J, Sprinkle TJ, Paty DW. A pathology-MRI study of the short-T2 component in formalin-fixed multiple sclerosis brain. Neurology 2000;55 :1506-10.

192. Stanisz G, Midha R, Munro CA, Henkelman RM. MR properties of rat sciatic nerve following trauma. Magnetic Resonance in Medicine 2001;45(3):-415.

193. Stanisz GJ, Kecojevic A, Bronskill MJ, Henkelman RM. Characterising white matter with magnetization transfer and T2. Magnetic Resonance in Medicine 1999;42(6):1128-36.

194. Li JG, Graham SJ, Henkelman RM. A flexible magnetization transfer line shape derived from tissue experimental data. Magnetic Resonance in Medicine 1997;37(6):866-71.

195. Harrison R, Bronskill MJ, Henkelman RM. Magnetization-Transfer and T-2 Relaxation Components in Tissue. Magnetic Resonance in Medicine 1995;33(4):490-6.

196. Wu X, Listinsky JJ. Effects of Transverse Cross Relaxation on Magnetisation Transfer. Journal of Magnetic Resonance Series B 1994;105:73-6.

197. Caines GH, Schleich T, Rydzewski JM. Journal of Magnetic Resonance 1991;95(3):558-66.

198. Yeung HN, Adler RS, Swanson SD. Transient decay of longitudinal magnetization in heterogeneous spin systems under selective saturation. IV. Reformulation of the spin-bath-model equations by the Redfield-Provotorov theory. Journal of Magnetic Resonance Series A 1994;106:37-45.

199. Yeung HN, Swanson SD. Transient Decay of Longitudinal Magnetization in Heterogeneous Spin Systems Under Selective Saturation. Journal of Magnetic Resonance 1992 Oct;99(3):466-79.

200. Iino M. Transition from Lorentzian to Gaussian line shape of magnetisation transfer spectrum in bovine serum albumin solutions. Magnetic Resonance in Medicine 1994;32:459-63.

201. Morrison C, Stanisz G, Henkelman RM. Modeling Magnetization-Transfer for Biological-Like Systems Using A Semisolid Pool with A Super-Lorentzian Lineshape and Dipolar Reservoir. Journal of Magnetic Resonance Series B 1995;108(2):103-13.

202. Charvolin I, Rigny P. Pulsed NMR in dynamically heterogeneous systems. Journal of Magnetic Resonance 1971;4:40-6.

203. Wennerstrom H. Proton nuclear magnetic resonance lineshapes in lamellar liquid crystals. Chemical Physics Letters 1973;18(1):41-4.

204. Bloom M, Burnell EE, Roeder WBW, Valic MI. Nuclear magnetic resonanced line shapes in lyotropic liquid crystals and related systems. Journal of Chemical Physics 1977;66:3012-20.

205. Quesson B, Thiaudiere E, Delalande C, Dousset V, Chateil JF, Canioni P. Magnetization transfer imaging in vivo of the rat brain at 4.7T: interpretation using a binary spin-bath model with a superLorentzian lineshape. Magnetic Resonance in Medicine 1997;38(6):974-80.

206. Fermi E. Physics of NMR spectroscopy in Medicine and Biology. North Holland Physics Publishing 1988.

207. Kubo R, Tomita K. A general theory of magnetic resonance absorption. Journal of the Physical Society of Japan 1954;9:888-919.

208. Sled JG, Pike GB. Quantitative imaging of magnetization transfer exchange and relaxation properties in vivo using MRI. Magnetic Resonance in Medicine 2001;46(5):923-31.

209. Cercignani M, Symms MR, Schmierer K, Boulby PA, Tozer DJ, Ron MA, Tofts PS, Barker GJ. Three-dimensional quantitative magnetisation transfer imaging of the human brain. NeuroImage 2005;27(2):436-41.

210. Abragam A, Goldman M. Nuclear magnetism: order and disorder. 1st ed. Oxford: Oxford University Press; 1982.

211. Goldman M. Quantum Description of High-resolution NMR in Liquids. New York: Oxford University Press; 1988.

212. Yarnykh VL. Pulsed Z-spectroscopic imaging of cross-relaxation parameters in tissues for human MRI: theory and clinical applications. Magnetic Resonance in Medicine 2002;47(5):929-39.

213. Yarnykh VL, Yuan C. Cross-relaxation imaging reveals detailed anatomy of white matter fiber tracts in the human brain. NeuroImage 2004 Sep;23(1):409-24.

214. Yarnykh VL, Yuan C. Cross-relaxation imaging reveals detailed anatomy of white matter fiber tracts in the human brain. NeuroImage 2004 Sep;23(1):409-24.

215. Ramani A, Tofts PS. Comparison of Continuous Wave Theory to Pulsed Multicentre Data. Proceedings of the International Society of Magnetic Resonance in Medicine 2000;8:2078.

216. Ramani A, Barker GJ, Tofts PS. Fast measurement of quantitative MT parameters in fixed multiple sclerosis brain. Proceedings of the International Society of Magnetic Resonance in Medicine 2001;9:259.

217. McGowan JC, Schnall MD, Leigh JS. Magnetization transfer imaging with pulsed off-resonance saturation: variation in contrast with saturation duty cycle. Journal of Magnetic Resonance Imaging 1994;4(1):79-82.

218. Ewing JR, Jiang Q, Boska MD, Zhang ZG, Brown SL, Li GH, Divine GW, Chopp M. T1 and magnetisation transfer at 7 Tesla in acute ischaemic infarct in the rat. Magnetic Resonance in Medicine 1999;41 :696-705.

219. Barker GJ, Schreiber WG, Gass A, Ranjeva JP, Campi A, van Waesberghe JHTM, Franconi JM, Watt HC, Tofts PS. A standardised method for measuring magnetisation transfer ratio on MR imagers from different manufacturers - The EuroMT sequence. Magnetic Resonance Materials in Physics Biology and Medicine 2005 May;18(2):76-80.

220. Barker GJ, Schreiber WG, Gass A, Ranjeva JP, Campi A, van Waesberghe JHTM, Franconi JM, Watt HC, Tofts PS. A standardised method for measuring magnetisation transfer ratio on MR imagers from different manufacturers - The EuroMT sequence. Magnetic Resonance Materials in Physics Biology and Medicine 2005 May;18(2):76-80.

221. Tyler DJ, Gowland PA. Rapid quantitation of Magnetization Transfer using pulsed off-resonance irradiation and Echo Planar Imaging. Magnetic Resonance in Medicine 2005;53:103-9.

222. Adler RS, Swanson SD, Yeung HN. A three-component model for magnetization transfer. Solution by projection-operator technique, and application to cartilage. Journal of Magnetic Resonance Series B 1996;110(1):1-8.

223. Ceckler T, Maneval J, Melkowits B. Modelling magnetization transfer using a three-pool model and physically meaningful constraints on the fitting parameters. Journal of Magnetic Resonance 2001;151(1):9-27.

224. Tessier JJ, Dillon N, Carpenter TA, Hall LD. Interpretation of magnetization transfer and proton cross-relaxation spectra of biological tissues. Journal of Magnetic Resonance Series B 1995;107(2):138-44.

225. Gochberg DF, Kennan RP, Robson MD, Gore JC. Quantitative imaging of magnetization transfer using multiple selective pulses. Magnetic Resonance in Medicine 1999;41(5):1065-72.

226. Lee RR, Dagher AP. Low power method for estimating the magnetization transfer bound pool macromolecular fraction. Journal of Magnetic Resonance Imaging 1997;7(5):913-7.

227. Ropele S, Seifert T, Enzinger C, Fazekas F. Method for quantitative imaging of the macromolecular ^{1}H fraction in tissues. Magnetic Resonance in Medicine 2003;49 :864-71.

228. Tozer DJ, Ramani A, Barker GJ, Davies GR, Miller DH, Tofts PS. Quantitative magnetization transfer mapping of bound protons in multiple sclerosis. Magnetic Resonance in Medicine 2003 Jul;50(1):83-91.

229. Chai JW, Chen C, Chen JH, Lee SK, Yeung HN. Estimation of in vivo proton intrinsic and cross-relaxation rate in human brain. Magnetic Resonance in Medicine 1996;36(1):147-52.

230. Karampekios S, Papanikolaou N, Papadaki E, Maris T, Uffman K, Spilioti M, Plaitakis A, Gourtsoyiannis N. Quantification of magnetization transfer rate and native T1 relaxation time of the brain: correlation with magnetization transfer ratio measurements in patients with multiple sclerosis. Neuroradiology 2005;47:189-96.

231. Parker GJM, Barker GJ, Tofts PS. Accurate multislice gradient echo T-1 measurement in the presence of non-ideal RF pulse shape and RF field nonuniformity. Magnetic Resonance in Medicine 2001;45(5):838-45.

232. Yarnykh VL, Yuan C. Cross-relaxation imaging reveals detailed anatomy of white matter fiber tracts in the human brain. NeuroImage 2004 Sep;23(1):409-24.

233. Barker GJ, Simmons A, Arridge S, Tofts PS. A simple method for investigating the effects of non-uniformity of radiofrequency transmission and radiofrequency reception in MRI. The British Journal of Radiology 1998;71:59-67.

234. Fazekas F, Ropele S, Enzinger C, Seifert T, Strasser-Fuchs S. Quantitative magnetization tranfer imaging of pre-lesional white-matter changes in multiple sclerosis. Multiple Sclerosis 2002;8 :479-84.

235. Ropele S, Strasser-Fuchs S, Augustin M, Stollberger R, Enzinger C, Hartung HP, Fazekas F. A comparison of magnetization transfer ratio, magnetization transfer rate, and the native relaxation time of water protons related to relapsing-remitting multiple sclerosis. American Journal of Neuroradiology 2000;21(10):1885-91.

236. Tozer DJ, Ramani A, Barker GJ, Davies GR, Miller DH, Tofts PS. Quantitative magnetization transfer mapping of bound protons in multiple sclerosis. Magnetic Resonance in Medicine 2003 Jul;50(1):83-91.

237. Tofts PS, Cercignani M, Tozer DJ, Symms MR, Davies GR, Ramani A, Barker GJ. Quantitative Magnetization Transfer Mapping of Bound Protons in Multiple Sclerosis. Magnetic Resonance in Medicine 2005;53:492-3.

238. Davies GR, Ramani A, Dalton C, Tozer DJ, Wheeler-Kingshott CAM, Barker GJ, Thompson AJ, Miller DH, Tofts PS. Preliminary magnetic resonance study of the macromolecular proton fraction in white matter: a potential marker of myelin? Multiple Sclerosis 2003;9:246-9.

239. Whitaker JN, Mitchell GW, Cutter GR. Clinical outcomes and documentation of partial beneficial effects of immunotherapy for multiple sclerosis. Annals of Neurology 1995;37(1):5-6.

240. Ridha BH, Tozer DJ, MacManus DG, Symms MR, Fox NC, Tofts PS. Quantitative magnetization transfer: a pilot study in Alzheimer's disease. Proceedings of the International Society of Magnetic Resonance in Medicine 2004;11:2327.

241. Sled JG, Levesque I, Santos AC, Francis SJ, Narayan S, Brass SD, Arnold DL, Pike GB. Regional variations in normal brain shown by quantitative magnetization transfer imaging. Magnetic Resonance in Medicine 2004;51(2):299-303.

242. Levesque I, Sled JG, Narayan S, Santos AC, Brass SD, Francis SJ, Arnold DL, Pike GB. The Role of Edema and Demyelination in Chronic T1 Black Holes: A Quantitative Magnetization Transfer study. Journal of Magnetic Resonance Imaging 2005;21:103-10.

243. Kiefer C, Slotboom J, Buri C, Gralla J, Remonda L, Dierks T, Strik WK, Schroth G, Kalus P. Differentiating hippocampal subregions by means of quantitative magnetisation transfer and relaxometry: preliminary results. NeuroImage 2004;23:1093-9.

244. Strange BA, Dolan RJ. Segregating the functions of the human hippocampus. Neurobiology 1999;96:4034-9.

245. Vavasour IM, Whittall K, MacKay A, Li DK, Vorobeychik G, Paty D. A comparison between magnetization transfer ratios and myelin water percentages in normals and multiple sclerosis patients. Magnetic Resonance in Medicine 1998;40(5):763-8.

246. Yarnykh VL, Yuan C. Cross-relaxation imaging reveals detailed anatomy of white matter fiber tracts in the human brain. NeuroImage 2004 Sep;23(1):409-24.

247. Yarnykh VL, Yuan C. Cross-relaxation imaging reveals detailed anatomy of white matter fiber tracts in the human brain. NeuroImage 2004 Sep;23(1):409-24.

248. van Buchem MA, McGowan JC, Kolson DL, Polansky M, Grossman RI. Quantitative volumetric magnetization transfer analysis in multiple sclerosis: Estimation of macroscopic and microscopic disease burden. Magnetic Resonance in Medicine 1996;36(4):632-6.

249. van Buchem MA, Udupa JK, McGowan JC, Miki Y, Heyning FH, Boncoeur-Martel MP, Kolson DL, Polansky M, Grossman RI. Global volumetric estimation of disease burden in multiple sclerosis based on magnetization transfer imagin. American Journal of Neuroradiology 1997;18:1287-90.

250. Tofts PS, Steens SCA, Dehmeshki J, Hofman P, van Waesberghe JH, van Buchem MA. Matching MTR Histograms for Multi-Centre Studies. Proceedings of the International Society of Magnetic Resonance in Medicine 1990;2.

251. Samson RS, Wheeler-Kingshott CAM, Tozer DJ, Tofts PS. A simple correction for B1 inhomogeneities in MTR measurements. Proceedings of the International Society of Magnetic Resonance in Medicine 2004;12th annual meeting, Kyoto 2004:2703.

252. Samson RS, Wheeler-Kingshott CAM, Symms MR, Tozer DJ, Tofts PS. A simple correction for B1 field errors in magnetization transfer ratio measurements. Magnetic Resonance Imaging 2006;24(3):255-63.

253. Stollberger R, Wach P. RF field mapping *in vivo*. Proceedings of the International Society of Magnetic Resonance in Medicine 1988;works-in-progress volume:106.

254. Tofts PS. Standing waves in uniform water phantoms. Journal of Magnetic Resonance Series B 1994;104 :143-7.

255. Barker GJ, Schreiber WG, Gass A, Ranjeva JP, Campi A, van Waesberghe JHTM, Franconi JM, Watt HC, Tofts PS. A standardised method for measuring magnetisation transfer ratio on MR imagers from different manufacturers - The EuroMT sequence. Magnetic Resonance Materials in Physics Biology and Medicine 2005 May;18(2):76-80.

256. Young IR, Payne JA. Slice-shape artifact changes with precession angle in rapid MR imaging. Magnetic Resonance in Medicine 1987;5:177-81.

257. Hua J, Hurst GC. Analysis of on- and off-resonance magnetization transfer techniques. Journal of Magnetic Resonance Imaging 1995;5(1):113-20.

258. Insko EK, Bolinger L. Mapping of the Radiofrequency Field. Journal of Magnetic Resonance Series A 1993;103 :82-5.

259. Sled JG, Pike GB. Standing-wave and RF penetration artifacts caused by elliptic geometry: an electrodynamic analysis of MRI. IEEE Trans Medical Imaging 1998;17:87-97.

260. Alecci M, Collins CM, Smith MB, Jezzard P. Radio Frequency Magnetic Field Mapping of a 3 Tesla Birdcage Coil: Experimental and Theoretical Dependence on Sample Properties. Magnetic Resonance in Medicine 2001;46 :379-85.

261. Collins CM, Smith MB. Signal-to-noise ratio and absorbed power as functions of main magnetic field strength, and definition of "90 degrees" RF pulse for the head in the birdcage head coil. Magnetic Resonance in Medicine 2001;45:684-91.

262. Ibrahim TS, Lee R, Baertlein BA, Abduljalil AM, Zhu H, Robatille PM. Effect of RF coil excitation on field inhomogeneity at ultra high fields: a field optimized TEM resonator. Journal of Magnetic Resonance Series A 2001;103:82-5.

263. Tofts PS. The Measurement Process: MR Data Collection and Image Analysis. In: Tofts PS, editor. Quantitative MRI of the Brain: Measuring Changes Caused by Disease. 1st ed. Chichester: John Wiley & Sons; 2003. p 17-54.

264. Ropele S, Filippi M, Valsasina P, Korteweg T, Barkhof F, Tofts PS, Samson RS, Miller DH, Fazekas F. Assessment and Correction of B1 induced errors in Magnetization Transfer Ratio Measurements. Magnetic Resonance in Medicine 2005;53:134-40.

265. Stollberger R, Wach P. Imaging of the Active B1 Field In Vivo. Magnetic Resonance in Medicine 1996;35 :246-51.

266. Hoult DI. The solution of the Bloch equation in the presence of a varying B1 field - an approach to selective pulse analysis. Journal of Magnetic Resonance 1979;35:69-86.

267. Bakker CJG, de Graaf CN, van Dijk P. Derivation of quantitative information in NMR imaging: a phantom study. Physics in Medicine and Biology 1984;29(12):1511-25.

268. Barker GJ. 3D fast FLAIR: A CSF-nulled 3D Fast Spin Echo Pulse Sequence. Magnetic Resonance Imaging 1998;16(7):715-20.

269. Stevenson VL, Parker GJM, Barker GJ, Birnie K, Tofts PS, Miller DH, Thompson AJ. Variations in T1 and T2 relaxation times of normal appearing white matter and lesions in multiple sclerosis. Journal of the Neurological Sciences 2000;178(2):81-7.

270. Rydberg JN, Riederer SJ, Rydberg CH, Jack CR. Contrast Optimization of Fluid-Attenuated Inversion Recovery (FLAIR) Imaging. Magnetic Resonance in Medicine 1995;34:868-77.

271. Listerud J, Mitchell JR, Bagley LJ, Grossman RI. OIL FLAIR: Optimized Interleaved Fluid-Attenuated Inversion Recovery in 2D Fast Spin Echo. Magnetic Resonance in Medicine 1996;36:320-5.

272. Barker GJ, Schreiber WG, Gass A, Ranjeva JP, Campi A, van Waesberghe JHTM, Franconi JM, Watt HC, Tofts PS. A standardised method for measuring magnetisation transfer ratio on MR imagers from different manufacturers - The EuroMT sequence. Magnetic Resonance Materials in Physics Biology and Medicine 2005 May;18(2):76-80.

273. Studholme C, Hill DLG, Hawkes DJ. An overlap invariant measure of 3D medical image alignment. Pattern Recognition 1999;32(1):71-86.

274. Bland JM, Altman DG. Statistical methods for assessing agreement between two methods of clinical measurement. Lancet 1986;1(8476):307-10.

275. Tofts PS, Steens SCA, Dehmeshki J, Hofman P, van Waesberghe JH, van Buchem MA. Matching MTR Histograms for Multi-Centre Studies. Proceedings of the International Society of Magnetic Resonance in Medicine 1380;2(1380).

276. Harvey I, Tofts PS, Morris JK, Wicks DAG, Ron MA. Sources of T1 variance in normal human white matter. Magnetic Resonance Imaging 1991;9:53-9.

277. Tofts PS, Steens SCA, van Buchem MA. MT: Magnetisation Transfer. In: Tofts PS, editor. Quantitative MRI of the Brain. 1st ed. Chichester: John Wiley & Sons; 2003. p 257-98.

278. Mendelson D, Heinsbergen JF, Kennedy SD, Szczepaniak LS, Lester CC, Bryant RG. Comparison of agarose and cross-linked protein gels as magnetic resonance imaging phantoms. Magnetic Resonance Imaging 1991;9 :975-8.

279. Walker PM, Balmer C, Ablett S, Lerski RA. A test material for tissue characterisation and system calibration in MRI. Physics in Medicine and Biology 1989;34 (1):5-22.

280. Koenig SH, Brown RD. A molecular theory of relaxation and magnetisation transfer: application to cross-linked BSA, a model for tissue. Magnetic Resonance in Medicine 1993;30 :685-95.

281. Koenig SH, Brown RD, Ugolini R. Magnetization transfer in cross-linked bovine serum albumin solutions at 200 MHz: a model for tissue. Magnetic Resonance in Medicine 1993;29(3):311-6.

282. Kellar KE, Koenig SH, Briley-Saebo K, Spiller M. Agarose gels as a stimulated tissue matrix for MRI: the importance of a 3-D gel structure and magnetization transfer. Proceedings of the International Society of Magnetic Resonance in Medicine 1998;1567.

283. Barker GJ, Schreiber WG, Gass A, Ranjeva JP, Campi A, van Waesberghe JHTM, Franconi JM, Watt HC, Tofts PS. A standardised method for measuring magnetisation transfer ratio on MR imagers from different manufacturers - The EuroMT sequence. Magnetic Resonance Materials in Physics Biology and Medicine 2005 May;18(2):76-80.

284. Barker GJ, Schreiber WG, Gass A, Ranjeva JP, Campi A, van Waesberghe JHTM, Franconi JM, Watt HC, Tofts PS. A standardised method for measuring magnetisation transfer ratio on MR imagers from different manufacturers - The EuroMT sequence. Magnetic Resonance Materials in Physics Biology and Medicine 2005 May;18(2):76-80.

285. Tozer DJ, Ramani A, Barker GJ, Davies GR, Miller DH, Tofts PS. Quantitative magnetization transfer mapping of bound protons in multiple sclerosis. Magnetic Resonance in Medicine 2003 Jul;50(1):83-91.

286. Grad J, Bryant RB. Nuclear magnetic cross-relaxation spectroscopy. Journal of Magnetic Resonance 1990;90:1-8.

287. Koenig SH, Brown RD. Field Cycling Relaxometry of Protein Solutions and Tissue: Implications for MRI. Progress in Nuclear Magnetic Resonance Spectroscopy 1991;22(6):487-567.

288. Bouchard L, Bronskill MJ. Magnetic resonance imaging of thermal coagulation effects in a phantom for calibrating thermal therapy devices. Medical Physics 2000 May;27(5):1141-5.

289. Bertini I, Luchinat C, Parigi G, Quacquarini G, Marzola P, Cavagna FM. Off-resonance experiments and contrast agents to improve magnetic resonance imaging. Magnetic Resonance in Medicine 1998;(124):131.

290. Zhou D, Bryant RB. Magnetization Transfer, Cross-Relaxation, and Chemical Exchange in Rotationally Immobilized Protein Gels. Magnetic Resonance in Medicine 1994;32 :725-32.

291. Grad J, Mendelson D, Hyder F, Bryant RB. Direct measurements of longitudinal relaxation and magnetization transfer in heterogeneous systems. Journal of Magnetic Resonance 1990;86:416-9.

292. Barker GJ, Schreiber WG, Gass A, Ranjeva JP, Campi A, van Waesberghe JHTM, Franconi JM, Watt HC, Tofts PS. A standardised method for measuring magnetisation transfer ratio on MR imagers from different manufacturers - The EuroMT sequence. Magnetic Resonance Materials in Physics Biology and Medicine 2005 May;18(2):76-80.

293. Venkatesan R, Lin W, Gurleyik K, He YY, Paczynski RP, Powers WJ, Hsu CY. Absolute measurements of water content using magnetic resonance imaging: preliminary findings in an *in vivo* focal ischemic rat model. Magnetic Resonance in Medicine 2000;43 :146-50.

294. Barker GJ, Schreiber WG, Gass A, Ranjeva JP, Campi A, van Waesberghe JHTM, Franconi JM, Watt HC, Tofts PS. A standardised method for measuring magnetisation transfer ratio on MR imagers from different manufacturers - The EuroMT sequence. Magnetic Resonance Materials in Physics Biology and Medicine 2005 May;18(2):76-80.

295. Tofts PS, Lloyd D, Clark CA, Barker GJ, Parker GJM, McConville P, Baldock C, Pope JM. Test liquids for quantitative MRI measurements of self-diffusion coefficient in vivo. Magnetic Resonance in Medicine 2000;43 :368-74.

296. Samson RS, Thornton JS, Wheeler-Kingshott CAM, McLean MA, Williams SCR, Tofts PS. Absolute Internal Thermometry in MRI Phantoms using 1H-MRS to 50 milli-degree level precision. Proceedings of the International Society of Magnetic Resonance in Medicine 2005;13:2511.

297. Samson RS, Thornton JS, McLean MA, Williams SCR, Tofts PS. 1H-MRS internal thermometry in test-objects (phantoms) to within 0.1 K for quality assurance in long-term quantitative MR studies. NMR in Biomedicine 2006 Aug;19(5):560-5.

298. Le Bihan D, Delannoy J, Levin RL. Temperature Mapping with MR Imaging of Molecular Diffusion: Application of Hyperthermia. Radiology 1989;171:853-7.

299. Delannoy J, Chen C, Turner R, Levin RL, Le Bihan D. Noninvasive Temperature Imaging Using Diffusion MRI. Magnetic Resonance in Medicine 1991;19:333-9.

300. Hindman JC. Proton Resonance Shift of Water in the Gas and Liquid States. The Journal of Chemical Physics 1965;44(12):4582-92.

301. Corbett R, Tollefsbol G, Laptook A. Measurement of Brain Temperature *in vivo* using ^{1}H NMR Spectroscopy. Proceedings of the Society of Magnetic Resonance, 2nd Annual Meeting 1994;516.

302. Lutz NW, Kuesel AC, Hull WE. A ^{1}H-NMR Method for Determining Temperature in Cell Culture Perfusion Systems. Magnetic Resonance in Medicine 1993;29(1):113-8.

303. De Porter J, Wagter C, De Deene Y, Thomsen C, Stahlberg F, Achten E. Noninvasive MRI thermometry with the proton resonance frequency (PRF) method: In vivo results in human muscle. Magnetic Resonance in Medicine 1995;33:74-81.

304. Cady EB, D'Souza PC, Penrice J, Lorek A. The Estimation of Local Brain Temperature by *in vivo* ^{1}H Magnetic Resonance Spectroscopy. Magnetic Resonance in Medicine 1995;33:862-7.

305. Martin M, Labouesse J, Canioni P, Merle M. *N-Acetyl-L*-Aspartate and Acetate 1H NMR Signal Overlapping under Mild Acidic pH Conditions. Magnetic Resonance in Medicine 1993;29:692-4.

306. Wishart DS, Bigam CG, Yao J, Abildgaard F, Dyson HJ, Oldfield E, Markley JL, Sykes BD. H-1, C-13 and N-15 Chemical Shift referencing in biomolecular NMR. Journal of Biomolecular NMR 1995;6(2):135-40.

307. Rice JR, Milbrandt RH, Madsen EL, Frank GR, Boote EJ, Blechinger JC. Anthropomorphic ^{1}H MRS Head Phantom. Medical Physics 1998 Jul;25(7):1145-56.

308. DeMarco A. pH Dependence of Internal References. Journal of Magnetic Resonance 1977;26:527-8.

309. Jackson JS, Tozer DJ, Tofts PS. Measurement of subtle scanner changes using a constant temperature phantom. Proceedings of the European Society for Magnetic Resonance in Medicine and Biology 2004;431.

310. Vanhamme L, van den Boogart A, Van Huffel S. Improved Method for Accurate and Efficient Quantification of MRS Data with Use of Prior Knowledge. Journal of Magnetic Resonance 1997;129(1):35-43.

311. Naressi A, Couturier C, Castang I, de Beer R, Graveron-Demilly D. Java-based graphical user interface for MRUI, a software package for quantitation of *in vivo*/medical magnetic resonance spectroscopy signals. Computers in Biology and Medicine 2001 Jul;31(4):269-86.

312. Taylor JR. An Introduction to Error Analysis: The Study of Uncertainties in Physical Measurements. 2nd ed. Sausalito, CA, USA: University Science Books; 1997.

313. Thornton JS, Cady EB, Bainbridge AB, Priest AN, Iwata O, Iwata S, Shanmugalingam S, Wyatt JS, Ordidge RJ. Automatic determination of relative peak positions in non-water-suppressed proton spectra for cerebral temperature mapping by spectroscopic imaging. Proceedings of the International Society of Magnetic Resonance in Medicine 2003;11:263.

314. Press WH, Teukolsky SA, Vetterling WT, Flannery BP. Numerical Recipes in C. The Art of Scientific Computing. 2nd ed. New York: Cambridge University Press; 1992.

315. Bevington PR, Robinson DK. Data Reduction and Error Analysis in the Physical Sciences. 3rd ed. McGraw-Hill Higher Education; 2003.

316. Marquardt DW. Journal for the Society for Industrial and Applied Mathematics 1963;11:431-41.

317. Priestley MB. Spectral Analysis and Time Series. 1st ed. London: Academic Press; 1981.

318. Cramer H. Mathematical Methods of Statistics. 1st ed. Princeton University Press; 1946.

319. Norton JP. An Introduction to Identification. 1st ed. London: Academic Press; 1986.

320. Davison AC. Statistical Models. 1st ed. Cambridge University Press; 2003.

321. Rao MM. Stochastic Processes. Inference Theory. 1 ed. Dordrecht: Kluwer Academic Publishers; 2000.

322. Jones JA, Hodgkinson P, Barker AL, Hore PJ. Optimal Sampling Strategies for the Measurement of Spin-Spin Relaxation Times. Journal of Magnetic Resonance Series B 1996;113:25-34.

323. Gudbjartsson H, Patz S. The Rician Distribution of Noisy MRI Data. Magnetic Resonance in Medicine 1995;34 :910-4.

324. Wheeler-Kingshott CAM, Parker GJM, Symms M, Hickman SJ, Tofts PS, Miller DH, Barker GJ. ADC Mapping of the Human Optic Nerve: Increased Resolution, Coverage, and Reliability With CSF-Suppressed ZOOM-EPI. Magnetic Resonance in Medicine 2002;47 :24-31.

325. Tarantola A. Inverse Problem Theory. 1st ed. Amsterdam: Elsevier; 1987.

326. Gentle JE. Random Number Generation and Monte Carlo Methods. 2nd ed. New York: Springer; 2003.

327. Rubenstein RY. Simulation and the Monte Carlo Method. 1st ed. Chichester: Wiley; 1981.

328. Tozer DJ, Ramani A, Barker GJ, Davies GR, Miller DH, Tofts PS. Quantitative magnetization transfer mapping of bound protons in multiple sclerosis. Magnetic Resonance in Medicine 2003 Jul;50(1):83-91.

329. Knuth DE. The Art of Computer Programming. 2nd ed. Reading, Massachussetts: Addison-Wesley Publishing Company; 1981.

330. Yarnykh VL, Yuan C. Cross-relaxation imaging reveals detailed anatomy of white matter fiber tracts in the human brain. NeuroImage 2004 Sep;23(1):409-24.

331. Edelstein WA, Bottomley PA, Pfeifer LM. A signal-to-noise calibration procedure for NMR imaging systems. Medical Physics 1984;11:180-5.

332. Tozer DJ, Ramani A, Barker GJ, Davies GR, Miller DH, Tofts PS. Quantitative magnetization transfer mapping of bound protons in multiple sclerosis. Magnetic Resonance in Medicine 2003 Jul;50(1):83-91.

333. Barker GJ, Schreiber WG, Gass A, Ranjeva JP, Campi A, van Waesberghe JHTM, Franconi JM, Watt HC, Tofts PS. A standardised method for measuring magnetisation transfer ratio on MR imagers from different manufacturers - The EuroMT sequence. Magnetic Resonance Materials in Physics Biology and Medicine 2005 May;18(2):76-80.

334. Samson RS, Thornton JS, McLean MA, Williams SCR, Tofts PS. 1H-MRS internal thermometry in test-objects (phantoms) to within 0.1 K for quality assurance in long-term quantitative MR studies. NMR in Biomedicine 2006 Aug;19(5):560-5.

335. Tozer DJ, Ramani A, Barker GJ, Davies GR, Miller DH, Tofts PS. Quantitative magnetization transfer mapping of bound protons in multiple sclerosis. Magnetic Resonance in Medicine 2003 Jul;50(1):83-91.

336. Samson RS, Symms MR, Tofts PS. Optimisation of quantitative MT (qMT) sequence acquisition parameters. Proceedings of the International Society of Magnetic Resonance in Medicine 2006;14:2493.

337. Tofts PS, Cercignani M, Tozer DJ, Symms MR, Davies GR, Ramani A, Barker GJ. Quantitative Magnetization Transfer Mapping of Bound Protons in Multiple Sclerosis - correction. Magnetic Resonance in Medicine 2005;53:492-3.

338. Yarnykh VL, Yuan C. Cross-relaxation imaging reveals detailed anatomy of white matter fiber tracts in the human brain. NeuroImage 2004 Sep;23(1):409-24.

Appendix A: Derivation of Bi-exponential solutions to the Bloch Equations following the application of an MT pulse

If it is assumed that the free pool magnetisation (as a function of time t) is given by:

$$M_Z^A(t) = M_0^A + c_1 e^{-\lambda_1 t} + c_2 e^{-\lambda_2 t} \quad \text{A 1}$$

Equations 5.10 and 5.11 can be rewritten as:

$$\frac{dM_Z^A}{dt} = aM_Z^A + bM_Z^B + k \quad \text{A 2}$$

$$\frac{dM_Z^B}{dt} = cM_Z^A + dM_Z^B + l \quad \text{A 3}$$

where:

$a = -(R_A + RM_0^B)$ A 4

$b = RM_0^A$ A 5

$c = -(R_B + RM_0^A)$ A 6

$d = RM_0^B$ A 7

$k = R_A M_0^A$ =constant A 8

$l = R_B M_0^B$ =constant A 9

If a solution is of the form $Y(t)=K\exp(\lambda t)Y_0$, then the matrix **Z,** which is given by:

$$\mathbf{Z} = \begin{pmatrix} a & b \\ c & d \end{pmatrix} \quad \text{A 10}$$

has the property:

$$\mathbf{ZY_0} = \lambda \mathbf{Y_0} \quad \text{A 11}$$

where λ is an eigenvalue of the matrix **Z**, and there must exist a non-zero eigenvector $Y_0 = \begin{pmatrix} x_0 \\ y_0 \end{pmatrix}$. The eigenvector $\mathbf{Y_0}$ is the direction vector of the line on which the solution exists. If the solutions of the system are thought of as describing trajectories of moving objects, the eigenvector $\mathbf{Y_0}$ can be thought of as describing the motion of an object along a straight line.

Expanding equation A 11 gives:

$ax_0 + by_0 = \lambda x_0$ OR $(a-\lambda)x_0 + by_0 = 0$ A 12

$cx_0 + dy_0 = \lambda y_0$ OR $cx_0 + (d-\lambda)y_0 = 0$ A 13

Since $\mathbf{Y_0}$ is a non-zero vector, its components x_0 and y_0 cannot both be equal to zero at the same time, therefore the determinant of the system must be equal to zero:

$$(a-\lambda)(d-\lambda) + (ad-bc) = 0 \qquad \text{A 14}$$

Expansion of this equation results in the so-called characteristic polynomial, a quadratic in the eigenvalues λ:

$$\lambda^2 - (a+d)\,\lambda + (ad-bc) = 0 \qquad \text{A 15}$$

Therefore the quadratic formula can be used to solve for the eigenvalues. If eqn A 14 is rewritten as:

$$A\lambda^2 + B\lambda + C = 0 \qquad \text{A 16}$$

(where A = 1, B = -(a+d), and C = (ad-bc)), then the two possible solutions for the eigenvalues λ are given by:

$$\lambda_{1,2} = \frac{-B \pm \sqrt{B^2 - 4AC}}{2A} = \frac{(a+d) \pm \sqrt{(a+d)^2 - 4(ad-bc)}}{2} \qquad \text{A 17}$$

If there are two real, distinct roots (as would be the case for bi-exponential magnetisation evolution), the relation $B^2 - 4AC > 0$ must hold.

$$\lambda_{1,2} = \frac{(R_A+R_B+RM_0^A+RM_0^B) \pm \sqrt{(R_A+R_B+RM_0^A+RM_0^B)^2 - 4(R_AR_B+R_ARM_0^A+R_BRM_0^B)}}{2} \qquad \text{A 18}$$

which simplifies to:

$$\lambda_{1,2} = \frac{1}{2}\left\{\left[RM_0^A + RM_0^B + R_A + R_B\right] \pm \sqrt{(RM_0^B - RM_0^A + R_A - R_B)^2 + 4R^2M_0^BM_0^A}\right\} \qquad \text{A 19}$$

By substituting for M_z^A in the differential equation for M_Z^B it is also found that:

$$M_Z^B = \frac{1}{RM_0^A}\left[RM_0^AM_0^B + c_1\left(RM_0^B + R_A - \lambda_1\right)e^{-\lambda_1 t} + c_2\left(RM_0^B + R_A - \lambda_2\right)e^{-\lambda_2 t}\right] \qquad \text{A 20}$$

Therefore the longitudinal magnetisation of each of the two pools is a function of two exponential decay functions, with time constants λ_1 and λ_2. The constants c_1 and c_2 can be calculated from the initial conditions of the system. At time t=0:

$$M_Z^A(0) = c_1 + c_2 + M_0^A \qquad \text{A 21}$$

By substituting $c_1 = M_Z^A - M_0^A - c_2$ in equation A20, again with t=0 so that the exponential terms disappear, equation A22 results for the restricted pool magnetisation evolution:

$$M_Z^B = \frac{1}{RM_0^A}\left[RM_0^B + \left(M_Z^A - M_0^A - c_2\right)\left(RM_0^B + R_A - \lambda_1\right) + c_2\left(RM_0^B + R_A - \lambda_2\right)\right] \qquad \text{A 22}$$

and c_1 and c_2 are given by A 23 and A 24:

$$c_1 = \frac{\left\{\left(M_Z^A - M_0^A\right)\left(R_A + RM_0^B - \lambda_2\right) - RM_0^A\left(M_0^B - M_Z^B\right)\right\}}{\left(\lambda_1 - \lambda_2\right)} \qquad \text{A 23}$$

$$c_2 = \frac{\left\{RM_0^A\left(M_0^B - M_Z^B\right) - \left(M_Z^A - M_0^A\right)\left(R_A + RM_0^B - \lambda_1\right)\right\}}{\left(\lambda_1 - \lambda_2\right)} \qquad \text{A 24}$$

Appendix B: Approximate solutions for pulsed MT incorporating partial saturation of the semi-solid pool and the free pool (developed by Pike (reference [41]))

It is assumed that the magnetisation immediately following the pair of instantaneous and coincident restricted pool saturation and free pool excitation pulses is given by:

$$\mathbf{M}_Z^+ = \mathbf{S}\mathbf{M}_Z^- \quad \text{B 1}$$

Where **S** is a diagonal saturation matrix, with elements S_A and S_B for the free and restricted pools respectively, and the saturation fraction $S_{A,B}$ is between 0 and 1. S_B is assumed to originate only from the saturation pulse. S_A is the fractional direct saturation produced by the MT pulse multiplied by cos α to account for the effect of the excitation pulse (flip angle α).

The sequence was decomposed into different time intervals to describe each stage of the experiment. The evolution of magnetisation in each stage of the qMT experiment was described by the following equation:

$$\mathbf{M}_Z(t) = \mathbf{A}\mathbf{M}_Z(0) + \mathbf{B}\mathbf{M}_0 \quad \text{B 2}$$

where **A** and **B** are 2 x 2 matrices with elements corresponding to the coupled Bloch equations, given by:

$$a_{1,1} = [E_2(\lambda_1 - R_A + RM_0^B) - E_1(\lambda_2 - R_A + RM_0^B)]/(\lambda_1 - \lambda_2) \quad \text{B 3}$$

$$a_{1,2} = [(E_2 - E_1)RM_0^B]/(\lambda_1 - \lambda_2) \quad \text{B 4}$$

$$a_{2,1} = [(E_1 - E_2)(\lambda_1 - R_A + RM_0^B)(\lambda_2 - R_A + RM_0^B)]/[RM_0^B(\lambda_1 - \lambda_2)] \quad \text{B 5}$$

$$a_{2,2} = [E_1(\lambda_1 - R_A + RM_0^B) - E_2(\lambda_2 - R_A + RM_0^B)]/(\lambda_1 - \lambda_2) \quad \text{B 6}$$

$$b_{1,1} = [E_1(\lambda_2 - R_A + RM_0^B) - E_2(\lambda_1 - R_A + RM_0^B) + \lambda_1 - \lambda_2]/(\lambda_1 - \lambda_2) \quad \text{B 7}$$

$$b_{1,2} = [(E_2 - E_1)RM_0^B]/(\lambda_1 - \lambda_2) \quad \text{B 8}$$

$$b_{2,1} = [(E_2 - E_1)(\lambda_1 - R_A + RM_0^B)(\lambda_2 - R_A + RM_0^B)]/[RM_0^B(\lambda_1 - \lambda_2)] \quad \text{B 9}$$

$$b_{2,2} = [E_2(\lambda_1 - R_A + RM_0^B) - E_1(\lambda_2 - R_A + RM_0^B) + \lambda_1 - \lambda_2]/(\lambda_1 - \lambda_2) \quad \text{B 10}$$

where $E_1=\exp(-\lambda_1 t)$, $E_2=\exp(-\lambda_2 t)$, and the eigenvalues $\lambda_{1,2}$ are given by equation A 18.

The magnetisation at the end of each TR', $\mathbf{M}_Z^*$ can therefore be written as:

$$\mathbf{M}_Z^*(t) = \mathbf{A}\mathbf{M}_Z^+(0) + \mathbf{B}\mathbf{M}_0 = \mathbf{A}\mathbf{S}\mathbf{M}_Z^-(0) + \mathbf{B}\mathbf{M}_0 \quad \text{B 11}$$

A steady state exists when $\mathbf{M}_Z^- = \mathbf{M}_Z^*$. Solving for $\mathbf{M}_Z^-$ therefore yields the following solution for the steady state magnetisation $M_Z^-(t)$:

$$\mathbf{M}_Z^-(t) = [\mathbf{I} - \mathbf{A}\mathbf{S}]^{-1}\mathbf{B}\mathbf{M}_0 \quad \text{B 12}$$

Therefore, by computing $\left[\mathbf{I} - \mathbf{AS}\right]^{-1}\mathbf{BM}_0$, and multiplying the result by (sin α)exp(-TE/T_{2A}^{*}) to account for the attenuation due to T_2 decay during the echo delay, the observed transverse magnetisation can be written as:

$$M_Y^A = M_0^A \sin\alpha S_A' \exp(-TE/T_2^*)\left(\frac{\lambda_1(1-E_1S_B)(1-E_2)-\lambda_2(1-E_1)(1-E_2S_B)-R_A(E_1-E_2)(1-S_B)}{\lambda_1(1-E_1S_B)(1-E_2S_A)-\lambda_2(1-E_1S_A)(1-E_2S_B)-(R_A+RM_0^B)(E_1-E_2)(S_A-S_B)}\right)$$

B 13

It can be observed that if the Bloch equations are decoupled, by setting the MT exchange rate R between the two pools equal to zero, and removing the effect of the saturation pulse (i.e. setting S_A'=1), this equation reduces to equation 5.37.

Appendix C: Approximate solutions to the pulsed MT experiment incorporating Redfield-Provotorov theory for the semi-solid pool due to Sled and Pike (references [42], [197])

The coupled Bloch equations were written in a similar form to reference [41]:

$$\frac{\mathbf{M}(t)}{dt} = \mathbf{A}(t)\mathbf{M}(t) + \mathbf{B}\mathbf{M}_0 \qquad \text{C 1}$$

where **M** is a magnetisation vector, $\mathbf{M_0}$ is the fully relaxed state of the magnetisation, and **A** and **B** are matrices corresponding to the coefficients of the coupled Bloch equations.

The pulse sequence was broken down into components of free precession (fp), continuous wave irradiation (cw) of the restricted pool, or instantaneous saturation (is) of the free pool (by either pulse). The saturation is described by a diagonal saturation matrix **S** with elements [S_f 1 1], and the fractional saturation of the free pool S_f can be calculated by solving for the magnetisation of the free pool following the given pulse using the coupled Bloch equations; the ratio of the free pool magnetisation before and after the pulse is the saturation fraction.

During each of these time intervals the matrix **A** could be assumed to be constant. Also, since the transverse magnetisation of the free pool is decoupled from the other components in each of these cases, only longitudinal magnetisation components were computed, and transverse components were assumed to disappear through relaxation and spoiling. The state of the magnetisation after a period t for each of these cases is denoted $F_*(\mathbf{M},t)$ (where * is replaced by fp, cw, or is for the particular part of the sequence being modelled) and is given by:

$$F_{fp}(\mathbf{M},t)=\exp(-\mathbf{A}_{fp}t)\mathbf{M}+[\mathbf{I}-\exp(-A_{fp}t)]\mathbf{M_0} \qquad \text{C 2}$$

$$F_{cw}(\mathbf{M},t)=\exp(-\mathbf{A}_{cw}t)\mathbf{M}+[\mathbf{I}-\exp(-A_{cw}t)]\mathbf{M_0} \qquad \text{C 3}$$

$$F_{is}(\mathbf{M})=\mathbf{SM} \qquad \text{C 4}$$

To compute the saturation fraction S_A for the free pool, the magnetisation of the free pool following the given pulse is calculated using the above equation for the derivative of the magnetisation vector, with R_A and R set equal to zero and the initial condition $\mathbf{M}=\mathbf{M_0}$. The ratio of M_Z^A before and after the pulse is S_A. This was performed by numerically solving the Bloch equations to obtain the free pool magnetisation immediately before and after the pulse, and taking a ratio.

$\mathbf{M}_{cw}^{ss}$ is the steady state magnetisation vector established after a long period of continuous wave irradiation of the restricted pool and is given by:

$$\mathbf{M}_{ss}^{cw} = \begin{bmatrix} \dfrac{M_0^A\left(R_B R M_0^B + R_B R_A + R_A R M_0^A + R_{RFB} R_A\right)}{R_B R_A + R_B R M_0^B + R_A R M_0^A + R_{RFB} R_A + R_{RFB} R M_0^B} \\ \dfrac{M_0^B\left(R_B R_A + R_B R M_0^B + R_A R M_0^A\right)}{R_B R_A + R_B R M_0^B + R_A R M_0^A + R_{RFB} R_A + R_{RFB} R M_0^B} \end{bmatrix} = \begin{bmatrix} \dfrac{M_0^A\left(P + R_{RFB} R_A\right)}{(P+Q)} \\ \dfrac{M_0^B P}{(P+Q)} \end{bmatrix} \quad \text{C 5}$$

where $P = R_B R_A + R_B R M_0^B + R_A R M_0^A, Q = R_{RFB} R_A + R_{RFB} R M_0^B$

The steady state magnetisation of a periodic pulse sequence is given by:

$\mathbf{M}(t+TR')=\mathbf{M}(t)$ C 6

For example, a simplified SPGR sequence could be described in the following 3 steps: instantaneous saturation of the free pool by the excitation pulse, instantaneous saturation of the free pool by the MT pulse, and a period of continuous wave irradiation of the restricted pool (of duration TR'). The magnetisation **M** after this type of sequence would then be given by:

$\mathbf{M}=F_{cw}(\mathbf{S_2 S_1 M}, TR)$ C 7

where $\mathbf{S_1}$ and $\mathbf{S_2}$ are the fractional saturation matrices due to the MT and excitation pulses respectively.

The observed magnetisation M_{xy}^A is given by:

$$\mathbf{M}_{xy}^A = g M_0^A M_{Z,ss}^A \sin\alpha \quad \text{C 8}$$

where α is the flip angle of the excitation pulse and gM_0^A is a constant reflecting the apparent proton density and other hardware dependent factors including the scanner receiver 'gain'.

The eigenvalues $\lambda_{1,2}$ of the matrix $\mathbf{A_{cw}}$ are given by:

$$\lambda_{1,2} = \frac{1}{2}\left\{\left[R M_0^A + R M_0^B + R_A + R_B + R_{RFB}\right] \pm \sqrt{(R M_0^B - R M_0^A + R_A + R_B + R_{RFB})^2 - 4\left(R_A R_B + R M_0^A R_B + R_A R M_0^B + R_A R_{RFB} + R M_0^A R_{RFB}\right)}\right\} \quad \text{C 9}$$

and, as before $E_1=\exp(-\lambda_1 t)$, $E_2=\exp(-\lambda_2 t)$